

Wang, Qian (2015) Analysing and evaluating a thermal management solution via heat pipes for lithium-ion batteries in electric vehicles. PhD thesis, University of Nottingham.

Access from the University of Nottingham repository:

http://eprints.nottingham.ac.uk/29358/1/PhD%20Thesis_FULL_single%20sided.pdf

Copyright and reuse:

The Nottingham ePrints service makes this work by researchers of the University of Nottingham available open access under the following conditions.

This article is made available under the University of Nottingham End User licence and may be reused according to the conditions of the licence. For more details see:
http://eprints.nottingham.ac.uk/end_user_agreement.pdf

A note on versions:

The version presented here may differ from the published version or from the version of record. If you wish to cite this item you are advised to consult the publisher's version. Please see the repository url above for details on accessing the published version and note that access may require a subscription.

For more information, please contact eprints@nottingham.ac.uk



The University of
Nottingham

UNITED KINGDOM • CHINA • MALAYSIA

**Analysing and Evaluating a Thermal
Management Solution via Heat Pipes for
Lithium-ion Batteries in Electric Vehicles**

QIAN WANG, B.Eng.

Thesis submitted to
the University of Nottingham
for the degree of Doctor of Philosophy

May 2015

Dedication

*To my Mum and Dad,
for their love, support, and encouragement.*

致我亲爱的老爸老妈，
谢谢你们对我的爱，支持和鼓励。

Abstract

Thermal management is crucial in many engineering applications because it affects the electrical, material, and other properties of the system. Heat pipes have been used extensively for thermal management because of high effective thermal conductivity under two-phase heat transfer, low cost, lightweight, and the flexibility in size and shape options. A recent study focuses on the use of heat pipes for battery thermal management (BTM) in electric vehicles (EVs), which explores a new area for heat pipe applications and will be covered in this thesis.

The battery, as one and only energy source in an EV, establishes a vital barrier for automotive industry because it can make the car more expensive and less reliable. The electro-thermal characterisation of lithium-ion batteries becomes today's forefront topic, and suitable models are needed in order to control and manage battery safety and thermal behaviour. A commonly used battery model for control-oriented applications is through an equivalent circuit analogy approach. This leads to phenomenological models, which do not capture the physical principles of the battery cell, but a representation of the input/output relationship (typically voltage as a function of a current input). An assumption of temperature uniformity throughout the whole system is usually made for such model. In a real case, however, a battery cell has an internal temperature distribution due to thermal resistance and internal heat generation. Therefore, for BTM system designs and optimisations, it is desired to use a set of governing equations describing first principle physical and chemical

properties of the battery (e.g. kinetics, transport phenomena, energy dissipation of a cell) to account for internal temperature dynamics.

The modelling methodology developed in this thesis is a one-dimensional electrochemical model, decoupled and coupled with a three-dimensional flow and heat transfer model. Decoupling serves as an effective tool to evaluate cooling/preheating solutions by eliminating the dependency of temperature in battery heat generation. It relies on experimental measurements to capture the thermal effects of electrochemical processes within a cell. Coupling, on the other hand, is achieved by creating the dependency of the generated heat source and the cell temperature obtained from lumped heat transfer. This approach allows for a complete mapping of a lithium-ion battery cell temperature with respect to time and space.

Using finite element method (FEM) to evaluate battery models, coupled or decoupled with BTM, helps validate the development of model and experimental prototype. A prototype for a 2-cell prismatic battery cooling and preheating using heat pipes is therefore developed. The model is general and flexible in structure, which allows cooling parameters such as flow velocity, cooling temperature, element geometry, etc., to be easily defined and adjusted. A full experimental characterisation based on this model has been performed. The experimental results are used to characterise system thermal performance as well as validating material properties/parameters for simulation inputs. The battery cells used in this experiment are two surrogate cells filled with atonal 324. The eligibility of substituting atonal 324 for lithium-ion battery electrolytes has been assessed and confirmed. It is expected that a prototype can cover a wide range of operating conditions and simulate a much more

dynamic thermal response. This indicates that the cooling/heating solution will not be limited to one type of battery but suits for various batteries with a broader range of cooling/heating needs. Significantly, the consistency shown between the FEM and the experiment based on the 2-cell model facilitates BTM simulation at pack level, which is a scale-up model containing 30 lithium-ion batteries. The work described in this study demonstrates that heat pipes can be very beneficial to reduce thermal stress on batteries leading to thermally homogenous packs.

Additionally, an attempt of integrating biomimetic wicks for ultra-thin flat plate heat pipes (FPHPs) is made in response to space limitations in microelectronics cooling. To date, no one has devised an ultra-thin FPHP with enough vapour space by constructing different wicks for each heat pipe segment, especially under anti-gravity condition. It is thus interesting to see whether a new type of wick structure can be made to achieve an optimum heat transfer potential without jeopardising vapour zone or hindering heat transfer in evaporator and condenser.

Publications

Peer-Reviewed Journals (Published)

- [1] **Q. Wang**, B. Jiang, Q.F. Xue, H.L. Sun, B. Li, H.M. Zou, and Y.Y. Yan, “Experimental Investigation on EV Battery Cooling and Heating by Heat Pipes,” *Applied Thermal Engineering*, in press, accepted manuscript, available online 7 October 2014.
- [2] **Q. Wang**, J.J. Hong, and Y.Y. Yan, “Biomimetic Capillary Inspired Heat Pipe Wicks,” *Journal of Bionic Engineering*, v 11, n 3, p 469-480, July 2014.
- [3] X.F. Zheng, C.X. Liu, Y.Y. Yan, and **Q. Wang**, “A Review of Thermoelectrics Research – Recent Developments and Potentials for Sustainable and Renewable Energy Applications,” *Renewable and Sustainable Energy Reviews*, v 32, p 486-503, April 2014.
- [4] H.M. Zou, B. Jiang, **Q. Wang**, C.Q. Tian, and Y.Y. Yan, “Performance Analysis of a Heat Pump Air Conditioning System Coupling with Battery Cooling for Electric Vehicles,” *Energy Procedia*, v 61, p 891-894, 2014.

Peer-Reviewed Journals (In Review)

- [5] **Q. Wang**, B. Jiang, B. Li, and Y.Y. Yan, “A Critical Review of Lithium-ion Battery Thermal Model, the Development of Low Carbon Vehicles and the Solutions of Thermal Management,” submitted to *Renewable and Sustainable Energy Reviews*.

- [6] **Q. Wang**, B. Jiang, and Y.Y. Yan, “Investigating Heat Pipe Based Li-ion Battery Thermal Management for Electric Vehicles,” submitted to Applied Energy.

Conference Proceedings (Accepted)

- [7] T. Yamaguchi, **Q. Wang**, Y.Y. Yan, and J.J. Hong, “Numerical Simulation of Liquid-Gas Two-Phase Flow with Large Density Difference in Multi-Layered Sintered Wick by the Lattice Boltzmann Method,” Proceedings of the 15th International Heat Transfer Conference (IHTC-15), Kyoto, Japan, August 10-15, 2014.
- [8] H.M. Zou, B. Jiang, **Q. Wang**, Y.Y. Yan, and C.Q. Tian, “Performance Analysis of a Heat Pump Air Conditioning System Coupling with Battery Cooling for Electric Vehicles,” the 6th International Conference on Applied Energy (ICAE 2014), Taipei, Taiwan, May 30-June 02, 2014.
- [9] **Q. Wang**, B. Jiang, Q.F. Xue, H.L. Sun, B. Li, H.M. Zou, and Y.Y. Yan, “Experimental Investigation on EV Battery Cooling and Heating by Heat Pipes,” The Heat Transfer Symposium 2014, Beijing, China, May 6-9, 2014.
- [10] T. Yamaguchi, **Q. Wang**, and Y.Y. Yan, “Numerical Analysis of Two-Phase Flow in Sintered Copper Wick by Lattice Boltzmann Method,” ASME 2013 11th International Conference on Nanochannels, Microchannels, and Minichannels, Sapporo, Japan, June 16-19, 2013.

- [11] **Q. Wang**, and Y.Y. Yan, “A Novel Integral Wick Structure for Ultra-thin Flat Heat Pipes,” The Proceedings of 11th International Heat Pipe Symposium, Beijing, China, June 9-12, 2013, p 138-145.
- [12] **Q. Wang**, and Y.Y. Yan, “Heat Pipes Research and Applications to Automotive Thermal Management,” International Microsystem, Packaging, Assembly and Circuits Technology (IMPACT) Conference, Taipei, Taiwan, October 24-26, 2012.
- [13] **Q. Wang**, and Y.Y. Yan, “The Challenges of Developing Thermal Management for Pure Electric Cars – the Role It Will Play, the Impacts on Car Industry, and A Recent Innovation,” The 2012 International Conference on Advanced Vehicle Technologies and Integration (VTI 2012), Changchun, China, July 16-19, 2012.

Acknowledgements

First and foremost I want to thank my principle supervisor, Professor **Yuying Yan**, Chair in Thermofluids Engineering and Head of HVACR & Heat Transfer Research Group. He has been very supportive since the day I began working on my final year project as an undergraduate. He encouraged me to think creatively and act decisively. It has been an honour to be his Ph.D. student. I appreciate all his efforts of time, ideas, and funding to make my Ph.D. experience productive and stimulating.

I also feel privileged to have worked with those people and group as part of a team to make this research possible. The members of FAW Group have contributed immensely to this research project, especially Dr. **Qingfeng Xue**, for his insightful advices and critics. I am grateful for having Dr. **Yupeng Wu** (secondary supervisor) and Dr. **Shenyi Wu** (internal assessor) as my academic supports, and Dr. **Bo Li** and Dr. **Bin Jiang** as my experiment advisors. I would like to acknowledge **Dave Oliver** and **Dave Taylor** for helping me set up test rigs. I very much appreciated their amazing skills in crafting and knowledge in experimentation. Special thanks to Dr. **Yong Li** and his master student Mr. **Wenjie Zhou** from South China University of Technology for fabricating integral wick structure for ultra-thin flat plate heat pipes. I also thank Dr. **Xiao Yang** (Thermacore Europe, Ltd.) for inspirational discussions in heat pipe technology, and Dr. **Nigel Neate** for providing Scanning Electron Microscopy (SEM) training to visualise wick sample surfaces.

I gratefully acknowledge the main funding source from FAW Group that made my Ph.D. work possible.

Lastly, I would like to thank my family for all their love, support, and encouragement. To my grandparents, thank you for spoiling me and loving me unconditionally. I am truly feeling blessed. To my parents, thank you for being supportive in all my pursuits. Thanks for always being there for me during the good and the bad. I am forever indebted to you. I love you all. Thank you.

Qian Wang (Cissy)

University of Nottingham

January 2015

Contents

ABSTRACT	I
PUBLICATIONS.....	IV
ACKNOWLEDGEMENTS	VII
CONTENTS	IX
LIST OF TABLES.....	XII
LIST OF FIGURES.....	XIV
NOMENCLATURE	XXIII
CHAPTER 1 INTRODUCTION.....	1
1.1 PROJECT AIMS AND OBJECTIVES.....	3
1.2 THESIS OUTLINES	4
CHAPTER 2 LITERATURE REVIEW.....	7
2.1 LITHIUM-ION BATTERIES FOR ELECTRIC VEHICLES	7
2.1.1 General Considerations.....	7
2.1.2 Mechanism and Configuration	12
2.1.3 Market Penetration and Potential	15
2.2 THERMAL ANALYSIS OF LITHIUM-ION BATTERIES.....	18
2.2.1 Safety and Thermal Runaway.....	18
2.2.2 Sub-zero Temperature Performance	22
2.3 BATTERY THERMAL MANAGEMENT STRATEGIES	25
2.3.1 Design Considerations	25
2.3.2 Thermal Management Strategies.....	28
2.4 SUMMARY.....	48
CHAPTER 3 METHODOLOGY.....	49
3.1 OVERVIEW OF BATTERY MODELS.....	49
3.1.1 Electrochemical Models	50
3.1.2 Electrical Models.....	53
3.2 HEAT GENERATION MODELLING	56
3.3 COUPLING AND DECOUPLING.....	59
3.4 FINITE ELEMENT ANALYSIS (FEA).....	67
3.5 SUMMARY.....	71

CHAPTER 4 DEVELOPMENT OF BATTERY THERMAL MODEL AND VALIDATION.....	73
4.1 DESCRIPTION OF BATTERY PACK.....	73
4.2 MODEL DEVELOPMENT.....	78
4.2.1 Battery Model	79
4.2.2 Flow and Heat Transfer Model	92
4.2.3 Mesh Sensitivity Analysis.....	97
4.3 MODEL VALIDATION	103
4.4 SUMMARY.....	107
CHAPTER 5 PROTOTYPE TESTING AND EVALUATION	109
5.1 DEVELOPMENT OF EXPERIMENT PROTOTYPE.....	109
5.1.1 Prototype Validation.....	112
5.2 EXPERIMENT SETUP	117
5.3 INSTRUMENTATION	119
5.4 DESCRIPTION OF TESTS.....	126
5.4.1 Battery Cooling.....	126
5.4.2 Battery Preheating.....	133
5.5 PROTOTYPE CHARACTERISATION	134
5.5.1 Battery Cooling.....	134
5.5.2 Battery Preheating.....	162
5.6 DATA REPEATABILITY & REPRODUCIBILITY	169
5.7 DATA REDUCTIONS AND MEASUREMENT UNCERTAINTIES	172
5.8 SUMMARY.....	175
CHAPTER 6 APPLICATION TO BATTERY THERMAL MANAGEMENT FOR ELECTRIC VEHICLES	178
6.1 A 30-LITHIUM-ION-CELL BATTERY PACK USING HEAT PIPE THERMAL MANAGEMENT.....	178
6.1.1 Battery Cell Model.....	179
6.1.2 Flow and Heat Transfer Model	183
6.1.3 Solver Sequence	186
6.2 BATTERY COOLING (SINGLE CELL, TIME DEPENDENT)	187
6.2.1 Decoupled.....	187
6.2.2 Coupled.....	189
6.3 BATTERY COOLING (30 CELLS, STATIONARY).....	195
6.3.1 Decoupled.....	195
6.3.2 Coupled (Quasi-Stationary)	199
6.4 BATTERY PREHEATING (30 CELLS, TIME DEPENDENT).....	203
6.5 SUMMARY.....	206
CHAPTER 7 EXPLORING BIOMIMETIC WICKS IN ULTRA-THIN FLAT PLATE HEAT PIPES FOR IMPROVED SURFACE WETTABILITY AND CAPILLARY LIMIT	208
7.1 CONCEPT DESIGN	208
7.1.1 Background.....	208
7.1.2 Biomimetic Possibility	210

7.1.3 Sintered Powder Wick Review	221
7.2 NOVEL HEAT PIPE WICK	225
7.2.1 Potential Mechanism	225
7.2.2 Mathematical Model	228
7.2.3 Results and Discussions	236
7.3 FABRICATION	240
7.4 SUMMARY	252
CHAPTER 8 CONCLUSIONS AND FUTURE WORK	254
8.1 CONCLUSIONS	254
8.2 FUTURE WORK	257
REFERENCES	260
APPENDIX A – THERMOCOUPLE CALIBRATION	1
APPENDIX B – FIN ANALYSIS	8
APPENDIX C – MEASUREMENT UNCERTAINTIES	11
APPENDIX D – SELECTED RAW DATA FROM TESTS	16

List of Tables

CHAPTER 2

Table 2.1: Properties of electric vehicle batteries that operate at ambient temperature (extracted from [17])	10
Table 2.2: The major components of lithium-ion batteries and their properties [18, 19].....	11
Table 2.3: List of major EV productions currently available and no longer available (by 2014)	16
Table 2.4: Thermal stability of components used in a lithium-ion battery (values measured from differential scanning calorimetry on electrodes) [19].....	19
Table 2.5: EV incidents	21
Table 2.6: Suggested operating temperature range for lithium-ion batteries ...	28
Table 2.7: A comparison among air, refrigerant and coolant BTM	39
Table 2.8: Composite PCMs in vehicular applications	43

CHAPTER 3

Table 3.1: Fundamentals of electrochemical model for lithium batteries	51
Table 3.2: Equations of electrical model for lithium batteries	55
Table 3.3: Summary of battery thermal model equations	58
Table 3.4: A summary of thermal-electrochemical models used in literature..	62
Table 3.5: Standalone thermal models (decoupled) in various studies	65

CHAPTER 4

Table 4.1: Lithium-ion cell specifications	75
Table 4.2: Model development in COMSOL Multiphysics	78
Table 4.3: Lithium-ion battery cell charge/discharge condition.....	80
Table 4.4: 1D lithium-ion battery model domain and boundary condition settings	84
Table 4.5: 3D symmetrical conjugate heat transfer model domain and boundary condition settings	94
Table 4.6: Mesh sensitivity analysis based on a 3D symmetrical model for a 4C charge/discharge rate under a 600s cycle.....	100

CHAPTER 5

Table 5.1: Surrogate battery cell versus WEIZHI lithium-ion battery cell	111
Table 5.2: L-shaped heat pipe specification	112

Table 5.3: List of instrumentation	121
Table 5.4: Aluminium fin parameters.....	130
Table 5.5: Plate perforation	132
Table 5.6: Summary of the effective thermal resistance R_{eff}	144
Table 5.7: Heating time consumption within 0.5 hours of heating	168

APPENDIX A

Table A.1: K-type thermocouple measurements before calibration.....	5
Table A.2: K-type thermocouple measurements after calibration.....	6

APPENDIX C

Table C.1: Measurement uncertainties for system without fins under 10°C...	11
Table C.2: Measurement uncertainties for system without fins under 20°C...	11
Table C.3: Measurement uncertainties for system without fins under 30°C...	12
Table C.4: Measurement uncertainties for system without fins under 35°C...	12
Table C.5: Measurement uncertainties for system with fins under 10°C.....	13
Table C.6: Measurement uncertainties for system with fins under 20°C.....	14
Table C.7: Measurement uncertainties for system with fins under 30°C.....	14
Table C.8: Measurement uncertainties for system with fins under 35°C.....	15

List of Figures

CHAPTER 1

Figure 1.1: Dimensioned 30-cell battery pack (front and top view, dimensions in mm).....	2
--	---

CHAPTER 2

Figure 2.1: Ragone plot of various electrochemical energy storage and conversion devices [7] including recently reported SOFC [8].	8
Figure 2.2: Lithium-ion battery mechanism during charge and discharge [20].	12
Figure 2.3: Battery cell configurations (modified from [22-25]).	14
Figure 2.4: Lithium-ion battery cell-, module-, and pack-level demonstrated by two vehicle examples: Tesla Roadster [26, 27] and Nissan Leaf [28].	14
Figure 2.5: Lithium-ion battery pack for a PHEV (A123 Systems) [21].	15
Figure 2.6: Illustrating three stages of the thermal response (thermal runaway path) obtained from SONY/GEN1/GEN2 lithium-ion cell [66]: (a) Stage 1-2 in scope; (b) Stage 3.	21
Figure 2.7: BTM mapping.	27
Figure 2.8: Temperature impact on life, safety and performance of lithium-ion batteries [95].	27
Figure 2.9: EV and HEV thermal and stress issues [104].	28
Figure 2.10: Air BTM methods [118].	31
Figure 2.11: (a) Insight pack [119]; (b) Prius pack [120]; and (c) Highlander pack [121] using air BTM.	32
Figure 2.12: Liquid BTM methods [118].	36
Figure 2.13: Liquid BTM using (a) refrigerant for battery cooling or (b) coolant for battery cooling/heating [122].	37
Figure 2.14: Tesla Roadster battery cooling (modified from [26, 60, 130, 131]).	37
Figure 2.15: (a) PCM BTM concept; (b) AllCell hybrid air/PCM system design [136].....	40
Figure 2.16: Hybrid air/PCM BTMS for EV normal operation	41
Figure 2.17: Pulsating heat pipe cooling a HEV lithium-ion battery pack [163].	46
Figure 2.18: Flat heat pipe cooling a HEV lithium-ion battery pack [164].....	47
Figure 2.19: Cylindrical flattened heat pipe cooling for a 118×63×13mm 8Ah LiFePO ₄ battery pack [165].	47
Figure 2.20: Aluminium grooved flat plate heat pipe put horizontally with condenser in contact with ambient air flow and water spray to cool the battery [166].	47

CHAPTER 3

Figure 3.1: Dual lithium-ion insertion cell sandwich structure developed by [171].....	50
Figure 3.2: Various equivalent circuit models used for vehicle batteries (modified from [174, 175, 177]: (a) Rint model; (b) RC model; (c) Thevenin model; and (d) PNGV model).....	54
Figure 3.3: Thermal-electrochemical coupled modelling approach [168].	60
Figure 3.4: Multi-scale physics and micro-macroscopic modelling approach applied into a lithium-ion battery (modified from [191, 192]).....	60
Figure 3.5: Coupled thermal-electrical model for an A123 LiPO4/graphite battery [193].....	61
Figure 3.6: A comparison of thermal energy generated using local heat generation and lumped thermal models under adiabatic conditions [197].	63
Figure 3.7: Heat generated due to various terms contributing to the total heat (a) under 2C discharge of a lithium-ion cell; and (b) under various discharge C rates [197].	64
Figure 3.8: Heat transfer from internal battery cell to the cell container surface and to the surroundings.....	66
Figure 3.9: Comparison of predicted cell temperature between thermo-electrochemical coupled and decoupled model during (a) 1C charging and (b) 1.5V float charging [168].....	66
Figure 3.10: Approximating the circumference of a circle by line elements [213]: (a) circle of radius R; (b) uniform and nonuniform meshes used to represent the circumference of the circle; (c) a typical element.	67
Figure 3.11: 2D thermal modelling of a HEV module without/with air cooling (modified from [95, 214]).....	69
Figure 3.12: Finite element model details for battery cell using (a) internal core heating; (b) external jacket heating; (c) internal jacket heating; (d) internal fluid heating [126].	70
Figure 3.13: (a) Panasonic NiMH battery module (7.2V, 6.5A) used in 2001 Toyota Prius; (b) FEA of 2001 Panasonic module (with case – left; without case – right); (c) model prediction for 2004 module, temperature distribution after 3min from the start of 100A discharge [216].	71

CHAPTER 4

Figure 4.1: System layout.....	75
Figure 4.2: Heat pipe BTMS demonstration with marked cell numbers and dimensions in mm.....	77
Figure 4.3: Decoupled model.	79
Figure 4.4: Heat generation rate per unit cell under charge/discharge current. 80	
Figure 4.5: Coupling between the cell and flow and heat transfer model using the average values for the temperature and battery heat generation.....	82
Figure 4.6: 1D isothermal lithium-ion battery model created in COMSOL Multiphysics 4.3b.	82

Figure 4.7: 1:1 EC:DEC/LiPF ₆ electrolyte conductivity obtained from experimentally measured data (COMSOL stored data) using interpolation function according to concentration.	86
Figure 4.8: The voltage of the electrode materials measured from experiment.	87
Figure 4.9: Discharge curves based on 0.2C, 1C, 2C, 3C, 4C & 6C rate.	88
Figure 4.10: Wave function (angular frequency = $2 \times \pi / 600$).	89
Figure 4.11: Cell potential and battery load at 4C rate under 600 s cycle time.	89
Figure 4.12: Total power dissipation density (W/m ³) simulated from 1D lithium-ion battery under a 4C charge-discharge cycle of 600 s: (a) at 300 s and 600 s; (b) at 299.95 s and 599.95 s.	90
Figure 4.13: COMSOL Multiphysics 4.3b user interface.	93
Figure 4.14: FEM model geometry.	93
Figure 4.15: Varying mesh density for a 3D axi-symmetrical model: (a) coarse; (b) normal; and (c) fine mesh.	99
Figure 4.16: Battery surface temperature contour at 300 s obtained from (a) coarse (b) normal and (c) fine mesh.	101
Figure 4.17: 2D plot battery surface temperature contour at 600 s obtained from (a) coarse (b) normal and (c) fine mesh.	103
Figure 4.18: (a) Heat pipe effective thermal conductivity parameter validation under steady state battery cooling; (b) battery surface temperature change from initial temperature of 35°C using $k_{hp} = 3,600$ W/mK; (c) various heat pipe effective thermal conductivities from -10°C under 40°C preheating to match with experiment data; (d) 1200 s preheating behaviour with initial temperature of -20°C ($T_{amb} = -20^\circ\text{C}$, $T_{g-w} = 20^\circ\text{C}$ or 40°C , $q_{g-w} = 2.38$ l/min).	107

CHAPTER 5

Figure 5.1: Prototype geometries and dimensions (in mm).	110
Figure 5.2: Validation relationship.	113
Figure 5.3: Steady state temperature contour of the battery surface cooled by heat pipe under 1C (3.78 W/cell), 2C (11.92 W/cell), and 4C (41.27 W/cell) discharge ($T_{amb} = 35^\circ\text{C}$, $T_{g-w} = 20^\circ\text{C}$, $q_{g-w} = 2.38$ l/min).	114
Figure 5.4: Steady state temperature results with one side of the surface cooled by heat pipe under 1C (3.78 W/cell), 2C (11.92 W/cell), and 4C (41.27 W/cell) discharge ($T_{amb} = 35^\circ\text{C}$, $T_{g-w} = 20^\circ\text{C}$, $q_{g-w} = 2.38$ l/min).	115
Figure 5.5: Time-dependent average surface temperature change under a cycle time of 600s using heat source generated from 1D battery model based on an alternating charge/discharge current at 4C rate ($T_{amb} = 35^\circ\text{C}$, $T_{inlet} = 20^\circ\text{C}$, $q_{g-w} = 2.38$ l/min).	116
Figure 5.6: Experiment schematic.	118
Figure 5.7: In situ experiment details.	118
Figure 5.8: Arrangement of thermocouples on the testing L-shaped heat pipe (T_1 - T_{10}) and on the back of the plate channels for battery surface temperature measurement (T_{b1} - T_{b7}).	119
Figure 5.9: Devices used in experiment.	120
Figure 5.10: Transient scenarios.	128

Figure 5.11: Arrangement of thermocouples on the testing L-shaped heat pipe with fins ($T_{f1} - T_{f10}$).	130
Figure 5.12: (a) Plate original; (b) Plate I; (c) Plate II; (d) Plate III; (e) Plate IV.	131
Figure 5.13: Thermal resistance of (a) anti-gravity L-shaped heat pipe (R_{hp}) and (b) total including the heat pipe and the aluminium plate (R_t) under 2.38 ± 0.01 l/min rate.....	135
Figure 5.14: Thermal conductivity of anti-gravity L-shaped heat pipe (K_{hp}) under (a) different cooling temperatures and (b) different power inputs under 2.38 ± 0.01 l/min rate	136
Figure 5.15: Heat transfer coefficient at the cooling end (h_c) under different (a) cooling temperatures and (b) power inputs under 2.38 ± 0.01 l/min rate.	137
Figure 5.16: 300 s cooling response performed at initial battery surface temperature of 40°C, 50°C, 60°C and 70°C cooled by 10°C, 20°C, 30°C, 35°C discharging coolant under 2.38 ± 0.01 l/min rate.....	138
Figure 5.17: 5 minutes temperature drop at initial battery surface temperature of 40°C, 50°C, 60°C and 70°C cooled by four test conditions: 1 – 10°C, 2 – 20°C, 3 – 30°C, 4 – 35°C discharging coolant under 2.38 ± 0.01 l/min rate.	138
Figure 5.18: Average battery surface temperature change ($T_{amb} = 35^\circ\text{C}$, $T_{g-w} = 20^\circ\text{C}$, $q_{g-w} = 2.38 \pm 0.03$ l/min).....	141
Figure 5.19: Average battery surface temperature drop rate in 10 minutes under seven test conditions ($T_{amb} = 35^\circ\text{C}$, $T_{g-w} = 20^\circ\text{C}$, $q_{g-w} = 2.38 \pm 0.03$ l/min).	141
Figure 5.20: Average battery surface temperature transient behaviour under two scenarios ($T_{amb} = 35^\circ\text{C}$, $T_{g-w} = 20^\circ\text{C}$, $q_{g-w} = 2.38 \pm 0.03$ l/min).	142
Figure 5.21: (a) Overall thermal resistance (R_{hp}) and (b) thermal conductivity (K_{hp}) of L-shaped heat pipe operated against gravity with fins ($R_{hp,wf}$, $K_{hp,wf}$) and no fins ($R_{hp,nf}$, $K_{hp,nf}$) obtained from experiment.	143
Figure 5.22: Heat transfer coefficient at the cooling end: (a) versus power input; (b) versus cooling temperature.	147
Figure 5.23: A comparison of battery cooling response in 300 s between heat pipe with fins and no fins condition at initial battery surface temperature of 40°C, 50°C, 60°C and 70°C cooled by 10°C, 20°C, 30°C, 35°C discharging coolant.	148
Figure 5.24: Temperature drop in 300 s at a given initial battery surface temperature (40°C, 50°C, 60°C and 70°C) under four test conditions: 1 – 10°C; 2 – 20°C; 3 – 30°C; and 4 – 35°C cooling.	149
Figure 5.25: Fin efficiency derived from (a) Eq. B.5 – B.6 (Appendix B) under different r_f/r_o and (b) experiment data.	150
Figure 5.26: A comparison of battery surface temperature change between heat pipe w. fins and w/o fins ($T_{amb} = 35^\circ\text{C}$, $T_{g-w} = 20^\circ\text{C}$, $q_{g-w} = 2.38 \pm 0.03$ l/min)	151
Figure 5.27: A comparison of average battery surface temperature drop rate in 10 minutes between heat pipe w. fins and w/o fins under four test conditions ($T_{amb} = 35^\circ\text{C}$, $T_{g-w} = 20^\circ\text{C}$, $q_{g-w} = 2.38 \pm 0.03$ l/min)	151
Figure 5.28: A comparison of battery surface temperature transient behaviour between heat pipe w. fins and w/o fins under Scenario 1 – 4 repeated cycles ($T_{amb} = 35^\circ\text{C}$, $T_{g-w} = 20^\circ\text{C}$, $q_{g-w} = 2.38 \pm 0.03$ l/min).....	152

Figure 5.29: A comparison of battery surface temperature transient behaviour between heat pipe w. fins and w/o fins under Scenario 2 – 3 repeated cycles ($T_{amb} = 35^{\circ}\text{C}$, $T_{g-w} = 20^{\circ}\text{C}$, $q_{g-w} = 2.38 \pm 0.03$ l/min).....	153
Figure 5.30: A comparison between battery alone and battery with heat pipe cooling at one side through infrared camera ($T_{amb} = 20 \pm 2^{\circ}\text{C}$, $T_{g-w} = 20^{\circ}\text{C}$, $q_{g-w} = 2.38 \pm 0.03$ l/min, 1 – 4C battery discharging conditions, colour band range: 15 – 40°C).....	154
Figure 5.31: A comparison of battery with heat pipe cooling at one side using solid plate and perforated plates (I-IV) through infrared camera ($T_{amb} = 20 \pm 2^{\circ}\text{C}$, $T_{g-w} = 20^{\circ}\text{C}$, $q_{g-w} = 2.38 \pm 0.03$ l/min, 1 – 4C battery discharging, colour band range: 15 – 40°C).....	155
Figure 5.32: Steady state surface temperature of plate and battery from (a) original; (b) I; (c) II; (d) III; (e) IV under 2C discharge (11.92 W/cell), colour range 25 – 35 °C ($T_{amb} = 35^{\circ}\text{C}$, $T_{g-w} = 20^{\circ}\text{C}$, $q_{g-w} = 2.38$ l/min).	158
Figure 5.33: Steady state surface temperature of the plate and battery from (a) original; (b) I; (c) II; (d) III; (e) IV under 4C discharge (41.72 W/cell), colour range 40 – 65 °C ($T_{amb} = 35^{\circ}\text{C}$, $T_{g-w} = 20^{\circ}\text{C}$, $q_{g-w} = 2.38$ l/min).	159
Figure 5.34: Surface temperature of plate and battery from (a) original; (b) I; (c) II; (d) III; (e) IV after 600 s ($T_{amb} = 20^{\circ}\text{C}$, $T_{g-w} = 20^{\circ}\text{C}$, $q_{g-w} = 2.38$ l/min, 2C battery discharge).....	161
Figure 5.35: 600 s average surface temperature change of surrogate battery and lithium-ion battery with heat pipe cooling using different plates (original, plate I-IV) obtained from FEM ($T_{amb} = 20^{\circ}\text{C}$, $T_{g-w} = 20^{\circ}\text{C}$, $q_{g-w} = 2.38$ l/min, 2C battery discharge).	162
Figure 5.36: Overnight cold exposure under $-25^{\circ}\text{C}/-15^{\circ}\text{C}$ and 20°C preheating afterwards (raw data collected from TC-08 data logger).	163
Figure 5.37: Heat pipe temperature change behaviour detected when exposing it under sub-zero temperatures.	164
Figure 5.38: Preheating performance obtained from $20^{\circ}\text{C}/40^{\circ}\text{C}$ glycol-water coolant discharging at constant ambient temperature of 0°C , -15°C and -20°C : (a) average battery surface temperature rise w/o fins; (b) average battery surface temperature rise w. fins; (c) average heat pipe condenser temperature rise w/o fins; (d) average heat pipe condenser temperature rise w. fins.....	166
Figure 5.39: Repeatability evaluation of cooling performance conducted by Operator A within a short timescale.....	170
Figure 5.40: Repeatability evaluation of preheating performance conducted by Operator A within a short timescale.....	170
Figure 5.41: Reproducibility evaluation of cooling performance conducted by Operator A over two time periods (3 months interval).	171
Figure 5.42: Reproducibility evaluation of preheating performance conducted by Operator A over two time periods (3 months interval).	171

CHAPTER 6

Figure 6.1: EV driving cycles provided by FAW: (a) Cycle 1; (b) Cycle 2. ...	180
Figure 6.2: Single battery cell heat generation obtained from: (a) Cycle 1; (b) Cycle 2.	181

Figure 6.3: Cell potential and current load from an alternating 4C charge-discharge cycle obtained from 1D electrochemical model.....	182
Figure 6.4: Total heat dissipation Q_h (W/m^3) of negative electrode, positive electrode, separator, and all domains at selected times ($t = 0$ s, 299.95 s, 300 s, 599.95 s, 600 s, 899.95 s, 900 s, 1199.95 s, 1200 s, 1499.95 s, 1500 s, 2100 s).....	182
Figure 6.5: A 30-cell battery pack using heat pipe thermal management built in COMSOL 4.3b.....	184
Figure 6.6: Meshing (normal mesh size).....	184
Figure 6.7: Mesh statistics using normal mesh settings.	185
Figure 6.8: BTM comparative analysis between using heat pipe and using air convection under: (a) Cycle 1 – repeated 4 times; (b) Cycle 2 – repeated 6 times ($T_{amb} = 35^\circ C$, $T_{air} = T_{inlet} = 20^\circ C$, $v_{air} = v_{g-w} = 0.75$ m/s).....	188
Figure 6.9: Sections cut from the battery pack for model demonstration.	189
Figure 6.10: Temperature and velocity profile of Section A at $t = 300$ s, 600 s, 900 s, 1200 s, 1500 s, and 2100 s under (a) $q = 0.0595$ l/s and (b) $q = 0.595$ l/s ($T_{amb} = 35^\circ C$, $T_{inlet} = 20^\circ C$).	191
Figure 6.11: Temperature and velocity profile of Section B at $t = 300$ s, 600 s, 900 s, 1200 s, 1500 s, and 2100 s under (a) $q = 0.0595$ l/s and (b) $q = 0.595$ l/s ($T_{amb} = 35^\circ C$, $T_{inlet} = 20^\circ C$).	192
Figure 6.12: Battery temperature change (maximum and average) of the selected battery cells cooled at both sides and one side in a 30-cell battery pack (Section A and Section B) under a 2100 s 4C charge-discharge cycle mentioned in Fig. 6.3 ($T_{amb} = 35^\circ C$, $T_{inlet} = 20^\circ C$, $q = 0.0595$ l/s and 0.595 l/s).	193
Figure 6.13: Pressure distribution across the liquid zone of (a) Section A and (b) Section B under $v = 0.0595$ l/s at $t = 600$ s.	193
Figure 6.14: Pressure distribution across the liquid zone of (a) Section A and (b) Section B under $v = 0.595$ l/s at $t = 600$ s.	194
Figure 6.15: Slices of velocity distribution across the liquid zone of (a) Section A and (b) Section B under $q = 0.0595$ l/s at $t = 600$ s.	194
Figure 6.16: Slices of velocity distribution across the liquid zone of (a) Section A and (b) Section B under $q = 0.595$ l/s at $t = 600$ s.	195
Figure 6.17: Steady state temperature and velocity profile of the 30-cell battery pack under 1 – 4C discharge at (a) $q = 0.0595$ l/s and (b) $q = 0.595$ l/s ($T_{amb} = 35^\circ C$, $T_{inlet} = 20^\circ C$).	197
Figure 6.18: Pressure contour profile of the 30-cell battery pack under (a) $q = 0.0595$ l/s and (b) $q = 0.595$ l/s ($T_{amb} = 35^\circ C$, $T_{inlet} = 20^\circ C$).	197
Figure 6.19: Velocity profile (8 slices of y-z plane) of the 30-cell battery pack under (a) $q = 0.0595$ l/s and (b) $q = 0.595$ l/s ($T_{amb} = 35^\circ C$, $T_{inlet} = 20^\circ C$).	198
Figure 6.20: Steady state temperature and velocity profile of the 18-cell battery pack (cooled at both sides) under 1 – 4C discharge at (a) $q = 0.0595$ l/s and (b) $q = 0.595$ l/s ($T_{amb} = 35^\circ C$, $T_{inlet} = 20^\circ C$).	199
Figure 6.21: Quasi-stationary temperature and velocity profile of the battery pack that contains 30 cells and 18 cells at the heat generation rate $Q_{h,t}$ obtained from coupling 1D electrochemical battery model and heat transfer model at (a) $t = 300$ s and (b) $t = 600$ s.	201
Figure 6.22: Quasi-stationary temperature and velocity profile of the battery pack that contains 30 cells and 18 cells at the heat generation rate $Q_{h,t}$	

obtained from coupling 1D electrochemical battery model and heat transfer model at (a) $t = 299.95$ s and (b) $t = 599.95$ s.	202
Figure 6.23: Estimated heat power requirement under 50%, 75% and 100% efficiency.	204
Figure 6.24: Thermal response of 30-cell battery under 40°C preheating in 900s.....	205

CHAPTER 7

Figure 7.1: MRI scanning of live plants. (a) Musa X Paradisiaca. (b) Salix Flamingo. (c-d) 3D water flow distribution in xylem vessels obtained from (c) Musa X Paradisiaca and (d) Salix Flamingo. (e-f) Cross-sectional and longitudinal view of water distribution of (e) Musa X Paradisiaca and (f) Salix Flamingo (Note: signal intensity level helps reflect water distribution, blue indicates low intensity, i.e. less water; red indicates high intensity, i.e. more water). (g) MRI scanned rate of water transport J_v (mm/s) in the xylem vessel of Salix Flamingo (an average peak velocity of 0.2 mm/s was obtained).	214
Figure 7.2: Novel integral wick design for evaporator, adiabatic and condenser in flat heat pipes.....	226
Figure 7.3: Heat and liquid flow path in the evaporator.....	227
Figure 7.4: Liquid forming meniscus bridges at acute-angles among wick pores.	228
Figure 7.5: Illustrating wick pore distribution scenarios.....	228
Figure 7.6: Illustrating (a) liquid flow paths in the heat pipe; and schematic of a unit for (b) a one-scale sintered copper powder porous medium from the condenser to the evaporator (liquid return path: one flow direction); (c) a two-scale sintered copper powder porous medium in heat pipe evaporator (liquid evaporator path: one flow direction).....	232
Figure 7.7: Microscale capillary with solid-fluid and fluid-fluid interfaces. .	234
Figure 7.8: Capillary pressure P_c versus wick pore radius r (25~200 μm) at two volume porosities $\varepsilon_1 = 0.4$ and $\varepsilon_2 = 0.75$, $\eta = 8.94 \times 10^{-4}$ Pa·s, $\sigma = 0.07$ N/m, $\lambda = 1$, $\rho = 5.61 \times 10^3$ kg/m ³ (for sintered copper powder density [297]).	237
Figure 7.9: Calculated capillary speed dh/dt versus height h (gravity-assisted) at $r_1 = 25$ μm , $\varepsilon_1 = 0.4$, $r_2 = 50$ μm , $\varepsilon_2 = 0.75$, $\eta = 8.94 \times 10^{-4}$ Pa·s, $\sigma = 0.07$ N/m, $\lambda = 1$, $\tau = \sqrt{2}$	238
Figure 7.10: Calculated capillary speed dh/dt versus height h (horizontal) at $r_1 = 25$ μm , $\varepsilon_1 = 0.4$, $r_2 = 50$ μm , $\varepsilon_2 = 0.75$, $\eta = 8.94 \times 10^{-4}$ Pa·s, $\sigma = 0.07$ N/m, $\lambda = 1$, $\tau = \sqrt{2}$	238
Figure 7.11: Calculated capillary speed dh/dt versus height h (anti-gravity) at $r_1 = 25$ μm , $\varepsilon_1 = 0.4$, $r_2 = 50$ μm , $\varepsilon_2 = 0.75$, $\eta = 8.94 \times 10^{-4}$ Pa·s, $\sigma = 0.07$ N/m, $\lambda = 1$, $\tau = \sqrt{2}$	239
Figure 7.12: Schematic of the present flat plate heat pipe (FPHP) with dimensions in mm.....	241
Figure 7.13: FPHP fabricating assemblies with dimensions in mm.....	241
Figure 7.14: FPHP parts: (a) upper wick mould; (b) bottom wick mould; (c) upper copper plate; (d) bottom copper plate.....	242

Figure 7.15: Fabricated samples: (a) upper plate; (b) bottom plate; (c) final product.	243
Figure 7.16: Fabrication in process – powder filling.....	244
Figure 7.17: Fabrication in process – holding.	245
Figure 7.18: Fabrication in process – furnace sintering.	245
Figure 7.19: Fabrication in process – upper and bottom plates after sintering.	245
Figure 7.20: Fabrication in process – holding sintered upper and bottom plates.	246
Figure 7.21: Fabrication in process – product after welding.....	246
Figure 7.22: Fabrication in process – product after inserting tail pipe and welding.	247
Figure 7.23: Fabrication in process – water filling trials.....	247
Figure 7.24: Fabrication in process – (a) 1 st degassing equipment; (b) 2 nd degassing equipment.....	248
Figure 7.25: Fabrication in process – TIG welding machine.	249
Figure 7.26: SEM micrographs showing the integral wick sample (150 – 200 μm dendritic powders sintered at 960°C at the evaporator: (a) planar view; (b) profile view.	250
Figure 7.27: SEM micrographs showing the integral wick sample (150 – 200 μm dendritic powders sintered at 960°C at the condenser: (a) planar view; (b) profile view.	251
Figure 7.28: SEM micrographs showing the surface morphology of the wick particles (150 – 200 μm dendritic powders sintered at 960°C: (a) evaporator substrate; (b) evaporator pillar; (c) condenser substrate; (d) condenser pillar.....	252
Figure 8.1: Thermocouple arrangement on the flat plate heat pipe.....	258
Figure 8.2: Performance test setup for the flat plate heat pipe sample at horizontal orientation.....	259
Figure 8.3: Testing the flat plate heat pipe at various angles including anti-gravity conditions (40°, 90°) and gravity-assisted conditions (-40°, -90°).	259

APPENDIX A

Figure A.1: 16 K-type thermocouples measured readings compared with standard readings before calibration.	2
Figure A.2: 16 K-type thermocouples offsets prior to calibration.	3
Figure A.3: Example of using fitting curve for thermocouple 16.	3
Figure A.4: 16 K-type thermocouples measured readings compared with standard readings after calibration.....	4
Figure A.5: 16 K-type thermocouples offsets after calibration.	4

APPENDIX B

Figure B.1: Thermal resistance network at the condenser.....	8
--	---

APPENDIX D

Figure D.1: Steady state cooling, 2.5 W/cell 35°C ambient 20°C cooling.	16
Figure D.2: Steady state cooling, 5 W/cell 35°C ambient 20°C cooling.	16
Figure D.3: Steady state cooling, 10 W/cell 35°C ambient 20°C cooling.	17
Figure D.4: Steady state cooling, 15 W/cell 35°C ambient 20°C cooling.	17
Figure D.5: Steady state cooling, 20 W/cell 35°C ambient 20°C cooling.	18
Figure D.6: Steady state cooling, 30 W/cell 35°C ambient 20°C cooling.	18
Figure D.7: Steady state cooling, 40 W/cell 35°C ambient 20°C cooling.	19
Figure D.8: Transient cooling, 4 repeated cycles at 35°C ambient 20°C cooling.	19
Figure D.9: $-22 \pm 3^\circ\text{C}$ overnight for 15+ hours.....	20
Figure D.10: $-15 \pm 3^\circ\text{C}$ overnight for 20+ hours.....	20
Figure D.11: $-15 \pm 1^\circ\text{C}$ ambient 20°C preheating.....	21
Figure D.12: $-15 \pm 1^\circ\text{C}$ ambient 40°C preheating.....	21
Figure D.13: $-12 \pm 2^\circ\text{C}$ ambient 20°C preheating.....	22
Figure D.14: $-10 \pm 2^\circ\text{C}$ ambient 40°C preheating.....	22

Nomenclature

A	Surface area (m ²)	F	Faraday's constant (96,485 C equiv. ⁻¹)
A _f	Total surface area (m ²)	f _±	Molecular activity coefficient of the electrolyte
A _r	Surface area of unfinned portion of the heat pipe (m ²)	h	Heat transfer coefficient (W/m ² K)
A _s	Cell surface area exposed to the convective cooling medium (m ²)	h _f	Heat transfer coefficient of the ambient fluid (W/m ² K)
a _s	Specific interfacial area of an electrode (m ²)	h _r	Heat transfer coefficient of the heat pipe (W/m ² K)
B _i	Biot number	I	Current density (A)
C _b	Bulk capacitor (μF)	I _L	Load current (A)
C _c	Surface capacitor (μF)	i _{oj}	Exchange current density (A/m ²)
C _p	Specific heat capacity (J/kg°C)	J _v	Rate of transport in the xylem (mm/s)
c	Salt concentration (mol/m ³)	j ^{Li}	Transfer current (A)
c _e	Volume-average lithium concentration in the electrolyte (mol/m ³)	k _a , k _c	Anodic/cathodic rate constant (m/s)
c _l	Electrolyte salt concentration (mol/m ³)	k ^{eff}	Diffusional conductivity (W/mK)
D _e ^{eff}	Effective diffusion coefficient	k _D ^{eff}	Effective ionic conductivity (W/mK)
D _l	Electrolyte salt diffusivity	l _{eff}	Heat pipe effective length (m)
D _s	Mass diffusion coefficient of lithium-ion in the electrolyte	<i>m</i>	Mass flow rate (kg/s)
E _{act} [∥]	Activation energy		

N	Number of fins	R_f	Thermal resistance of unfinned portion of heat pipe (K/W)
Nu	Nusselt number	R_t	Terminal resistance (Ω)
P	Pressure (Pa)	R_w	Thermal resistance of the wick (K/W)
P_A	Absolute pressure (Pa)	r	Radial coordinate along active material particle (m)
Pr	Prandtl number	r_c	Effective capillary radius (m)
Q_h	General source (W/m^3)	R	Effective radius of the wick (m)
Q_{in}, Q_{out}	Heat supplied by the heaters/heat dissipated by the heat pipe (W)	r_h	Hydraulic radius (m)
Q_j	Joule heat (kJ/mol)	S	Specific surface area (m^2)
Q_p	Polarisation heat (kJ/mol)	s	Tube length (m)
Q_r	Reaction heat (kJ/mol)	T	Temperature (K or $^{\circ}C$)
Q_s	Total fluid flow discharge rate (kg/s)	T_b	Fin base temperature ($^{\circ}C$)
q	Heat generation (W/m^3) or flow rate (kg/s)	T_{batt}	Average temperature of the battery surface ($^{\circ}C$)
R	Universal gas constant, or radius (m) or resistance (Ω)	T_c, T_e	Temperature of the condenser/evaporator ($^{\circ}C$)
R_c	Capacitor resistance (Ω)	$T_{c,fin}$	Temperature of the condenser (heat pipe with fins) ($^{\circ}C$)
R_e	End resistance (Ω) or Reynolds number	T_f	Temperature of the cooling fluid ($^{\circ}C$)
R_f	Thermal resistance of fins (K/W)	T_{fin}	Temperature of the fin stack ($^{\circ}C$)
R_o	Internal resistance or ohmic resistance (Ω)	T_{in}, T_{out}	Inlet/outlet temperature ($^{\circ}C$)
R_p	Thermal resistance of the heat pipe wall (K/W)	T_{∞}	Medium temperature ($^{\circ}C$)
		t_+	Transport number

t_{\pm}°	Transference number of the Li^+ with respect to the velocity of solvent	u	Velocity (m/s)
U	Open circuit potential (V)	v	Velocity of the electrolyte (m/s)
U_L	Terminal voltage (V)	V	Cell voltage (V)
U_{oc}	Open-circuit voltage (V)	x^*	Graetz number (dimensionless flow axial distance)

Greek Symbols

α_{aj}, α_{cj}	Anodic/cathodic transfer coefficient of electrode reaction	μ	Dynamic viscosity (Pa·s)
γ	Bruggeman coefficient or ratio of specific heats	ρ	Composite/average density of the battery (kg/m^3)
δ_f	Fin thickness (m)	σ	Surface tension at the liquid-vapour interface (N/m)
ε	Volume porosity	σ^{eff}	Effective conductivity of the solid phase (W/mK)
ε_e	Volume porosity of electrolyte	σ_1	Electrolyte conductivity (W/mK)
η_j	Local surface overpotential (V)	ϕ_e	Volume-average electrical potential in electrolyte (V)
θ	Contact angle	ϕ_1	Electrolyte potential (V)
θ_e	Angle subtended by the line segment	ϕ_s	Electric potential (V)
λ	Composite/average thermal conductivity (W/mK)	ψ	Individual property
ψ_{ref}	Property value defined at reference temperature		

Chapter 1

Introduction

Heat pipes offer passive strategies to effectively facilitate heat transfer over a long distance with minimal temperature difference from one end to the other. They represent an essential field in effective cooling as many applications in science, industry, and domestic practises rely on them. In a recent study [1], heat pipe was proposed for battery thermal management (BTM) in electric vehicles (EVs). As electrical energy storage such as lithium-ion batteries play an essential role in EVs, their potential life and safety are strongly affected by thermal state. Problems such as high temperatures leading to premature failure or poor electrical performance were found in lithium-ion battery packs, because they are made of many cells interconnected in series and parallel arrangements with tightly confined spaces. A thermal management solution must be implemented in batteries to prevent potential thermal runaway caused by non-uniform battery temperature distribution, and aging due to unevenly distributed electrical performance resultant from thermal impact. These issues require a comprehensive investigation on the applied heat pipe BTM in terms of system design and thermal constraint analysis.

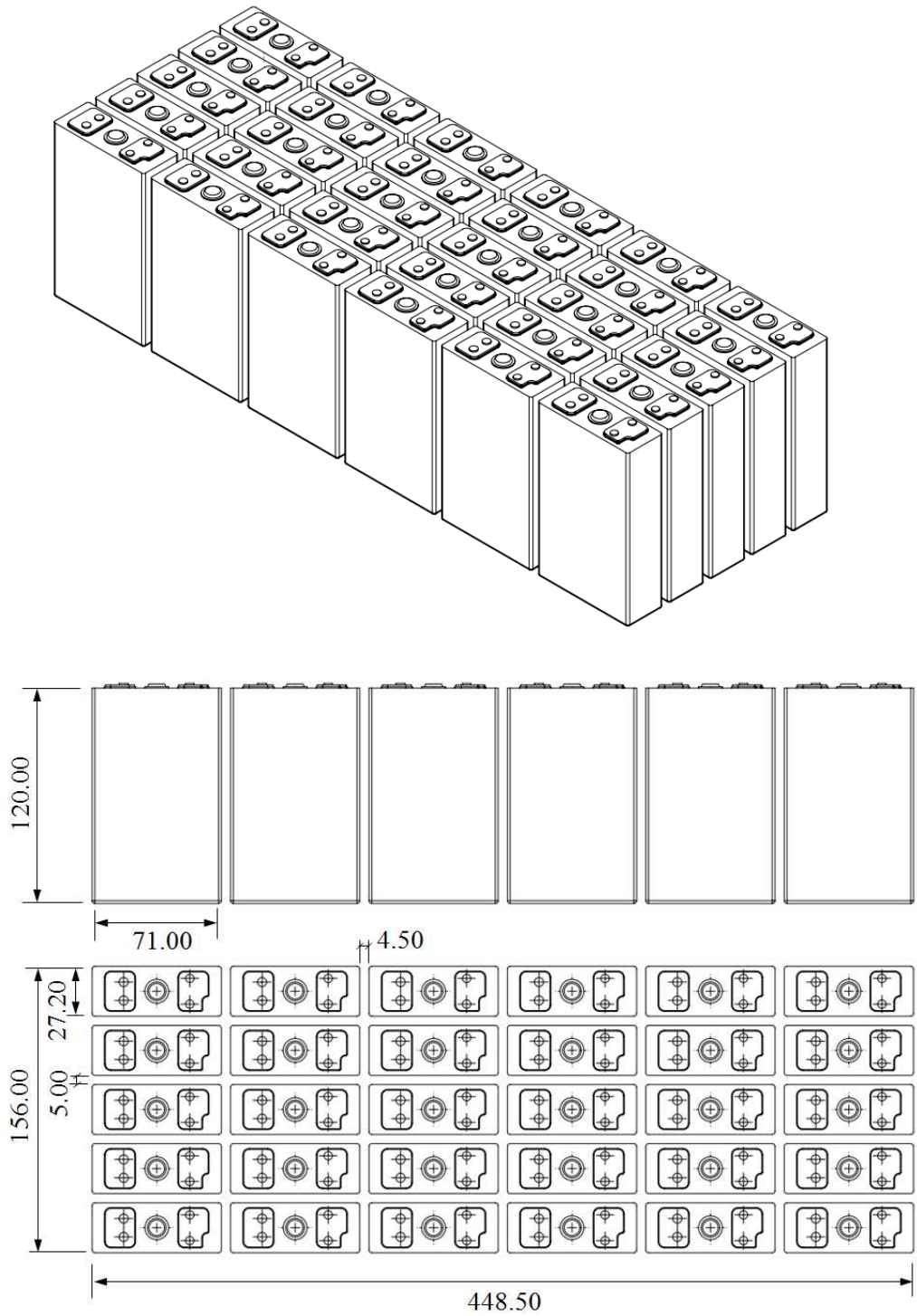


Figure 1.1: Dimensioned 30-cell battery pack (front and top view, dimensions in mm).

A 332 V, 49.5 Ah lithium-ion battery pack was provided for use in an EV.

Fig. 1.1 shows 1/10 of it for this study. The pack is assembled from 30

prismatic lithium-ion cells (WEIZHI model, 3.2 V, 16.5 Ah, $120.0 \times 71.0 \times 27.2 \text{ mm}^3$) forming a close-packed rectangular array (4.5 – 5 mm gap) inside an aluminium box. EV needs to satisfy all-weather conditions so the battery pack is sealed from the outside. Vehicle performance and space consideration require the cell to be packed closely but since the batteries generate a substantial amount of heat, this may cause potential safety hazards such as thermal runaway, fire or explosion. It is thus of great importance that BTM is employed to maintain the cell temperature over an acceptable range at all times.

In addition, capillary transport in porous medium, i.e. the wicks, will be studied as it plays an important role in heat pipe heat transfer. Many attempts have been made to enhance the capillary performance including the utilisation of mimic biology, which is often accompanied by hierarchical surface structure in micro or nano-scale applications. This indicates that by synthesising certain biomimetic function, a novel wick structure for heat pipes, especially for ultra-thin flat plate heat pipes (FPHPs), can be developed to enable a deeper insight into the fluid mechanics behind biomimetic inspired capillary dominated problems.

1.1 Project Aims and Objectives

The objectives of this research are to investigate the feasibility of applying heat pipes into BTM for EVs, and to determine how and to what degree of significance this technology can benefit battery performance. Literature reviews on lithium-ion batteries with regard to thermal analysis and thermal

management approaches are provided. Using finite element analysis (FEA) to evaluate electrochemical battery models, coupled or decoupled with BTM, helps validate the development of model and experimental prototype. A full experimental characterisation of heat pipe-based battery cooling and heating has been performed via two surrogate battery cells. This provides a quick platform to study the system heat transfer performance under stationary and time dependent conditions. A scaled-up model is then established, which aims to evaluate the application of BTM in EVs.

Furthermore, effort in modifying FPHP wicks by mimicking biology is made. FPHP can be used in areas where spatial limitation is encountered and for device such as battery cells with small gaps that requires a large surface area to volume ratio. The concept is to apply different wick structure for each heat pipe segment (i.e. evaporator, adiabatic section, and condenser) with enough vapour space while producing excellent capillary limit. Thermal characteristics of such wick structure have been mathematically modelled, and fabrication is reported.

1.2 Thesis Outlines

Chapter 1 provides research aims and objectives, outlining the amount of work completed in each chapter.

Chapter 2 investigates lithium-ion batteries for EVs from three perspectives: properties, mechanism and market potential. Thermal analysis of safety and thermal runaway, and sub-zero temperature performance are highlighted. Various BTM strategies have been studied, which mainly focus on

BTM external including the use of air, liquid, phase change material (PCM), and heat pipe.

Chapter 3 introduces finite element analysis (FEA) for battery models coupled and decoupled with heat transfer model. Both electrochemical models and electrical models for lithium-ion batteries are investigated, and finite element method (FEM) modelling for battery thermal performance using commercial software packages has been reviewed.

Chapter 4 focuses on a small-scaled FEM computational model as it encapsulates identical features of larger automotive packs and is advantageous to simulate aggressive usage pattern or ‘off-normal’ thermal abuses conditions. An experimental prototype based on this configuration is validated and studied. This is used as a proxy to reality to evaluate the thermal characteristics of the proposed heat pipe thermal management solution.

Chapter 5 consists of experiment setup, instrumentation and test results. Prototype characterisation has been made in terms of system parametric evaluation, steady state/transient cooling/preheating performance, and the effect of adding fins or perforated plates. The experimental investigation covers an extensive range of battery thermal environments including sub-zero temperatures exploring the potential of the heat pipe solution. Applying heat pipes to reduce thermal stress on batteries and improve temperature uniformity under all weather conditions is evaluated.

Chapter 6 extends the heat pipe BTM applied to EVs using FEM modelling at pack level. With validated FEM models from Chapter 4, the development of actual solution can be speeded up to reduce large-scale experimental prototype construction. The temperature profile of a 30-cell

battery pack under cooling and preheating has been created. The average heat source in the lithium-ion battery cell is obtained using either a combination of experimental data and established equations, or a full 1D electrochemical model. The model developed aims at simulating and predicting the thermal behaviour of lithium battery packs under a set of operating conditions.

Chapter 7 explores the biomimetic potential in wicks for FPHPs. Hierarchical structure adopted from nature in terms of wetting phenomenon and capillary effect is considered for this novelty. Potential mechanism, mathematical models, and fabrication are reported.

Chapter 8 concludes this research study with future work suggested.

Chapter 2

Literature Review

2.1 Lithium-ion Batteries for Electric Vehicles

2.1.1 General Considerations

Electric Vehicle (EV), which was invented ahead of the first gasoline-powered vehicle, consists of mainly four elements: an energy source (the battery), a power convertor, an electric motor, and a mechanical transmission [2]. A vehicle driven by an electric motor is very energy efficient in terms of high energy efficiency (a standard electric motor is expected to display an efficiency over 90%), torque and power output characteristics (e.g. a high-torque at low revolution speed, quicker torque response, and recovering kinetic energy into electricity from braking torque) [3, 4]. Shimada [5] compared the energy efficiency of FCV (fuel cell vehicles), HEV (hybrid electric vehicles), CNG (compressed natural gas), and BEV (battery electric vehicle) based on the input energy per 1 km during 10 – 15 mode driving cycle test [6]. BEV (or EV) has shown to have the lowest input energy proportional to CO₂ discharge and the highest fuel economy. The heat loss of an EV, in addition, is significantly small compared to that from the engine vehicle. However, the fuel density of batteries in comparison with liquid fuel or gas fuel is extremely low

implying that EV has to carry a large amount of battery cells in order to achieve the same performance offered by the engine-vehicle.

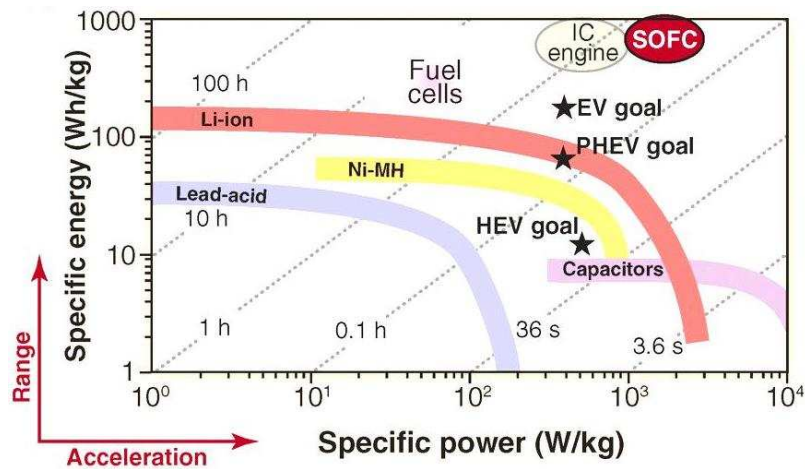


Figure 2.1: Ragone plot of various electrochemical energy storage and conversion devices [7] including recently reported SOFC [8].

A Ragone plot for various batteries, electrochemical capacitors, and fuel cells (including recently reported solid oxide fuel cell (SOFC) [8]) made for many applications ranging from consumer electronics to vehicles is provided in Fig. 2.1. The specific power translates to the acceleration in a vehicle (how quickly the energy can be delivered); while the specific energy, the driving range (how much energy is available). A point in Ragone plot represents the amount of time during which the energy per unit mass (vertical axis) can be delivered at the power per unit mass (horizontal axis). Time is plotted as the diagonal line (the ratio between the energy and power densities) indicating the time to get the charge in or out of the device. It can be noted that lithium-ion batteries are superior to other cell chemistries for EV, PHEV (plug-in hybrid electric vehicle) and HEV but no battery system can compete with gasoline (i.e. internal combustion or IC-engine). For IC-engine, fuel is consumed so the

specific energy refers to the initial mass of the fuel, approximately half a kilogram of fuel per kilogram of engine [9]. If taking 25% efficiency of an IC-engine then 800 Wh/kg of fuel plus engine can be obtained. For batteries, the weight remains the same during discharge, and Linden [10] reported that lithium-ion batteries are well-suited for vehicle applications because they have nearly twice the amount of specific energy and energy density (150 Wh/kg and 400 Wh/L respectively) relative to the practical nickel-metal hydride (NiMH) batteries (75 Wh/kg and 240 Wh/L), which had previously dominated the HEV market.

Apart from acceleration and driving performance, other criteria such as cost, calendar life, and safety are also critical. The cost of an EV battery is significant, and arguably, prohibitive. \$/kWh is an important quantity in evaluating cost. The United States Advanced Battery Consortium (USABC) outlined \$/kWh goals for battery technology to reach to a commercially viable level, which was \$200 – 300/kWh versus current costs of \$750 – 1,000/kWh [11]. Cluzel and Douglas [12] presented both conservative and optimistic scenario results of battery pack cost based on different EV classes and the reported cost ranged from \$587 – 1,327/kWh in 2011. Additionally, Gaines and Cuenca [13] broke down the materials cost of a 10 Ah lithium-ion high power cell and pointed out that cathode, separator and electrolyte contribute the most to the total battery cost taking up 28%, 23% and 20% respectively. It is generally believed that lithium-ion batteries have not yet achieved the potential of cost reductions and the search for reducing potential cost is encouraged by material substitution, increased packaging efficiencies, process

development, increased manufacturing yields and/or inexpensive production [14-16].

Table 2.1: Properties of electric vehicle batteries that operate at ambient temperature (extracted from [17])

Energy density Q_{\max} (Wh/kg)	Power density P_{\max} (W/kg)	Fastest 80% recharge time t (min)	80% discharge cycles before replacement N	Estimated large-scale production cost per kWh \$	Open- circuit cell voltage V (V)
Lead-acid 35	150	/	1000	60	2.1
Advanced lead-acid 45	250	/	1500	200	/
Valve regulated lead-acid 50	150+	15	700+	150	/
Metal foil lead-acid 30	900	15	500+	/	/
Nickel-iron 50	100	/	2000	150–200	1.2
Nickel-zinc 70	150	/	300	150–200	1.7
Nickel-cadmium 50	200	15	2000	300	1.2
Nickel-metal hydride (NiMH) 70	200	35	2000+	250	1.23
Lithium-ion 120–150	120–150	<60	1000+	150	3.6
Aluminium-air 220	30	/	/	/	1.5
Zinc-air 200	80–140	/	200	100	1.65

Table 2.1 demonstrates a list of storage battery types currently being used or is going to be used in EVs. Notably, high-temperature batteries, which have a long period of development and pilot production, are not used in EV productions. Only ambient operating temperature batteries are considered for EVs to ensure good performance and safety. A suitable cycle life for a

practical battery is suggested to be 1,000 cycles, equivalent to 3 – 4 years. Open-circuit voltage is also crucial, which determines the required number of cells to form a battery pack reflecting battery complexity and potential reliability. The higher the voltage becomes, the better the ratio of the active components in the cell over the passive containing materials. From Table 2.1, lithium-ion batteries seem to be the best among other cell chemistries due to high energy and power density, long life cycles, ambient operating temperature, and high open-circuit cell voltage. Lithium-ion batteries can store more energy per mass compared to NiMH, and achieve high cell voltage of 3.6 V in contrast with 1.23 V obtained by NiMH. More importantly, lithium-ion refers to a family of battery chemistries (Table 2.2), which indicates material flexibility and potential in cost reduction through material substitution.

Table 2.2: The major components of lithium-ion batteries and their properties [18, 19]

Abbrev.	LCO	LNO	NCA	NMC	LMO	LFP	LTO
Name	Lithium cobalt oxide	Lithium nickel oxide	Lithium nickel cobalt aluminium oxide	Lithium nickel, manganese cobalt oxide	Lithium manganese spinel	Lithium iron phosphate	Lithium titanate
Positive electrode	LiCoO ₂	LiNiO ₂	Li(Ni _{0,85} Co _{0,1} Al _{0,05})O ₂	Li(Ni _{0,33} Mn _{0,33} Co _{0,33})O ₂	LiMn ₂ O ₄	LiFePO ₄	LMO, NCA, ...
Negative electrode	Graphite	Graphite	Graphite	Graphite	Graphite	Graphite	Li ₄ Ti ₅ O ₁₂
Cell voltage (V)	3.7-3.9	3.6	3.65	3.8-4.0	4.0	3.3	2.3-2.5
Energy density (Wh/kg)	150m Ah/g	150	130	170	120	130	85
Power	+	o	+	o	+	+	++
Safety	-	o	o	o	+	++	++
Lifetime	-	o	+	o	o	+	+++
Cost	--	+	o	o	+	+	o

2.1.2 Mechanism and Configuration

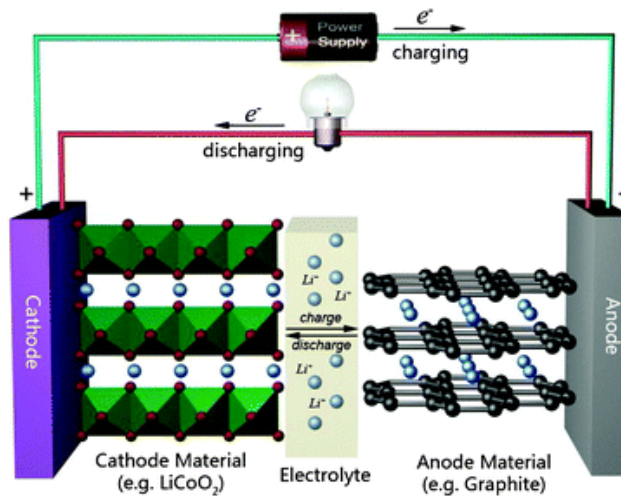
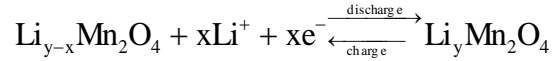


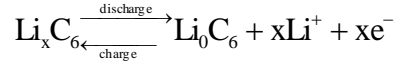
Figure 2.2: Lithium-ion battery mechanism during charge and discharge [20].

Fig. 2.2 gives the mechanism of a lithium-ion battery. Lithium-ions (Li^+) move from the negative electrode (anode) to the positive electrode (cathode) via a separator diaphragm to form a discharge cycle, and vice versa when charging. The anode is usually made of carbon, and the most commercially popular material is graphite. The cathode is a lithium-containing compound and is generally one of these three materials: a layered oxide (e.g. lithium cobalt oxide – LiCoO_2), a polyanion (e.g. lithium iron phosphate – LiFePO_4) or a spinel (e.g. lithium manganese oxide – LiMn_2O_4). The electrolyte refers to a solution of lithium salt in a non-aqueous solvent such as ethylene carbonate or diethyl carbonate. The current collector for negative and positive electrode is made of copper (Cu) and aluminium (Al) respectively. Taking LiMn_2O_4 /graphite as an example, the electrochemical reactions occurring at the electrode/electrolyte interfaces are described below.

Composite positive electrode:



Composite negative electrode:



As illustrated by Fig. 2.2, Li^+ inserts into solid particles of the cathode and de-inserts from solid particles of the anode during discharge. Lithium-ion diffusion in the solid phase and the electrolyte depletion will always limit cell discharge. Significantly, heat is generated within the cell and dissipated to the surroundings in all directions. If the heat is dissipated only through the tabs on the top of the two electrodes, temperature gradient will be developed along the cell height leading to non-uniform electrode reaction rates.

Three configurations of lithium-ion battery cell are shown in Fig. 2.3. Both cylindrical and prismatic lithium-ion batteries at cell-, module-, and pack-level for EVs have been demonstrated in Fig. 2.4. For a purely cooling purpose, the prismatic type seems to be most suitable for vehicles because a relatively large surface area in dissipating heat from cell interior to exterior is available. However, due to factors such as production maturity, availability, safety, lifecycle, and cost, cylindrical cells are still in frequent uses (e.g. Tesla, BMW mini). For automotive applications, cells are connected together in different configurations and packaged with control and safety circuitry to form a battery module. Modules are then combined with additional control circuitry, a battery thermal management system, and power electronics to form a battery pack. Fig. 2.5 displays a complete lithium-ion battery pack for a PHEV made by A123 Systems [21].

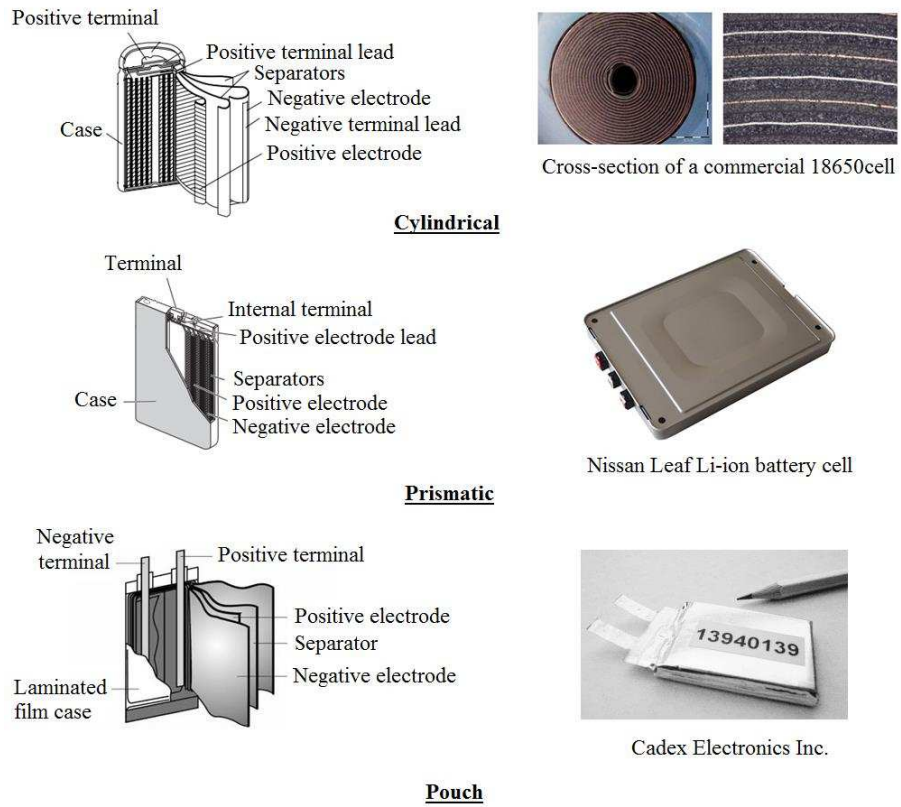


Figure 2.3: Battery cell configurations (modified from [22-25]).

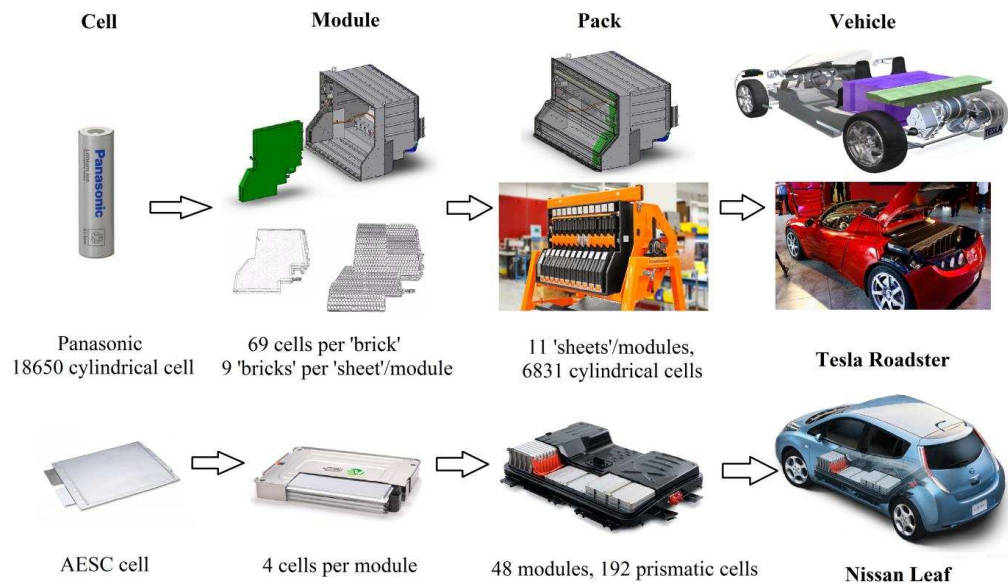


Figure 2.4: Lithium-ion battery cell-, module-, and pack-level demonstrated by two vehicle examples: Tesla Roadster [26, 27] and Nissan Leaf [28].

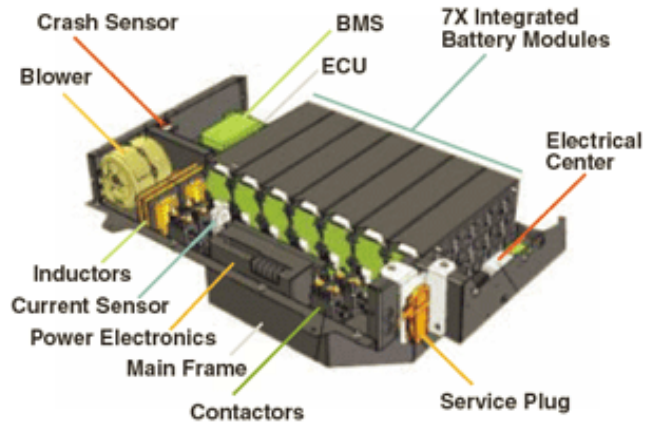


Figure 2.5: Lithium-ion battery pack for a PHEV (A123 Systems) [21].

2.1.3 Market Penetration and Potential

The direction of EV development can be predicted by introducing major work done by specialist niche manufactures. Table 2.3 summarises some major EV productions currently available/discontinued in the market. It seems that NiCd (Citröen, Ford, Peugeot and Renault) and NiMH (GM, Honda and Toyota) were the most two favourites for EV batteries back in 2000. The aim inconsistency made by those manufacturers indicates the immaturity of battery technology back then, such that scarce evidence of EV mass production to the public was seen. However, in recent 5 years, lithium-ion batteries become the top candidate in EV manufacturers due to lightweight, higher energy and power density, improved nominal range, and reasonable fast charging time. The commercial success of EVs listed in Table 2.3 suggests that lithium-ion batteries will possibly be the preferred solution to overcome energy storage and driving range challenges encountered by many battery-powered vehicles.

Table 2.3: List of major EV productions currently available and no longer available (by 2014)

Model type	Battery type	Battery weight (kg)	Top speed (km/h)	Range (km)	Charge time (h)	Sale/ lease price	Date
Currently Available (general information found in [29-38])							
BMW i3	22 kWh Lithium-ion	230 [39]	150	130–160	0.5–9	\$52,000 [40]	2013
BYD e6	75 kWh LiFePO ₄	500 [41]	140	330	10–20 min	\$52,000 [42]	2010
Chevrolet Spark EV	21.3 kWh nanophosphate Lithium-ion	254 [43]	144	132	0.33-7	From \$12,170 [44]	2013
Citroën C-Zero (also called Mitsubishi i i-MiEV)	16 kWh Lithium-ion	240 (200 [45])	130	100–160 (170)	0.5–7 (0.5–14)	\$48,000 [46] (>\$38,000) [47]	2010 (2009)
Ford Focus	23 kWh Lithium-ion	300 [48]	135	122	3–4, 18–20	\$35,170 [49]	2011
Nissan Leaf	24 kWh Lithium-ion	294 [50]	150	117–200	0.5–20	\$35,430	2010
Tesla Model S	60–85 kWh Lithium-ion	535–556 [51]	193–214	370–426	1.5–20 min	\$63,570 [52]	2012
Venturi Fetish	54 kWh Lithium-ion polymer	450 [53]	200	340	3–8	\$400,000	2006
Volkswagen e-Up!	18.7 kWh Lithium-ion	230 [54]	130	160	0.5	\$34,500	2013

No Longer Available (general information from [17, 55])

Ford Th!nkCity	11.5 kWh NiCd	260 [56]	90	85	5–8	/	1999 –2002
GM EV1	16.2 kWh Lead-acid	594 [57]	129	95	6	\$399 per month	1996 –2003
GM EV1	26.4 kWh NiMH	481 [58]	129	130	6	\$480 per month	1996 –2003
Honda EV Plus	26.2 kWh NiMH	374	129	190	6–8	\$455 per month	1997 –1999
Nissan Hypermini	15 kWh Lithium-ion	/	100	115	4	\$23,350 –36,000	1999 –2001
Nissan Altra EV	32 kWh Lithium-ion	365 [59]	120	190	5	\$50,999	1998 –2000
Peugeot 106 électrique (also called Citroën Saxo électrique)	12 kWh NiCd	/	90 (91)	150 (80)	7–8 (7)	\$14,700 –27,000 (\$12,300 excluding batteries)	1995 –2003
Renault Clio Electric	11.4 kWh NiCd	/	95	80	/	\$16,000 –27,400	/
Toyota RAV 4	27 kWh NiMH	380	125	200	10	\$45,000	1997 –2002
Tesla Roadster	53 kWh Lithium-ion	450 [60]	209	390	3–5	> \$92,000	2008 –2012

Note: charge time varies depending on the charging method. Long hours of charging may be needed when using conventional charger (e.g. onboard charger, charged from household); short period of charging can be achieved by a quick charger system (50 – 80% of battery capacity charged) (e.g. AC/DC fast charging station, Tesla Superchargers, etc.) or battery swap (1.5 min demonstrated by Tesla Motor).

2.2 Thermal Analysis of Lithium-ion Batteries

2.2.1 Safety and Thermal Runaway

For high voltage batteries such as lithium-ion battery in particular, prioritising safety at every step of the battery development including material selection, cell design, electronic controls and module assembly is essential but challenging. According to Doughty and Roth [61], safety is required to be evaluated at every level, i.e. the cell, the module, the pack and ultimately, the vehicle level. This is because failure at one level will escalate to much more severe failures at a higher level. The international standard ISO 6469 [62] addresses safety specifications for electrically propelled road vehicles including onboard electrical energy storage (Part 1), functional safety means and protection against failures (Part 2), and protection of persons against electrical hazards (Part 3). Safety devices are required to be incorporated into EV batteries to protect against off-normal operations and manage consequences of heat and gas generation. One of these devices is battery management system that regulates electrical distribution and prevents from over-voltage, under-voltage, excessive current, as well as elevated temperature.

Various battery chemistries have different responses to failure, but the most common failure mode of a cell under abusive conditions is the generation of heat and gas [63]. The possible exothermic reactions and thermal stability of lithium-ion batteries have been reviewed in [64] and [61]. Table 2.4 summarises the identified reaction of the components used in a lithium-ion battery. It shows that the components are completely stable below 80°C, but once the temperature reaches to 120 – 130°C, the passivation layer (SEI –

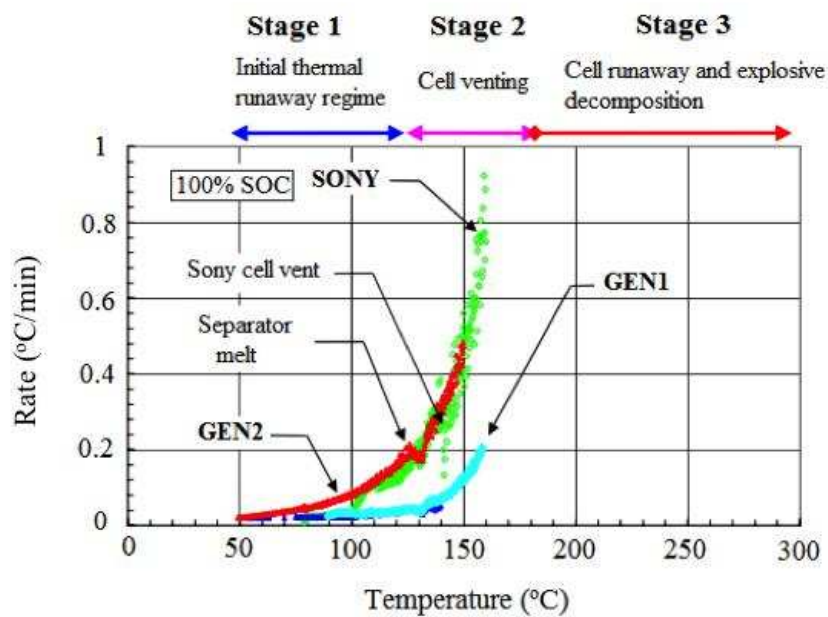
solid-electrolyte interface) starts dissolving progressively in the electrolyte, which causes electrolyte to react with the least protected surface of graphite generating heat.

Table 2.4: Thermal stability of components used in a lithium-ion battery (values measured from differential scanning calorimetry on electrodes) [19]

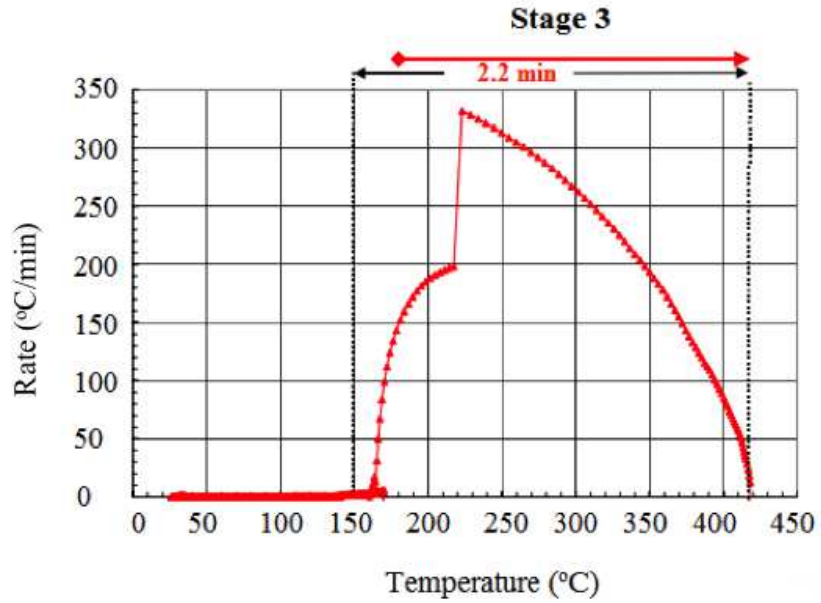
Temperature (°C)	Associated reactions	Energy (J/g)	Comment
120 – 130	Passivation layer	200 – 350	Passive layer breaks, solubilisation starts below 100°C
130 – 140	PE separator melts	-90	Endothermic
160 – 170	PP separator melts	-190	Endothermic
200	Solvents-LiPF ₆	300	Slow kinetic
200 – 230	Positive material decomposition	1000	O ₂ emission reacts with solvents
240 – 250	LiC ₆ + binder	300 – 500	
240 – 250	LiC ₆ + electrolyte	1000 – 1500	

Roth et al. [65] tested three different lithium-ion cells (SONY/GEN1/GEN2) under elevated temperature abusive conditions. Data summarised by Doughty [66] illustrates a general path to thermal runaway in lithium-ion cells, which can be categorised into three stages (Fig. 2.6): 1) initial thermal runaway regime; 2) cell venting; 3) cell runaway and explosive decomposition. Thermal runaway describes the condition when elevated temperature triggers heat-generating exothermic reactions and potentially increases the temperature leading to more deleterious reactions [64]. If no heat dissipation method is available, the internal cell temperature will continue to

increase rapidly. Once the temperature exceeds the onset temperature, the heat release will be accelerated due to increased electrolyte reduction at the anode (Stage 2). Additional heating may cause the cell to generate more than 10 °C/min self-heating rate resulting in thermal runaway (Stage 3). As a consequence, this will progress into battery fire and explosion. Examples of EV incidents listed in Table 2.5 may give an idea of how car crash or charging/discharging batteries leads to potential overheating or fire explosion. In order to improve lithium-ion battery safety, shutdown separators or pressure releasing devices, safer electrolytes and positive electrode materials, special additives and coatings [67], and an appropriate thermal management strategy are suggested to provide additional safety by limiting thermal runaway and preventing cell from rapid self-heating.



(a)



(b)

Figure 2.6: Illustrating three stages of the thermal response (thermal runaway path) obtained from SONY/GEN1/GEN2 lithium-ion cell [66]: (a) Stage 1-2 in scope; (b) Stage 3.

Table 2.5: EV incidents

EV Type	Incident	Place & date	Investigation summary
BYD e6	Caught fire after car crash	Shenzhen, China, 2012	Electric arcs caused by short circuit; however 72 out of 96 (75%) single cell batteries did not catch on fire and no flaws in safety design [68]
Chevrolet Volt	Caught fire after crash test	USA, 2011	No higher risk of fire than gasoline-powered vehicles according to National Highway Traffic Safety Administration (NHTSA) [69]
Dodge Ram 1500 PHEV	Overheated battery packs	2012	No injuries, Chrysler recalled as a precaution [70]

Fisker Karma	Home fire in Texas and a fire incident in parking lot in California	Texas and California, 2012	Unknown; Internal fault made the fan to fail, overheat and started fire, not lithium-ion battery pack [71]
Mitsubishi i-MiEV	Caught fire at Mizushima battery pack assembly plant when charging/discharging; battery cells in an Outlander PHEV in Yokohama overheated and melted	2013	Problem related to a change in manufacturing process, the cause has not been officially announced [72]
Tesla Model S	Caught fire after hitting debris on highway	Kent, Washington, 2013	Fire began in the battery pack but potential damage was avoided due to isolation of fire barriers inside the battery pack, fire risks are lower when driving a car powered by a battery than that powered by gasoline [73]
Zotye M300 EV	Caught fire	Hangzhou, China, 2011	Lack of quality during manufacturing, problems include leaking of battery cells, insulation damage between battery cells and container, short circuits [74]

2.2.2 Sub-zero Temperature Performance

Sub-zero climate will make the battery efficiency drop leaving discharge capacity minimal [75]. This directly affects vehicle mobility and driving range, and subsequently, the life cycle. A good example of this is 2012 Nissan Leaf, which has only 63 miles at -10°C but 138 miles under ideal condition [76]. For pure EVs, due to the fact that no combustion engine is available to provide heating, a significant proportion of battery energy will be used for heating the

battery and the cabin shortening the driving range even more by 30 – 40%. USABC [77] suggests the testing manual for EV batteries, which can be categorised into ‘well-performed battery in cold weather’ if it absorbs a fast charge from 20% to 60% depth of discharge (DOD), or 40% to 80% state of charge (SOC) in 15 minutes. According to QC/T 743-2006 [78], the discharge capacity requirement for lithium-ion battery at -20°C should be no less than 70% of its rated capacity. However, few batteries are capable of maintaining at such rated capacity under sub-zero temperatures.

Huang et al. [79] and Lin et al. [75] pointed out that a lithium-ion battery might be able to be discharged normally at low temperatures, but not so during reverse charging process. Nagasubramanian [80] reported that the commercial 18650 lithium-ion battery at -40°C has only 5% of energy density and 1.25% of power density compared to that obtained at 20°C . Shidore and Bohn [81] summarised the percentage drop in EV range based on three initial temperature conditions (20°C , 0°C and -7°C) during UDDS and UDDSx1.2 aggressive driving cycles. 0%, 9%, and 13% drop in EV range was resulted respectively under UDDS, and 10.7% drop was observed under UDDSx1.2 for an initial temperature of 0°C compared to 20°C . In addition, capacity fade due to lithium plating upon charging in cold climate has been studied [75, 82]. Zhang et al. [83] generalised that both energy and power of the lithium-ion batteries will be reduced once the temperature falls down to -10°C . Shi et al. [84] conducted an experiment comparing the discharge capacity of the lithium-ion battery used for EVs under -20°C and 20°C ; and showed that 62.6% was obtained at -20°C , smaller than the rated standard.

Poor lithium-ion battery performance under cold climates is therefore reviewed [83, 85, 86], which can be summarised into four factors: 1) low conductivity of the electrolyte and solid electrolyte interface on the electrode surface [87, 88]; 2) declined solid-state Li diffusivity [79, 83]; 3) high polarisation of the graphite anode [75, 89]; and 4) the sluggish kinetics and transport processes caused by increased charge-transfer resistance on the electrolyte-electrode interfaces [79, 83]. Three contributing factors of the PHEV lithium-ion battery impacts from low ambient temperature at -7°C and 0°C have been quantified [81]. These include limited battery propulsion and regenerative power accounting for 34% of the total reduction in battery power, high battery internal resistance leading to 8 – 12%, and other losses that attribute to 54 – 58%. 10 times increase in resistance, in addition, has been measured from the commercial 18650 lithium-ion battery at -20°C [90]. Stuart and Hande [91] explained the charging/discharging difficulty at cold temperatures and addressed the concern of potential hazards due to increased charge-transfer resistance. The highly nonlinear overvoltage equivalent resistance (R_{ov}) increases so much at a sufficiently low temperature and SOC, making the battery almost unusable. High R_{ov} also causes excessive gassing resulting in a loss of electrolyte, or case rupturing if the internal pressure generated due to gassing exceeds the capacity of the relief valves. The problems can be solved by formulating [87, 88] or replacing the chemical substances [92, 93] inside the lithium-ion batteries, and seeking for viable battery preheating methods in order to avoid loss in energy and power capability [80, 85] as well as severe battery degradation under sub-zero climates.

2.3 Battery Thermal Management Strategies

2.3.1 Design Considerations

Temperature effects, heat sources and sinks, EV/HEV batteries, and temperature control should be considered before designing a good BTM (Fig. 2.7). Either low ($<15^{\circ}\text{C}$) or high temperature ($>50^{\circ}\text{C}$) will progressively reduce the cycle life, and the threat of thermal runaway at a temperature higher than 70°C leads to cell failure. Pesaran [94] benchmarked the operating temperature for a variety of batteries including lead-acid, NiMH, and lithium-ion. He pointed out that the suitable range should be between 25°C to 40°C with a maximum of 5°C difference from module to module. He [95] later on demonstrated the temperature impacts on life, safety and performance of lithium-ion batteries (Fig. 2.8) and suggested a range of $15 - 35^{\circ}\text{C}$ as desired working temperature. Ladrech [96] also provided a temperature band for lithium-ion batteries obtained from suppliers, and divided the range into four sections namely decline of battery capacity and pulse performance ($0 - 10^{\circ}\text{C}$), optimal range ($20 - 30^{\circ}\text{C}$), faster self-discharge ($30 - 40^{\circ}\text{C}$), and irreversible reactions and short-circuit ($40 - 60^{\circ}\text{C}$). According to Sato [97], charging efficiency and life cycle can be drastically reduced if the battery temperature exceeds 50°C . Khateeb et al. [98] showed that the thermal runaway of the lithium-ion cells initiates at the temperature range of $70 - 100^{\circ}\text{C}$ jeopardising battery safety. Moreover, Lu et al. [99] made a detailed summary of stages that progress to thermal runaway and stated that the SEI breakdown starts at 80°C . These works all imply that the maximum working temperature for lithium-ion batteries should be kept below 40°C ; and the minimum, above 15°C .

The heat sources and sinks can be identified from the effects of internal impedance and chemical reactions during charge or discharge. Precautions should be taken to avoid unexpected overheating or temperature rise that leads to cell failure. The cooling/heating methods available for EV and HEV batteries are required to be considered separately as EV battery is more subject to low temperature rise, whereas HEV battery is likely to encounter high temperature rise. Fig. 2.9 explains the thermal impacts faced by both EV and HEV through comparing them at the same battery handling power. EV operates at a deep discharge rate (1C) while HEV tends to operate at a very high rate (10C). As a result, EV battery may still need to be heated up at low temperature, whereas HEV can have overheating problem even though they both dissipate the same amount of heat.

Two major problems caused by temperature can be found when it comes to battery cooling: 1) the temperature exceeds permissible levels during charge or discharge; and 2) uneven temperature distribution attributes to a localised deterioration [100]. Effective battery cooling should be able to maintain the allowed maximum cell temperature, reduce the temperature difference between cells, and ensure the cell being operated under the optimal working temperature range [101, 102]. Viable battery preheating methods, in addition, are required to eliminate loss in energy and power capability [80, 85] as well as severe battery degradation under sub-zero climates. The battery preheating system must be equipped with an ultimate energy optimisation, which provides an efficient and flexible solution in maximising the operating range without jeopardising cabin comfort and battery performance. The system must function well in driving, charging, and long-term parking.

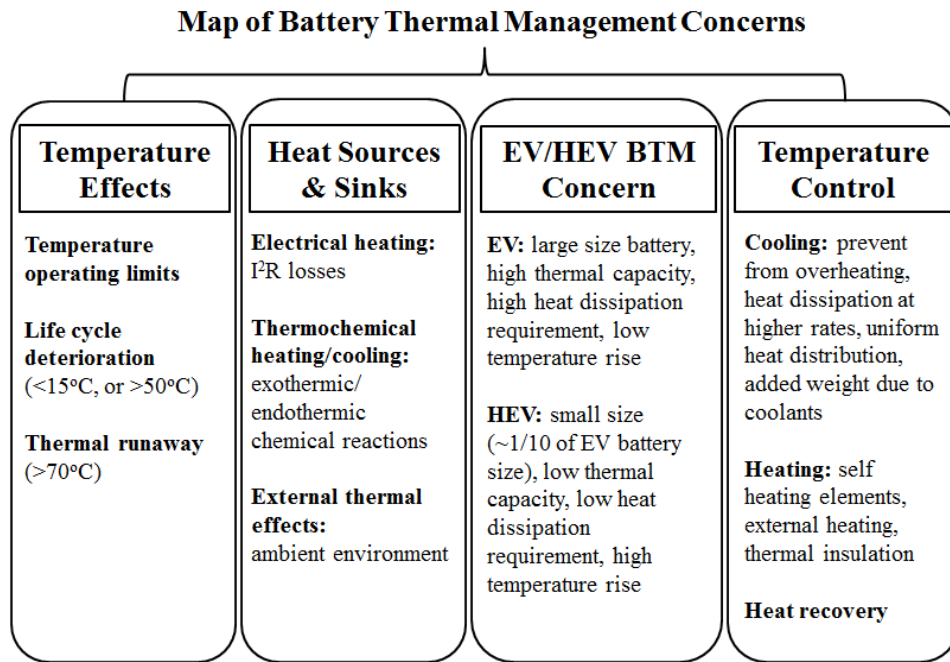


Figure 2.7: BTM mapping.

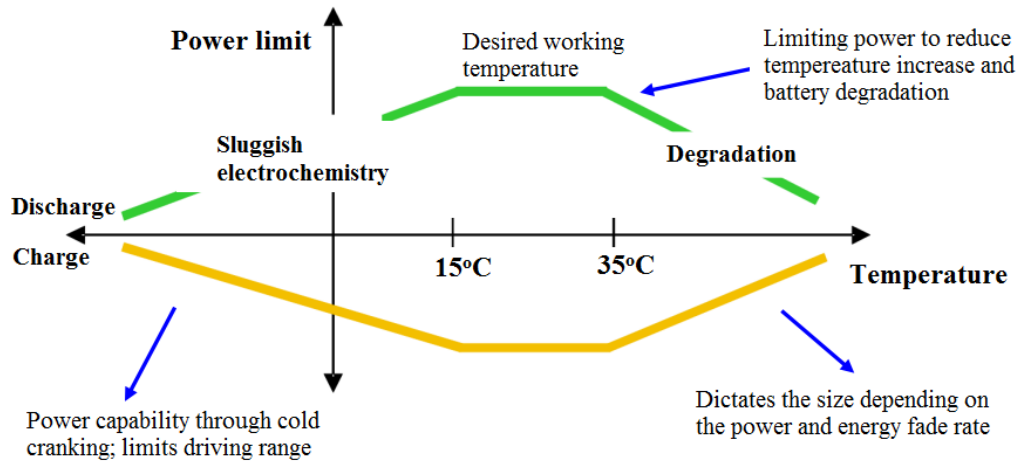


Figure 2.8: Temperature impact on life, safety and performance of lithium-ion batteries [95].

Table 2.6: Suggested operating temperature range for lithium-ion batteries

Ref (s)	Advised Temperature Range for optimal performance (°C)	Battery type
Sato [97]	< 50	Lithium-ion
Pesaran [94]	25 – 40	Lead-acid, NiMH, and Lithium-ion
Panasonic [103]	0 – 45 for charge -10 – 60 for discharge	Lithium-ion
Ladrech [96]	20 – 30	Lithium-ion
Pesaran et al. [95]	15 – 35	Lithium-ion

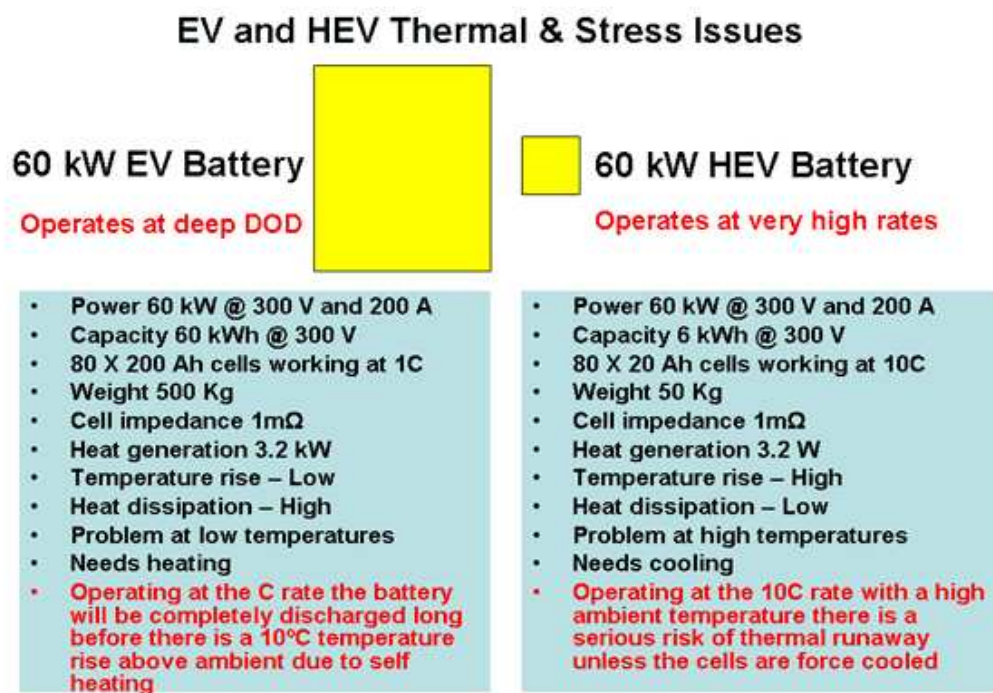


Figure 2.9: EV and HEV thermal and stress issues [104].

2.3.2 Thermal Management Strategies

Battery thermal management (BTM) is therefore required to help the battery operate at a desirable working temperature range at all times preventing battery degradation [105, 106], thermal runaway [107-109], and dropped discharge capacity due to sub-zero climate [75]. The thermal management

strategies can be either internal or external. Internal cooling has been investigated as an alternative to allow heat to be removed directly from the source without having to be rejected through the battery surface. Choi and Yao [110] suggested using forced circulation of the electrolyte in lead-acid batteries to improve heat removal and cell temperature uniformity but it was not practical for lithium-ion batteries. Parise [111] came up with the idea of using thermoelectric coolers in lead-acid cell partitions and/or between positive-negative plate pairs where the heat was produced. A recent study conducted by Bandhauer and Garimella [112] introduced microchannel phase change internal cooling concept to improve thermal gradients and temperature uniformity in a commercially available C/LiFePO₄ lithium-ion batteries. The microchannels were incorporated in either a thick current collector or into a sheet of inert material placed in between a split current collector. Additionally, internal battery preheating involves the use of self-internal heating and mutual pulse heating [86], or alternating current (AC) heating [91]. It is recognised that the internal BTM for lithium-ion batteries is limited and should be further explored due to its potential of higher temperature uniformity within an individual cell and among cells in a pack.

BTM external to the batteries will be discussed extensively in this thesis. It can be categorised into passive (only the ambient environment is used) or active (a built-in source provides heating and/or cooling), or based on medium [64, 100, 113]: 1) air for cooling/heating/ventilation; 2) liquid for cooling/heating; 3) phase change materials (PCMs); 4) heat pipe for cooling/heating; and 5) combination of 1)-4).

2.3.2.1 Air

Either natural or forced air convection can be used for air BTM. Fig. 2.10 illustrates three air BTM methods including passive air cooling, passive air cooling/heating, and active air cooling/heating. Choi and Yao [114] investigated lead-acid batteries and advised the difficulty in mitigating the temperature sufficiently by either natural or forced air convection. Chen and Evans [115] argued that neither passive nor active air cooling can efficiently dissipate heat in large-scale batteries, and Pesaran et al. [116] found out that air cooling is adequate for parallel HEVs but not for EVs and series HEVs. Kim and Persaran [117] claimed that passive air cooling is possible for batteries of low energy density, but for batteries of high energy density such as lithium-ion batteries, an active air system is required. Large thermal gradients between the cell centre and the battery pack boundary can be resulted if no active air thermal management is provided. Those thermal gradients lead to unequal charge or discharge capacity of the battery cell, hence a proper active air cooling device to obtain an optimal battery performance is necessary. Increasing the heat transfer coefficient of the surrounding air by forced air cooling is critical in spite of design complexity and additional power requirements.

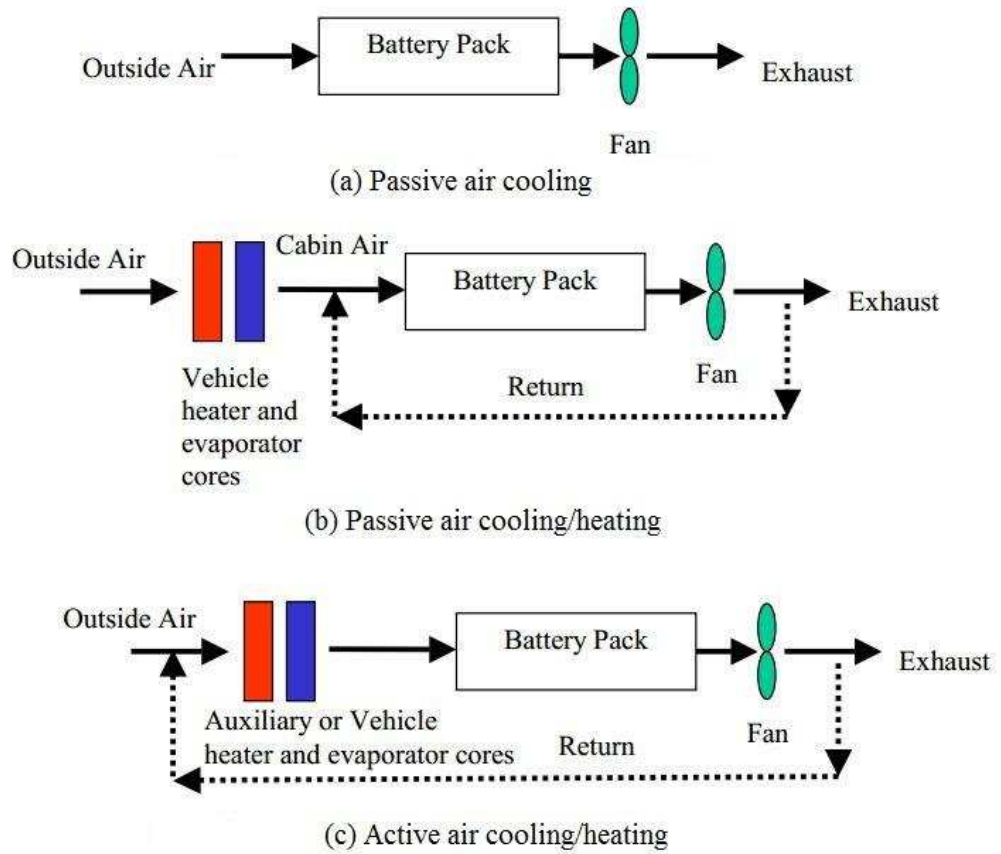
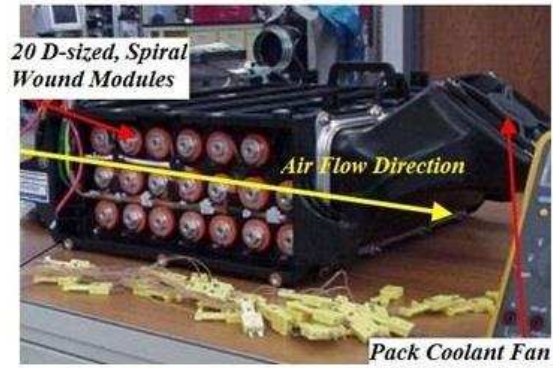
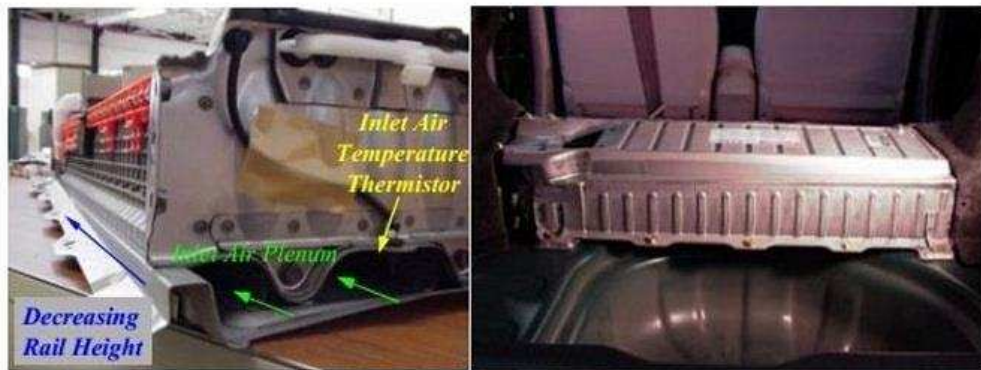


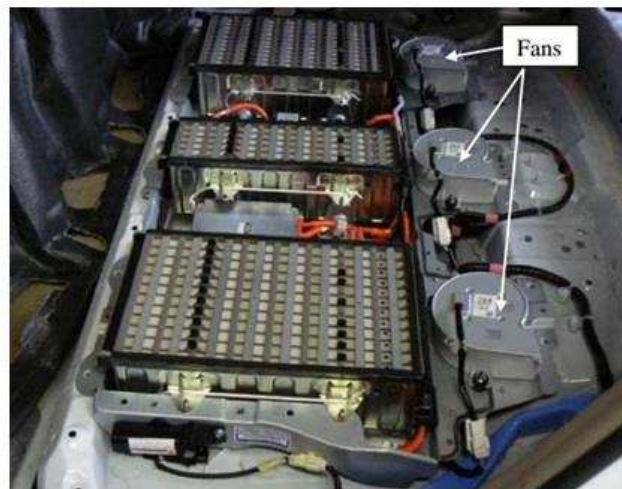
Figure 2.10: Air BTM methods [118].



(a) Insight pack



(b) Prius pack



(c) Highlander pack

Figure 2.11: (a) Insight pack [119]; (b) Prius pack [120]; and (c) Highlander pack [121] using air BTM.

There are two ways that an active air BTM adopts [122]. One is to take the air directly from air-conditioned vehicle cabin to either cool or heat the battery. The other is to utilise the treated air from a secondary loop, which consists of a separate micro air conditioning unit. Both methods consume relatively large proportion of space for air ducts, blower, and/or air conditioning unit, and add a substantial amount of weight to the whole system. Despite the fact that the latter is much more complex and costly, it performs better by using independent/pre-treated air to cool or heat the battery.

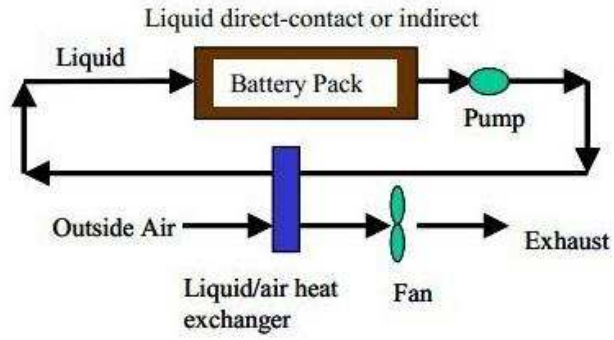
The 2000 Honda Insight [119, 123], 2001 Toyota Prius [119, 120, 123], and Toyota Highlander [121] utilise conditioned air taken from the cabin and exhaust to the ambient. Each battery pack (NiMH batteries) has unique module arrangement to mitigate temperature mal-distribution across the cells. Insight pack (Fig. 2.11 (a)) has a configuration similar to an aligned tube-bank and employs a small ‘muffin’ fan to force air convection between modules. Prius pack (Fig. 2.11 (b)) uses a parallel airflow scheme and the air is drawn by a 12-volt blower installed above the driver’s side rear tire well. The Highlander pack (Fig. 2.11 (c)), in addition, contains three fans for separate module units, which is good in eliminating efficiency loss resultant from excessive heat. In the test conducted on Prius pack, the observed thermal gradient was 4 – 8.3°C dependent on the blower speed and ambient temperature [120]. The surface temperature was monitored in a few discrete locations so the true maximum temperature differential was unknown. However, it is clear that air is not the best heat transfer medium to maintain excellent temperature uniformity for lithium-ion battery packs, which have more inherent safety risks than NiMH battery packs [64].

Improvements towards air BTM have been performed but with encountered difficulties. Nelson et al. [124] discussed that air cooling method was ineffective to cool the battery down to 52°C if the initial battery temperature was higher than 66°C. Lou [125] designed a cinquefoil battery pack for NiMH batteries with aim of heat transfer enhancement. For such air thermal control method, making the temperature difference below 5°C seemed to be impossible and a high degree of temperature uniformity was developed between the location near and away from the fan. More recently, Mahamud and Park [102] proposed a reciprocating method to create a much uniform temperature profile mitigating the temperature gradient. This was proven to be better than conventional unidirectional air cooling.

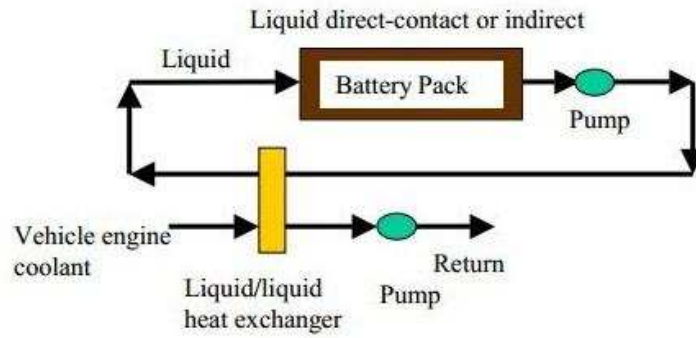
2.3.2.2 Liquid

As opposed to air, liquid BTM is regarded as a better solution and can be divided into passive or active (Fig. 2.12), or by the transfer medium: refrigerants or coolant (e.g. water, glycol, oil, or acetone) (Fig. 2.13). Pesaran [118] and Bandhauer [64] qualitatively compared air and liquid method in terms of heat transfer coefficient, thermal conductivity, viscosity, density, and fluid velocity. The degree of temperature mal-distribution for the airflow system seems to be noticeable due to lower specific heat and thermal conductivity. Using oil achieved the heat transfer coefficient 1.5 – 3 times higher than air [118]; and water or water/glycol, more than 3 times [64]. This indicates that the temperature difference will be reduced to 1/3 of that obtained from air achieving fine temperature uniformity. Notably, the difference between using refrigerant and coolant is that the former does not require extra

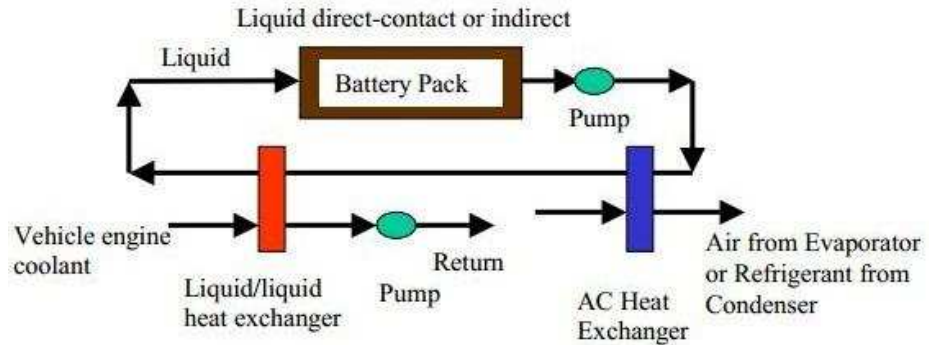
loops for chiller and heating elements. This implies that for battery preheating during winter, refrigerant will not be able to transfer heat energy to the battery thus can be less attractive. There are mainly three ways to achieve liquid BTM [118]: 1) through discrete tubing or a jacket around each battery module; 2) submerging modules in direct contact with a dielectric fluid (e.g. silicon-based or mineral oils) to avoid electrical shorts; and 3) positioning the modules onto liquid heated/cooled plates. The plates refer to thin metals having one or more internal channels discharged with refrigerant or coolant. Available external battery heating source during winter can be provided by using jacket or fluid heating from an electric heater [126, 127], a bioethanol heater (14.5 litres) used by Volvo C30 Electric [128], or a biogas (methane) engine proposed by Shimada [129].



(a) Passive liquid cooling

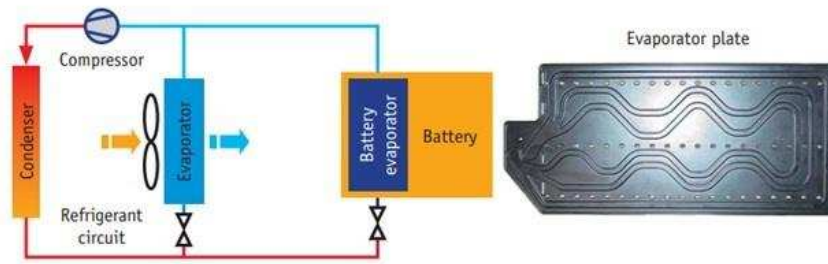


(b) Active moderate liquid cooling/heating

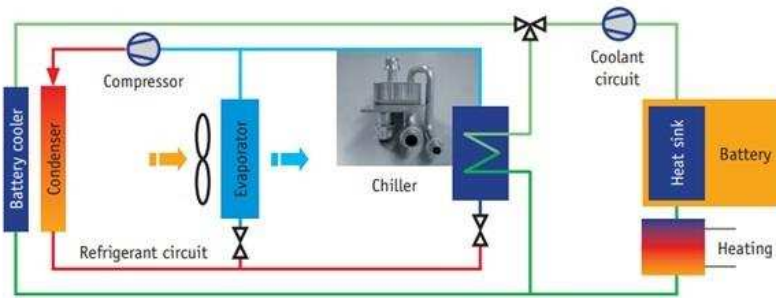


(c) Active liquid cooling/heating

Figure 2.12: Liquid BTM methods [118].



(a) Direct refrigerant-based cooling



(b) Secondary circuit with chiller and heat sink in battery

Figure 2.13: Liquid BTM using (a) refrigerant for battery cooling or (b) coolant for battery cooling/heating [122].

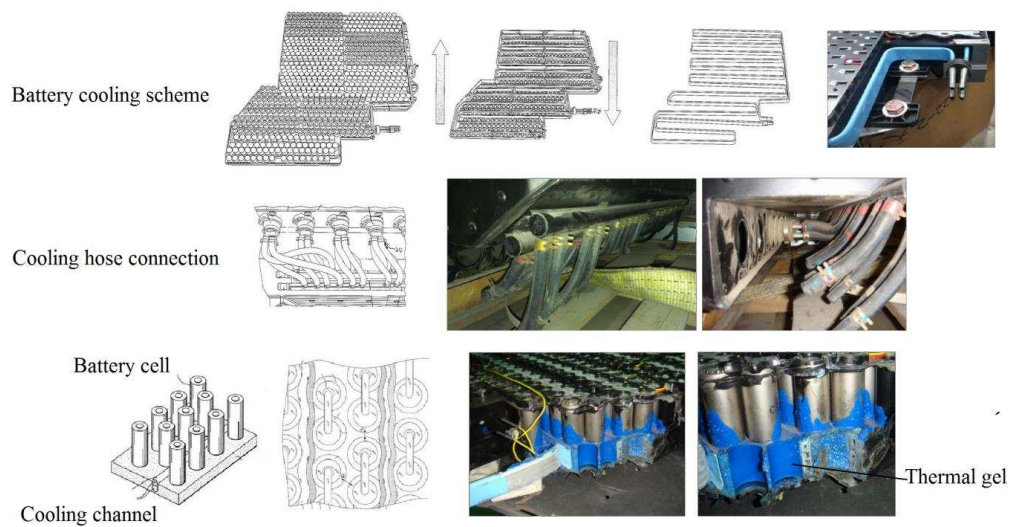


Figure 2.14: Tesla Roadster battery cooling (modified from [26, 60, 130, 131]).

Examples of liquid BTM used in cars can be found in [116, 118] with regard to different EV or HEV types; in [124] who investigated coolant cooling/heating for a Gen-2 lithium-ion batteries-based PNGV; in [122] that illustrates a direct refrigerant-based cooling in Mercedes S400 BlueHYBRID; and in [132] who reported active liquid cooling/heating implemented in Volt and Tesla. The battery cooling system in Tesla Roadster uses water-glycol (1:1) mixture as coolant. A thermal interface (blue) is overmoulded onto the cooling tube forming a base below the battery pack (Fig. 2.14). This serves as a heat sink so that the cooling liquid can be discharged to provide efficient cooling.

Improvements towards liquid BTM are suggested by Jarrett and Kim [133], who modelled serpentine-channel cooling plates in various geometries and concluded that ‘a narrow inlet channel widening towards the outlet’ is able to equalise the heat transfer achieving uniform temperature. Such configuration balances the effects of coolant velocity, heat transfer area, and fluid-solid temperature gradient. Similarly, Faass and Clough [134] modified the cooling channel pathing geometry that produces an area of high turbulence and an area of low pressure drop. Jin et al. [135] proposed a novel minichannel liquid cold plate with oblique fins at optimised angle and width to cool EV batteries.

Table 2.7 lists strengths and weaknesses offered by air, refrigerant, and coolant BTM. Air BTM is suitable for cell types, whereas liquid BTM that usually adopts cooling/heating plates within the assembled battery cells prefers prismatic or pouch cell geometry. To summarise, air cooling takes up more space, adds up more weight due to additional air ducts and blowers, consumes larger compressor, generates potential noise disturbance, and is less effective at

maintaining a uniform temperature. If the battery demands a tighter temperature control especially in some hotter environments, air is not as competitive as liquid. However, for refrigerant-based cooling, the battery cannot be heated in winter. Battery heating seems to be important as much, if not more, as battery cooling because the performance of a cold battery is sluggish and may directly affect vehicle mobility and driving range. Therefore, using coolant is much more preferred in liquid BTM. The trade-offs, however, are high space requirements, extra weight, and increased complexity due to additional pumps, valves, chiller, and radiators. The ultimate concern is to either invest an expensive but relatively compact liquid coolant system with higher battery power output, or a cheap but bulky air cooling system with low performance of the same battery size. Not surprisingly, many automobile manufacturers would rather go for a cheaper option, which is to construct a slightly larger battery pack with air cooling system.

Table 2.7: A comparison among air, refrigerant and coolant BTM

	Advantages	Disadvantages
Air cooling/heating	<ul style="list-style-type: none"> • Suitable for all cell types • Simple • Cheap • Battery heating in winter 	<ul style="list-style-type: none"> • Low heat transfer rate • Ineffective temperature uniformity • High space requirements • Additional weight problems • Potential noise disturbance
Refrigerant cooling	<ul style="list-style-type: none"> • High heat transfer rate • Allow battery to handle a larger pulse of power • Effective temperature uniformity • Low space requirements 	<ul style="list-style-type: none"> • No battery warming • Electric shortage due to liquid leakage

<p style="text-align: center;">Coolant cooling/heating</p>	<ul style="list-style-type: none"> • High heat transfer rate • Allow battery to handle a larger pulse of power • Effective temperature uniformity • Battery heating in winter 	<ul style="list-style-type: none"> • Expensive (the most costly) • Electric shortage due to liquid leakage • High space requirements • Increased complexity and weight
---	---	--

2.3.2.3 PCM

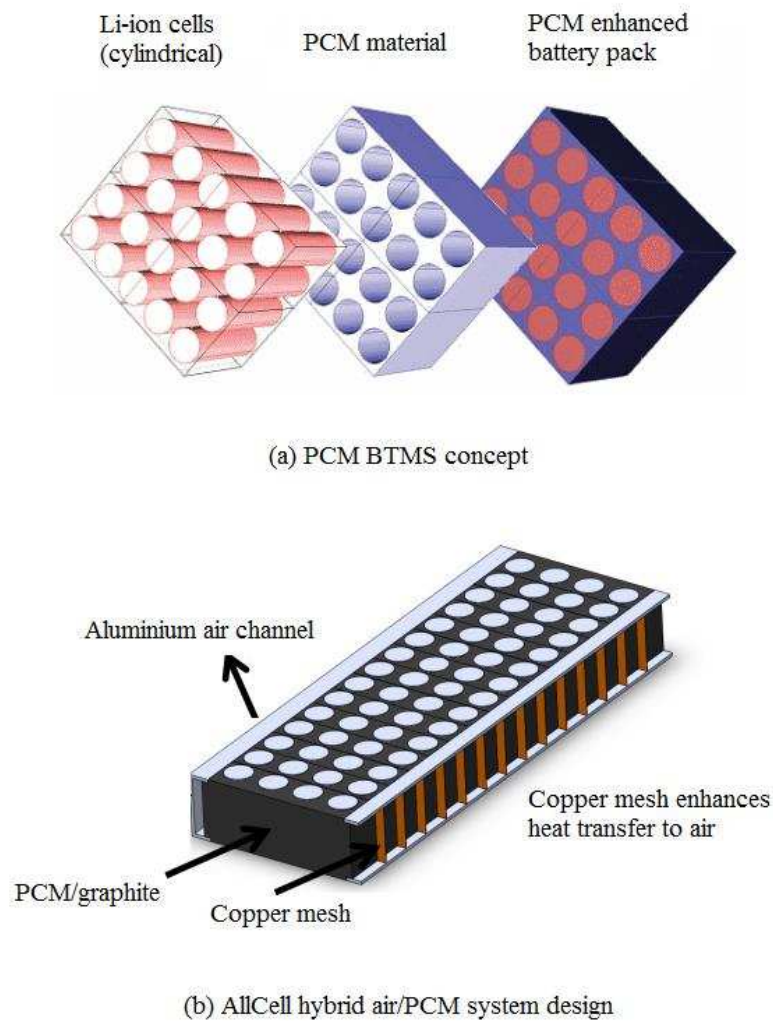


Figure 2.15: (a) PCM BTM concept; (b) AllCell hybrid air/PCM system design [136].

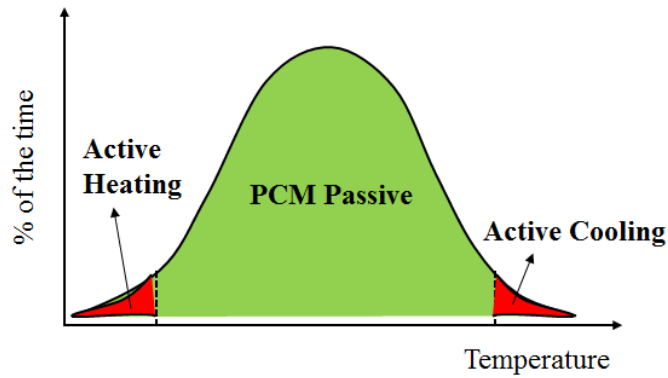


Figure 2.16: Hybrid air/PCM BTMS for EV normal operation

As an alternative to direct liquid or air cooling/heating, researchers at Illinois Institute of Technology [98, 101, 137-140] pioneered a new passive BTM solution by using PCM (Fig. 2.15). PCM is the material with a large latent heat of fusion and a desirable melting point that can store or release large amounts of energy. The heat transfer route starts from the battery, which generates heat, and goes to the PCM and then to the battery case in contact with the ambient air. PCM eliminates the need for active cooling/heating during the majority of operating time because it delays the temperature rise when the ambient is cold, and maintains the battery below ambient during hot days (Fig. 2.16). The battery module used in Fig. 2.15 was formed from commercial cylindrical 18650 lithium-ion cells surrounded in a rectangular enclosure. The PCM is a paraffin wax with a melting temperature ranging from 40°C to 44°C and a latent heat of melting/solidification of 195 kJ/kg. The wax fills the voids between the cells with solid and liquid phase densities of 822 and 910 kg/m³ respectively. This reflects lightweight advantage and material flexibility that PCM exhibits. Rao et al. [141] listed the major criteria in selecting proper PCMs for BTM and melting point comes to the first. This value should, as a matter of fact, be chosen in the range of the operating

temperature that a battery desires. They stated that it is preferable to have a PCM with melting temperature below 45°C and a desired maximum temperature below 50°C to achieve effective heat dissipation and improved temperature uniformity.

In the study of Khateeb et al. [139], data showed that by using PCM (paraffin wax), the centre cells temperature increased by 26.25 – 30°C while the edge cells increased by only 18.75 – 22.5°C. This indicates the poor thermal conductivity of PCM, and hence, it did not melt uniformly. The PCM near the centre cells was completely melted during the first discharge cycle, but those that near the cooled walls did not start melting until the beginning of the third discharge cycle. If the PCM completely melts, an additional thermal resistance between the cooling fluid and the batteries will be created leading to a worse situation than direct air cooling. Low thermal conductivity also becomes problematic when it comes to battery preheating in cold environments, and the thermal gradient among the cells can be significant if it is externally warmed. More importantly, the volume expansion after melting is inevitable, so additional volume spacing between the battery cells is required and leak-proof design to avoid PCM liquid leakage is crucial.

To reduce the thermal gradient inside the battery pack and solve the conflict between large heat storage capacity and low thermal conductivity (0.25 W/mK for paraffin wax), many approaches towards making composite PCMs have been conducted and they include 1) embedding a metal matrix into PCM; 2) impregnating porous materials [142-146]; 3) adding high thermal conductivity substances in paraffin [147, 148]; and 4) developing latent heat thermal energy storage systems with unfinned and finned structures [149-151].

The improved thermal conductivity for the composite PCM (PCM/graphite matrix) from references [98, 139, 140] ranges from 3 W/mK to 16.6 W/mK. Examples of using composite PCM in vehicular applications have been summarised in Table 2.8. However, the thermal conductivity increases at the cost of decreased latent heat storage capacity. In order to achieve a good performance, a proper thermal conductivity ratio between PCM and battery cells ($k_{\text{pcm}}:k_c$) must be satisfied [141]. Moreover, with aim of eliminating battery safety risks, PCM properties such as stability, non-poisonous, non-flammable and non-explosive are critical. That is, a stable and stronger PCM based battery module to resist thermo-mechanical effects during operation is required. Alrashdan et al. [152] undertook a systematic experiment analysing the effects of the thermo-mechanical behaviours of paraffin wax/expanded graphite composite PCM for lithium-ion batteries. They observed that the increased percentage of paraffin wax will enhance tensile, compressive and burst strengths at room temperatures, but not so obvious under elevated temperatures.

Table 2.8: Composite PCMs in vehicular applications

Applications	Ref(s)	Composite PCM properties
For a large lithium-ion battery pack targeting at HEV/EV applications	Khateeb et al. [98] (electric scooters)	PCM/aluminium foam: $k_{\text{eff}} = k_{\text{pcm}}\varepsilon + (1-\varepsilon)k_{\text{al}}$, $\rho_{\text{eff}} = \rho_{\text{pcm}}\varepsilon + (1-\varepsilon)\rho_{\text{al}}$, $c_p = c_p\varepsilon + (1-\varepsilon)c_{p,\text{al}}$, $h = 195$ kJ/kg
	Sabbah [140]	PCM/graphite matrix: $k_{\text{eff}} = 16.6$ W/mK, $\rho_{\text{eff}} = 866$ kg/m ³ , $c_p = 1,980$ J/kgK, $T_m = 52-55^\circ\text{C}$, $h_{\text{eff}} = 181$ kJ/kg
	AllCell Technologies LLC (AllCell®) [153]	PCM/graphite matrix module

	Kizilel et al. [101]	PCM/graphite matrix: $k_{\text{eff}} = 16.6 \text{ W/mK}$, $\rho_{\text{eff}} = 789 \text{ kg/m}^3$, $c_p = 1,980 \text{ J/kgK}$, $T_m = 42\text{-}45^\circ\text{C}$, $h_{\text{eff}} = 123 \text{ kJ/kg}$
	Li et al. [154]	PCM/copper metal foam: $k_{\text{eff}} = 11.33, 6.35, 0.8 \text{ W/mK}$ from different samples
For a comparison study based on a simulated single cylindrical battery cell	Duan [155]	PCM 1 provided by the Glacier Tek Inc.: $k_{\text{pcm}} = 0.55 \text{ W/mK}$, $\rho_{\text{pcm}} = 840 \text{ kg/m}^3$, $c_p = 2,100 \text{ J/kgK}$, $T_m = 18^\circ\text{C}$, $h_{\text{pcm}} = 195 \text{ kJ/kg}$; PCM 2 by Laird Technologies: $k_{\text{pcm}} = 2.23 \text{ W/mK}$, $c_p = 1,390 \text{ J/kgK}$, $T_m = 50^\circ\text{C}$
For cylindrical NiMH and rectangular lithium-ion batteries	Rao [141, 156, 157]	PCM/graphite matrix: parameters collected from references – not specified, $\rho_{\text{pcm}} = 910 \text{ kg/m}^3$, $T_m = 50^\circ\text{C}$

2.3.2.4 Heat Pipe

Heat pipes are considered versatile in many industrial applications for their efficient cooling and thermal management, but heat pipe BTM has not been fully acknowledged. Similar to the passive strategy offered by PCM, applying heat pipes to cool or heat the battery provides efficient heat transfer when and where needed at low power consumption. The mechanism of a heat pipe is that the heat can be transferred through latent heat of vaporisation from the evaporator to the condenser, and the working fluid can be passively transported back to the evaporator by capillary pressure developed within a porous wick lining. Operating in this fashion, the heat can be continuously absorbed and released.

The combination of heat pipe and air cooling was adopted in early studies. For instance, Swanepoel [158] proposed to use pulsating heat pipes (PHPs) to

thermally manage Optima Spirocell lead acid batteries and control HEV components. Simulation and experiment results showed that a well-designed PHP system required the diameter of the heat pipe to be less than 2.5 mm and ammonia as working fluid. Wu et al. [159] suggested to use the heat pipes with aluminium fins to cool a large-scale lithium-ion battery, but difficulties in heat dissipation at the battery centre were found if no cooling fan at the condenser section was provided. Jang and Rhi [160] used a loop thermosyphon cooling method, which also combined the heat pipe with air cooling. Barantsevich and Shabalkin [161] introduced the testing aspects of ammonia axial grooved heat pipes to thermally control the solar battery drive, and Park et. al [162] obtained a numerical optimisation for a loop heat pipe to cool the lithium-ion battery onboard a military aircraft. More recently, Burban et al. [163] tested an unlooped PHP (2.5 mm inner tube diameter) with an air heat exchanger for cooling electronic devices in hybrid vehicles (Fig. 2.17). Steady state and transient performance with a hybrid driving cycle (New European Driving Cycle) was conducted and various heat pipe working fluids, inclinations, and different air speeds were investigated. Moreover, Tran et al. [164] proposed a flat heat pipe for cooling HEV lithium-ion batteries under natural and forced convection and highlighted the thermal performance under various heat pipe positions (Fig. 2.18).

The combination of heat pipe and liquid cooling is scarce and only two examples can be found. One is from Rao et al. [165], who experimentally examined the heat pipe based battery cooling for commercial prismatic LiFePO₄ batteries. The condenser of the heat pipe was cooled by a water bath at $25 \pm 0.05^\circ\text{C}$ (Fig. 2.19). More recently, Zhao et al. [166] proposed to use

ultra-thin flat plate heat pipe (aluminium, grooved, filled with acetone) coupled with water spray (Fig. 2.20). It seems that the heat pipe has the potential of handling increased heat flux more efficiently than the conventional heat sink, but the feasibility of applying heat pipes into vehicle batteries needs to be further examined. Factors such as cost, weight, mass production, material compatibility, transient behaviour under high frequency and large amplitude variable input power, and thermal performance degradation influenced by vehicle shock and vibration should be evaluated. Unlike air and liquid BTM, heat pipe BTM is still under initial development. It is also encouraged that the research on heat pipe BTM can be extended at pack level such that the impact of thermal accumulation from various cycle performances could be fully understood.

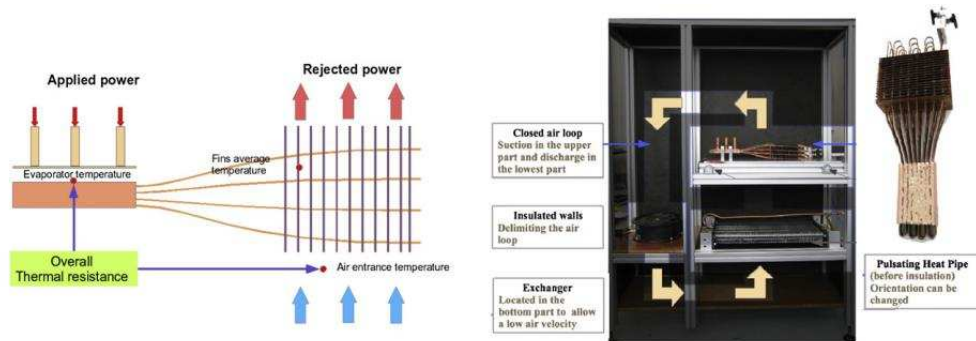
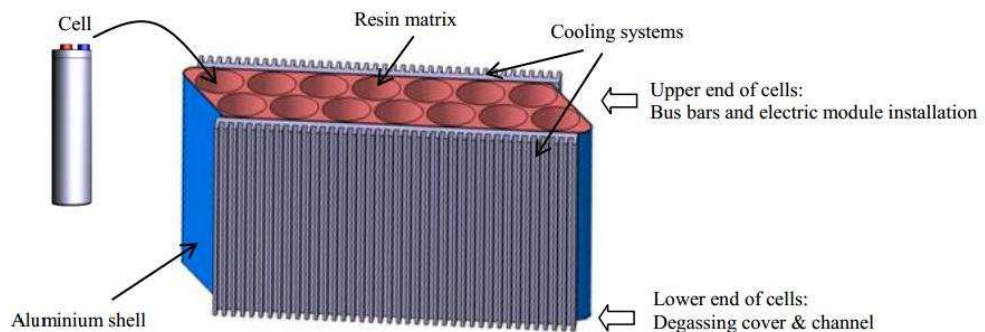


Figure 2.17: Pulsating heat pipe cooling a HEV lithium-ion battery pack [163].



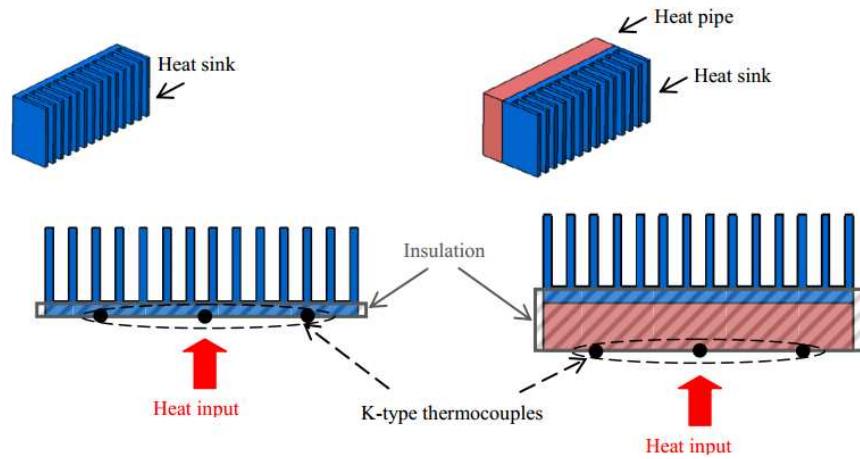


Figure 2.18: Flat heat pipe cooling a HEV lithium-ion battery pack [164].

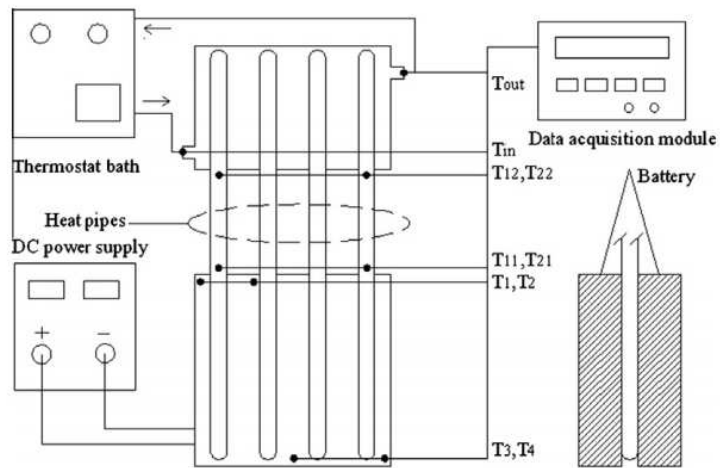


Figure 2.19: Cylindrical flattened heat pipe cooling for a 118×63×13mm 8Ah LiFePO₄ battery pack [165].

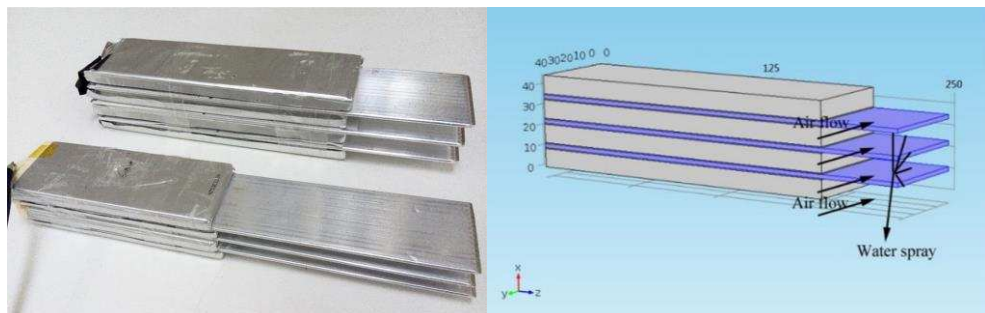


Figure 2.20: Aluminium grooved flat plate heat pipe put horizontally with condenser in contact with ambient air flow and water spray to cool the battery [166].

2.4 Summary

The existing BTM strategies for lithium-ion batteries in HEVs and EVs have been reviewed. BTM plays an essential role in eliminating thermal impacts of lithium-ion batteries, which improves temperature uniformity across the battery pack, prolongs battery lifespan, and enhances the safety of large packs. Temperature effects, heat sources and sinks, EV/HEV batteries, and temperature control should be considered before designing a good BTM.

The thermal management strategies can be either internal or external. Limited internal BTM for lithium-ion batteries was reported, which needs further investigation. BTM external to the batteries has been discussed extensively and they are categorised based on medium: air, liquid, PCM, heat pipe, or the combinations. Cheap air BTM is suitable for all cell configurations but the majority use is for NiMH battery packs in HEVs. Liquid BTM is regarded as a better solution compared to air and has been commercialised in cooling lithium-ion batteries in Mercedes S400 BlueHYBRID and Tesla Roadster. PCM comes to consideration as it eliminates the need for active cooling/heating during the majority of the operating time. But low thermal conductivity becomes problematic when it comes to battery cooling or preheating.

Using heat pipes for BTM is relatively new and the potential of combining heat pipes with air or liquid cooling needs to be further explored. Finding the cheapest, lightest and the most effective solution such as PCM and heat pipe is important to provide efficient heat transfer at low power consumption, but research should be extended at pack level such that the impact of thermal accumulation from various cycle performances could be fully understood.

Chapter 3

Methodology

3.1 Overview of Battery Models

Battery modelling can be defined using a set of equations under specific conditions of interest. The choice of equations or the mathematical description of batteries is significant in predicting the behaviour of the system. The thermal behaviour of a lithium-ion battery can be strongly affected by electrochemical and chemical processes occurring inside the cell during charge and discharge [167]. Battery heat generation is complex, which requires knowledge of how electrochemical reaction rates vary with time and temperature, and how current is distributed especially within large size batteries.

The battery thermal model can be thermal and electrochemical/electrical coupled or decoupled, depending on the heat generation. A fully coupled model uses newly generated parameters for current and potential from the model to calculate the heat generation, so that the temperature distribution in relation with the current and potential can be predicted [168]. The decoupled model may sometimes employ empirical equations based on experimental data. A partially-coupled approach can also be adopted where the heat generation

rate applied at one thermal environment (nonisothermal) was from that obtained previously at a given thermal environment (isothermal model) [169].

Two categories of the numerical models for obtaining the heat generation will be discussed in this section: electrochemical model (or first principle model) and equivalent circuit model.

3.1.1 Electrochemical Models

The electrochemical model is by far the most used method and is usually a one-dimensional physics-based electrochemical model, which has a set of governing equations (Eq. 3.1 – 3.5, Table 3.1) describing kinetics, transport phenomena and energy dissipation of a cell. It was first developed by Newman's group [170, 171] based on a macro-homogeneous and isothermal model approach [172]. The model (Fig. 3.1) can be established from two composite electrodes and a separator, along with one-dimensional transport of lithium-ions from the negative electrodes to the positive electrode through the separator. A good agreement with the experimental data performed later by Doyle [173] showed the applicability of such model to almost any of the existing li/lithium-ion systems.

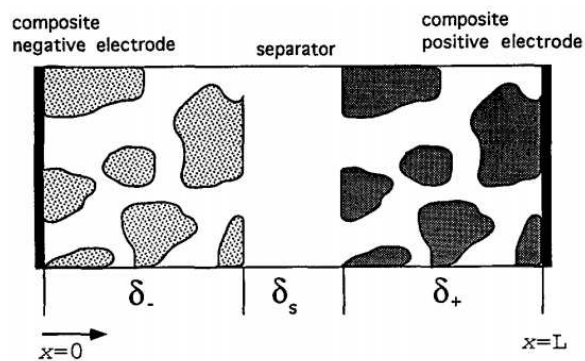


Figure 3.1: Dual lithium-ion insertion cell sandwich structure developed by [171].

Table 3.1: Fundamentals of electrochemical model for lithium batteries

Physic Fundamentals	Equations
<p><u>Electrochemical kinetics</u></p> <p>Reaction rate (Butler-Volmer equation)</p>	$\bar{j}_{nj} = a_s i_{oj} \left(\exp\left(\frac{\alpha_{aj} F}{RT} \eta_j\right) - \exp\left(-\frac{\alpha_{cj} F}{RT} \eta_j\right) \right) \quad (3.1)$ <p>a_s – specific interfacial area of an electrode i_{oj} – exchange current density (a function of lithium concentrations in both electrolyte and solid active materials, $i_{oj} = k(c_e)^{\alpha_{aj}} (c_{s,max} - \bar{c}_{se})^{\alpha_{aj}} (\bar{c}_{se})^{\alpha_{cj}}$, where c_e is volume-average lithium concentration in the electrolyte; k is the constant, determined by the initial exchange current density and species concentration) α_{aj}, α_{cj} – anodic and cathodic transfer coefficient of electrode reaction F – Faraday’s constant (96,485 C equiv.⁻¹) R – universal gas constant T – absolute temperature in Kelvin η_j – local surface overpotential ($\eta_j = \phi_s - \phi_e - U$, where ϕ_s, ϕ_e is volume-average electrical potential in solid phase and electrolyte; U is open circuit potential)</p>
<p><u>Phase transition & Ion transport</u></p> <p>Solid phase conservation of Li⁺ species</p>	$\frac{\partial}{\partial t} c_s - \frac{D_s}{r^2} \frac{\partial}{\partial r} \left(r^2 \frac{\partial}{\partial r} c_s \right) = 0 \quad (3.2)$ <p>with boundary conditions $D_s \frac{\partial}{\partial r} c_s \Big _{r=0} = 0$,</p> $-D_s \frac{\partial}{\partial r} c_s \Big _{r=R_s} = \frac{j^{Li}}{a_s F}$ <p>D_s – mass diffusion coefficient of lithium-ion in the electrolyte r – radial coordinate along active material particle R_s – radius of solid active material particle j^{Li} – transfer current resulting from the lithium insertion/de-insertion at the electrode/electrolyte interface, which consumes/generates the species Li⁺,</p> $j^{Li} = \begin{cases} a_{s,a} \bar{i}_{n,a} \\ 0 \\ a_{s,c} \bar{i}_{n,c} \end{cases} \quad \text{in the anode, separator and cathode}$

<p>Electrolyte phase conservation of Li⁺ species</p>	$\frac{\partial}{\partial t} \varepsilon_e c_e - \nabla \cdot (D_e^{\text{eff}} \nabla c_e) - (1 - t_+^o) \frac{j^{\text{Li}}}{F} + \frac{i_e \cdot \nabla t_+}{F} = 0 \quad (3.3)$ <p>with boundary conditions $\frac{\partial}{\partial X} c_e \Big _{x=0} = \frac{\partial}{\partial X} c_e \Big _{x=L} = 0$ for 1D analysis</p> <p>ε_e – volume fraction/porosity of electrolyte D_e^{eff} – effective diffusion coefficient (Bruggeman relation, $D_e^{\text{eff}} = D_e \varepsilon_e^{1.5}$) t_+^o – transference number of the Li⁺ with respect to the velocity of solvent (a function of electrolyte concentration, if assuming constant, $\frac{i_e \cdot \nabla t_+}{F} = 0$)</p>
<p><u>Energy dissipation</u></p> <p>Charge conservation in the solid phase</p> <p>Charge conservation in the electrolyte</p>	$\nabla \cdot (\sigma^{\text{eff}} \nabla \phi_s) - j^{\text{Li}} = 0 \quad (3.4)$ <p>with boundary conditions</p> $-\sigma_-^{\text{eff}} \frac{\partial \phi_s}{\partial X} \Big _{x=0} = \sigma_+^{\text{eff}} \frac{\partial \phi_s}{\partial X} \Big _{x=L} = \frac{I}{A},$ $\frac{\partial \phi_s}{\partial X} \Big _{x=\delta_-} = \frac{\partial \phi_s}{\partial X} \Big _{x=L-\delta_+} = 0 \text{ for 1D analysis}$ <p>σ^{eff} – effective conductivity of the solid phase</p> $\nabla \cdot (k^{\text{eff}} \nabla \phi_e) + \nabla \cdot (k_D^{\text{eff}} \nabla \ln c_e) + j^{\text{Li}} = 0 \quad (3.5)$ <p>with boundary conditions $\frac{\partial \phi_e}{\partial X} \Big _{x=0} = \frac{\partial \phi_e}{\partial X} \Big _{x=L} = 0$ for 1D analysis</p> <p>k^{eff} – diffusional conductivity (Bruggeman relation, $k^{\text{eff}} = k \varepsilon_e^{1.5}$) k_D^{eff} – effective ionic conductivity (</p> $k_D^{\text{eff}} = \frac{2RTk^{\text{eff}}}{F} (t_+^o - 1) \left(1 + \frac{d \ln f_{\pm}}{d \ln c_e} \right), \text{ where } f_{\pm} \text{ is}$ <p>molecular activity coefficient of the electrolyte)</p>

3.1.2 Electrical Models

The equivalent circuit model, which does not consider the physical fundamentals of the battery cells, provides a simple structure to capture the input/output relationship of the battery. It utilises common electrical components such as resistors, capacitors, and voltage sources to form a circuit network [174]. Typical equivalent circuit models used for vehicle batteries are Rint model (or Internal Resistance model), Resistance Capacitance (RC) model, Thevenin model, and PNGV (Partnership for New Generation of Vehicles) model [174-180]. Rint model (Fig. 3.2 (a)) assumes that the battery is an ideal voltage source in series with the resistance. RC model (Fig. 3.2 (b)) was developed by SAFT Battery Company containing capacitors within the branches of the circuit to show more close-to-real battery characteristics. A one or two RC block model without parasitic branch is generally accepted for lithium cells according to [179]. In addition, Thevenin model (Fig. 3.2 (c)) has been widely used in early battery management system and was developed based on Rint model, which connects a parallel RC network in series and takes into account of polarisation. Finally, the PNGV model (Fig. 3.2 (d)) was modified from Thevenin model with a slight increase in circuit elements (a capacitor $1/U'oc$ in series is added) [180]. Table 3.2 summarises basic equations for those models.

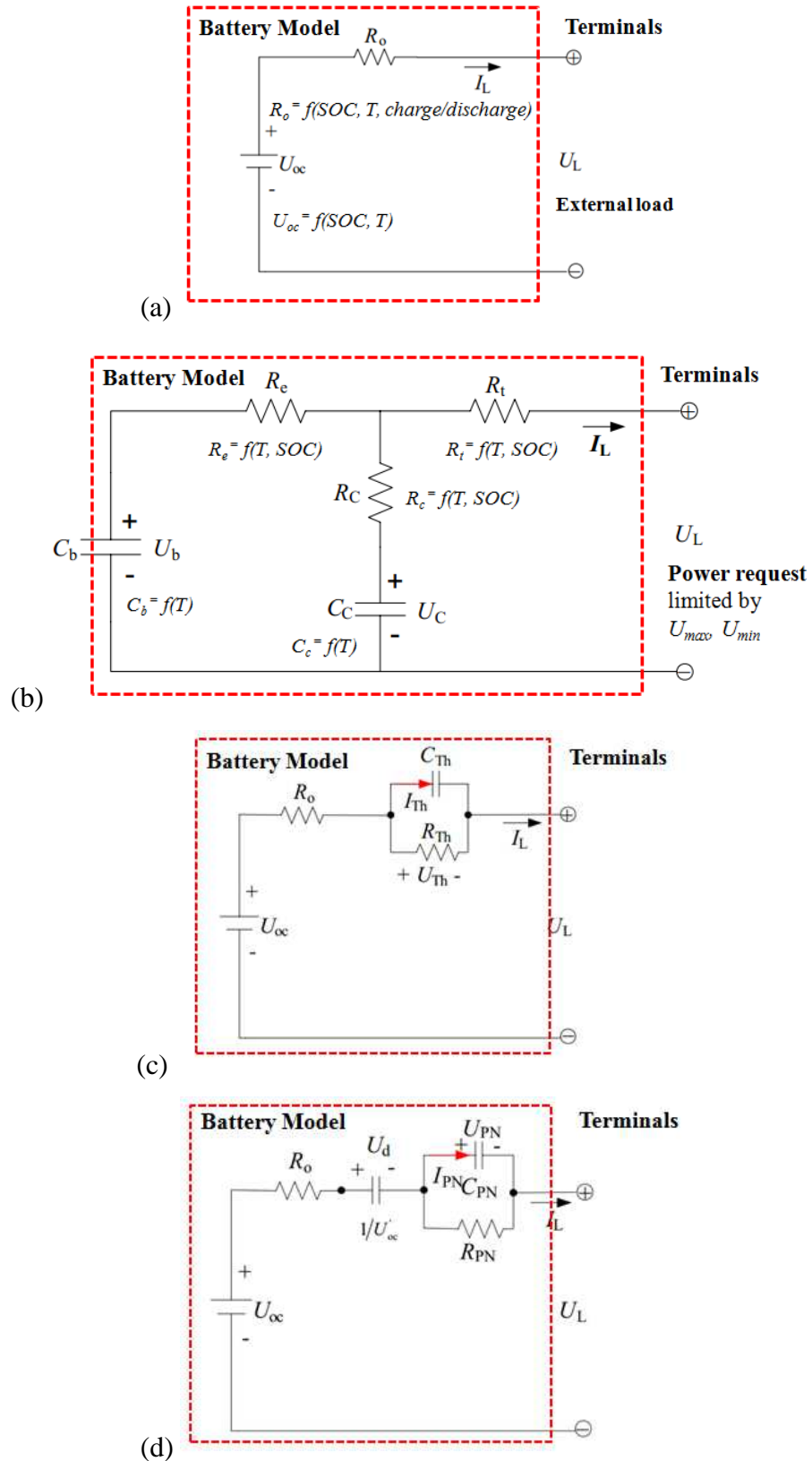


Figure 3.2: Various equivalent circuit models used for vehicle batteries (modified from [174, 175, 177]): (a) Rint model; (b) RC model; (c) Thevenin model; and (d) PNGV model.

Table 3.2: Equations of electrical model for lithium batteries

Model	Equations
Rint Model (Internal Resistance Model)	$U_L = U_{oc} - I_L R_o \quad (3.6)$ <p> U_L – terminal voltage U_{oc} – open-circuit voltage I_L – load current (+ discharge, - charging) R_o – internal resistance or ohmic resistance </p>
RC Model	$\begin{bmatrix} \dot{U}_b \\ \dot{U}_c \end{bmatrix} = \begin{bmatrix} -1 & 1 \\ C_b(R_e + R_c) & C_b(R_e + R_c) \end{bmatrix} \begin{bmatrix} U_b \\ U_c \end{bmatrix} + \begin{bmatrix} -R_c \\ -R_e \\ C_c(R_e + R_c) \end{bmatrix} [I_L] \quad (3.7)$ $[U_L] = \begin{bmatrix} R_c & R_e \\ R_e + R_c & R_e + R_c \end{bmatrix} \begin{bmatrix} U_b \\ U_c \end{bmatrix} - \left[R_t + \frac{R_e R_c}{R_e + R_c} \right] [I_L] \quad (3.8)$ <p> C_c – surface capacitor (small capacitance, which mainly represents the surface effects of a battery) C_b – bulk capacitor (large capacitance, which represents the ample capability of a battery to store charge) U_b, U_c – voltages across capacitor C_b and C_c R_t – terminal resistance R_e – end resistance R_c – capacitor resistance </p>
Thevenin Model	$\dot{U}_{Th} = -\frac{U_{Th}}{R_{Th} C_{Th}} + \frac{I_L}{C_{Th}} \quad (3.9)$ $U_L = U_{oc} - U_{Th} - I_L R_o \quad (3.10)$ <p> C_{Th} – equivalent capacitance that reflects the transient response during charge and discharge U_{Th} – voltage across C_{Th} R_{Th} – polarization resistance I_{Th} – outflow current </p>
PNGV Model	$\dot{U}_d = U'_{oc} I_L \quad (3.11)$ $\dot{U}_{PN} = -\frac{U_{PN}}{R_{PN} C_{PN}} + \frac{I_L}{C_{PN}} \quad (3.12)$

	$U_L = U_{oc} - U_d - U_{PN} - I_L R_o \quad (3.13)$
	U_d, U_{PN} – voltages across I/U'_{oc} and C_{PN} I_{PN} – outflow current of C_{PN}

3.2 Heat Generation Modelling

The battery thermal model accounts for heat accumulation, convection, conduction and heat generation (Eq. 3.14, Table 3.3). To note, the term $\rho c_p v \cdot \nabla T$, i.e. the convective heat transfer inside the battery, is always neglected because liquid electrolytes in a lithium-ion battery tend to show limited mobility. Another commonly used method is called lumped thermal model, which balances accumulation, convective heat dissipation to the surroundings, and heat generation (Eq. 3.15, Table 3.3). By assuming the battery as a lumped body, the temperatures of the battery are considered to be uniformly distributed in all directions at all times during transient heat transfer. This often applies to the condition where single cells have small thickness so that the Biot number ($Bi = \frac{hL}{\lambda} \ll 1$) is less than 1.

Battery heat is generated due to activation, concentration and ohmic losses [181]. Various equations have been applied to calculate the heat generation rate in lithium-ion batteries. The local heat generation (Eq. 3.16, Table 3.3) has shown to be more accurate but is very complex. Bernardi et al. [182] formulated the thermodynamic energy balance on a single cell, and a simplified form (Eq. 3.17, Table 3.3) has been readily accepted in small lithium-ion batteries if assuming no heat from mixing or phase change, uniform temperature or SOC, and only one electrochemical reaction takes

place [168]. This equation can be used if the experimental over-potential and entropic heat coefficients are known.

Attempts to experimentally examine the irreversible electrochemical heat generation for lithium-ion batteries can be obtained from two methods: accelerated-rate calorimetry (ARC) and isothermal heat conduction calorimetry (IHC) [181]. The ARC method allows the heat generation rate to be calculated based on an energy balance between the battery (heat source) and a constant temperature sink. The IHC method maintains the battery at a constant temperature throughout the whole operation and uses high-accuracy thermopiles attached to the surface of the battery to measure the heat rate. For reversible heat, the most common way is to measure the open-circuit potential (OCP) variation with temperature at a constant SOC [183-185]. However, studies (summarised in Table VII from Bandauer [64]) that used the aforementioned experimental methods have only been investigated where the total heat generation was obtained under currents no greater than 2C, and many were carried out under ambient temperature of 20°C or 25°C. Temperature influence was always omitted or for those who investigated it, the chosen temperature range was small. According to Hong et al. [186], small temperature changes cause significant heat accumulation, greater than the heat rejection of the device in some cases. Moreover, Sato [97] analysed the thermal behaviour of lithium-ion batteries (Sony 18650 cell) and developed a heat intake and release model (Eq. 3.18 – 3.19, Table 3.3). The heat generation equations, which constitute reaction heat Q_r , polarisation heat Q_p , and Joule heat Q_j during charging and discharging have been established and the obtained results (used a constant R_i at 50% DOD) agreed well with experiment.

Table 3.3: Summary of battery thermal model equations

Heat Transfer and Energy Balance	
Battery thermal model [187]	$\rho_p \left(\frac{\partial T}{\partial t} + v \cdot \nabla T \right) \approx \frac{\partial(\rho_p T)}{\partial t} = \nabla \cdot \lambda \nabla T + q \quad (3.14)$ <p> ρ – composite/average density of the battery c_p – composite/average heat capacity per unit mass under constant pressure v – velocity of the electrolyte λ – composite/average thermal conductivity in x, y, z direction q – heat generation </p>
Lumped thermal model [188]	$\frac{d(\rho_p T)}{dt} = h A_s (T - T_\infty) + q \quad (3.15)$ <p> h – heat transfer coefficient for forced convection from each cell A_s – cell surface area exposed to the convective cooling medium T – free stream temperature of the cooling medium </p>
Heat Generation Modelling	
Local heat generation [187, 189, 190] (can be linked with electrochemical model)	$q = a_{sj} i_{nj} (\phi_s - \phi_e - U_j) + a_{sj} i_{nj} \left(T \frac{\partial U_j}{\partial T} \right) + \sigma^{\text{eff}} \nabla \phi_s \cdot \nabla \phi_s + k^{\text{eff}} \nabla \phi_e \cdot \nabla \phi_e + k_d^{\text{eff}} \nabla \ln c_e \cdot \nabla \phi_e \quad (3.16)$ <p> 1st term: irreversible heat 2nd term: entropic effect (i.e. reversible heat) 3rd: ohmic heat arising from the solid phase 4th & 5th term: ohmic heats in the electrolyte phase </p>
Simplified heat generation [182] (obtained from experiment, in commonly use)	$q = I(U_{oc} - V) - I \left(T \frac{dU_{oc}}{dT} \right) \quad (3.17)$ <p> 1st term: joule heating 2nd term: entropy change I – discharge current density U_{oc} – open circuit potential V – cell voltage </p>

Heat generation (Sato [97])	$Q_{\text{charge}} = -3.37 \times 10^{-2} Q_1 I_c + 3.60 R_{t,c} I_c^2 \quad (3.18)$
	$Q_{\text{discharge}} = 3.37 \times 10^{-2} Q_1 I_d + 3.60 R_{t,d} I_d^2 \quad (3.19)$
	<p>Q_r – reaction heat, $Q_r = -3.37 \times 10^{-2} Q_1 I$</p> <p>$Q_p$ – polarisation heat, $Q_p = 3.60 R_p I^2$</p> <p>Q_j – joule heat, $Q_j = 3.60 R_e I^2$</p> <p>Q_1 – heat generated (kJ/mol) from positive electrode ($\text{LiCoO}_2 \rightarrow \text{Li}_{1-x}\text{CoO}_2 + x\text{Li}^+ + xe^-$) and negative electrode ($\text{C} + x\text{Li}^+ + xe^- \rightarrow \text{CLi}_x$)</p> <p>$I_c, I_d$ – battery charge/discharge current</p> <p>R_p – resistance due to polarisation</p> <p>R_e – internal resistance</p> <p>$R_{t,c}, R_{t,d}$ – total electrical resistance during charging/discharging</p>

3.3 Coupling and Decoupling

Many studies extended the one-dimensional electrochemical model to include an energy balance to capture temperatures within the cell. Gu and Wang [168] demonstrated a diagram (Fig. 3.3) of thermal-electrochemical coupled modelling approach and the coupled model takes into account of multi-scale physics in lithium-ion battery including kinetics (electrochemical kinetics), phase transition (solid-phase lithium transport), ion transport (lithium transport in electrolyte), energy dissipation (charge conservation/transport), and heat transfer (thermal energy conservation). Fig. 3.4 illustrates such micro-macroscopic modelling approach applied into a lithium-ion vehicle battery. An example of a thermal-electrical coupled model used for an A123 $\text{LiPO}_4/\text{graphite}$ battery is demonstrated in Fig. 3.5. A control-oriented model block is used to form the coupled model and it can be built from two

subsystems namely equivalent circuit models and thermal models with parameter estimation linked in between for real time implementation.

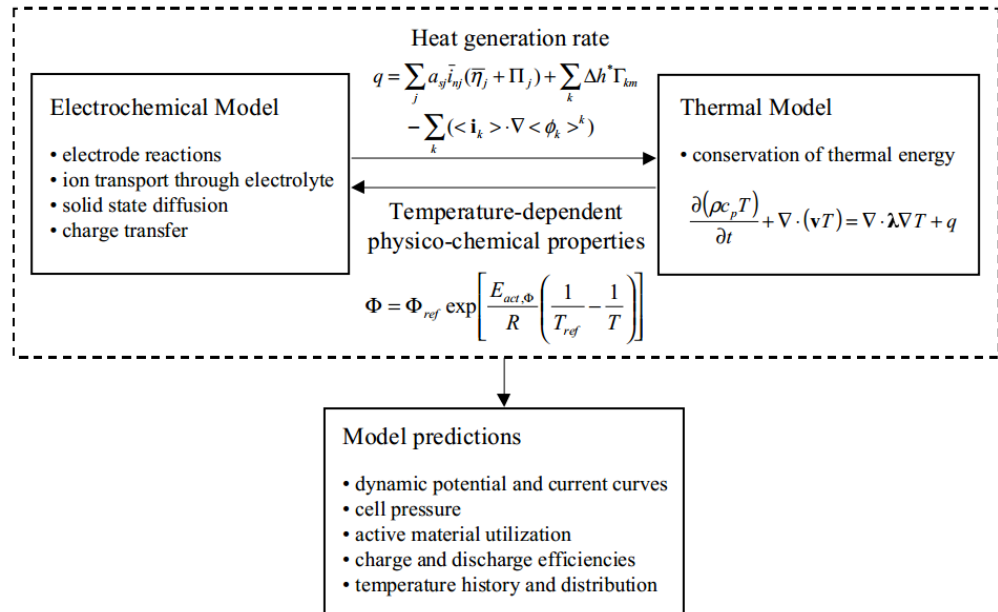


Figure 3.3: Thermal-electrochemical coupled modelling approach [168].

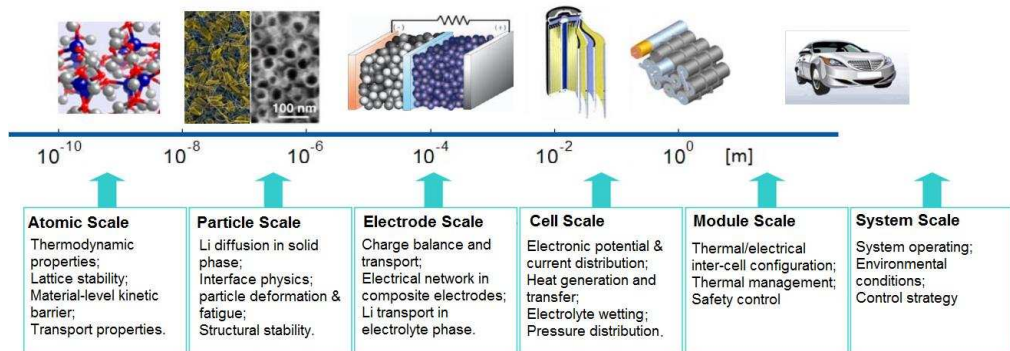


Figure 3.4: Multi-scale physics and micro-macroscopic modelling approach applied into a lithium-ion battery (modified from [191, 192]).

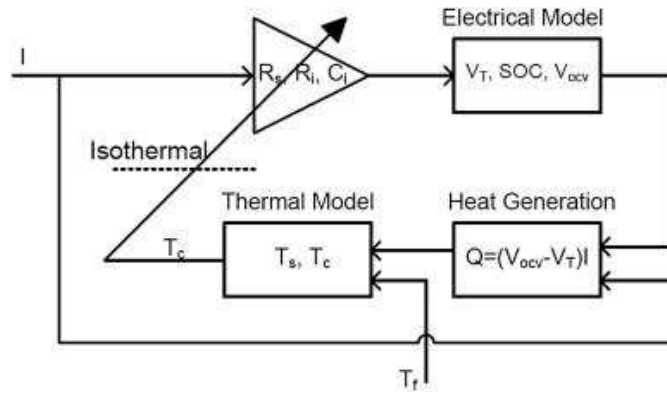


Figure 3.5: Coupled thermal-electrical model for an A123 LiPO4/graphite battery [193].

A summary of the coupled thermal-electrochemical models used in literature is provided in Table 3.4. Arrhenius law (Eq. 3.20) can be applied to mass transport and kinetic parameter ψ to couple electrochemical and thermal models. Significantly, the lumped thermal model used by [169, 194-196] that neglects spatial temperature variation by assuming the temperature is uniform all over the cell (small Biot number, $Bi \ll 1$) may result in an error of 15% in total thermal energy under higher discharge rates [197] (Fig. 3.6). The local heat generation method performed by [189, 194, 195, 197-199] has shown to be more accurate. Srinivasan and Wang [197] plotted the heat generated due to various factors that contribute to the total heat (Fig. 3.7). They pointed out that the reversible heating effect can be important at low discharge rates (0.01 – 1C) (Fig. 3.7 (a)), but will be dominated by irreversible (reaction and ohmic) heating at high discharge rates (1 – 10C) (Fig. 3.7 (b)). Furthermore, 2D thermal models have been used in most studies because a larger aspect ratio of the cell is available. The need for a 2D model can only be reduced if the cell has a smaller aspect ratio or the current collectors have increased thickness with two orders of magnitude larger thermal conductivity [197].

$$\psi = \psi_{\text{ref}} \exp\left(\frac{E_{\text{act}}^{\psi}}{R} \left(\frac{1}{T_{\text{ref}}} - \frac{1}{T}\right)\right) \quad (3.20)$$

ψ_{ref} – property value defined at reference temperature T_{ref}

E_{act}^{ψ} - activation energy, which controls the temperature sensitivity of each individual property ψ

Table 3.4: A summary of thermal-electrochemical models used in literature

Refs.	Battery type (positive/ negative electrode)	Configuration	Electro- chemical model (ECM)	Thermal model (Eq. from Table 3.3)
Pals and Newman [169]	LiPEO ₈ - LiCF ₃ SO ₃ / LiTiS ₂	Small cell	1D ECM developed by Doyle et al. [170]	Eq. 3.15, Eq. 3.17
Song and Evan [198]	LiMn ₂ O ₄ / graphite	Prismatic		Eq. 3.14, Eq. 3.17 (2D)
Gu and Wang [189]	LiMn ₂ O ₄ / graphite	Large size lithium-ion cell for HEV/EV applications		Eq. 3.14, Eq. 3.16
Gomadam et al. [199]	LiCoO ₂ / graphite	Prismatic		Eq. 3.14, Eq. 3.16
Srinivasan and Wang [197]	LiMn ₂ O ₄ / graphite	Small cell		Eq. 3.14, Eq. 3.16 (2D)
Smith and Wang [194]	LiCoO ₂ / graphite	72 cell battery pack		Eq. 3.15, Eq. 3.16 (neglected reversible heating)
Kim and Smith [191, 200]	LiMn ₂ O ₄ / graphite	Cylindrical		Eq. 3.14 (2D)
Fang et al. [195]	NMC/ graphite	Cylindrical		Eq. 3.15, Eq. 3.16 (neglected reversible heating)
Lee et al.	LiMn ₂ O ₄ / graphite	Cylindrical		Eq. 3.14

[192]	graphite			(3D)
Cai and White [201]	LiFePO ₄ /graphite	/		Eq. 3.14, Eq. 3.16
Prada et al. [196]	LiFePO ₄ /graphite	Cylindrical		Eq. 3.15, Eq. 3.17
Baker and Verbrugge [202]	LiMn ₂ O ₄ /graphite	Thin film	2D	Eq. 3.14, Eq. 3.17 (2D)

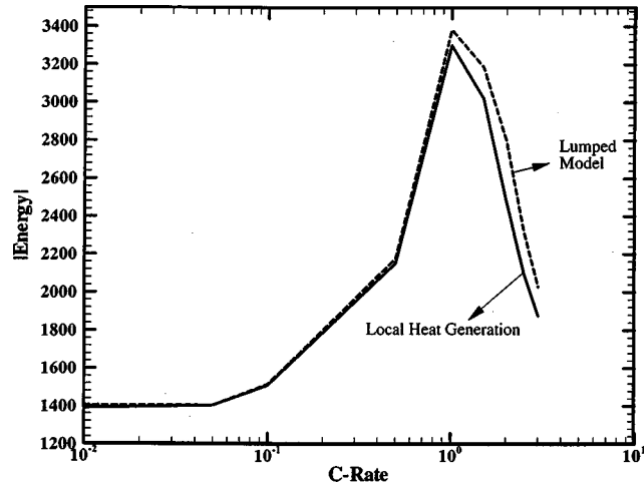
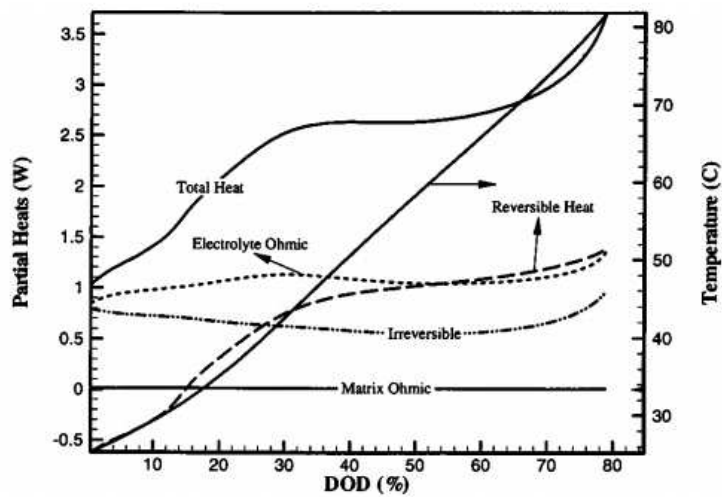


Figure 3.6: A comparison of thermal energy generated using local heat generation and lumped thermal models under adiabatic conditions [197].



(a)

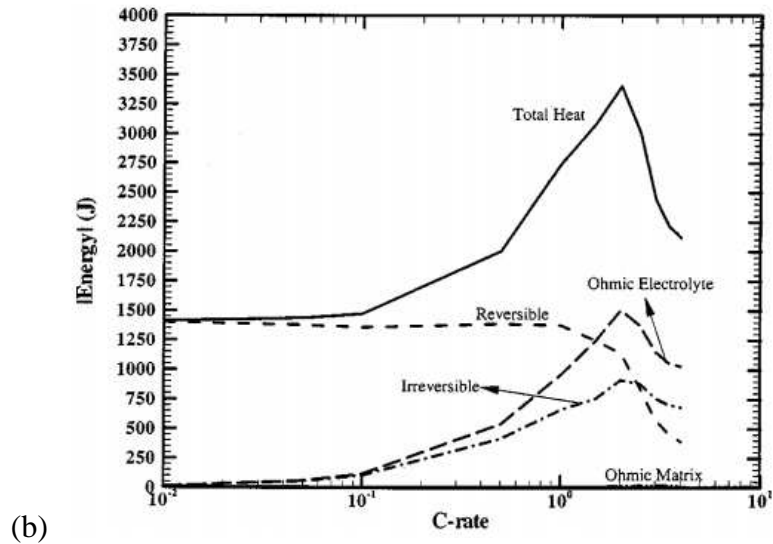


Figure 3.7: Heat generated due to various terms contributing to the total heat (a) under 2C discharge of a lithium-ion cell; and (b) under various discharge C rates [197].

For large-scale battery packs applied in HEVs and EVs, the collective thermal effects from electrochemical processes are normally obtained from experiment measurements and therefore treating such battery pack as the heat source in a standalone thermal model is possible [203]. Examples are shown in Table 3.5, which established 1–3D decoupled thermal models with the heat generation obtained from experiment. For such thermal model development, the heat is assumed to be generated within the solid domain (conductive heat transfer) and then be transferred to the surrounding medium at boundary surfaces (convection and radiation) (Fig. 3.8). Four assumptions can be made to estimate the battery thermal behaviour: 1) homogenous internal cell condition; 2) uniform temperature distribution of internal heat source; 3) no convection or thermal radiation exists inside the battery cell; 4) thermophysical properties are independent of temperature. However, the necessity of

decoupling needs to be justified since discrepancies in predicting battery cell temperature can be found between thermo-electrochemical coupled and decoupled model. As reported by Gu and Wang [168], no temperature difference was detected under 1C charging (constant current) and two convective heat transfer conditions (5, 25 W/m²K), but discrepancies were noted under 1.5 V float charging (constant voltage), especially at high percentage of normal cell capacity (Fig. 3.9).

Table 3.5. Standalone thermal models (decoupled) in various studies

Refs.	Battery type (positive/negative electrode)	Configuration	Thermal Model	Heat generation method
Chen and Evans [115]	LiV ₆ O ₁₃ /Li	Prismatic	2D	ED
Chen and Evans [204]	LiTiS ₂ /Li	Prismatic	3D	ED
Chen and Evans [205]	LiCoO ₂ /graphite	Prismatic	2D	ED
Hallaj et al. [184, 206]	LiCoO ₂ /graphite	Cylindrical	1D	ARC
Chen et al. [207]	LiCoO ₂ /graphite	Cylindrical	3D	ED
Onda et al. [208]	LiCoO ₂ /graphite	Cylindrical	1D	OCP
Chen et al. [209]	LiCoO ₂ /graphite	Cylindrical	2D	ED
Kim et al. [210, 211]	LiNiCoMnO ₂ /graphite	Prismatic	2D	ED
Taheri et al. [203]	LiNiCoMn ₂ O ₂ /graphite	Prismatic	3D	ED

Note: ED – Experimental data (such as over-potential and entropic heat coefficients to predict the heat generation rate); ARC – accelerated rate calorimeter; OCP – open-circuit potential;

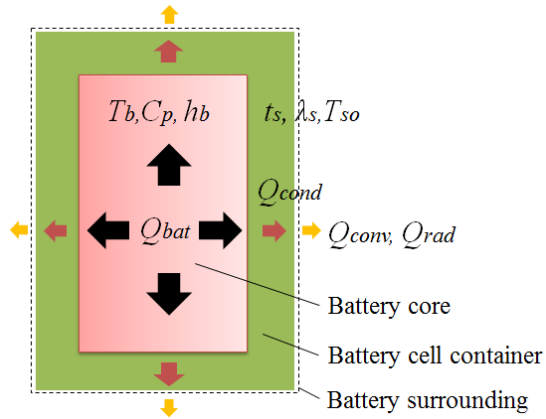


Figure 3.8: Heat transfer from internal battery cell to the cell container surface and to the surroundings.

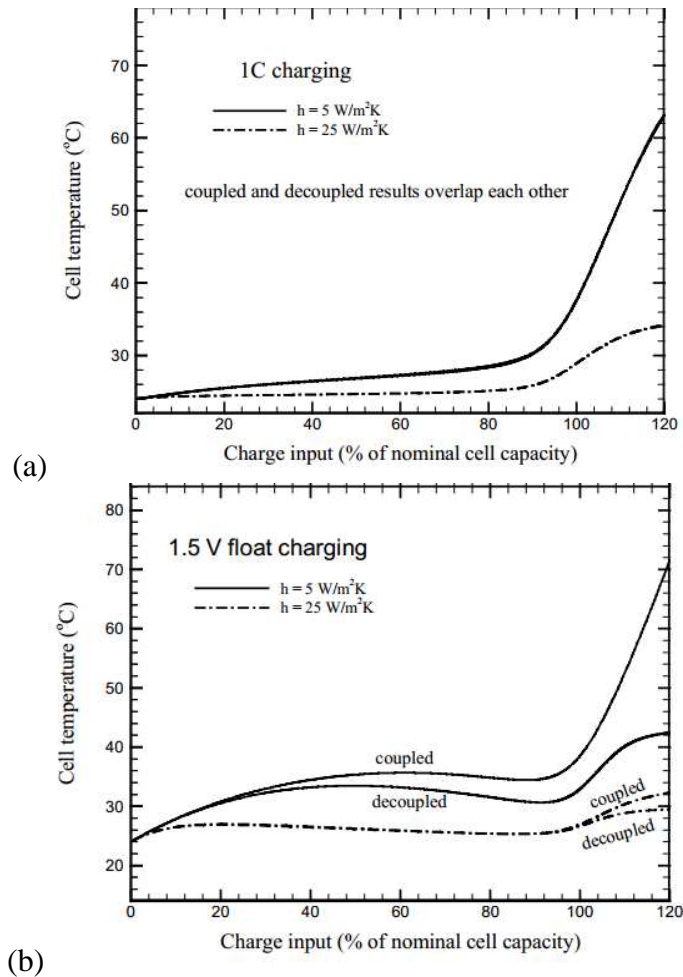


Figure 3.9: Comparison of predicted cell temperature between thermo-electrochemical coupled and decoupled model during (a) 1C charging and (b) 1.5V float charging [168].

3.4 Finite Element Analysis (FEA)

Finite element analysis (FEA) is a numerical method that helps find an approximate solution to partial differential equations (PDE) for a simplified model [212]. In FEA, a given domain can be divided into a number of subdomains (i.e. finite elements). The approximation function can be derived by applying a linear combination of algebraic polynomials over each finite element, and the algebraic relations among the undetermined coefficients (i.e. nodal values) are obtained from the governing equations. Notably, each individual segment of the solution must fit its adjacent segments. This ensures that the function and possible derivatives up to a chosen order at the connecting points are continuous [213]. The approximate solution can be characterised by using concepts from interpolation theory, and the degree of the interpolation functions is dependent on the number of nodes in the element and the order of the differential equations.

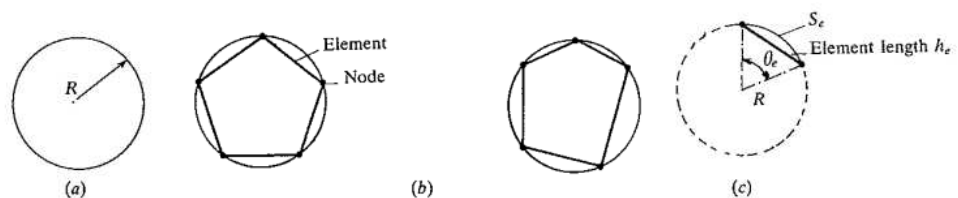


Figure 3.10: Approximating the circumference of a circle by line elements [213]: (a) circle of radius R ; (b) uniform and nonuniform meshes used to represent the circumference of the circle; (c) a typical element.

An example of approximating the perimeter of a circle using FEA is illustrated. The steps involved in computing an approximate value for the circle perimeter in Fig. 3.10 are 1) finite element discretisation; 2) element

equations; 3) assembly of element equations and solution; and 4) convergence and error estimate. The discretisation comes from segmenting the domain (i.e. the circumference of the circle) into a finite number n of subdomains (i.e. line segment). Each subdomain refers to an element. The collection of elements is called the finite element mesh. If all elements (i.e. line segments) are of the same length, the mesh is uniform; otherwise, non-uniform (Fig. 3.10 (b)). The points that connect each element are named nodes. For a typical element (i.e. line segment, Ω^e), the element equation to calculate the length h_e can be given by Eq. 3.21 below.

$$h_e = 2R \sin \frac{1}{2} \theta_e \quad (3.21)$$

R – radius of the circle

θ_e – angle subtended by the line segment

Then, based on the element equation, the approximate value of the total circle perimeter can be presented as the sum of the element equations, i.e. the assembly of the element equations.

$$P_n = \sum_{e=1}^n h_e \quad (3.22)$$

The exact solution of this problem is $p = 2\pi R$. It is noted that the error in the approximation decreases as the number of elements increases. As $n \rightarrow \infty$, the approximate P_n converges to the exact p , and the total error (also global error) in the approximation is

$$E = 2\pi R - P_n \quad (3.23)$$

FEA modelling for battery thermal performance has been performed using widely accepted commercial software packages such as ANSYS and COMSOL multiphysics. The earliest FEA model for HEV/EV batteries was made by Pesaran et al. [214]. They demonstrated a 2D FEA model of a HEV battery module under two circumstances (Fig. 3.11). Usually case and core of a cell are considered as two regions with different thermal conductivity. FEA helps calculate the effective thermal conductivity in each direction. Results show that air cooling can reduce the maximum temperature by 9°C while keeping the temperature difference across the module less than 10°C. For battery heating, a parametric 3D transient thermal finite element model of a typical battery pack was established and analysed [126]. Detailed finite element models via different heating methods can be found in Fig. 3.12. The 3D finite element thermal analysis of a Panasonic NiMH battery module (7.2 V, 6.5 A) for 2001 Toyota Prius HEV was studied by NREL [215] (Fig. 3.13 (a)). They later on developed the first electro-thermal analysis using ANSYS to estimate the temperature distribution in the 2004 Toyota Prius HEV cells [216] (Fig. 3.13 (c)).

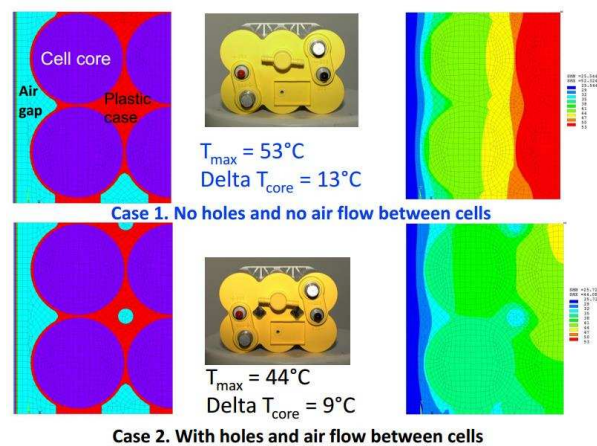


Figure 3.11: 2D thermal modelling of a HEV module without/with air cooling (modified from [95, 214]).

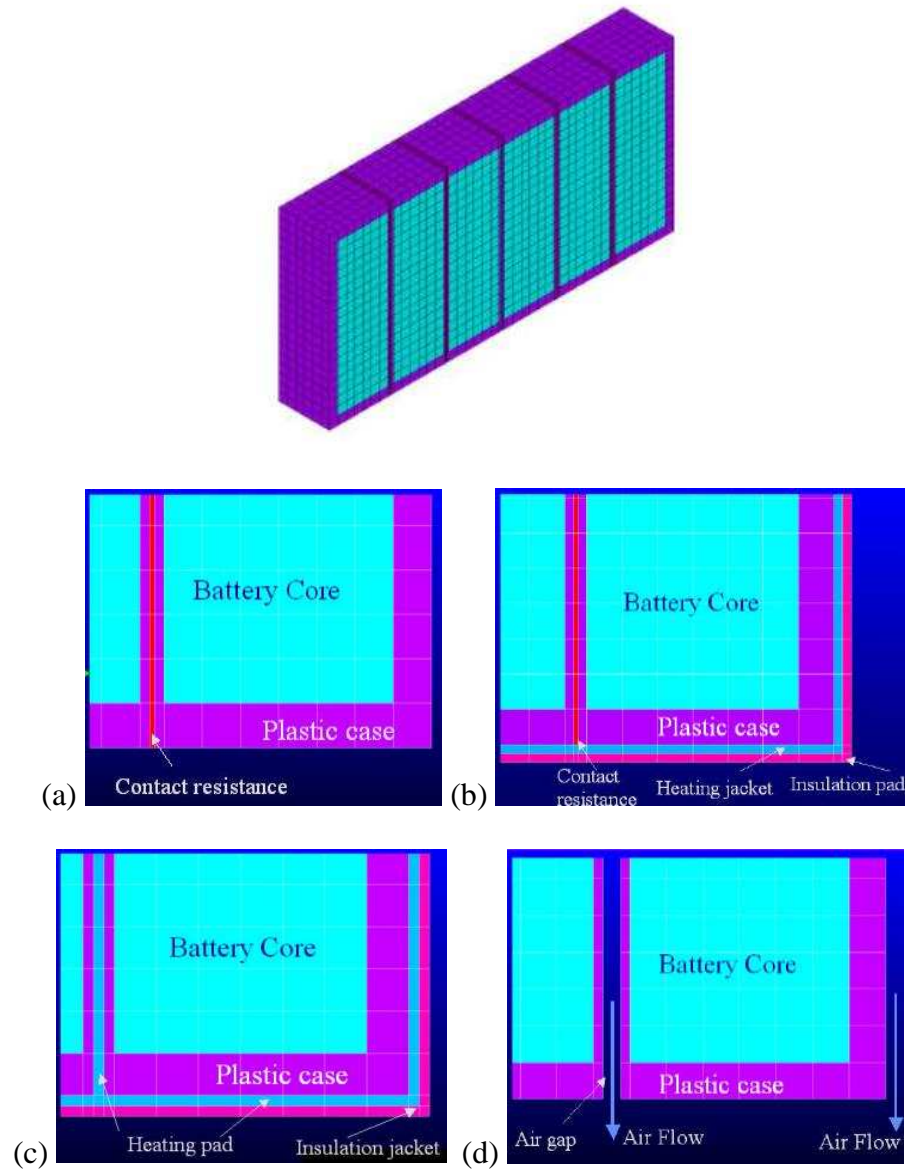


Figure 3.12: Finite element model details for battery cell using (a) internal core heating; (b) external jacket heating; (c) internal jacket heating; (d) internal fluid heating [126].

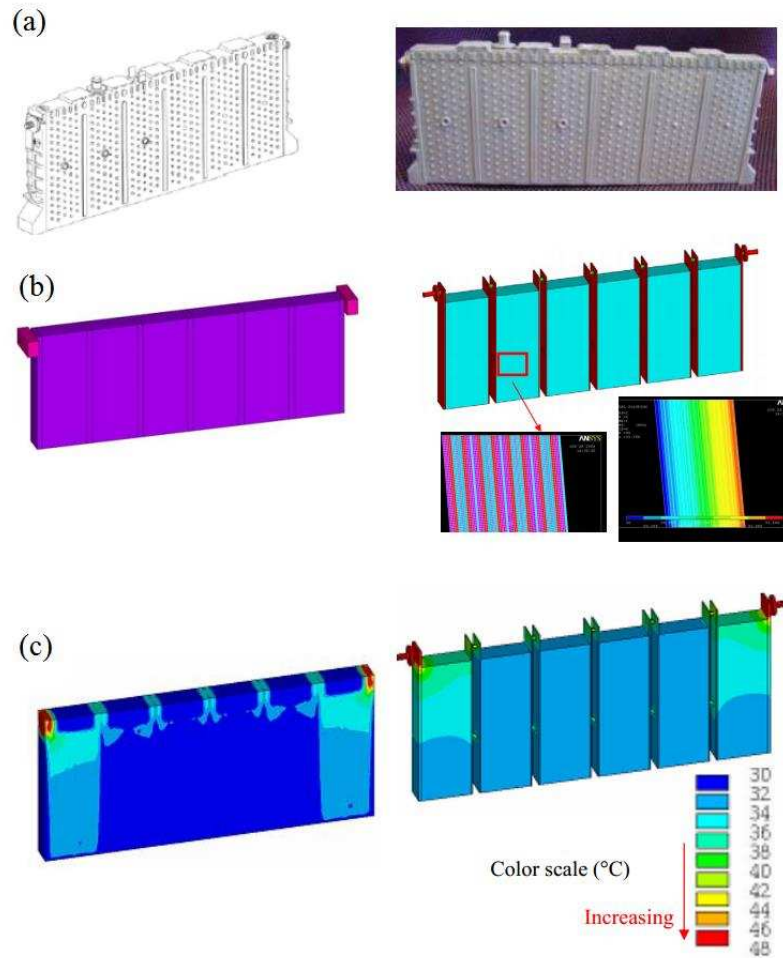


Figure 3.13: (a) Panasonic NiMH battery module (7.2V, 6.5A) used in 2001 Toyota Prius; (b) FEA of 2001 Panasonic module (with case – left; without case – right); (c) model prediction for 2004 module, temperature distribution after 3min from the start of 100A discharge [216].

3.5 Summary

Approaches for battery thermal modelling range from simple decoupled models, to partially coupled models, to complex fully coupled models. A battery thermal model can be either thermal-electrochemical coupled or decoupled, depending on the heat generation. A fully coupled model uses

newly generated parameters from electrochemical model to calculate the heat generation, while the decoupled model employs empirical equations based on experimental data. However, the majority of the experimental measurements has been conducted based on small cells at low charge/discharge rate near ambient temperatures, thus a standalone thermal model for an entire battery pack may not be accurate enough to predict the thermal behaviour.

Nevertheless, modelling through advanced software such as ANSYS and COMSOL becomes more accessible to battery developers, and the development of battery modelling is expected to benefit more testing conditions. FEA modelling for battery thermal performance in many commercialised HEVs/EVs has been reviewed reflecting the important role battery modelling plays.

Chapter 4

Development of Battery Thermal Model and Validation

4.1 Description of Battery Pack

A lithium-ion battery pack was designed for use in an EV as described briefly in Chapter 1 (Fig. 1.1). The properties of the battery cell are given by the manufacture (Table 4.1). Heat pipes are suggested to thermally manage the interior battery pack and help maintain the best cell operating temperature range under various working conditions. The BTM will be integrated with the cabin air conditioning that bypasses a cooling/heating loop to facilitate heat pipe heat transfer process (Fig. 4.1).

The cell distribution is of high density. 30 prismatic lithium-ion cells measuring $120 \times 71 \times 27.2 \text{ mm}^3$ were packed with small air gaps (5 mm) in between. The batteries are required to operate in a range of 15 – 40°C under all-weather conditions and the maximum operating temperature should be controlled below 70°C to avoid thermal runaway. The model geometry of the pack was developed in SolidWorks (Fig. 4.2). Component geometry was again modelled in SolidWorks as it provides better tools for part dimensioning. The upper end of cells is normally for electric wiring and installing, and the bottom

end of cells will be isolated from the liquid box to prevent issues such as short circuit or liquid leakage. The heat pipe is cylindrical sintered copper-water heat pipe with a diameter of 10 mm, which will be made into an 'L' shape and flattened at the part in contact with the battery surface. Using sintered copper powder as heat pipe wick structure has advantages of promoting heat transfer and liquid return in spite of the gravity. Detailed parameters can be found in Chapter 5.1 – Table 5.2. An aluminium plate with a U-shaped cutout will be placed between each cell gap for the purpose of temperature flattening. A liquid box underneath the battery pack serves as a heat exchanger allowing heat to be removed or supplied as requested. This facilitates the bi-directional characteristic offered by the sintered copper-water heat pipe, such that the system can provide either cooling or heating with no moving parts.

During cooling mode, the heat is generated from the battery cell and is transferred through two layers of conduction, i.e. the plate and the heat pipe wall. Then the heat enters into the base wall of the heat pipe evaporating the fluid inside the wicks. The vapour flows down to the cooling section due to the pressure difference between two ends and also the gravity, so that heat can be removed at the condenser through forced convection. The generated condensate inside the heat pipe will be drawn back to the evaporator by capillary force produced by the wick thus repeating the above process. As to battery preheating, the aforementioned condenser becomes the evaporator allowing an adequate amount of thermal energy from the pre-treated coolant inside the liquid box to be transferred to the battery surface.

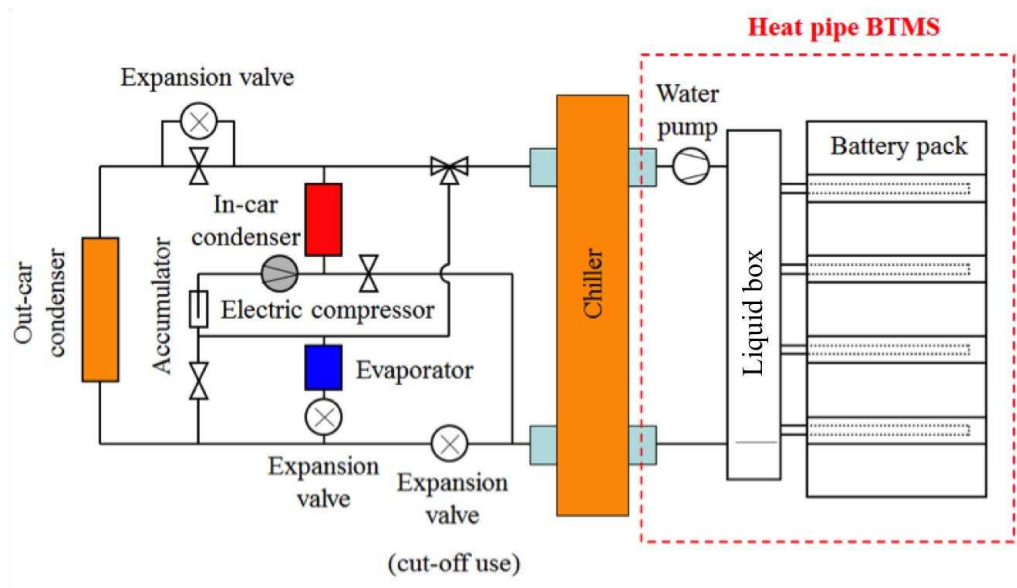


Figure 4.1: System layout.

Table 4.1: Lithium-ion cell specifications

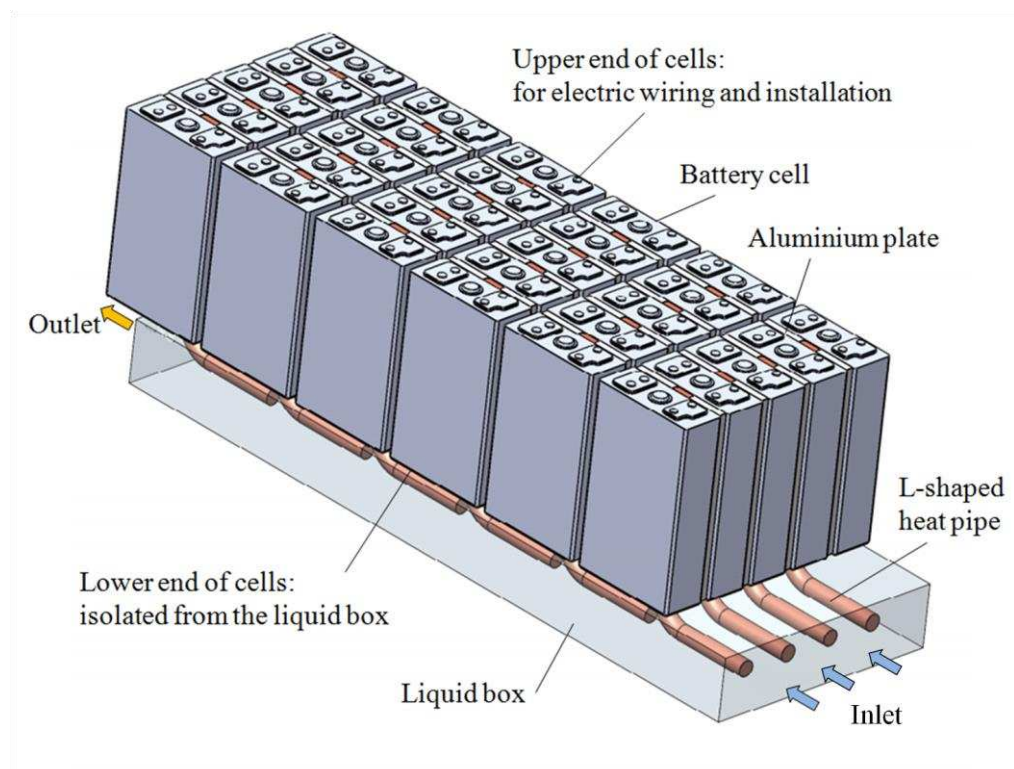
Battery Materials	
Electrolyte	LiPF ₆ , EC+EMC+PC
Cell material	Aluminium
Dimensions	
Length or Thickness (l), mm	27.2
Width (b), mm	71
Height (h), mm	120
Weight per cell, g	453±8
Electrical Parameters	
Nominal Voltage, V	3.2
Nominal Capacity, Ah	16.5
Internal Resistance R _t , mΩ	≤8
Specific Energy, Wh/kg	115
Energy Density, Wh/L	232
Specific Power	690
(50% depth of discharge, 10 sec), W/kg	
Power Density	1400
(50% depth of discharge, 10 sec), W/L	

Working Conditions

Minimum Discharge Voltage, V	2
Maximum Discharge Voltage, V	3.42
Maximum Charge Voltage, V	3.65±0.05
Maximum Continuous Discharge Current	4C
Maximum Discharge Current (peak<10sec)	6C
Maximum Continuous Charge Current	2C
Acceptable Operating Temperature, °C	-20-60
Advised Charging Temperature, °C	0-45

Thermo-physical Properties of Lithium-ion Battery

Density ρ , kg/m ³	2000
Specific heat capacity, C_p (J/kgK)	1060
Thermal conductivity, λ (W/mK)	$\lambda_l = \lambda_h = 60$; $\lambda_b = 0.8$



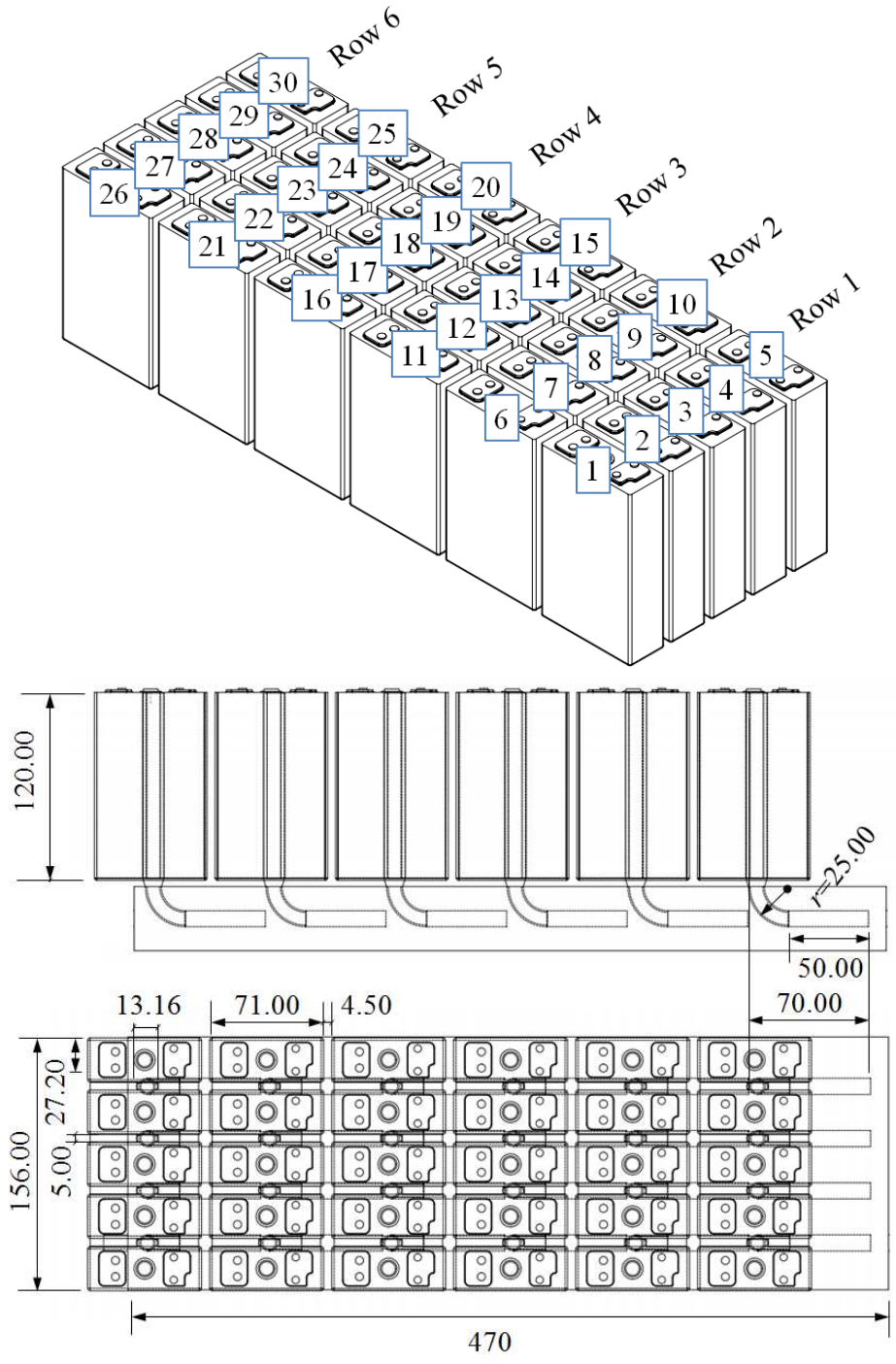


Figure 4.2: Heat pipe BTMS demonstration with marked cell numbers and dimensions in mm.

4.2 Model Development

3D finite element method (FEM) model was built in order to test and study the thermal behaviour of the vehicle battery pack, and to evaluate the heat pipe thermal management solution based on the pack temperature. The model was built in COMSOL Multiphysics 4.3b, which has a fully integrated environment allowing for a unified modelling workflow. It uses well-established approximation methods to solve partial differential equations via FEM and can easily extend conventional models for one type of physics into multiphysics that solve coupled physics phenomena [217]. Both fully coupled model (containing a full 1D electrochemical model for lithium-ion batteries) and decoupled model (based on the equations developed from Sato [97] for calculating heat generation rate of lithium-ion battery cell) were developed to estimate the BTM performance. A symmetrical structure, which has only one battery cell, was considered to study mesh sensitivity and validate the model by comparing results with the experiment. The model will be scaled-up to a larger size as depicted in Fig. 4.2 allowing pack level analysis. Table 4.2 summarises the physics models used in the decoupled and coupled model.

Table 4.2: Model development in COMSOL Multiphysics

	Decoupled	Coupled
1D electrochemical	×	√
Fluid flow dynamics	√	√
Heat transfer in solids and fluids	√	√

4.2.1 Battery Model

4.2.1.1 Decoupled

A decoupled method that treats lithium-ion batteries as heat source in a standalone 3D symmetrical model can be used to evaluate the proposed BTM system performance (Fig. 4.3). The heat generation is modelled as a uniform heat generation inside the volume of each cell (Fig. 3.8), and the rate was obtained using Eq. 3.18 – 3.19. Decoupled model eliminates the dependency of temperature in battery heat generation serving as an effective tool in evaluating heat pipe performance as well as system cooling/preheating behaviour.

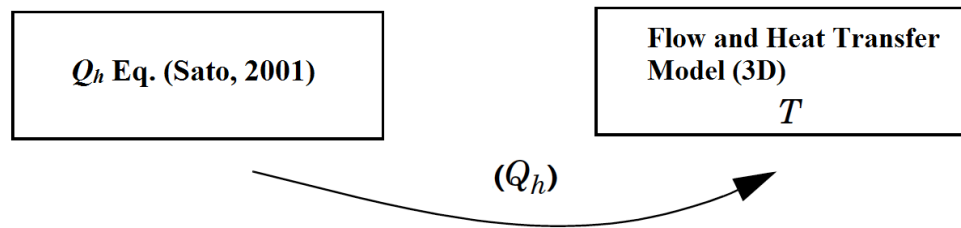


Figure 4.3: Decoupled model.

Table 4.3 presents the charge and discharge condition based on a rated capacity of 16.5 Ah lithium-ion cell demonstrated in Table 4.1. Note that the heat value per unit cell under corresponding charge and discharge conditions are calculated and demonstrated according to a representative value, i.e. 50% DOD (depth of discharge). The electrical resistance depends on the current network that links collector and electrode active materials by a nonconductive metal (i.e. the separator) and the electrolyte among others [97]. 50% DOD represents the baseline value of the internal resistance ratio of 1. Electric conductivity increases with elevated battery temperature. But for simplicity,

the heat generation rates calculated for decoupled model are based on an average value.

Table 4.3: Lithium-ion battery cell charge/discharge condition

	Current	Equivalent charge current (A)	Heat value/cell (W)
Charge Condition			
Pre-charge	0.05C	0.825	-0.07
	0.1C	1.65	-0.14
Standard/normal charge range	0.2C	3.3	-0.23
	0.5C	8.25	-0.26
	1C	16.5	+0.57
Max charge	2C	33	+5.50
Discharge Condition			
Standard/normal discharge range	0.2C	3.3	+0.41
	0.4C	6.6	+1.35
	1C	16.5	+3.78
	2C	33	+11.92
	3C	49.5	+24.42
Max discharge (continuous)	4C	66	+41.27
Max discharge (peak < 10s)	6C	99	+88.04

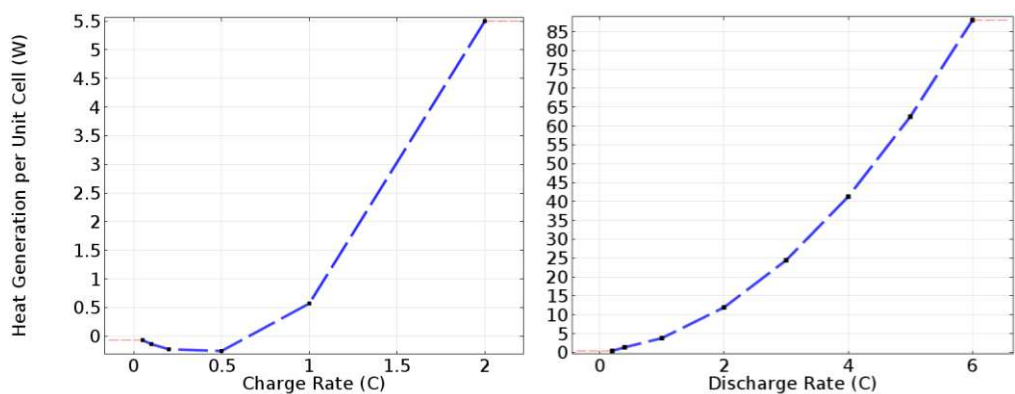


Figure 4.4: Heat generation rate per unit cell under charge/discharge current.

Negative sign indicates endothermic value, and positive, exothermic. Fig. 4.4 demonstrates how heat absorption and dissipation perform in the range from 0.05C (the minimum pre-charge current) to 2C (the specified maximum charge current). The heat value during endothermic process starts to increase from 0.05C to a peak value, and decrease to zero under approximately 0.75C where reaction heat is equal to the sum of polarisation heat and Joule heat. It will then release heat at 5.5 W/cell rate. The heat dissipation per unit cell under discharge rate from 0.2C to 6C is also indicated in Fig. 4.4. The heat generation during discharge is more substantial compared to that under charging. This is because the reaction heat becomes the most dominant factor and is positive during the entire process.

4.2.1.2 Coupled

A full 1D electrochemical model for lithium-ion batteries is also developed to calculate the average heat source in relation to the temperature profile of the battery cell. A 3D symmetrical model is used to model the conjugated heat transfer including laminar flow and heat transfer in solids (Fig. 4.5). Since the heat conductivity of the components of a lithium-ion battery is high compared to the heat generated, it is assumed that the battery will have a uniform temperature profile ($Bi = 0.0047 \sim 0.18 < 1$) and the battery chemistry will not be heavily affected by small temperature changes. The above two models will be coupled by the generated heat source and the average temperature based on lumped heat transfer.

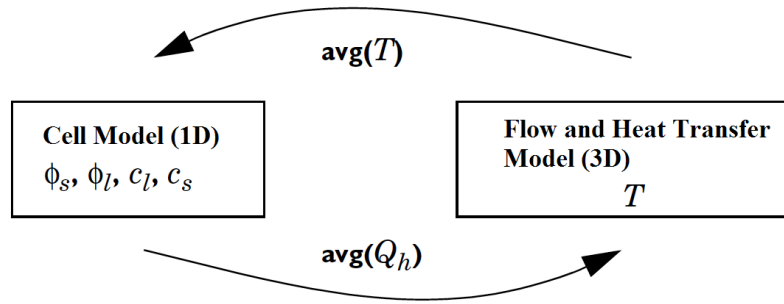


Figure 4.5: Coupling between the cell and flow and heat transfer model using the average values for the temperature and battery heat generation.

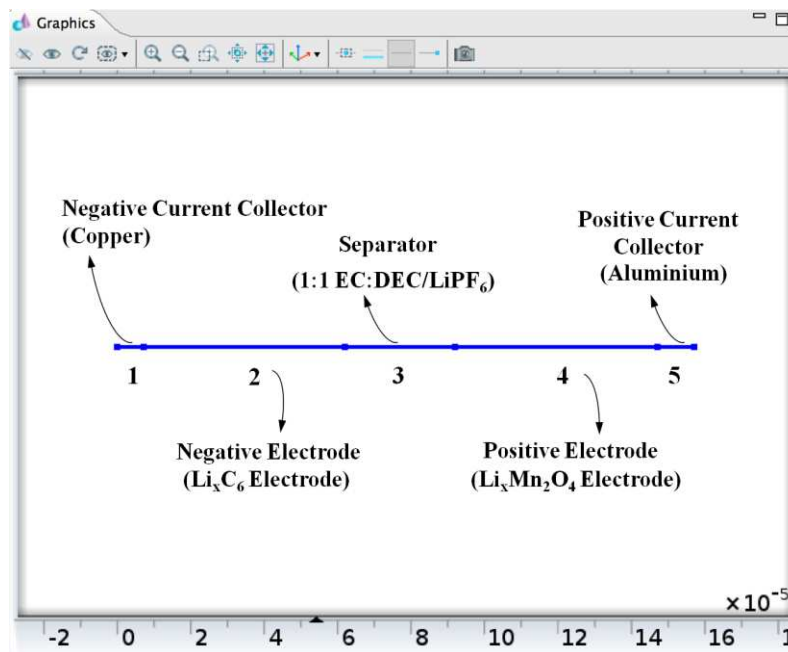


Figure 4.6: 1D isothermal lithium-ion battery model created in COMSOL Multiphysics 4.3b.

The cell model consists of 5 domains as illustrated below (Fig. 4.6):

- Negative current collector (copper, 7 μm)
- Negative porous electrode (Li_xC₆, 55 μm)
- Separator (electrolyte 1:1 EC/DMC in LiPF₆, 30 μm)
- Positive porous electrode (Li_xMn₂O₄, 55 μm)
- Positive current collector (Al, 10 μm)

The model involves 5 following processes [218]:

- Electronic current conduction in the electrodes
- Ionic charge transport in the electrodes and electrolyte/separator
- Material transport in the electrolyte, which allows to account for the effects of concentration on ionic conductivity and concentration overpotential (obtained from experiment)
- Material transport within the spherical particles that from the electrodes
- Butler-Volmer electrode kinetics using discharge curves (measured from experiment) to obtain the equilibrium potential

The boundary condition of 1D lithium-ion battery model will be summarised in Table 4.4. The electric potential in the electron conducting phase ϕ_s can be calculated using Ohm's law. For the porous electrodes effective conductivities σ_s^{eff} , it can be formulated using Eq. 4.1 where γ is the Bruggeman coefficient ($\gamma = 1.5$ to indicate a packed bed of spherical particles).

$$\sigma_s^{\text{eff}} = \sigma_s \xi^\gamma \quad (4.1)$$

The ionic charge balances and material balances are modelled using Eq. 4.2 – 4.5 for 1:1 EC:DEC/LiPF₆ electrolyte. Fickian diffusion equation (Eq. 4.5) describes the transport in the spherical particles and is expressed for the material balance of lithium in the particles in spherical coordinates. Butler-Volmer electrode kinetics (Eq. 4.14 – 4.16) can be used to obtain the local charge transfer current density in the electrodes.

Table 4.4: 1D lithium-ion battery model domain and boundary condition settings

Electrolyte (Domain 3)	
Equation	$\nabla \cdot \mathbf{N}_1 = R_1$ (4.2)
	$\nabla \cdot \mathbf{i}_1 = Q_1$ (4.3)
	$\mathbf{i}_1 = -\sigma_1 \nabla \phi_1 + \frac{2\sigma_1 RT}{F} \left(1 + \frac{\partial \ln f}{\partial \ln c_1}\right) (1 - t_+) \nabla \ln c_1$ (4.4)
	$\mathbf{N}_1 = -D_1 \nabla c_1 + \frac{\mathbf{i}_1 t_+}{F}$ (4.5)
Initial condition	<p>Electrolyte conductivity $\sigma_1 = \sum \int f(c) dc$ (depends on salt concentration c, see Fig. 4.7)</p> <p>Electrolyte salt diffusivity $D_1 = 3e-10$ (m²/s)</p> <p>Transport number $t_+ = 0.363$</p> <p>Activity dependence $\frac{\partial \ln f}{\partial \ln c_1} = 0$</p>
Domain 1-3	
Initial condition	<p>Electrolyte potential $\phi_1 = -0.1$ V</p> <p>Electrolyte salt concentration $c_1 = c_{1,0} = 2000$ mol/m³</p> <p>Electric potential $\phi_s = 0$ V</p>
Negative and Positive Current Collector (Domain 1, 5)	
Equation	$\nabla \cdot \mathbf{i}_s = Q_s$ (4.6)
	$\mathbf{i}_s = -\sigma_s \nabla \phi_s$ (4.7)
Negative and Positive Porous Electrode (Domain 2, 4)	
Equation	$\xi_1 \nabla \cdot \mathbf{N}_1 = R_1 = -\sum_m \frac{V_{Li+,m} \mathbf{i}_{v,m}}{F} + R_{1,src}$ (4.8)
	$\nabla \cdot \mathbf{i}_1 = \mathbf{i}_{v,total} + Q_1$, $\nabla \cdot \mathbf{i}_s = -\mathbf{i}_{v,total} + Q_s$, $\mathbf{i}_s = -\sigma_s^{eff} \nabla \phi_s$ (4.9)
	$\mathbf{i}_1 = -\sigma_1^{eff} \nabla \phi_1 + \frac{2\sigma_1^{eff} RT}{F} \left(1 + \frac{\partial \ln f}{\partial \ln c_1}\right) (1 - t_+) \nabla \ln c_1$ (4.10)
	$\mathbf{N}_1 = -D_{1,eff} \nabla c_1 + \frac{\mathbf{i}_1 t_+}{F}$ (4.11)
	$D_{1,eff} = \xi^{1.5} D_1$, $\sigma_{1,eff} = \xi^{1.5} D_1 \sigma_1$, $\sigma_s^{eff} = \xi^{1.5} \sigma_s$

	(4.12)
	$i_{v,\text{total}} = \sum_m i_{v,m} + i_{v,\text{dl}} \quad (4.13)$
Porous Electrode Reaction	$i_{\text{loc}} = i_0 \left(\exp\left(\frac{\alpha_a F \eta}{RT}\right) - \exp\left(\frac{-\alpha_a F \eta}{RT}\right) \right) \quad (4.14)$
	$\eta = \phi_s - \phi_l - E_{\text{eq}} \quad (4.15)$
	$i_0 = F(k_c)^{\alpha_a} (k_a)^{\alpha_c} (c_{s,\text{max}} - c_s)^{\alpha_a} (c_s)^{\alpha_c} \left(\frac{c_l}{c_{l,\text{ref}}}\right)^{\alpha_a} \quad (4.16)$
Properties	Anodic transfer coefficient $\alpha_a = 0.5$ Cathodic transfer coefficient $\alpha_c = 0.5$ Anodic rate constant $k_a = 2\text{e-}11$ m/s Cathodic rate constant $k_c = 2\text{e-}11$ m/s Electrolyte reference concentration $c_{l,\text{ref}} = 1$ mol/m ³
Domain 4, 5	
Initial condition	Electrolyte potential $\phi_l = -0.1$ V Electrolyte salt concentration $c_l = c_{l,0} = 2,000$ mol/m ³ Electric potential $\phi_s = 3.6$ V

The electrolyte conductivity and the equilibrium potential of the electrodes plotted in Fig. 4.7 and Fig. 4.8 are from experimental measured data stored in COMSOL. The equilibrium potential for the negative and positive electrodes can be expressed as a function of the measured state of charge (SOC) (Eq. 4.17).

$$\text{SOC} = \frac{c_{s,\text{Li}}^{\text{surf}}}{c_{s,\text{Li}}^{\text{max}}} \quad (4.17)$$

The initial values of SOC for the negative and positive electrodes are 0.17 and 0.56 respectively. This translates to an open circuit cell voltage of 4.27 V, which indicates a fully charged battery. Fig. 4.9 demonstrates the discharge curves based on 0.2C, 1 – 6C rate. The capacity of the battery varies at

different discharge rates and the end-of-discharge can be defined as the time when the cell voltage drops below 3 V. High discharge rates such as 4C and 6C make the battery capacity deliver less than half of the theoretical capacity of 16.5 Ah/m² obtained from 1C (Fig. 4.9).

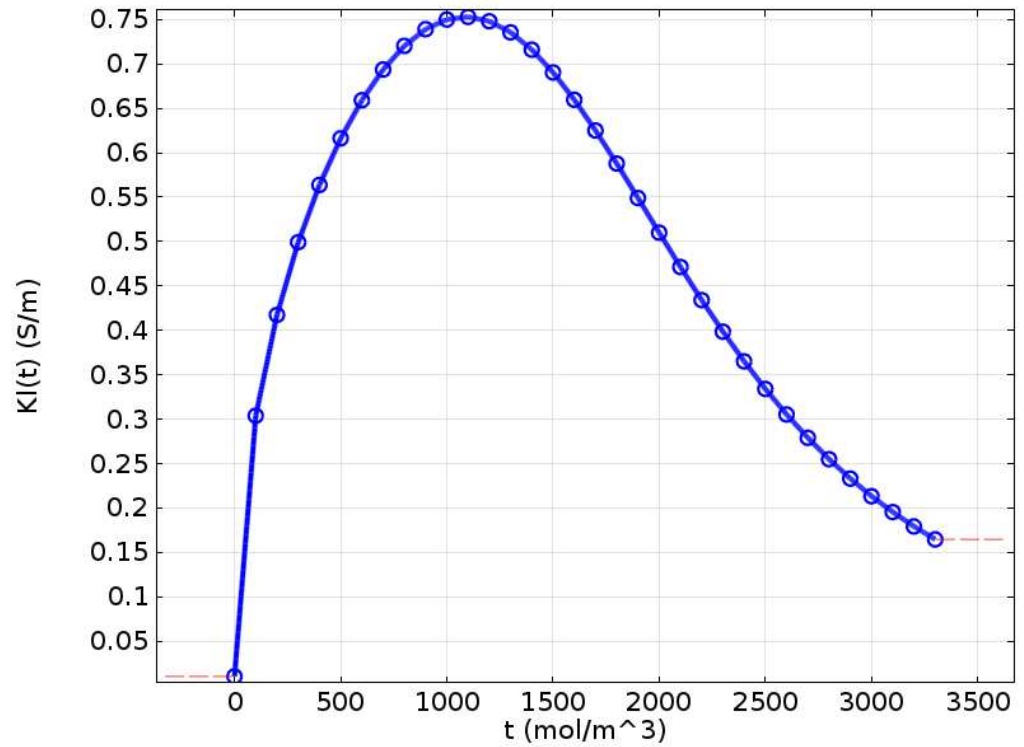


Figure 4.7: 1:1 EC:DEC/LiPF₆ electrolyte conductivity obtained from experimentally measured data (COMSOL stored data) using interpolation function according to concentration.

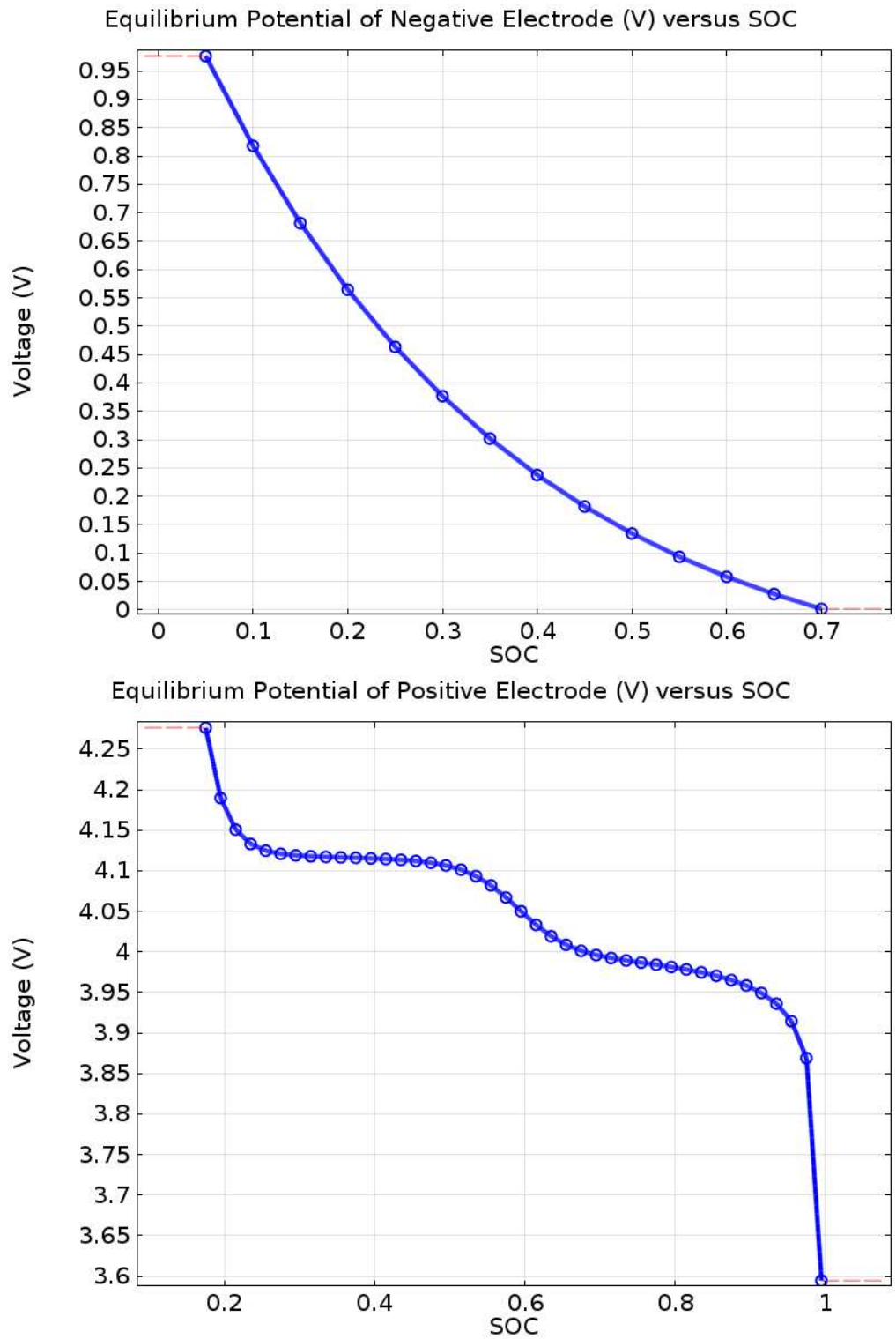


Figure 4.8: The voltage of the electrode materials measured from experiment.

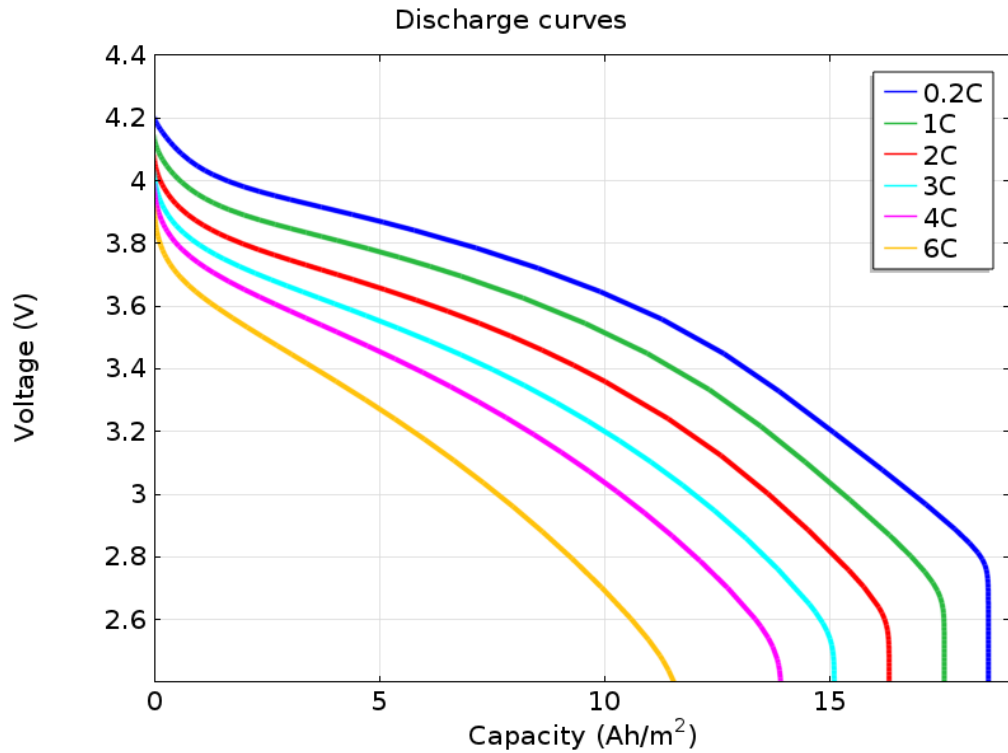


Figure 4.9: Discharge curves based on 0.2C, 1C, 2C, 3C, 4C & 6C rate.

The temperature is assumed to be the mean temperature of the battery using an integral function of component coupling (set as `aveop(mod.T)` in COMSOL). The applied current (i_{app}) is normally user-defined. The default expression will be expressed as a square wave function (`wv`) (Fig. 4.10) with an alternating charge/discharge current at 4C rate (continuous max) under a cycle time of 600 s. i_{app} can be written as:

$$i_{app} = i_{load} * (wv[t/1]) \quad (4.18)$$

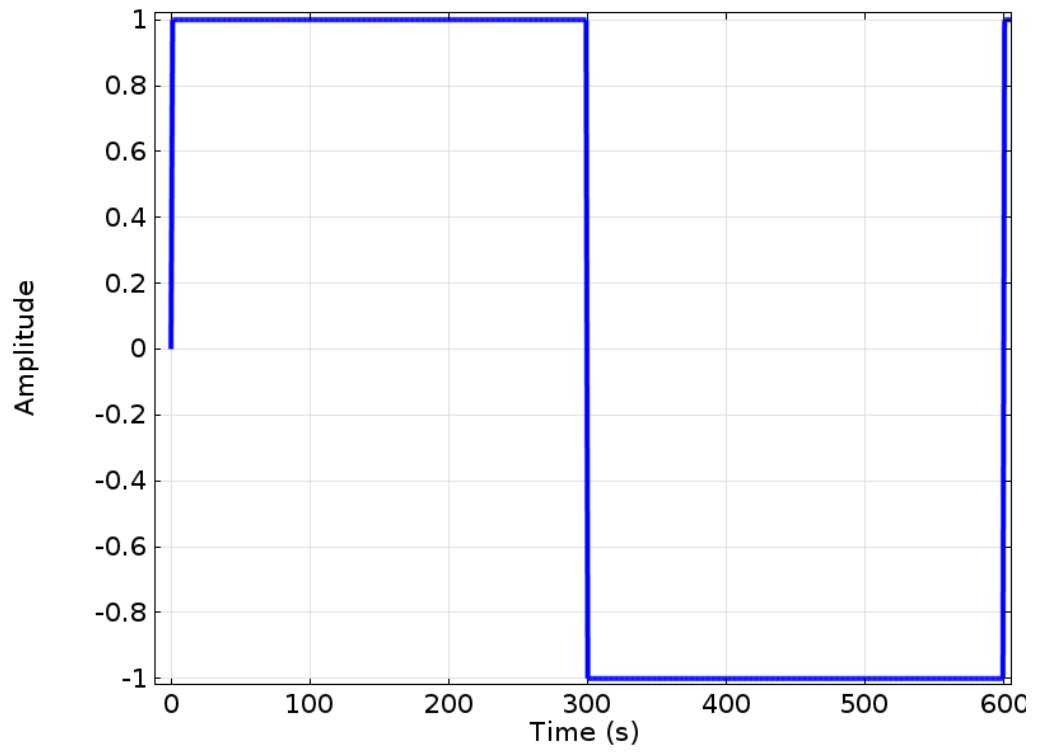


Figure 4.10: Wave function (angular frequency = $2 \times \pi / 600$).

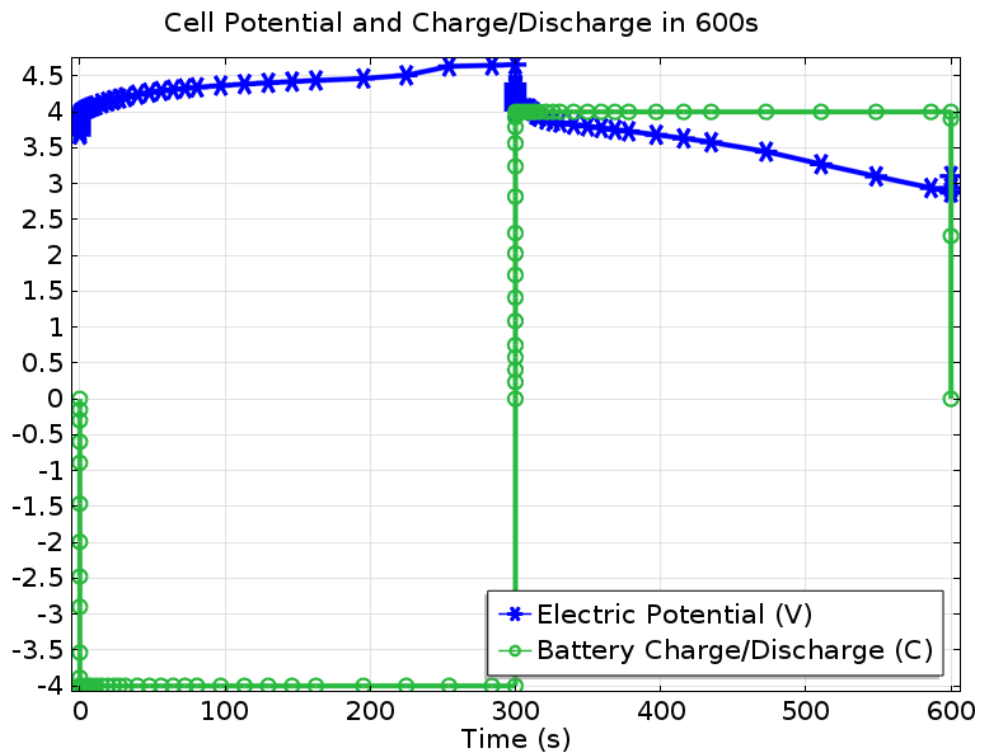
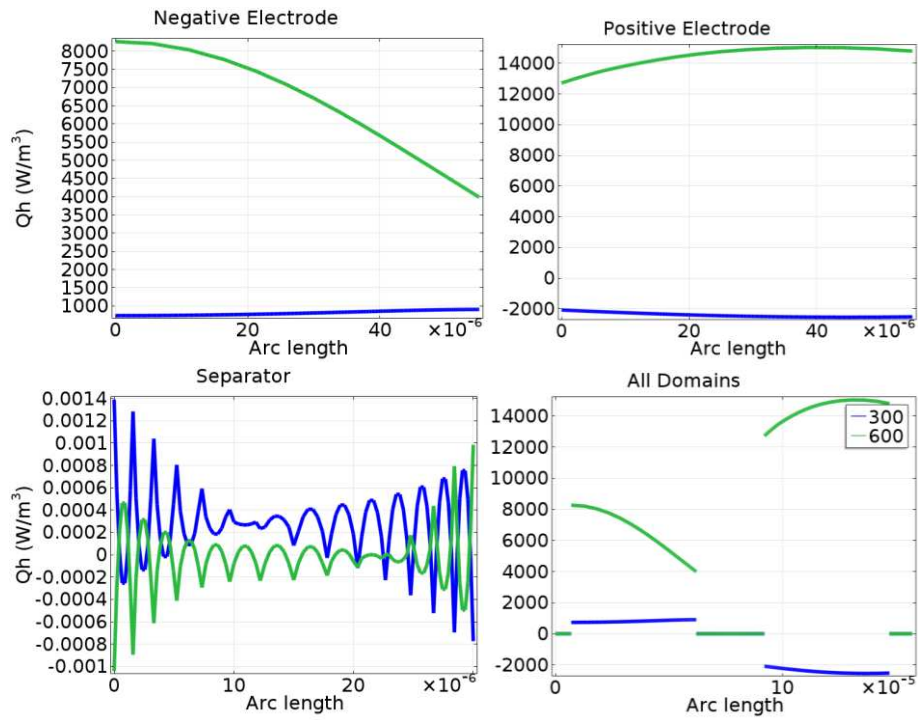
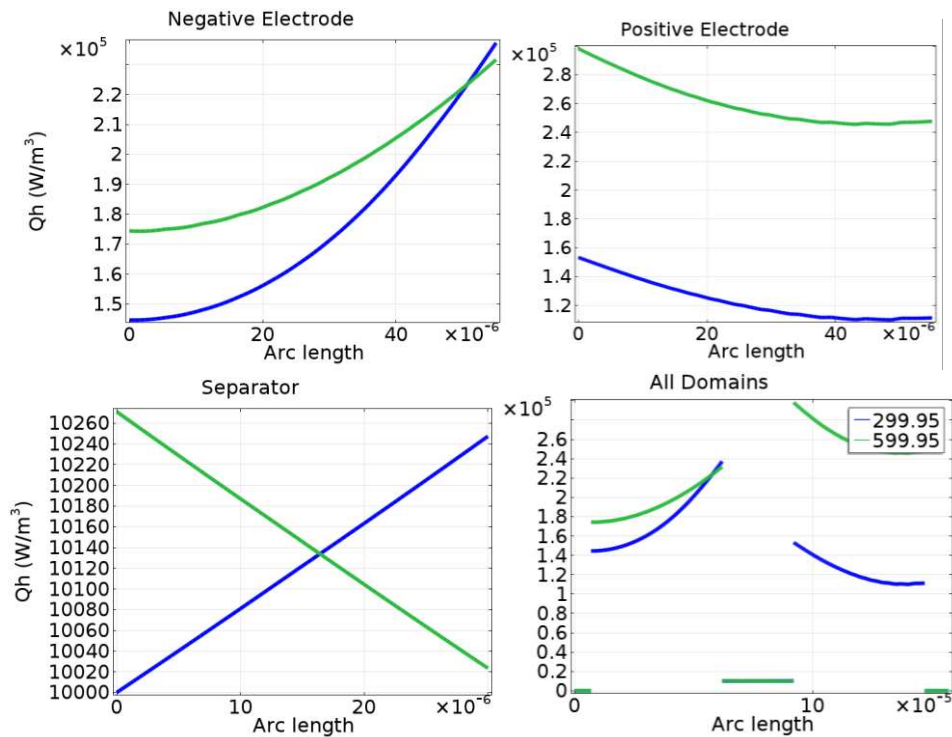


Figure 4.11: Cell potential and battery load at 4C rate under 600 s cycle time.



(a) $t = 300 \text{ s}, 600 \text{ s}$



(b) $t = 299.95 \text{ s}, 599.95 \text{ s}$

Figure 4.12: Total power dissipation density (W/m^3) simulated from 1D lithium-ion battery under a 4C charge-discharge cycle of 600 s: (a) at 300 s and 600 s; (b) at 299.95 s and 599.95 s.

Fig. 4.11 demonstrates the cell potential and battery load at 4C rate under a cycle time of 600 s based on the 1D electrochemical model. Fig. 4.12 shows the total heat dissipation resulted from negative electrode (Domain 2), positive electrode (Domain 4), separator (Domain 3) and the battery (Domain 1–5) at the end of each charge/discharge (i.e. at 300 s and 600 s) and 0.05 s before each charge/discharge (i.e. 299.95 s and 599.95 s) along corresponding 1D dimension arc length.

The heat generated from both current collectors (negative and positive) can be neglected. The heat comes mostly from the negative and positive electrode and is exothermic at all times (+1,000 W/m³ for charge at 300 s and +4,000 – 8,000 W/m³ under discharge at 600 s) for negative electrode. For positive electrode, the heat value is endothermic during charge (-2,000 W/m³ at 300 s) and exothermic under discharge (+12,000 – 16,000 W/m³ at 600 s). From Fig. 4.12 (a) for all domains, the heat added up during charge condition is negative, which means the battery absorbs heat during charge (-1,000 W/m³ at 300 s, i.e. -0.23 W/cell). For discharge condition, the heat dissipated from all domains becomes exothermic and approximately equals to +16,000 – 24,000 W/m³ at 600 s (equivalent to 3.71 – 5.56 W/cell).

Fig. 4.12 (b) shows the heat generated 0.05 s prior to each charge/discharge. The value changes significantly compared to that under 300s and 600s. Even the heat generated by the separator rises up from none to +10,000 – 10,260 W/m³ (equivalent to 2.32 – 2.38 W/cell). Both negative and positive electrodes dissipate heat, ranging from $+1.4 \times 10^5$ – 2.4×10^5 W/m³

(equivalent to 32.44 – 55.62 W/cell) and $+1.1 \times 10^5 - 3 \times 10^5$ W/m³ (equivalent to 25.49 – 69.52 W/cell) respectively.

The variations in heat generation during the load cycle is huge, but may not affect the overall temperature change as a considerable amount of time period is needed before reaching to thermal balance. The values obtained serve as references in comparison with the decoupled model, which accounts for an average heat value from -0.23 – 5.50 W/cell (-992 – 23,733 W/m³) during 0.2 – 2C charge, and 3.78 – 41.27 W/cell (+16,182 – 178,084 W/m³) under 1 – 4C discharge.

4.2.2 Flow and Heat Transfer Model

Conjugate heat transfer model is applied and symmetrical structures are built to save computing time while achieving accurate results. The model uses the laminar flow interface to solve for the velocity and pressure in the liquid zone and the heat transfer interface for the temperature field. First of all, a simple assembly of one battery cell, half plate and half heat pipe were established to study the effect of applying heat pipe to one side of the battery surface. The other surface with no heat pipe attached serves as a comparison purpose. The geometry was saved as an IGS file type and imported to COMSOL where it was meshed using free tetrahedral meshes. Fig. 4.13 shows a typical user interface of COMSOL Multiphysics 4.3b. Fig. 4.14 displays the model geometry that contains 5 domains:

- Battery cell (materials and properties obtained from lithium-ion battery model covered in Section 4.2.1, $120 \times 71 \times 27.2$ mm³)
- Plate (symmetrical, aluminium, $120 \times 71 \times 2.5$ mm³)

- Heat pipe (symmetrical, copper with user-defined thermal conductivity)
- Flow compartment (symmetrical, 5 mm thick aluminium container, 40 mm in depth for glycol-water mixture flow)

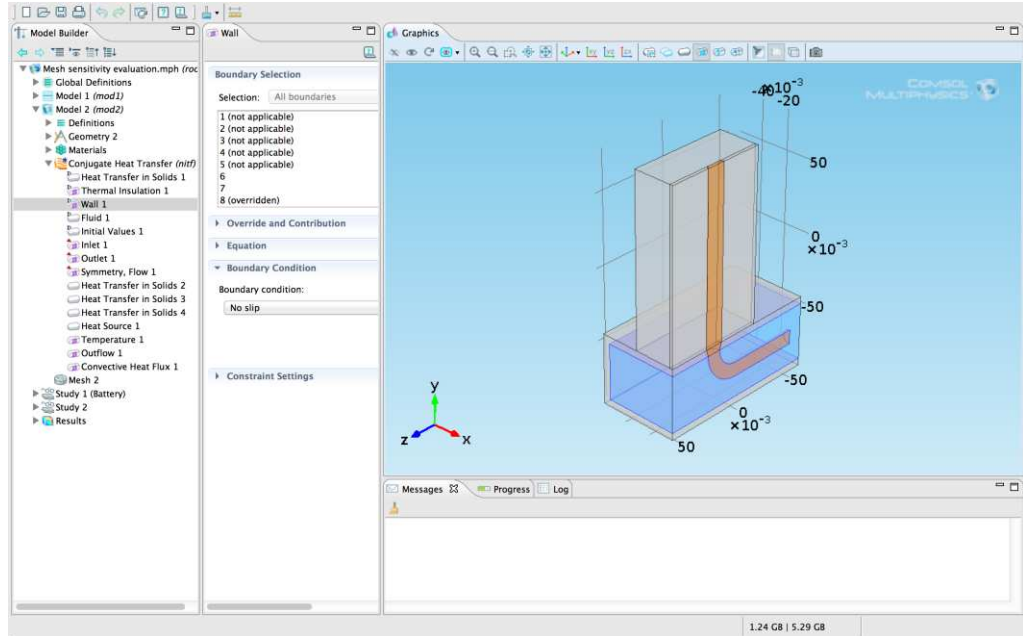


Figure 4.13: COMSOL Multiphysics 4.3b user interface.

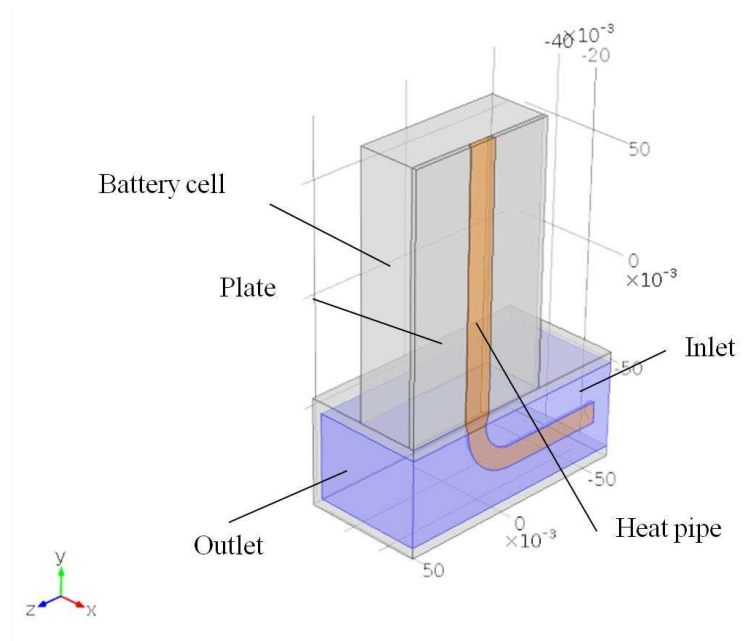
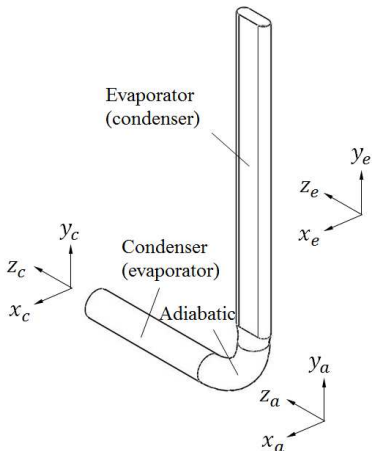


Figure 4.14: FEM model geometry.

Table 4.5 summarises the domain and boundary conditions for liquid and heat transfer. The flow compressibility is dependent on Mach number. For flow with less than 0.3 Mach number, the flow is considered as incompressible. Therefore, the flow equation follows Eq. 4.19. The energy equation (Eq. 4.21) is enabled to calculate the heat transfer within the model. Radiation is not considered in this study to save computing time and to allow quick comparison among complex structures. Surface-to-surface radiation between the battery cell and enclosure will be enabled in Chapter 6 to evaluate the heat pipe application for EV battery packs.

Table 4.5: 3D symmetrical conjugate heat transfer model domain and boundary condition settings

All Domains	
Equation	Laminar flow (incompressible): $(u \cdot \nabla)u = \nabla \left(p_l + \left(\nabla u + (\nabla u)^T \right) \right) + F \quad (4.19)$
	Continuity of mass: $\nabla \cdot (\rho u) = 0 \quad (4.20)$
	Heat transfer in solids and fluids: $\rho c_p u \cdot \nabla T = \nabla \cdot (k \nabla T) + Q \quad (4.21)$
Initial condition	Initial temperature $T = 35 \text{ }^\circ\text{C}$ Velocity field $u = 0 \text{ m/s}$ Pressure $P = 0 \text{ Pa}$
Battery Domain	
Material properties	Thermal conductivity, diagonal $k_x = \frac{\sum L_{\text{batt},i}}{\sum L_{\text{batt},i} / k_i} = 0.8$ W/mK , $k_y = k_z = \frac{\sum L_{\text{batt},i} k_i}{\sum L_{\text{batt},i}} = 60 \text{ W/mK}$

	<p>Density $\rho = \frac{\sum L_{\text{batt},i} \rho_i}{\sum L_{\text{batt},i}} = 2,000 \text{ kg/m}^3$</p> <p>Heat capacity at constant pressure $C_p = \frac{\sum L_{\text{batt},i} c_p}{\sum L_{\text{batt},i}} = 1,060 \text{ J/kgK}$</p>
Heat source	General source $Q_h = \frac{\sum Q_{\text{batt},i}}{V_{\text{batt}}} \text{ W/m}^3$
Plate Domain	
Material properties	<p>Thermal conductivity, $k = 160 \text{ W/mK}$</p> <p>Density $\rho = 2,700 \text{ kg/m}^3$</p> <p>Heat capacity at constant pressure $C_p = 900 \text{ J/kgK}$</p>
Heat Pipe Domain	
Material properties	<p>Effective thermal conductivity, diagonal</p> <p>$k_{x,e} = k_{z,e} = 100 \text{ W/mK}$, $k_{y,e} = 3,600 \text{ W/mK}$ (evaporator)</p> <p>$k_{x,c} = k_{y,c} = 100 \text{ W/mK}$, $k_{z,c} = 3,600 \text{ W/mK}$ (adiabatic and condenser)</p> 
Flow Compartment Domain	
Material properties	<p>Gauge pressure $P_A = 0 \text{ Pa}$</p> <p>Thermal conductivity $k = k_T \text{ W/mK}$</p> <p>Density $\rho = \rho_T \text{ kg/m}^3$</p> <p>Heat capacity at constant pressure $C_p = C_{pT} \text{ J/kgK}$</p> <p>Ratio of specific heats $\gamma = 1$</p> <p>Dynamic viscosity $\mu = \mu_T \text{ Pa}\cdot\text{s}$</p> <p>(Note: k_T, ρ_T, C_{pT}, and μ_T are from predefined COMSOL materials)</p>

Flow Compartment Boundaries	
Inlet	<p>Normal inflow velocity:</p> $\mathbf{u} = -u_0 \mathbf{n} \quad (4.22)$ <p>$U_0 = Q_{\text{flowrate}}/A = 0.0190 \text{ m/s}$ (based on $2.38 \pm 0.03 \text{ l/min}$ flow rate from experiment)</p> <p>\mathbf{n} – unit outward normal vector to the surface</p> <p>$T_{\text{inlet}} = 20 \text{ }^\circ\text{C}$</p>
Outlet	<p>Pressure, no viscous stress:</p> $p = p_0, \quad \left(\nabla \mathbf{u} + (\nabla \mathbf{u})^T \right)_n = 0 \quad (4.23)$ <p>$P_0 = 0 \text{ Pa}$</p> <p>Outflow</p> $-\mathbf{n} \cdot (-k \nabla T) = 0 \quad (4.24)$
Symmetry Boundary	
Flow	$\mathbf{u} \cdot \mathbf{n} = 0, \quad \mathbf{K} - (\mathbf{K} \cdot \mathbf{n})\mathbf{n} = 0, \quad \mathbf{K} = \left(\mu(\nabla \mathbf{u}) + (\nabla \mathbf{u})^T \right)_n \quad (4.25)$
All Domain External Boundaries	
Convective heat flux	$-\mathbf{n} \cdot (-k \nabla T) = h \cdot (T_{\text{ext}} - T) \quad (4.26)$ <p>Heat transfer coefficient $h = 4 \text{ W/m}^2\text{K}$</p> <p>External temperature $T_{\text{ext}} = 35^\circ\text{C}$</p>

The heat transfer model consists of conduction and convection, and sometimes radiation effects around edges and boundaries. The heat transfer in solids and liquids model uses the heat equation illustrated in Eq. 4.21. The battery is considered as a heat source, which describes heat generation within the domain. Three contributions are included [219]:

- The transport of fluid can be dominated by either convective or conductive heat transfer depending on fluid thermal properties and flow regime;

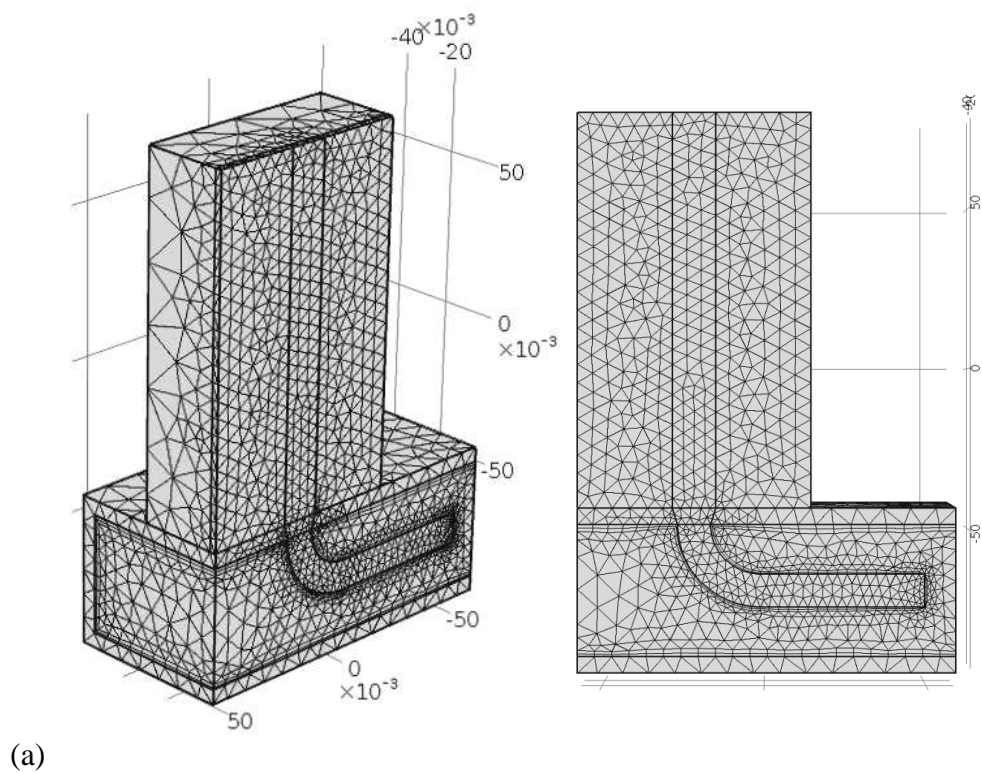
- The viscous effects that produces fluid heating can be neglected but may be noticeable for fast flow;
- The pressure work term might be included if the fluid density is temperature-dependent.

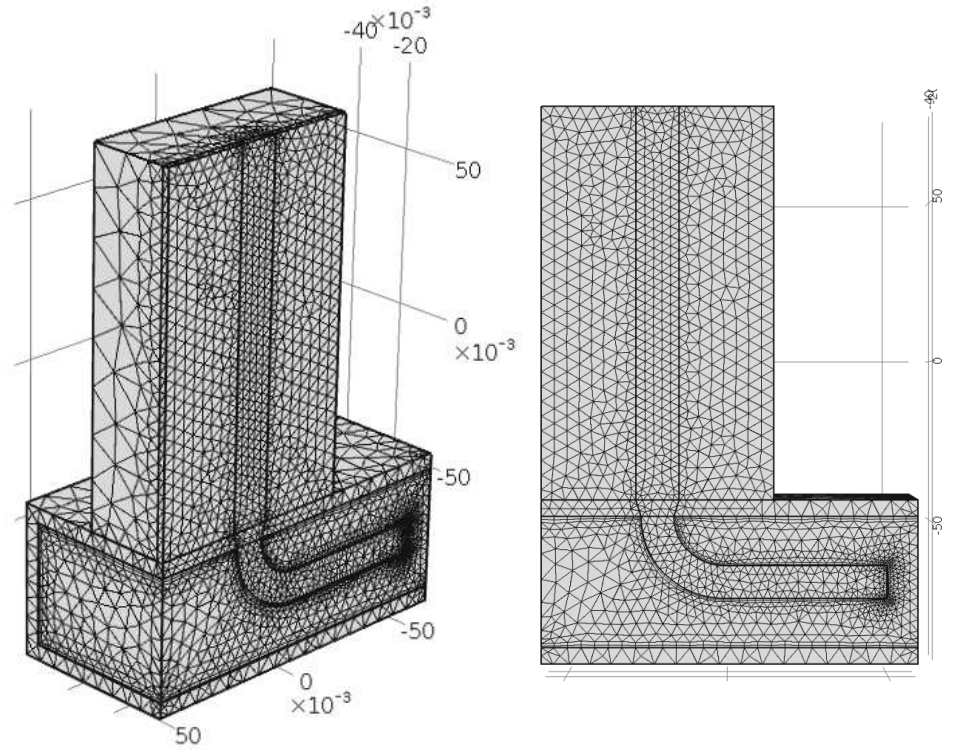
The heat pipe is treated as a highly conductive metal with orthotropic thermal conductivity (Table 4.5). This conductivity should be large enough to result in the same heat as that taken by the boiling heat pipe fluid, and is able to represent the effects of the real system under different working orientations. The value is taken as 3,600W/mK at cooling temperature of 20°C under 2.38 l/min (0.04 kg/s). Preheating transient performance is recorded from a sub-zero temperature (-20°C) after discharging glycol-water mixture to the heat pipe evaporator. The value for the effective thermal conductivity is 3,200 W/mK when discharging 20°C coolant and 4,800 W/mK under 40°C at the same discharging rate. Validation results can be found in Chapter 4.3.

4.2.3 Mesh Sensitivity Analysis

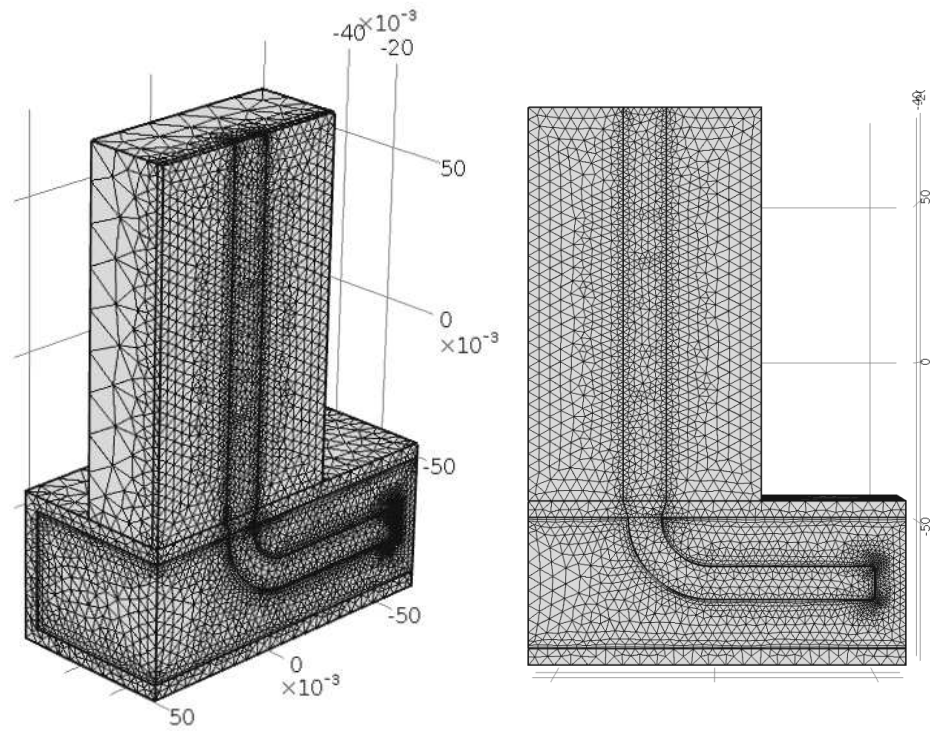
A mesh sensitivity analysis was performed in order to determine the accuracy of the results obtained by different mesh sizes. By applying three mesh densities (Fig. 4.15), the grid independence can be evaluated. For a normal mesh with 73,063 elements, it was indicated by 0.05°C (0.19%) and 0.157°C (0.49%) change in maximum battery surface temperature at 300 s and 600 s respectively when a higher grid size was refined (with 167,785 elements). A detailed comparison table (Table 4.6) and surface temperature contours (Fig. 4.16 – 4.17) were made to compare the results obtained from using coarse,

normal and fine mesh. Fine mesh had a better accuracy but the complexity and simulation time increased dramatically. Coarse mesh made the temperature contour very bumpy (Fig. 4.16 (a), 4.17 (a)), and the distribution was far less identical compared to that obtained from either normal or fine mesh. The contour lines resulted from normal mesh appeared to be exactly like fine mesh, with a few decimal differences. Normal mesh was therefore selected for all the simulations in this study due to reasonable accuracy and simulation time.





(b)

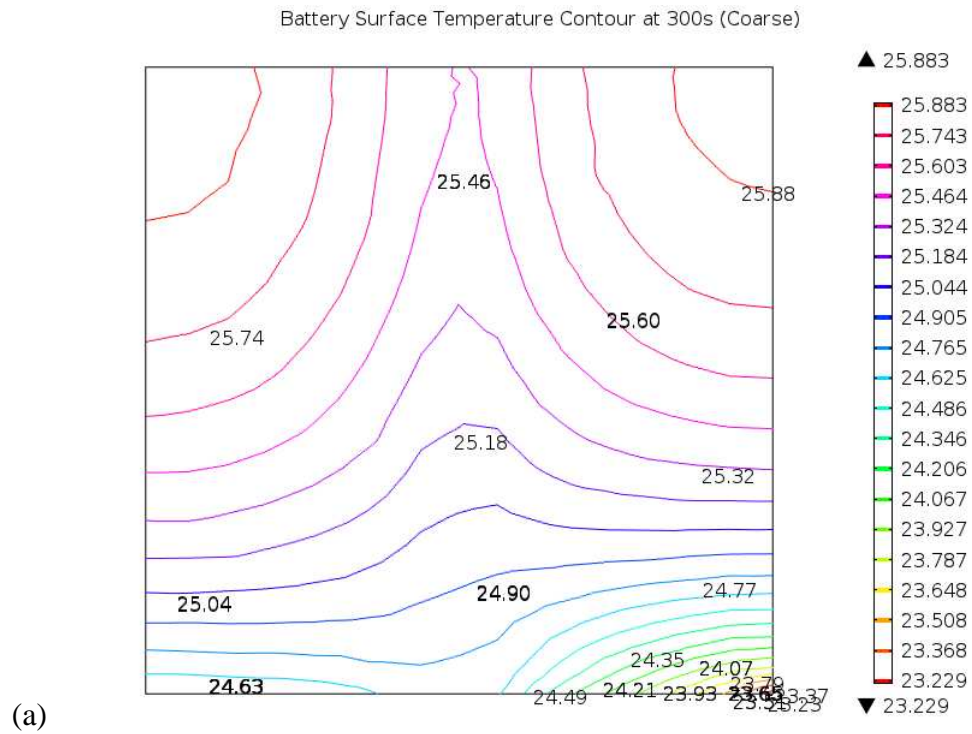


(c)

Figure 4.15: Varying mesh density for a 3D axi-symmetrical model: (a) coarse; (b) normal; and (c) fine mesh.

Table 4.6: Mesh sensitivity analysis based on a 3D symmetrical model for a 4C charge/discharge rate under a 600s cycle

	Coarse	Normal	Fine
No. element	33,946	73,063	167,785
Element quality	0.6052	0.6408	0.6596
Max Battery surface temperature (°C)	25.883 @ 300s 31.605 @ 600s	25.858 @ 300s 31.561 @ 600s	25.808 @ 300s 31.404 @ 600s
Min battery surface temperature (°C)	23.229 @ 300s 25.74 @ 600s	23.241 @ 300s 25.769 @ 600s	23.225 @ 300s 25.709 @ 600s
Simulation time	9 min 48 sec	40 min 52 sec	1 hour 39 min



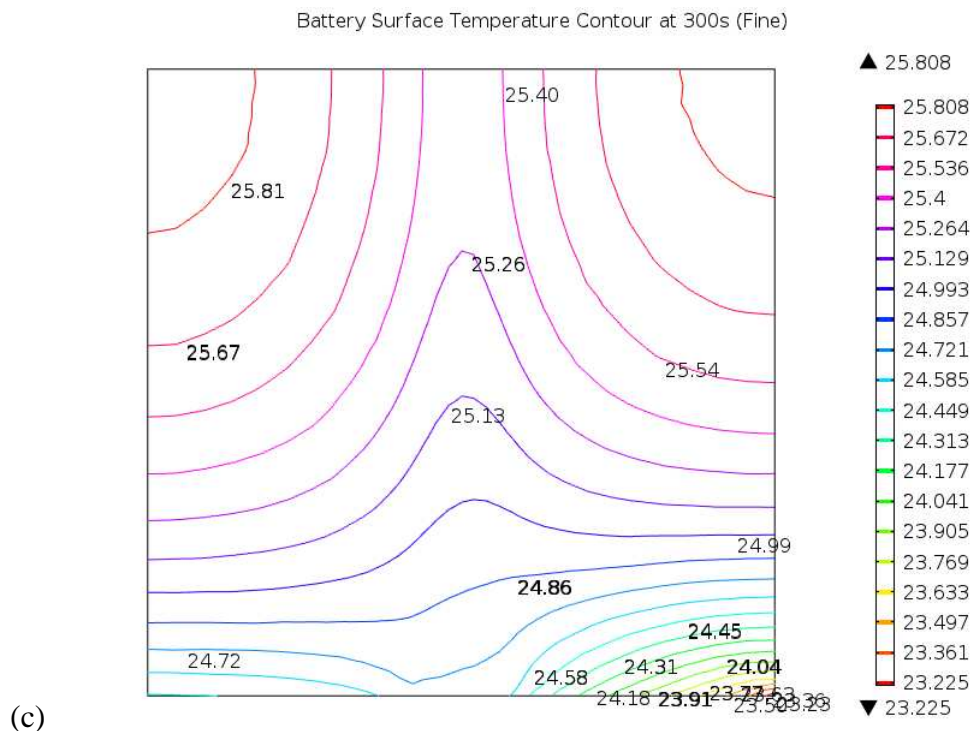
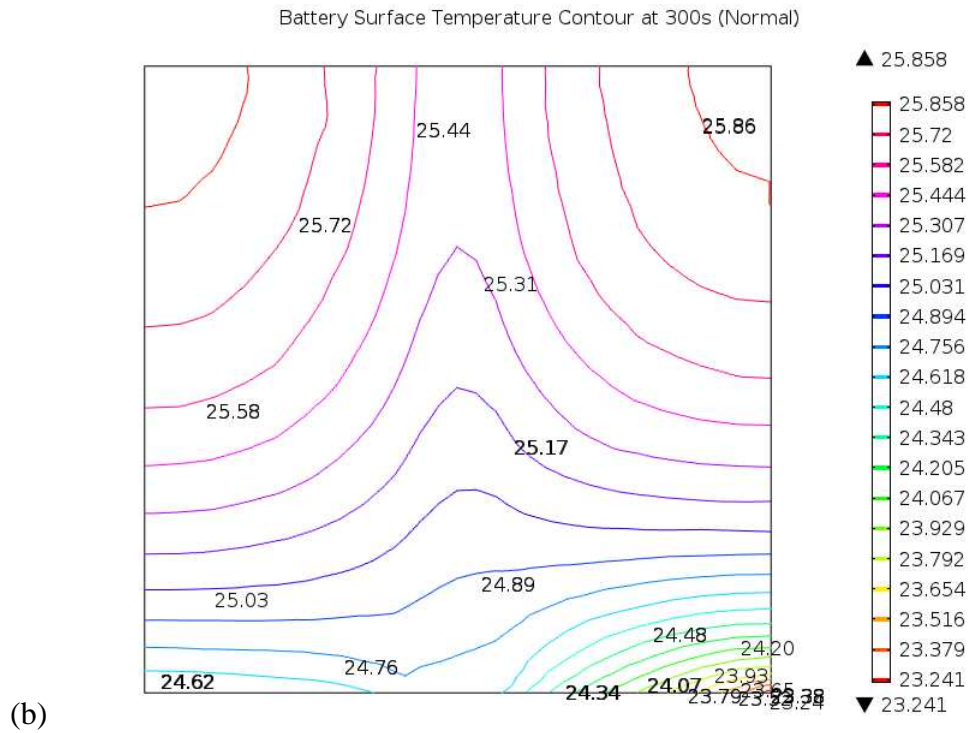
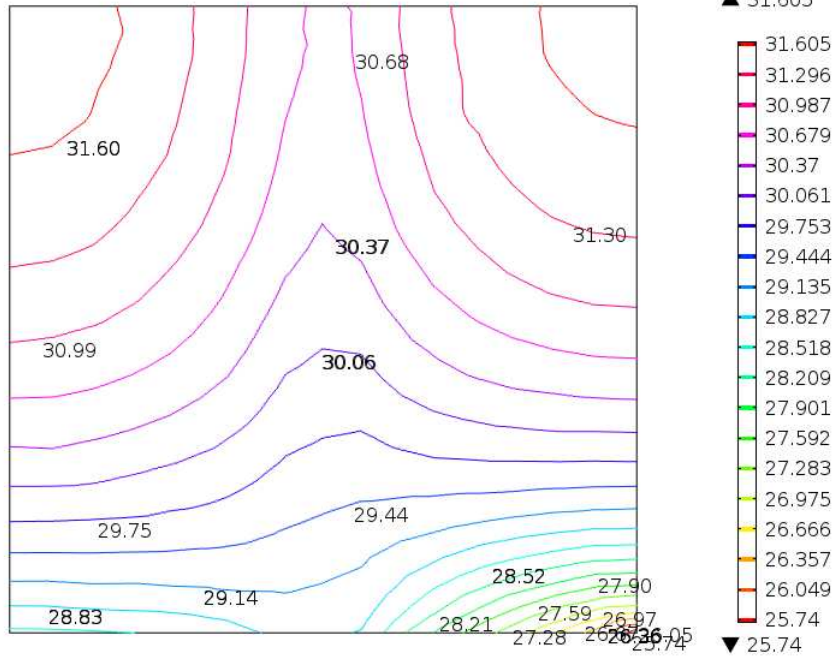


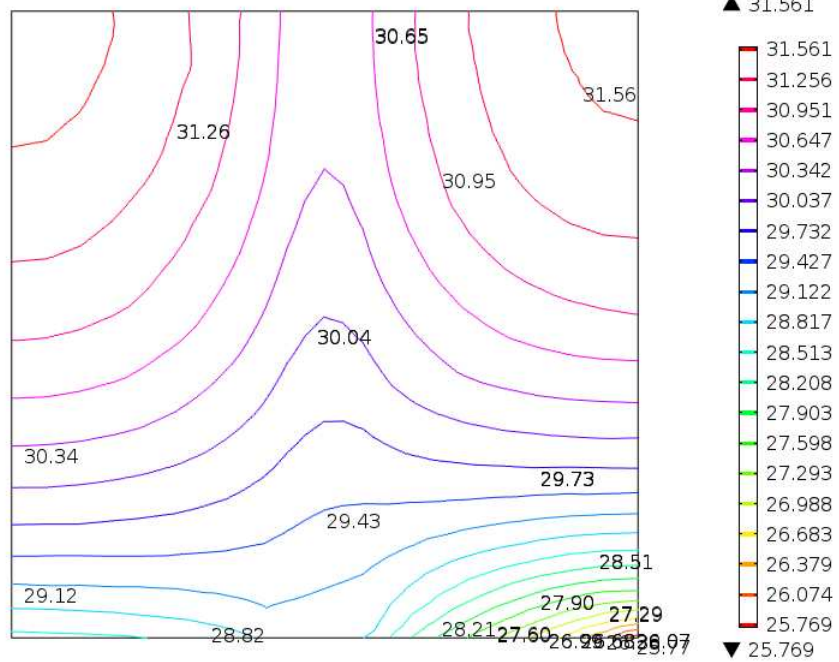
Figure 4.16: Battery surface temperature contour at 300 s obtained from (a) coarse (b) normal and (c) fine mesh.

Battery Surface Temperature Contour at 600s (Coarse)



(a)

Battery Surface Temperature Contour at 600s (Normal)



(b)

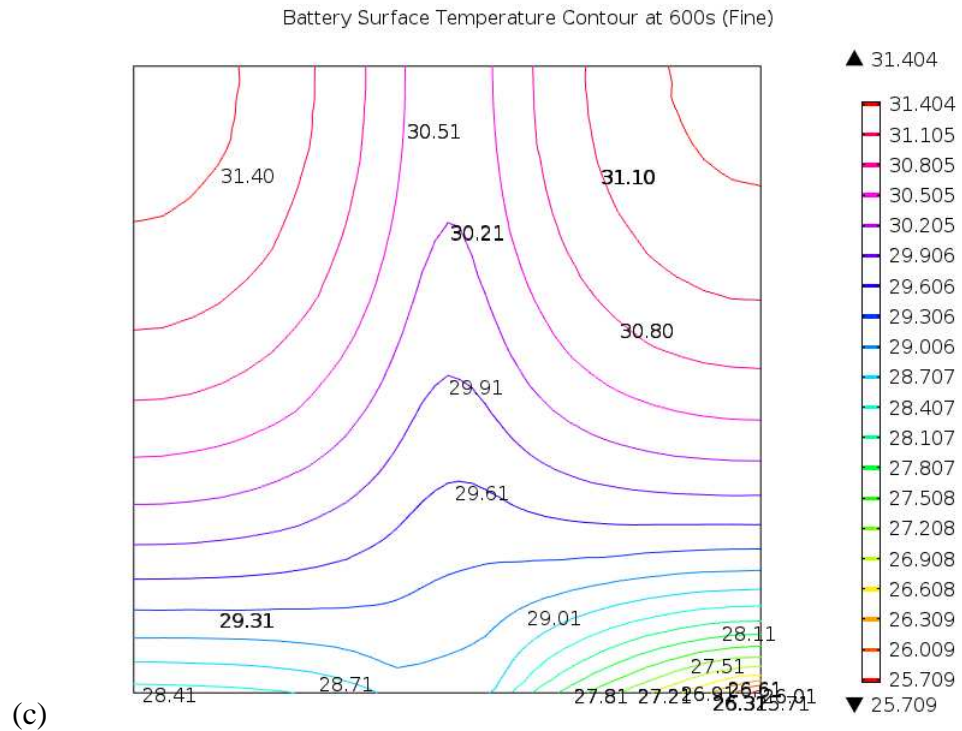


Figure 4.17: 2D plot battery surface temperature contour at 600 s obtained from (a) coarse (b) normal and (c) fine mesh.

4.3 Model Validation

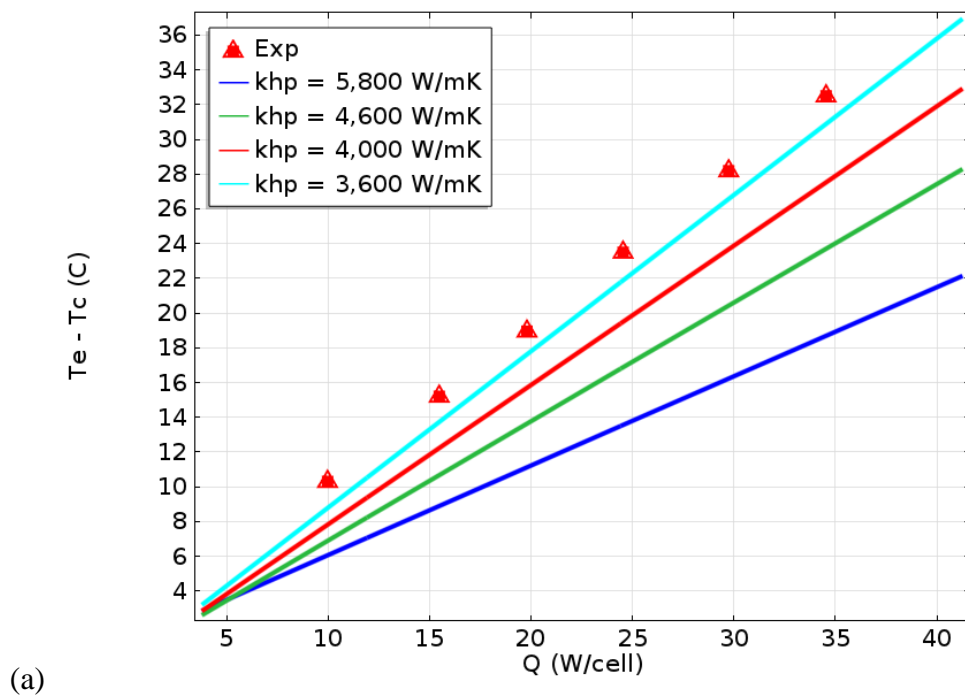
Validation is to find a reasonable representation of the actual system to reproduce system behaviour with enough fidelity to satisfy analysis and evaluation purpose. Three aspects can be considered during model validation [220]: 1) assumptions; 2) input parameter values and distributions; and 3) output values and conclusions. For this particular model, the thermal conductivity of the heat pipe is a key parameter (input) influencing system cooling and preheating performance, and the battery surface temperature (output) serves as the main criterion assessing the performance study. It is assumed that the thermal conductivity of the heat pipe maintains constant in

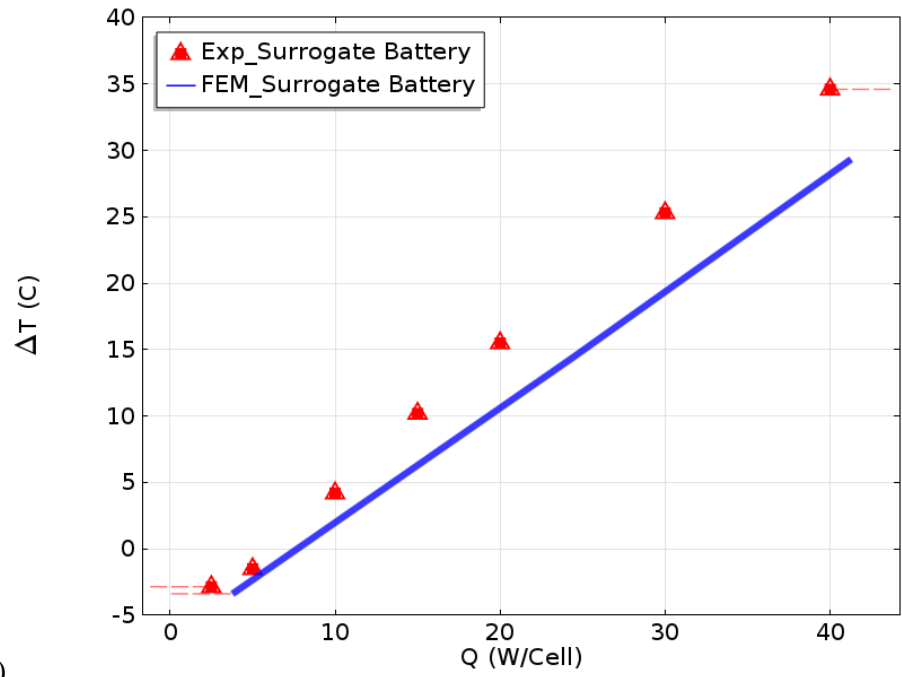
the model at a certain temperature and that the input value should be able to generate similar output (battery surface temperature) under various cooling/preheating conditions. The approach to model validation is through real system measurements. This can be done by comparing the average surface cell temperature change under cooling and preheating. Seven thermocouples were positioned on the surface of the battery cell in contact with the aluminium plate and the heat pipe, and heat generation rate per cell was applied through cartridge heaters. The results of the model validation are demonstrated in Fig 4.18.

For battery cooling, heat power ranging from 2.5 – 40 W/cell was applied to the battery and the temperature was measured after achieving steady state cooling condition. The coolant temperature was 20°C at a discharge rate of 2.38 l/min. Fig. 4.18 (a) shows the temperature difference between the heat pipe evaporator and condenser under various power inputs. Four different thermal conductivities for the heat pipe were simulated in COMSOL and results obtained from using 3,600 W/mK matched with the experimental data. Fig. 4.18 (b) compares the average battery surface temperature change at an initial temperature of 35°C between experiment and FEM results. It is confirmed that using 3,600 W/mK as the heat pipe effective thermal conductivity seems to be appropriate for steady state cooling although larger discrepancies were found at higher power inputs.

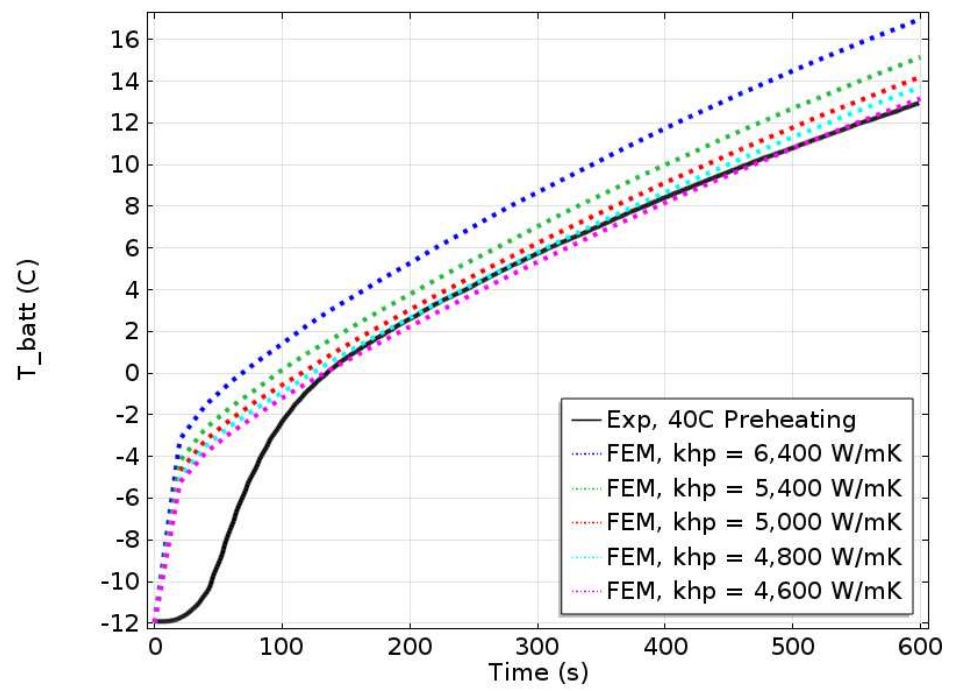
As to battery preheating, a parametric sweep study was performed by inputting various heat pipe thermal conductivities from 4,600 to 6,400 W/mK under 40°C transient preheating (Fig. 4.18 (c)). The value for heat pipe under 40°C heating was chosen as 4,600–4,800 W/mK as the resultant curve

resembled closely to the data obtained from the experiment. Similarly, 3,200 W/mK was determined for 20°C preheating. Fig. 4.18 (d) plots the transient preheating behaviour (both 20°C and 40°C glycol-water mixture preheating) of battery average surface temperature change starting from -20°C at an ambient temperature of -20°C and an inlet flow rate of 2.38 ± 0.03 l/min. Discrepancies were found to be significant during the first 100 s, but became negligible within 1,000 s. This is because the heat pipe can only be responsive if the temperature inside the heat pipe reaches to its working region. The effective thermal conductivity of the heat pipe changed dramatically from extremely low (frozen state) to somewhat high and constant (discharge pre-treated coolant at the evaporator). For FEM analysis, it is assumed that the effective thermal conductivity of the heat pipe is at a constant value throughout the entire process. Hence, the predicted value within the first 100 s is higher than the actual value.

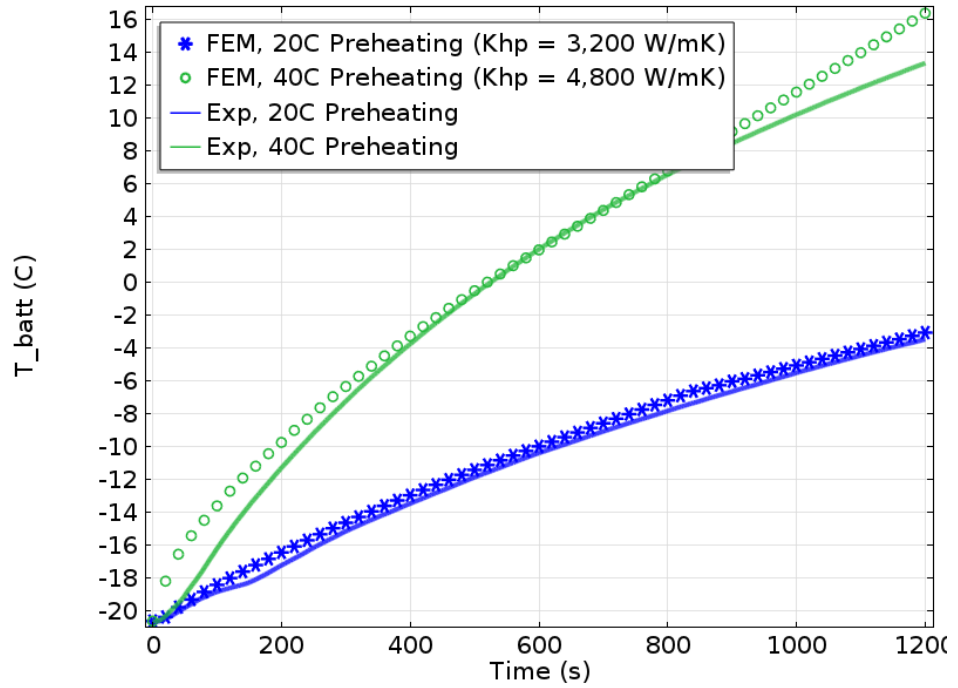




(b)



(c)



(d)

Figure 4.18: (a) Heat pipe effective thermal conductivity parameter validation under steady state battery cooling; (b) battery surface temperature change from initial temperature of 35°C using $k_{hp} = 3,600$ W/mK; (c) various heat pipe effective thermal conductivities from -10°C under 40°C preheating to match with experiment data; (d) 1200 s preheating behaviour with initial temperature of -20°C ($T_{amb} = -20^\circ\text{C}$, $T_{g-w} = 20^\circ\text{C}$ or 40°C , $q_{g-w} = 2.38$ l/min).

4.4 Summary

The development of battery thermal model and validation was performed in this chapter. A symmetrical small-scaled model that contains one battery cell with heat pipe cooling was built in COMSOL Multiphysics 4.3b. Both fully coupled model (contains a full 1D electrochemical model for lithium-ion batteries) and decoupled model (developed equations for calculating heat generation rate) were developed to estimate the BTM performance. Conjugate

heat transfer physics was also applied to the model, which uses the laminar flow interface to solve for the velocity and pressure in the liquid zone and the heat transfer interface for the temperature field. Mesh sensitivity analysis was performed by comparing battery surface temperature obtained from coarse, normal and fine mesh. In order to save computing time while achieving good results, normal mesh was selected for all simulations in this study. It is assumed that the heat pipe thermal conductivity maintains constant in the model at a certain temperature, and the obtained average battery surface temperature under various cooling/preheating conditions were compared with real system measurements. The value is taken as 3,600W/mK at cooling temperature of 20°C under 2.38 l/min (0.04 kg/s). For preheating transient performance, 3,200 W/mK under 20°C and 4,800 W/mK under 40°C can ensure similar preheating behaviour.

Chapter 5

Prototype Testing and Evaluation

5.1 Development of Experiment Prototype

A conceptual prototype for experiment that mimics the WEIZHI battery cooling and heating system is introduced. The purpose of this prototype is to evaluate the heat pipe thermal management method under pre-defined battery thermal conditions. It also serves the function of validating material properties and parameters for simulation inputs.

The prototype (Fig. 5.1) is built by two surrogate battery cells, of which the size and the container materials are exactly the same as WEIZHI battery cells. The battery core materials are substituted with atonal 324 to generate a total thermal capacity (468.18 J/K) similar to that of the lithium-ion battery cell (480.82 J/K) (Table 5.1). Two cartridge heaters will be inserted into each cell, which represent negative and positive electrode controlling the amount of thermal power generated. 46% glycol/water mixture (by vol.) will be used as the coolant inside the liquid box of which the freezing point can reach below -30°C. In addition, an aluminium plate will be sandwiched between two cells, with a U-shaped channel in the middle where the L-shaped heat pipe can be positioned. The heat pipe was manufactured with a theoretical maximum capillary limit of 157.57W at saturated temperature of 40°C without taking

flattening and bending impacts into account. This should be sufficient in dissipating the unwanted heat produced by the experiment prototype. Detailed parameters of the fabricated heat pipe are given in Table 5.2.

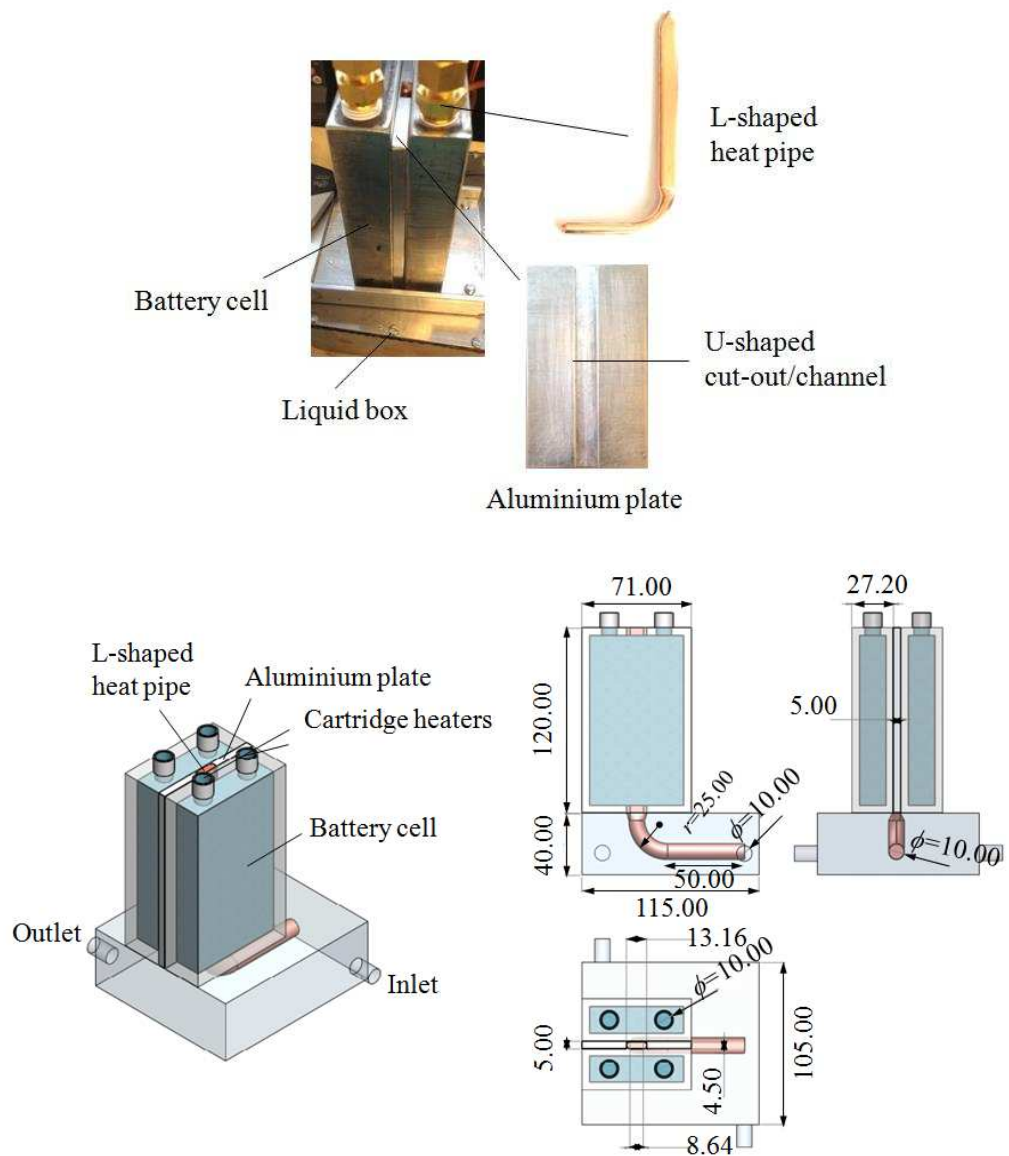


Figure 5.1: Prototype geometries and dimensions (in mm).

Table 5.1: Surrogate battery cell versus WEIZHI lithium-ion battery cell

Surrogate Battery Cell	
Battery Size (mm)	71×27.2×120
Container Thickness (mm)	4
Solid Material	Aluminium
Density, ρ (kg/m ³)	2670
Specific Heat Capacity, C_p (J/kgK)	900
Volume (cm ³)	94.86
Mass (kg)	0.253
Thermal capacity, $(mC_p)_s$ (J/K)	<u>268.44</u>
Liquid Material	Atonal 324, transformer oil
Density, ρ (kg/m ³)	895
Specific Heat Capacity, C_p (J/kgK)	1920
Volume (cm ³)	116.24
Mass (kg)	0.104
Thermal Capacity, $(mC_p)_l$ (J/K)	<u>199.74</u>
Total Thermal Capacity $(mC_p)_{srg}$ (J/K)	468.18
Lithium-ion Battery Cell (extracted from Table 4.1)	
Battery Size (mm)	71×27.2×120
Density, ρ (kg/m ³)	2000
Specific Heat Capacity, C_p (J/kgK)	1060
Volume (cm ³)	226.8
Mass (kg)	0.453
Thermal capacity, $(mC_p)_{batt}$ (J/K)	480.82

Table 5.2: L-shaped heat pipe specification

Materials	
Wick	Copper
Wick structure	Sintered copper wicks
Working fluid	Water
Dimensions	
Total length, l_t (mm)	206
Evaporator, l_e (mm)	120
Condenser, l_c (mm)	50
Outer Diameter, d_o (mm)	10
Wall thickness, t_b (mm)	0.5
Wick thickness, t_w (mm)	1
Thickness (flattened part), t_e (mm)	4.5
Effective Pore Radius, r_{eff} (μm)	40
Estimated Porosity, ε	0.45
Permeability, K (m^2)	8.03×10^{-11}
Bending Angle, θ	90°
Bending Radius, r (mm)	25
Water mass filling, m (g)	2.003

5.1.1 Prototype Validation

Model validation is to determine the feasibility of using FEM to predict the temperature behaviour of the chosen system based on the exact condition used in experiment. Prototype validation is to assess the eligibility of substituting atonal 324 for lithium-ion battery electrolytes (Fig. 5.2).

Fig. 5.3 shows the surface temperature contours obtained from using two different batteries with one side of the surface cooled by heat pipe: surrogate battery cell filled with atonal 324 and lithium-ion battery cell. Fig. 5.4

demonstrates the corresponding model temperature field (battery surface attached with aluminium plate and heat pipe). Due to low thermal conductivity of the surrogate battery cell along all directions, the temperature across the surrogate battery varies greatly in height and width compared to lithium-ion battery. For lithium-ion battery, the surface temperature contour was quite uniform because of high thermal conductivities along the axis of length and height. However, the surface temperature distribution between these two batteries was similar under low power inputs (< 10 W/cell), but variations became evident as power input increased to 41.27 W/cell. This indicates that the surrogate battery is more prone to temperature change, which requires the proposed thermal management solution to be able to perform under a wider range of operating conditions. This means that the surrogate battery can help extend the BTM application to accommodate for various types of batteries. Given that the objective of the developed prototype is to evaluate the system cooling and preheating performance, the discrepancies in surface temperature between surrogate battery cell and lithium-ion battery cell under higher power inputs become less important.

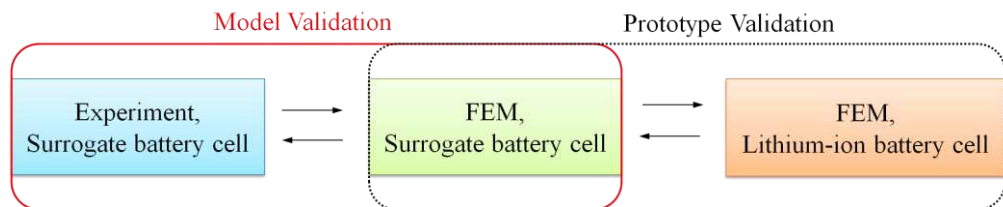


Figure 5.2: Validation relationship.

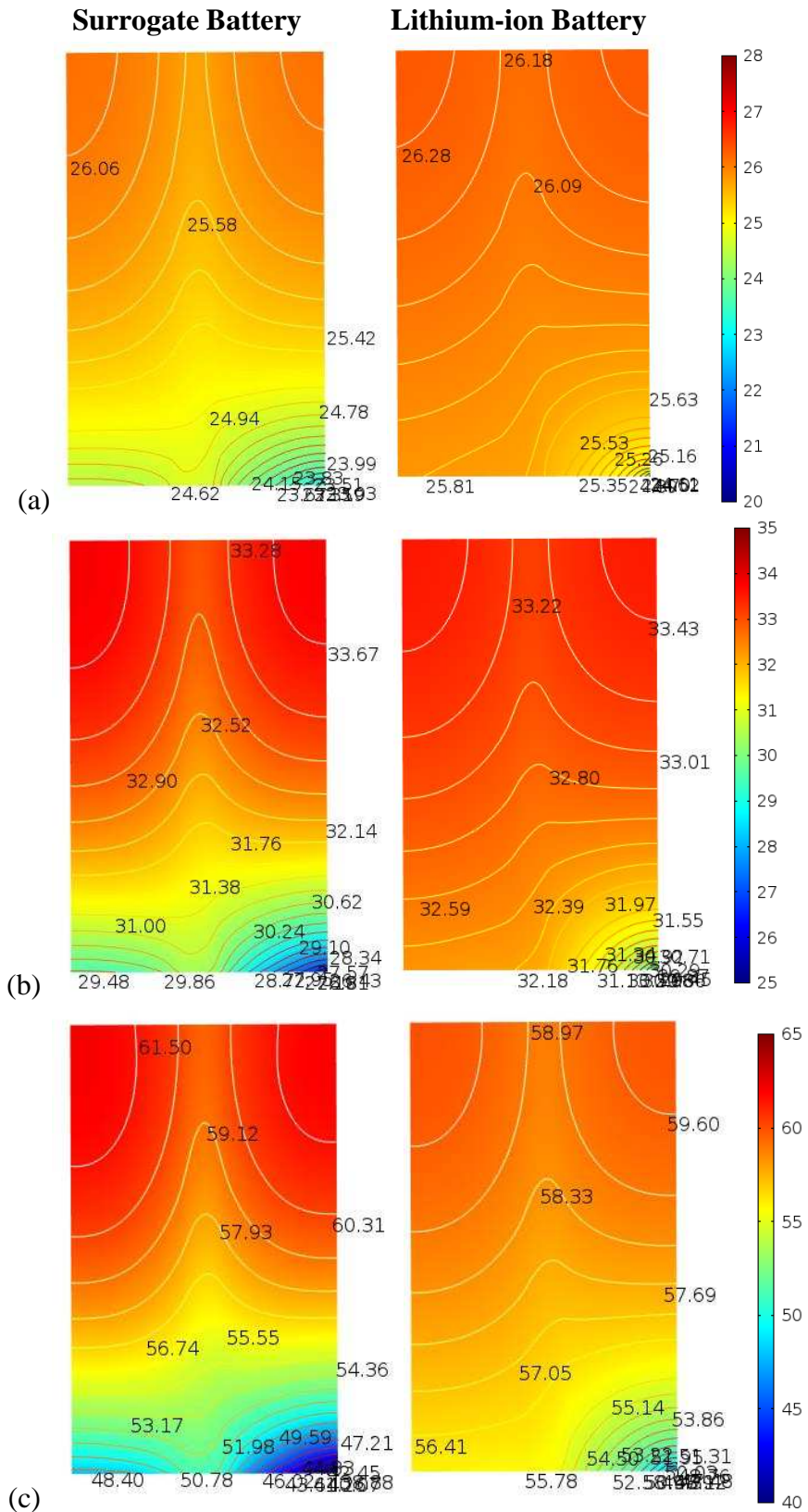


Figure 5.3: Steady state temperature contour of the battery surface cooled by heat pipe under 1C (3.78 W/cell), 2C (11.92 W/cell), and 4C (41.27 W/cell) discharge ($T_{\text{amb}} = 35^{\circ}\text{C}$, $T_{\text{g-w}} = 20^{\circ}\text{C}$, $q_{\text{g-w}} = 2.38 \text{ l/min}$).

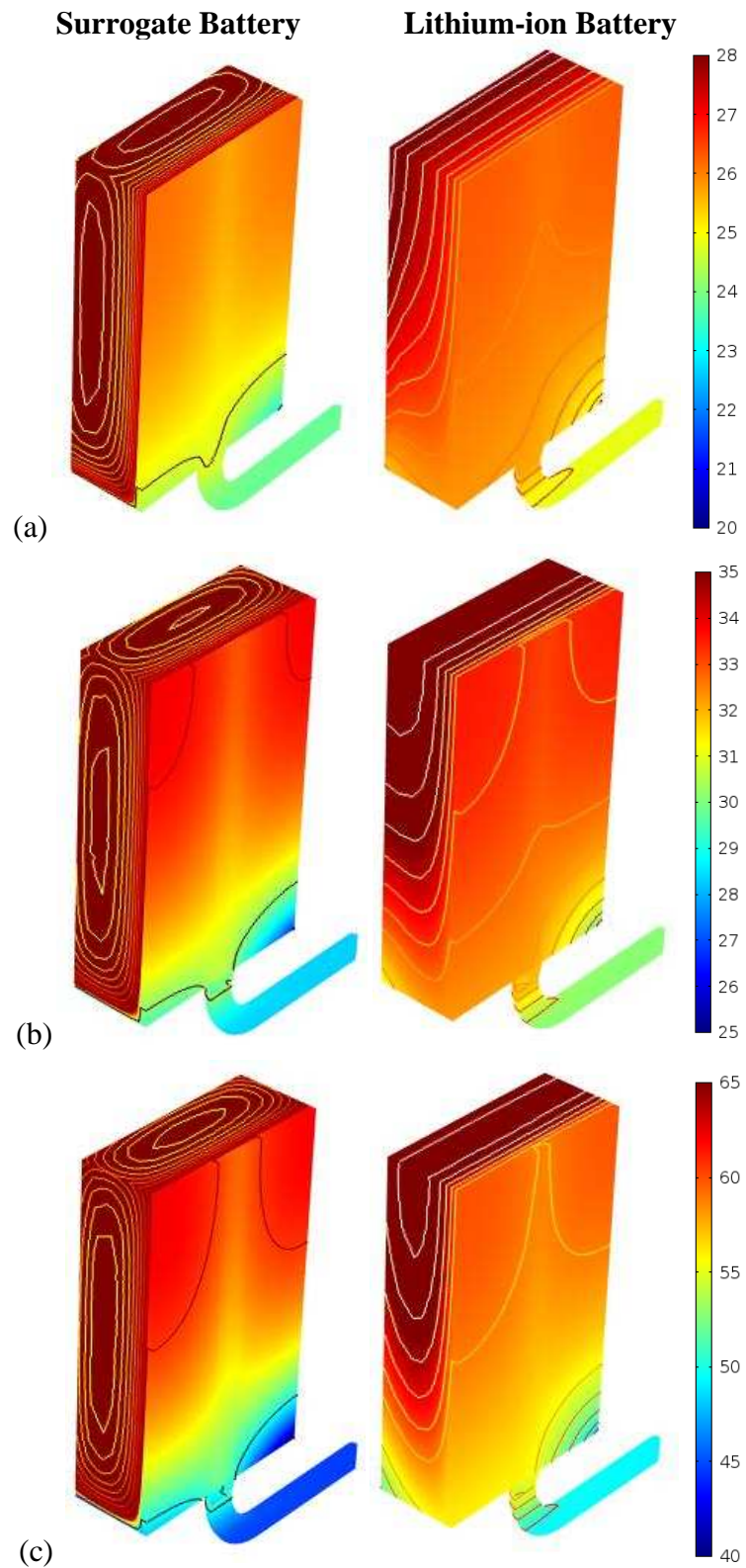


Figure 5.4: Steady state temperature results with one side of the surface cooled by heat pipe under 1C (3.78 W/cell), 2C (11.92 W/cell), and 4C (41.27 W/cell) discharge ($T_{\text{amb}} = 35^{\circ}\text{C}$, $T_{\text{g-w}} = 20^{\circ}\text{C}$, $q_{\text{g-w}} = 2.38 \text{ l/min}$).

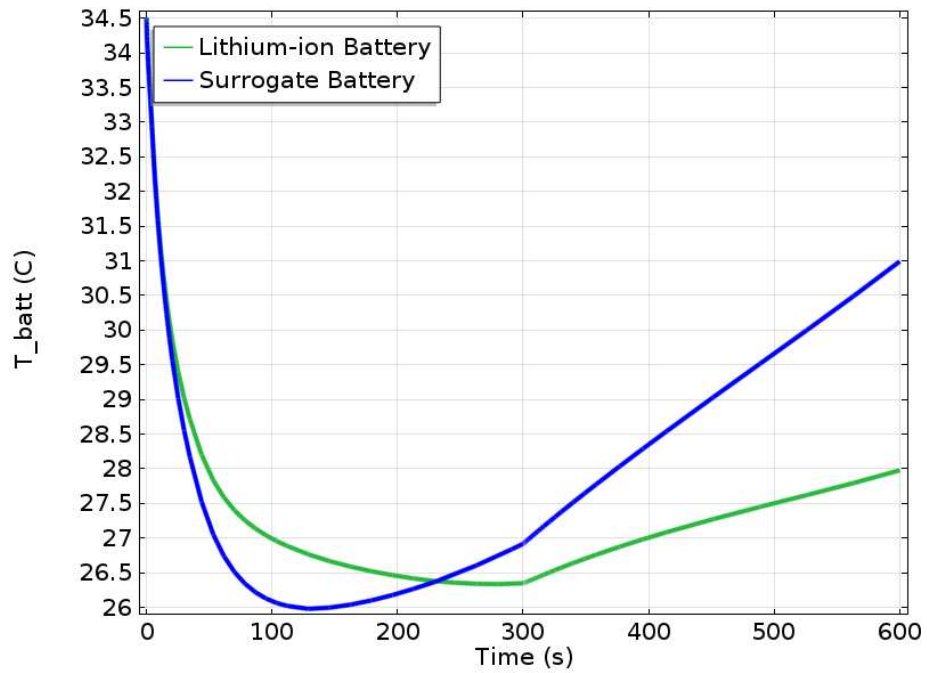


Figure 5.5: Time-dependent average surface temperature change under a cycle time of 600s using heat source generated from 1D battery model based on an alternating charge/discharge current at 4C rate ($T_{amb} = 35^{\circ}\text{C}$, $T_{inlet} = 20^{\circ}\text{C}$, $q_{g-w} = 2.38 \text{ l/min}$).

In addition, the transient test plotted in Fig. 5.5 suggested that the surrogate battery is more prone to temperature change and has larger temperature fluctuations. In other words, it is more difficult to regulate temperature uniformity and reduce temperature increase of the surrogate battery than the lithium-ion battery. In order to extend the applicability of the proposed thermal management method, it is necessary to expect a prototype that covers a wide range of operating conditions and simulates a much more dynamic thermal response. The prototype should be able to indicate that the proposed solution is suitable for one particular battery and may serve well for other batteries that require higher heat dissipation rates.

5.2 Experiment Setup

The test rig is designed based on two battery cells. Fig. 5.6 shows the experiment schematic. It mainly consists of a test unit, heating/cooling loops, a regulating system, data measurement and acquisition, power supply systems and an environmental controlled chamber. The unit was entirely isolated from the environment by the environmental chamber/freezer, and fluid loops were well insulated to minimise heat loss. Fig. 5.7 demonstrates the in situ experiment in details. Note that a heating block and a fan were used to create a desired summer ambient environment ($35 \pm 1^\circ\text{C}$), and a freezer was provided to create different sub-zero temperatures maintaining the chamber environment at $-25 \pm 2^\circ\text{C}$, $-15 \pm 2^\circ\text{C}$ and $0 \pm 1^\circ\text{C}$.

The battery cooling/heating system contains a liquid box, water baths, water pumps, inverter drives and circulating liquid loops (Fig. 5.6). The water bath A provides either heating or cooling to the battery cell by regulating pre-treated liquid coolant at a certain temperature. Water bath B adds another function of simulating battery thermal condition at a controlled temperature examining system transient performance. To note, water bath B only serves to provide a constant initial battery surface temperature at 40°C , 50°C , 60°C , and 70°C since it is difficult to control cartridge heaters to reach to a predetermined temperature. Due to the provision of inverter drive, the water pump can generate different mass flow rates with pre-determined temperatures to simulate different battery working conditions such as acceleration, braking, downhill, uphill, and even start-up condition during cold weather.

The regulating system has two parts: 1) controlling the heat power inputs; and 2) adjusting liquid coolant flow rate. The power input for the battery cell

can be regulated via DC power supply, and the flow rate can be changed from inverter drive. DC power supply is provided for cartridge heaters where input voltage (0 – 35 V) can be adjusted accordingly and AC power supply (220 V, 30 – 60 Hz) is used for water pump.

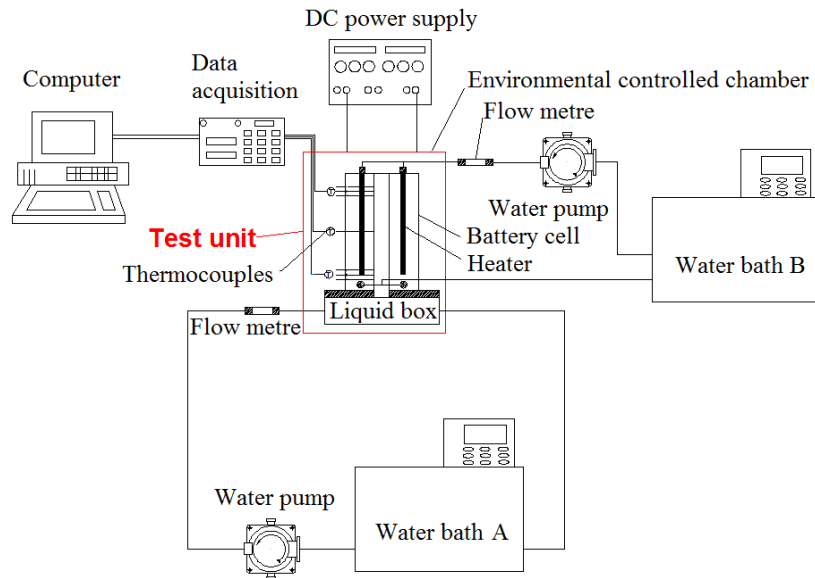


Figure 5.6: Experiment schematic.

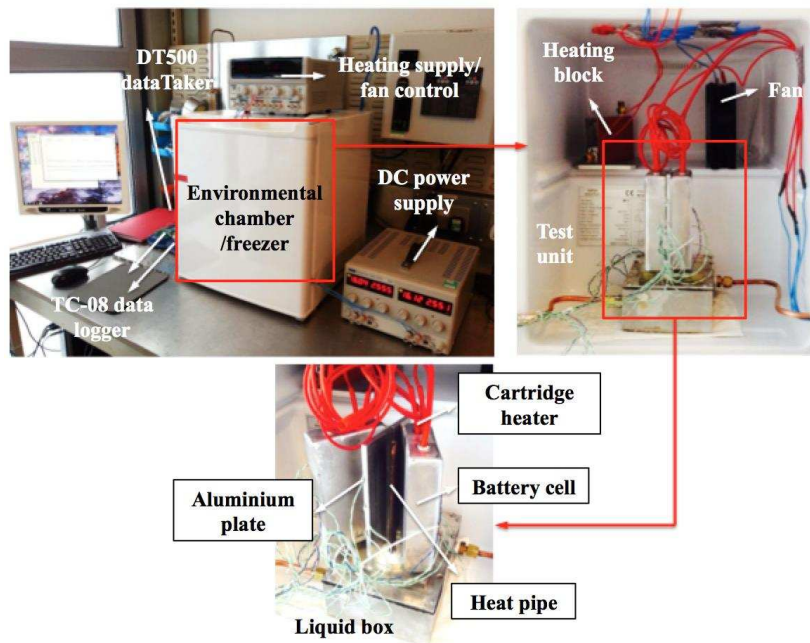


Figure 5.7: In situ experiment details.

The system measurement includes battery power input, battery surface temperature, inlet temperature and outlet temperature of the liquid box, and flow rate of the discharging coolant. The monitored battery surface temperatures can be measured by arranging thermocouples on the back of the plate where channels are constructed such that the thermocouples can be inserted in. Such arrangement is demonstrated in Fig. 5.8.

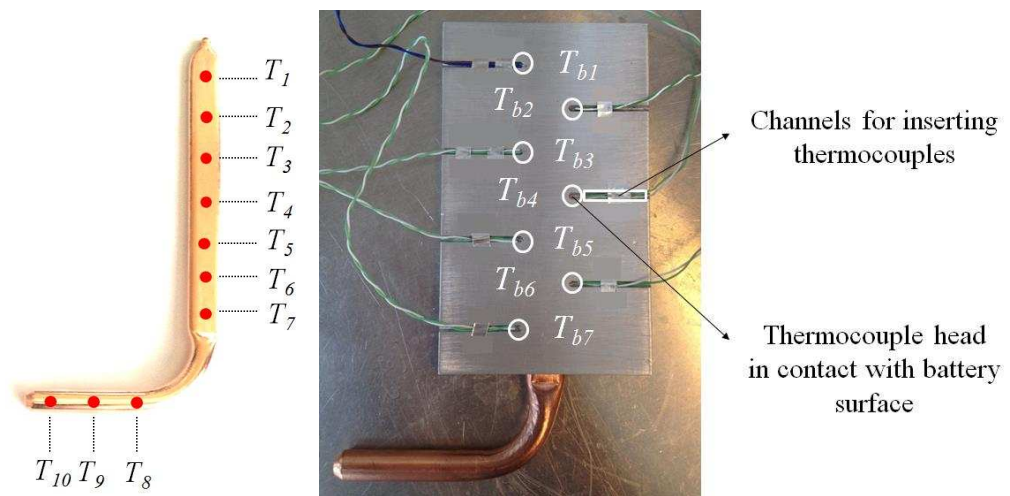


Figure 5.8: Arrangement of thermocouples on the testing L-shaped heat pipe (T_1 - T_{10}) and on the back of the plate channels for battery surface temperature measurement (T_{b1} - T_{b7}).

5.3 Instrumentation

A list of experimental instruments is demonstrated in Fig. 5.9. Detailed description of each device was made in Table 5.3.



Figure 5.9: Devices used in experiment.

Table 5.3: List of instrumentation

No.	Instrument	Operating Range	Accuracy	Comment	Quantity
1	TTi precision DC Bench Power Supply (EX354RD)	Voltage: 0 – 35 V Current: 0 – 4 A	Voltage Resolution: 10 mV with 0.3% of reading \pm 3 digits Current Resolution: 1mA with 0.5% of reading \pm 3 digits	Four 10 mm \times 100 mm stainless steel cartridge heaters were used to heat up the simulated battery core. DC dual power supply can be adjusted to obtain predetermined power for the battery.	1
2	Cartridge Heater	Voltage: 0 – 12 V Power: 0 – 40 W	/		4
3	PolyScience Low-profile Refrigerated/Heated Circulating Bath (WZ-12117-05)	-20 – 150 °C	\pm 0.05 °C	The low-profile refrigerated/heated circulating bath has a capacity of 6 litres with standard digital controller. It provides precise and stable cooling for laboratory and is ideal for routine applications. The cooling capacity at 0°C, 20°C and -10°C is 140 W, 200 W and 100 W respectively, and the heater wattage is 1600 W. The refrigerant it uses is CFC-free, and the container is made of 304 stainless steel.	2

4	Parker Hydraulic Gear Pump (Group 1 Gear Pump 2.5CC C/W)	4,000 RPM (max)	/	The hydraulic gear pump has specifications of max speed 4000 RPM, 3.75 l/min (flow at 1500 RPM), and 275 bar maximum continuous pressure. The vector control AC frequency inverter converts single phase 230 V input to three phase 230 V for a standard AC induction motor. It has Soft-PWM control with input current of 6.5A and input voltage of 200 –240 V single phase +10 –15% at 50/60 Hz \pm 5%. The above devices were used to control the flow rate of the discharged coolant.	1
5	Mitsubishi Vector Control AC Frequency Inverter (FR-E720-030SC)	Single Phase: 3 A Frequency Range: 0.2 – 400 Hz	0.01 Hz		1
6	Parker Inline Flow Transmitter (Grilamid-TR55)	5 – 70 °C 1 – 25 l/min	\pm 2%	The flow rate can be measured from Parker inline flow transmitter and read from DT500 dataTaker. The rotor inside the flow meter, which spins each blade obscures the infra-red signal and then converts it into standard pulse output signal read by DT500 dataTaker. Such digital flow metre can operate at any plane with negligible pressure drop. The maximum working pressure is 20 bar, with maximum 0.1 bar pressure drop at 15 l/min. The pulse output signal for flow is up to 25 l/min, and the calibration is	1
7	DataTaker (DT500)	10 differential or 30 single ended analog channels 4/4 input/output digital channels 3 fast counter channels 4 slow counter	Temperature Resolution: 0.1% Counter Resolution: 1 count		1

		channels		752 pulses per litre. The digital flow metre requires 5 VDC power supply, which can be provided by DT500 Datataker. The flow calibration was made by comparing with a standard measuring unit. The uncertainty of the flow measurement is $\pm 2.1\%$.	
8	RS Thermocouple (K-type)	-200 – 1250 °C	± 2.2 °C or $\pm 0.75\%$ above 0 °C	Welded tip thermocouples (K-type) have the fastest responding. They are nickel based and can exhibit good corrosion resistance. The standard accuracy is affected by deviations in the alloys (nickel-chromium). However, deviations between thermocouples differ little and a much higher accuracy can be achieved by individual calibration. Two TC-08 thermocouple data loggers are used to be connected with K-type thermocouples. The measurements are made very fast and accurately, and the high (20-bit) resolution ensures that minute changes in temperature can be detected. The low conversion time (100 ms) of TC-08 indicates that up to 10 temperature measurements can be taken every second.	16
9	Pico Thermocouple Data Logger (TC-08)	-270 – 1820 °C (8 channels)	$\pm 0.2\%$ or ± 0.5 °C		2

10	RS Portable Digital Thermometer (206-3738)	-50 – 1000 °C	Accuracy at 0.1°C resolution: ± 0.2% rdg + 1°C @ -50 – 199.9°C	All thermocouples were calibrated using the RS portable digital thermometer. Calibration was done by recording the readings of those 16 K-type thermocouples connected with corresponding two TC-08 thermocouple data loggers every 10 °C from -20 °C to 70 °C. A water bath filled with glycol-water mixture was served for providing a stable and constant temperature environment. The apparent temperature readings were compared with the standard temperature obtained from RS thermometer (Table A.1). The average accuracy of the thermocouples used was ±2.06% or ±0.61°C before calibration (with maximum accuracy of ±8.60% or ±2.01°C; for details, see Appendix A)	1
11	Curry Environment Controlled Chamber/Freezer (CTF34W12)	-20 – 55 °C	± 1 °C	In order to simulate the thermal environment inside the battery model, an environment controlled chamber/freezer was used with integrated heating (a heating block, a fan, and ISO-TECH DC power supply help create a desired summer ambient environment) and cooling. The temperature inside the	1
12	ISO-TECH Laboratory DC Power Supply (IPS-4303)	Channel 1-2: 0 – 30 V Channel 3: 2.2 – 5.2 V	± 5%		1

		Channel 4: 8 – 15 V; Current: 0–3 A or 1 A		chamber will be controlled at $35 \pm 1^\circ\text{C}$ representing summer operating condition. The freezer will be used to create different sub-zero temperatures maintaining the chamber environment at $-25 \pm 2^\circ\text{C}$, $-15 \pm 2^\circ\text{C}$ and $0 \pm 1^\circ\text{C}$ for battery preheating test.	
13	FLIR Thermal imaging camera (i7)	-20 – 250 °C	0.1 °C	A thermal imaging camera was used to capture surface temperature distribution during experiments	1

5.4 Description of Tests

5.4.1 Battery Cooling

This section describes battery cooling conducted through experiment. The evaluation was performed mainly through: 1) creating steady state battery operating environment to assess the performance of the proposed cooling system; 2) simulating aggressive battery charging/discharge scenarios to evaluate the transient behaviour of the cooling system; 3) analysing the effect of adding fins to the heat pipe condenser to improve heat transfer; and 4) comparing cooling effectiveness resulted from perforated plates with aim of reducing system weight.

5.4.1.1 Steady State Cooling Performance

In order to evaluate the thermal performance of the proposed heat pipe BTM test unit, a wide range of ‘off-normal’ working conditions for battery cooling will be investigated. The heat generation of the battery cell can be achieved by inserting two cartridge heaters into the battery cell, which represents the anode and cathode and supply a controllable power input from 2.5 W/cell to 40 W/cell. The temperature of the fluid inlet can be set according to presumed conditions: 1) 10°C (the lowest temperature of discharge coolant from vehicle air conditioning); 2) 20°C (normal ambient temperature); 3) 30°C; and 4) 35°C (worst summer condition).

Energy balance can be evaluated based on the heat energy obtained from the battery cells and that from the liquid box (Eq. 5.1–5.2). The test unit will be put into an environment-controlled chamber where the battery thermal

environment can be maintained at a desired temperature and a relative humidity.

$$Q_{in} = V_1 \cdot I_1 + V_2 \cdot I_2 \quad (5.1)$$

$$Q_{out} = C_p \dot{m}(T_{out} - T_{in}) \quad (5.2)$$

where

Q_{in} , Q_{out} – heat supplied by the heaters/heat dissipated by the heat pipe

V – the voltage read from the DC power supply

I – the current

C_p – specific heat capacity of the cooling liquid

\dot{m} – mass flow rate obtained from the flow meter

T_{in} , T_{out} – inlet/outlet temperature

5.4.1.2 Transient Cooling Cycle Scenarios

Two transient cooling scenarios are designed to simulate two dynamic battery thermal conditions (Fig. 5.10). It is assumed that the EV operates under a fast discharge and charge regime.

For Scenario 1, 6C discharge rate (peak value) within 10 s is used for acceleration, and 4C continuous discharging for aggressive driving experience will last for 15 minutes in order to use up the battery capacity. A rapid recharge rate (2C charge) will then be supplied right after the driving completes, which takes 30 minutes for a full charge. In order to make sure that the system can maintain a desirable battery operating temperature at all times even under the worst scenario, 4 continuous cycles will be performed to evaluate the effect of heat accumulation.

In addition, Scenario 2 is designed for a much more common but severe battery operating condition. 2C discharging and 2C charging are expected and will be repeated for 3 times. All tests will be carried out under a typical cooling temperature of 20°C and a constant 35°C ambient environment.

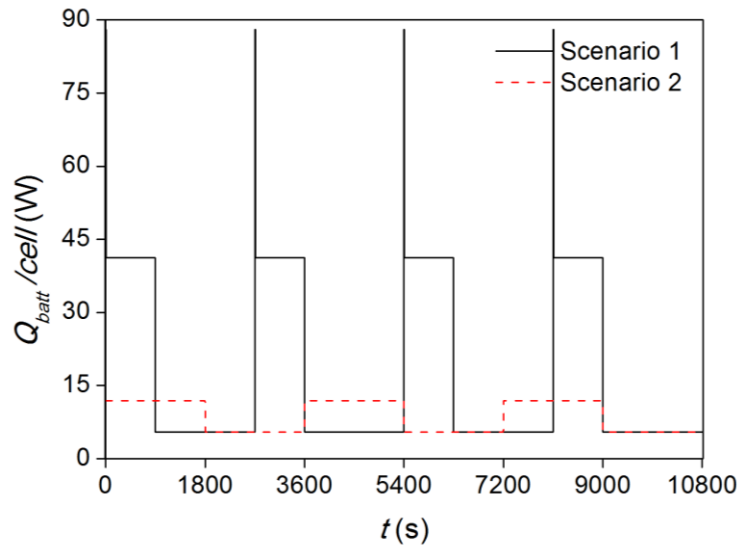


Figure 5.10: Transient scenarios.

5.4.1.3 Effect of Adding Fins

In order to improve system efficiency, adding fins to the heat pipe condenser to augment the heat transfer process is suggested. Fins are used to increase the surface area when the heat transfer coefficient is low, to enhance the structural strength for high pressure fluid flow, or to provide a thorough mixing if a highly viscous liquid is applied. Forced convection cooling of extended surfaces especially through heat pipe fin stacks is a primary cooling techniques used in electronic applications. Wei et al. [221] and Zhao and Avedisian [222] acknowledged the fin efficiency enhancement in forced convection by incorporating heat pipes. Due to high effective thermal conductivity of the heat pipe, the thermal path can be effectively bridged

between the heat source and fin base idealising the highest heat transfer rate achieved by fins. Numerous investigations on heat pipe embedded with fins have been performed to enhance cooling efficiency and/or compactness of the electronic devices [223-226], or for waste heat recovery such as domestic/industrial air conditioning [227] and heating automobiles using exhaust gas [228]. Wu et al. [159] and Burban et al. [163] suggested using finned heat pipes for BTM. However, those work only considered air as the conventional cooling fluid to remove heat from the fin surfaces, and fans are always used to enhance the overall heat transfer coefficient. This makes the fin-to-air heat transfer system bulky and noisy, and high thermal resistance of the fin stack will be experienced limiting the cooling capacity.

Thermal resistance is one of the major criteria in evaluating the thermal performance of heat pipes. Adding fins to the heat pipe usually attributes to the highest thermal resistance in the heat pipe system. Therefore, optimising fin stack translates to a more efficient heat pipe cooling system. Only a few optimisation problems of fin heat sink with embedded heat pipes were examined experimentally [223, 225, 226] and analytically [229]. In addition, the convection heat transfer coefficient is an inherent parameter in the overall thermal performance evaluation and hence the optimum dimension of fin stack configuration. Studies [230, 231] showed that the heat transfer over the annular fins exhibits complex 3D flow characteristics where the heat transfer coefficient in forced convection is non-uniform. Given current experiment limitations, the measurement of the local heat transfer coefficient under steady-state heat transfer conditions was hard to operate because the local fin

temperature and local heat flux were required. To simplify the problem, constant heat transfer coefficient over the fins will be assumed.

Table 5.4: Aluminium fin parameters

Fin type	Fin height l_f (mm)	Fin radius $r_f = r_o + l_f$ (mm)	Fin thickness δ_f (mm)	Number of fins N	Total fin area A_f (m ²)
Annular	5	10	0.5	10	0.005

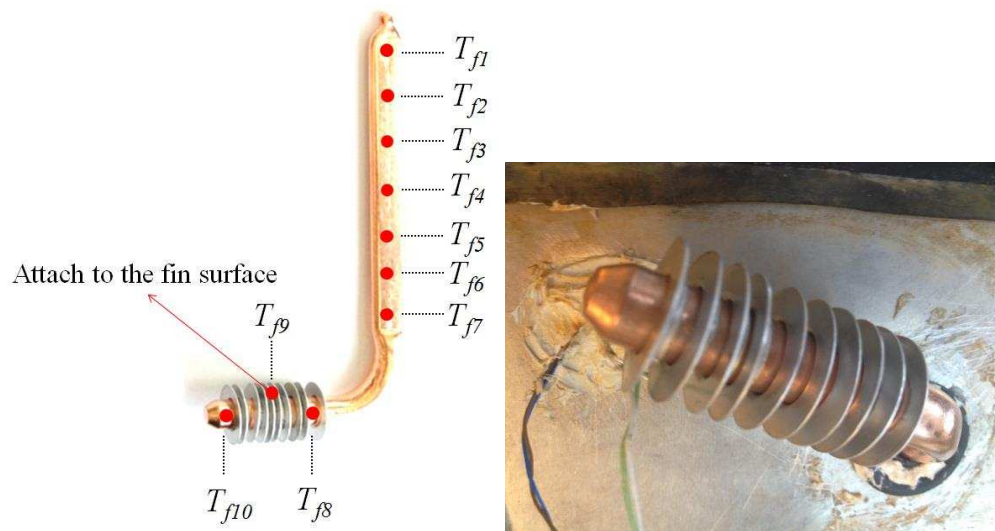


Figure 5.11: Arrangement of thermocouples on the testing L-shaped heat pipe with fins (T_{f1} - T_{f10}).

For this test, the fin height will be optimised at fixed fin thickness and fin pitch (Table 5.4). They will be stacked onto a 50 mm condenser tube with 10 fins every 5 mm yielding a fin spacing of 5.5 mm. Glycol-water mixture will be used as the cooling medium in contact with the fins. As opposed to air cooling, glycol-water mixture has higher specific heat capacity, density and thermal conductivity. This makes it comparatively effective to dissipate heat

over distance with less volumetric flow, reduced temperature difference, and no mechanical noises. The arrangement of thermocouples on the tested heat pipe is demonstrated in Fig. 5.11. Fin analysis is provided in Appendix B.

5.4.1.4 Effect of Perforated Plates

Four perforated plates (Fig. 5.12) were made to reduce system weight by 12.69% to 37.82% (Table 5.5). Different perforated patterns were constructed with hole diameters ranging from 2 mm to 6.8 mm. For holes in longitudinal direction, Plate I and II have same amount of holes and added surface area but different percentage of weight reduction. Plate II and III reduce similar amount of weight but III has more holes and 5 times of added surface area. Plate IV with holes in transverse direction was constructed at both sides. The depth of each hole was approximately 24 mm.

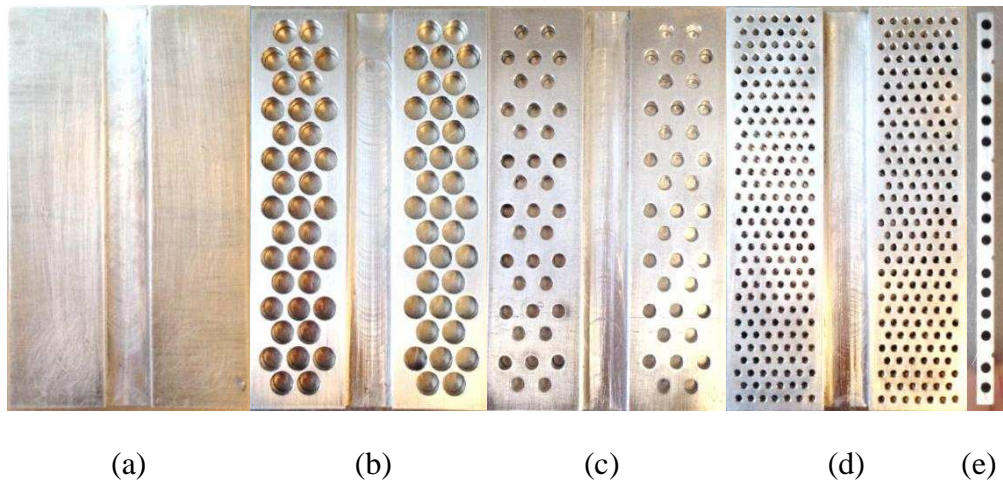


Figure 5.12: (a) Plate original; (b) Plate I; (c) Plate II; (d) Plate III; (e) Plate IV.

Table 5.5: Plate perforation

	Perforated pattern	Weight (g)	Weight reduction (%)	Number of holes	Surface area added (m ²)
Original	Solid	98.500	0	0	0
I	Longitudinal, hole $\phi = 6.8$ mm	61.252	37.82	74	0.0025
II	Longitudinal, hole $\phi = 4$ mm	85.998	12.69	74	0.0028
III	Longitudinal, hole $\phi = 2$ mm	79.620	19.17	404	0.0101
IV	Transverse, hole $\phi = 3$ mm	80.860	17.91	32	0.0072

A visual comparison of the battery surface temperature distribution between applying the heat pipe with the original solid plate and with perforated aluminium plate will be assessed through an infrared camera. This is to study the cooling effect and temperature uniformity brought by plate perforation. Only one battery cell attached with the plate and heat pipe will be exposed to $20 \pm 2^\circ\text{C}$ environment with free air convection and 20°C coolant cooling. 1–4C battery discharging conditions will be applied to the surrogate battery at power rates equivalent to 3.78 – 41.27 W/cell. Images will be taken every 30 minutes after a new power is inputted. Another visualisation method can be done through FEM modelling. This enables the evaluation to be extended for both surrogate battery and lithium-ion battery condition under steady state and transient cooling.

5.4.2 Battery Preheating

Before vehicle start-up or after long-term parking under cold climate, the battery needs to be preheated to achieve its optimal working temperature, which is at least above 0°C. The feasibility of using sintered copper-water heat pipes for EV battery preheating under sub-zero conditions is unknown. Sintered copper-water heat pipes are not functional when the temperature is lower than the freezing point, i.e. 0°C. Such potential freezing and thawing of the heat pipe may destroy the sealed joint when placed vertically. Therefore, it is necessary to evaluate the durability of the sintered copper-water heat pipe after long hours of cold exposure (overnight: 14 – 20 hours).

The freezer will be used to create different sub-zero temperatures maintaining the chamber environment at -25°C, -15°C and 0°C. For the preheating process, it is assumed that the heat energy is extracted through fluid heating from an electric heater or a bioethanol heater, and is transferred to each battery cell via heat pipes. The circulating bath will be used to supply either 20°C or 40°C preheated glycol-water mixture to the heat pipe evaporator inside the liquid box.

A comparison is required to test the thermal response performed by the test unit and the heat pipe alone. This gives a general idea of how fast the heat transfer of a heat pipe is, and to what degree the heat transfer slows down due to the aluminium plate and the battery cell. The fin effect may also be assessed to see if any significant deterioration or enhancement in heating performance is resulted for that the fins are at the heat pipe evaporator.

5.5 Prototype Characterisation

5.5.1 Battery Cooling

5.5.1.1 Parametric Evaluation: R_{hp} , K_{hp} , h_c and T_{g-w}

The thermal resistances of the L-shaped heat pipe that operated against gravity and the total components including the heat pipe and the aluminium plate under different cooling conditions were obtained. Fig. 5.13 (a) shows that R_{hp} decreased dramatically from 0.60 K/W to 0.49 K/W under 10°C cooling and from 0.51 K/W to 0.48 K/W under 20°C cooling as the power input increased from 10 W/cell to 35 W/cell, or 20 W to 70 W in total. High cooling temperature at the condenser such as 30°C and 35°C made R_{hp} increase approximately by 0.01 K/W and 0.03 K/W respectively. However, high cooling temperature at the condenser caused R_{hp} to drop drastically, from 0.60 K/W (10°C cooling) to 0.40 K/W (35°C cooling) at low power input (10 W/cell or 20 W in total), or from 0.49 K/W (10°C cooling) to 0.42 K/W (35°C cooling) at high power input (35 W/cell or 70 W in total). Increasing power input benefited the heat transfer of the heat pipe, and the optimum working condition appeared to be at 30°C due to a relatively constant thermal resistance of 0.45 K/W maintained under all heat fluxes. R_t (Fig. 5.13 (b)) behaved similar to that of the heat pipe, and 30°C cooling contributed to a constant heat transfer operation at all times. The added thermal resistance of the aluminium plate was 0.16 ± 0.02 K/W, which constituted 1/3 of the total thermal resistance.

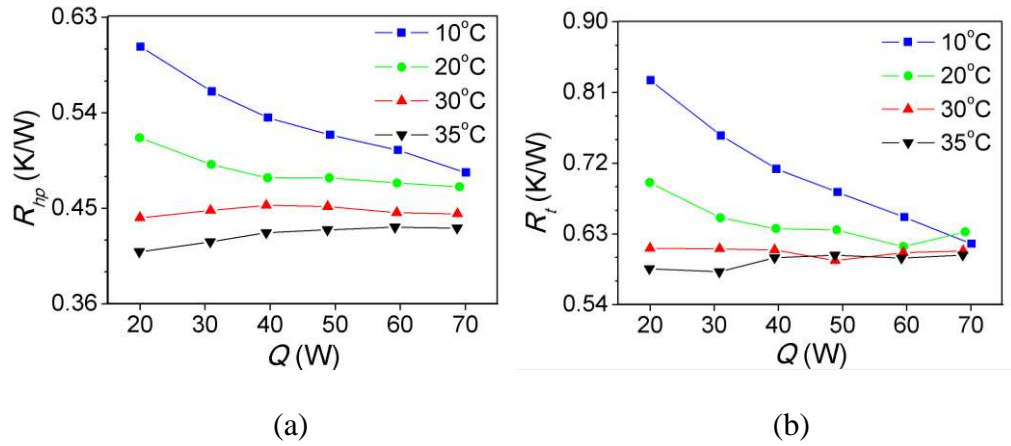


Figure 5.13: Thermal resistance of (a) anti-gravity L-shaped heat pipe (R_{hp}) and (b) total including the heat pipe and the aluminium plate (R_t) under 2.38 ± 0.01 l/min rate.

The thermal conductivities of the heat pipe (K_{hp}) based on different cooling temperatures and power inputs have been plotted (Fig. 5.14). Results show that high input power enhanced K_{hp} under low cooling temperatures by 800 W/mK (10°C cooling) and 400 W/mK (20°C cooling) from 20 W to 70 W. High cooling temperature also augmented K_{hp} as the input power went up, but not in the case of 35°C cooling. A sudden enhancement in K_{hp} can be seen from low power input of 10 W/cell (i.e. 20 W in total) when increasing the cooling temperature, achieving more than 1,300 W/mK increase from 10°C to 35°C. As the cooling temperature reached to 30°C, K_{hp} retained steady at a constant value of 3,400 W/mK under various power inputs. As mentioned before, the optimised temperature for cooling at the condenser was 30°C since little variations in K_{hp} were seen and K_{hp} values were considerably high.

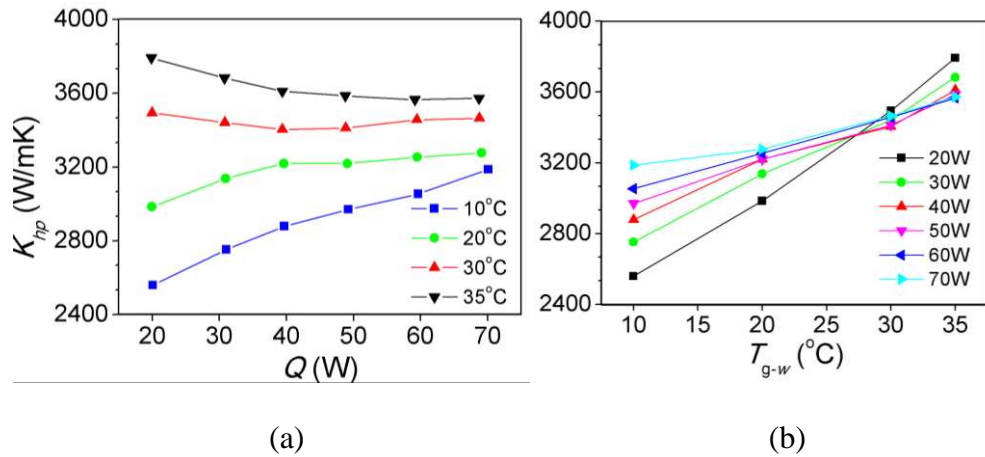


Figure 5.14: Thermal conductivity of anti-gravity L-shaped heat pipe (K_{hp}) under (a) different cooling temperatures and (b) different power inputs under 2.38 ± 0.01 l/min rate

Fig. 5.15 demonstrates the heat transfer coefficients of the cooling end (i.e. the heat pipe condenser) obtained from the experiment under various power inputs and coolant temperatures. The values ranged from 2,210 W/m²K to 3,130 W/m²K. At low cooling temperatures of 10°C and 20°C, h_c under different power inputs were steady, at a constant value of 2,250 W/m²K and 2,500 W/m²K respectively. Increasing cooling temperature at the condenser enhanced h_c especially at low power input of 20 W, with an increase of 1,000 W/m²K from 10°C to 35°C. However, the degree of heat transfer enhancement with increasing cooling temperature deteriorated at high power inputs especially in the range of 50 – 70 W. The discrepancies in heat transfer coefficient by applying different power inputs at the same cooling temperature only became evident at high cooling temperatures, with maximum difference of 300 W/m²K at 30°C and 500 W/m²K under 35°C. Again, 30°C seemed to be the optimised cooling temperature under power inputs from low to high, but

35°C might be desired if low power inputs (20 – 40 W, i.e. 10 – 20 W/cell) were supplied.

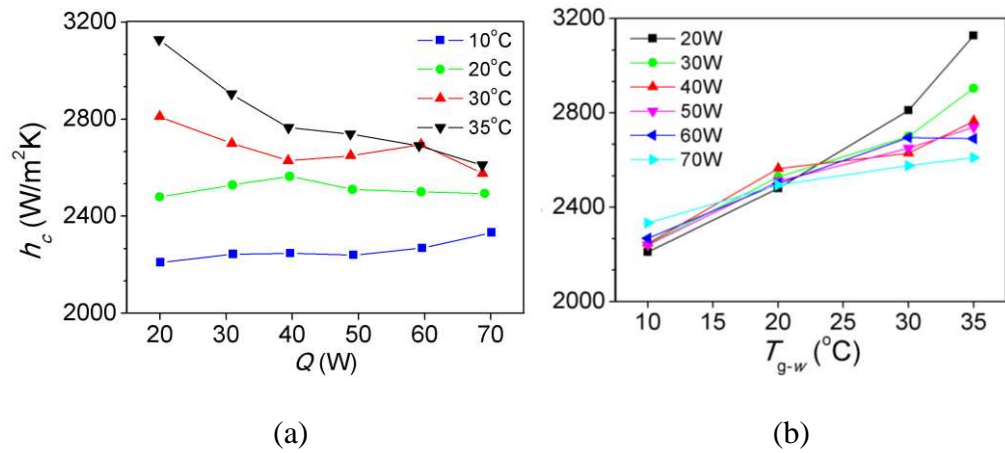


Figure 5.15: Heat transfer coefficient at the cooling end (h_c) under different (a) cooling temperatures and (b) power inputs under 2.38 ± 0.01 l/min rate.

Fig. 5.16 demonstrates the 300 s response of heat pipe based battery cooling at the presumed battery surface temperatures from 40°C to 70°C. High discharged coolant temperature led to a relatively low cooling effect, but the heat transfer was augmented at a high battery surface temperature such as 60°C and 70°C. The cooling response achieved under 30°C and 35°C appeared to be almost identical if the initial battery surface temperature was given at 70°C. Cooling the battery at the initial temperature of 40°C under 35°C cooling only resulted in 1.5°C drop after 5 minutes (Fig. 5.17). Temperature reduction appeared to be considerably effective at high initial battery temperature of 70°C achieving 13°C drop under 10°C cooling and 10°C drop under 35°C. Supplying low temperature water at 10°C significantly enhanced the cooling performance, with 6.5°C drop at battery surface temperature of 40°C compared to 1.5°C drop under 35°C cooling. It can be thusly concluded that the thermal

performance of the heat pipe is much more effective under either high battery surface temperature or low cooling temperature.

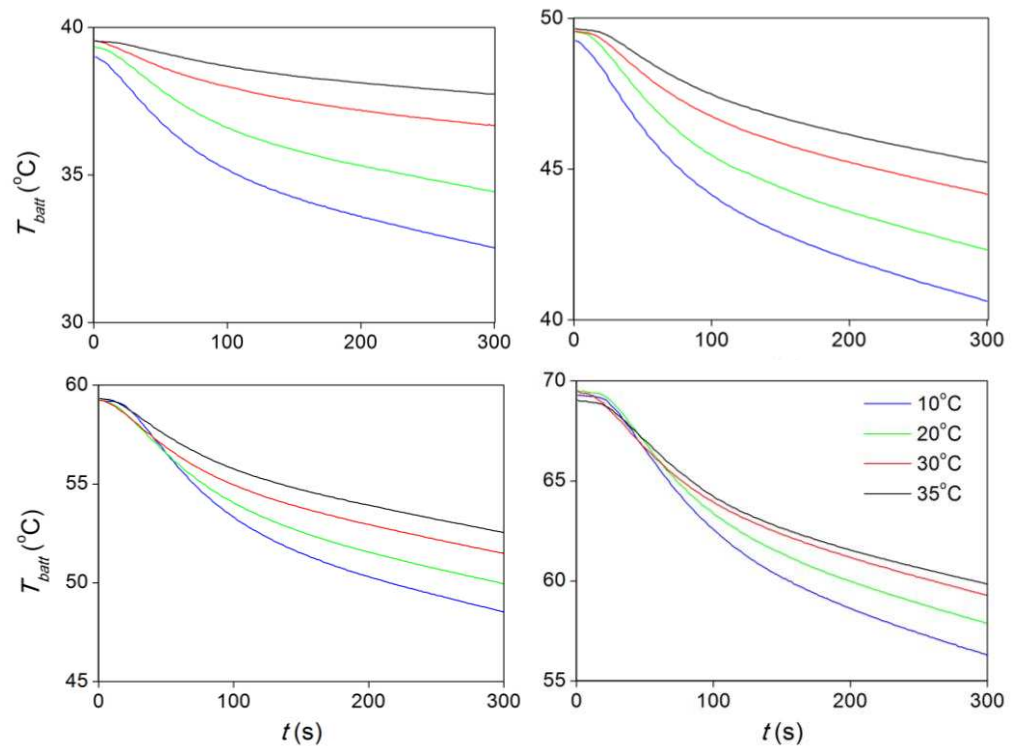


Figure 5.16: 300 s cooling response performed at initial battery surface temperature of 40°C, 50°C, 60°C and 70°C cooled by 10°C, 20°C, 30°C, 35°C discharging coolant under 2.38 ± 0.01 l/min rate.

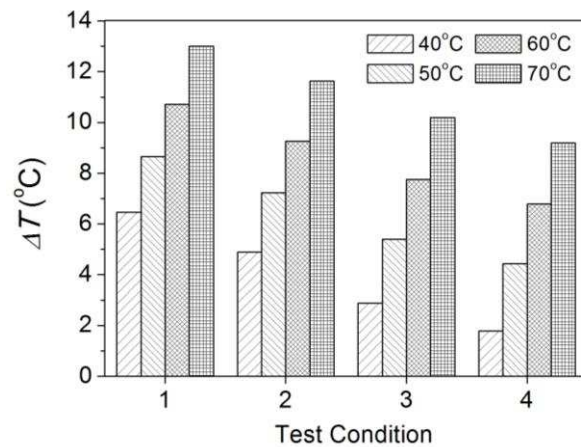


Figure 5.17: 5 minutes temperature drop at initial battery surface temperature of 40°C, 50°C, 60°C and 70°C cooled by four test conditions: 1 – 10°C, 2 – 20°C, 3 – 30°C, 4 – 35°C discharging coolant under 2.38 ± 0.01 l/min rate.

5.5.1.2 Steady State Cooling and Transient Cycle Cooling

Fig. 5.18 demonstrates the steady state cooling performance under a variety of battery thermal conditions from 2.5 W/cell to 40 W/cell. The coolant discharged to the liquid box was glycol-water mixture controlled at a constant temperature of 20°C and a steady flow rate of 2.38 ± 0.03 l/min. The ambient environment was maintained at 35°C using a heating block and a fan. The battery power supply was stopped once the battery surface temperature reached to a steady state condition for at least 10 minutes, and the battery will be then cooled for another 10 minutes. The proposed heat pipe cooling was able to keep the average battery surface temperature below 40°C under 2.5–10 W/cell, but every incremented 10 W/cell led to an approximately 10°C per 10 W/cell temperature increase rate of the battery surface. Steady state cooling performance indicates the degree of the proposed BTM performance reflecting its limitation in high heat flux applications. Heat pipe thermal management was able to maintain the battery surface temperature under 40°C if the battery generates less than 10 W/cell, which is normally the case in most vehicle batteries. It was also capable of keeping the battery temperature below 50°C if less than 20 W/cell was given. Thermal abuses conditions such as 20 – 40 W/cell are uncommon but if encountered, the heat pipe still helped reduce the battery temperature under 70°C avoiding potential thermal runaway. The average temperature drop in 10 minutes was obtained in Fig. 5.19. The cooling performance was considerably enhanced at higher initial battery surface temperature achieving 2.23 °C/min if the initial temperature was at 70°C, compared to 0.52 °C/min at 40°C.

In addition, real-time transient behaviours of the average battery surface temperature under two different scenarios were recorded and each scenario was repeated for 3–4 times. The test rig was maintained at a constant ambient temperature of 35°C before starting the cycle performance. The cooling performance was less affected by 6C discharge due to a short duration of 10 s, and no heat accumulation was observed after the cycle being repeated (Fig. 5.20). For Scenario 1, the peak temperature reached to 63°C after 4C maximum battery current was continuously discharged for 15 minutes, but the system was able to maintain the peak temperature under repeated cycles of battery working extremes. 2C battery charge made the battery temperature drop significantly achieving less than 35°C by the end of the cycle. The transient behaviours under those 4 cycles were almost identical. Scenario 2 showed that the heat pipe experienced a temperature drop at the beginning of the cycle after 20°C glycol-water mixture was discharged. The battery temperature under 2C battery discharge condition increased slowly to 41°C, and then dropped drastically after 2C charge condition was applied. The battery temperature at the end of the first cycle appeared to be slightly higher than that at the beginning, making the peak temperature of the second cycle higher than that under the first cycle. Nevertheless, the proposed cooling method was able to keep the battery peak temperature below 41°C at all times.

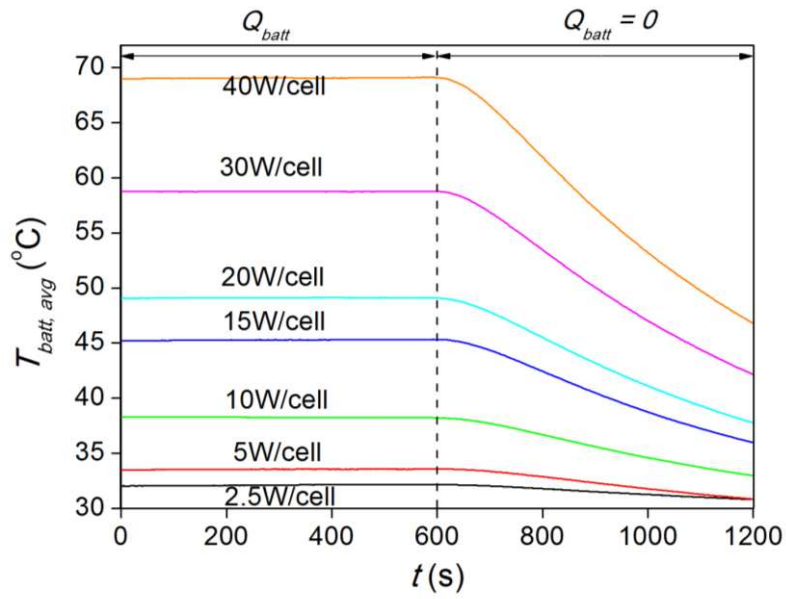


Figure 5.18: Average battery surface temperature change ($T_{amb} = 35^{\circ}\text{C}$, $T_{g-w} = 20^{\circ}\text{C}$, $q_{g-w} = 2.38 \pm 0.03$ l/min).

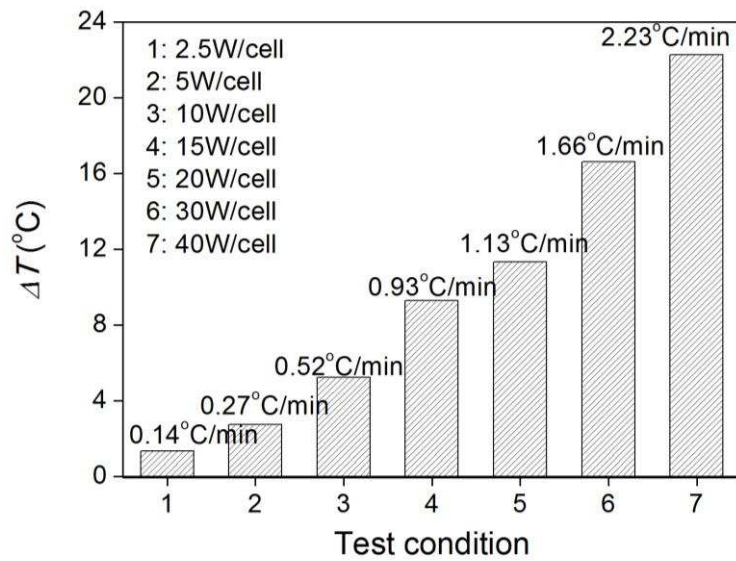


Figure 5.19: Average battery surface temperature drop rate in 10 minutes under seven test conditions ($T_{amb} = 35^{\circ}\text{C}$, $T_{g-w} = 20^{\circ}\text{C}$, $q_{g-w} = 2.38 \pm 0.03$ l/min).

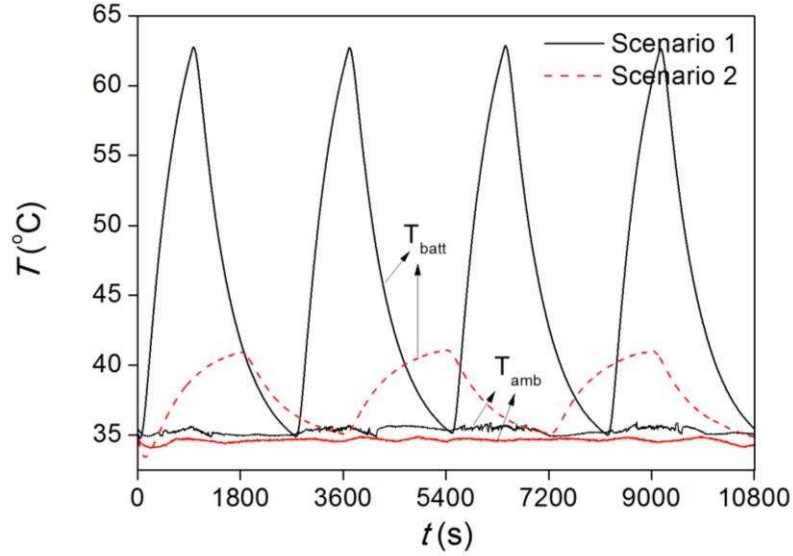


Figure 5.20: Average battery surface temperature transient behaviour under two scenarios ($T_{\text{amb}} = 35^{\circ}\text{C}$, $T_{\text{g-w}} = 20^{\circ}\text{C}$, $q_{\text{g-w}} = 2.38 \pm 0.03$ l/min).

5.5.1.3 Effect of Adding Fins

5.5.1.3.1 Parametric Evaluation: R_{hp} , K_{hp} , h_c and $T_{\text{g-w}}$

Battery cooling tests via heat pipe without and with fins were performed under four cooling temperatures (10°C , 20°C , 25°C and 35°C) at a set flow rate of 2.38 ± 0.01 l/min. Such flow rate induced laminar flow inside the liquid box and the heat pipe was operated against gravity. Data were recorded after achieving thermal equilibrium for at least 10 minutes. The thermal resistances and thermal conductivities under those conditions were obtained correspondingly in Fig. 5.21, and Table 5.6 summarises the effective heat pipe thermal resistances at a given power input under a fixed cooling temperature. Fin tended to not only add a considerable amount of thermal resistance by itself (0.08 K/W), but prohibited the heat and mass transfer inside the heat pipe

increasing thermal resistance by approximately 0.23 K/W, 0.17 K/W, 0.15 K/W, and 0.17 K/W under 10°C, 20°C, 30°C and 35°C cooling respectively.

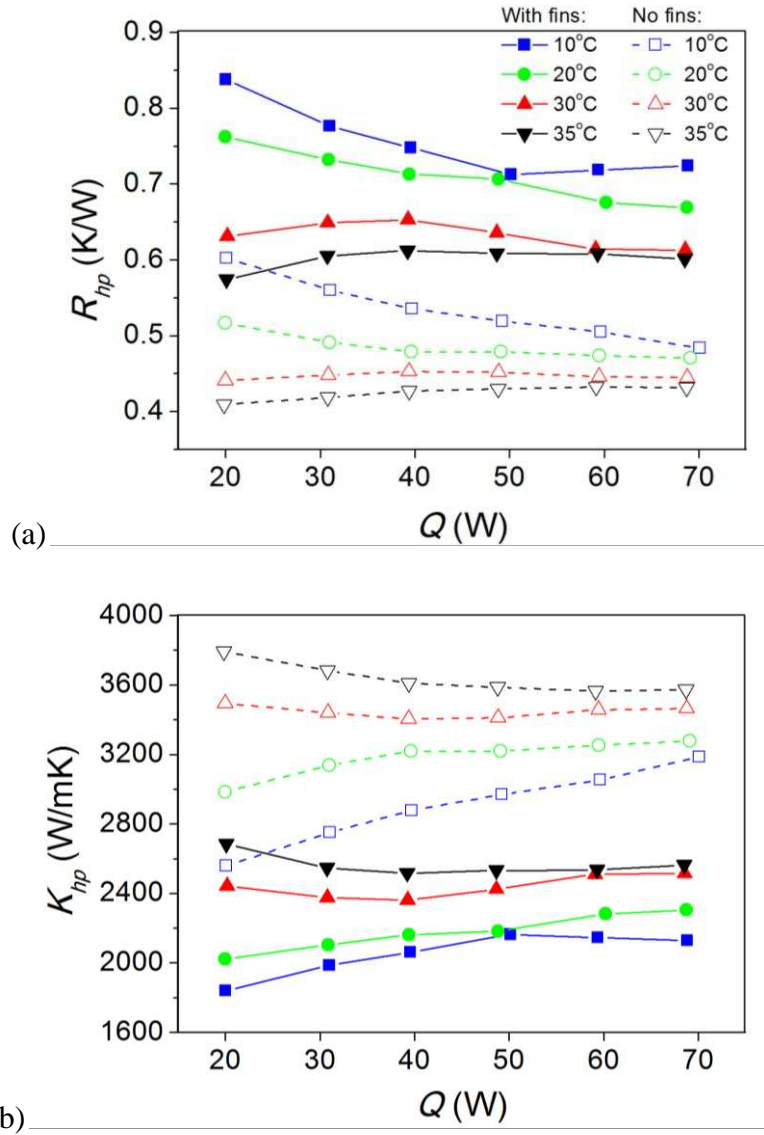


Figure 5.21: (a) Overall thermal resistance (R_{hp}) and (b) thermal conductivity (K_{hp}) of L-shaped heat pipe operated against gravity with fins ($R_{hp, wf}$, $K_{hp, wf}$) and no fins ($R_{hp, nf}$, $K_{hp, nf}$) obtained from experiment.

Table 5.6: Summary of the effective thermal resistance R_{eff}

T_w (°C)	10	20	30	35
	With fins			
$R_{\text{eff}, t}$ (K/W)	0.750	0.703	0.686	0.688
$R_{\text{eff}, hp}$ (K/W)	0.669	0.628	0.597	0.609
R_{fin} (K/W)	0.081	0.075	0.089	0.079
	No fins			
$R_{\text{eff}, hp}$ (K/W)	0.438	0.453	0.446	0.442

Note:

$R_{\text{eff}, t}$ – total effective thermal resistance (heat pipe and fins)

$R_{\text{eff}, hp}$ – effective thermal resistance (heat pipe)

R_{fin} – thermal resistance of fins

With fins available, the total thermal resistance doubled from that achieved without fins, and the difference in thermal resistance between 10°C and 35°C cooling cannot be neglected under high power inputs. An approximate 0.15 K/W was resulted under the range of 60 – 70 W when fins were added, while less than 0.08 K/W was obtained from no fins condition. High temperature cooling at the heat pipe condenser facilitated heat transfer inside the heat pipe, seen from the thermal resistance reduction when discharging coolant at 30 – 35°C. The heat pipe thermal resistances (both $R_{\text{hp},nf}$ and $R_{\text{hp},wf}$) seemed constant under those two temperatures within 20 – 70 W, but experienced a huge reduction under high power and low cooling temperature (10°C). The thermal conductivity plotted in Fig. 5.21 (b) indicates a stable operation achieved by fins. Although low thermal conductivity was realised by adding fins to the heat pipe condenser, the operation under different

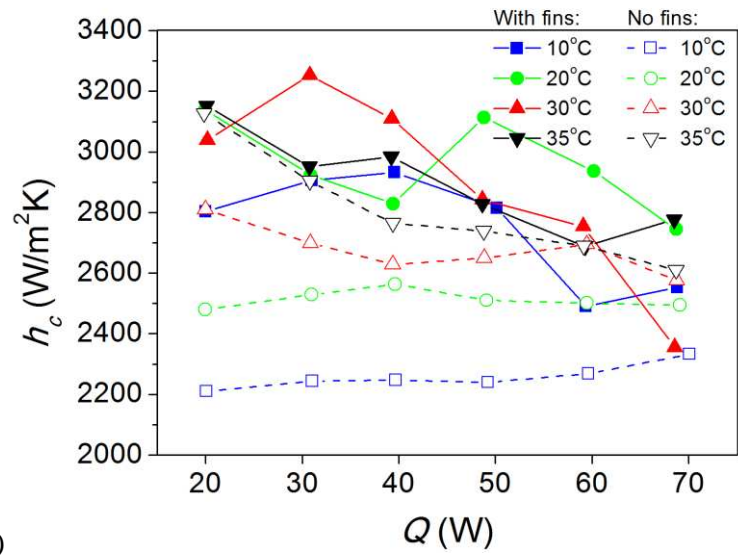
cooling temperatures was much more established than that obtained without fins. Thermal conductivity was reduced by 800 – 1,200 W/mK under low power inputs and by 1,000 W/mK under high power inputs.

It is argued that the increased thermal resistance with the fins addition can be attributed to two aspects: 1) increased contact thermal resistance between the fin and the heat pipe base due to loose fit; 2) inadequate temperature measurements located at the fins as well as the base. Fig. 5.11 shows that only one temperature point was selected for fins, and the other two points were located at the heat pipe base with one set at the end of the base. This may increase temperature difference between the measured points, contributing to the calculated thermal resistance being increased and thermal conductivity being reduced in relation to the original heat pipe setup.

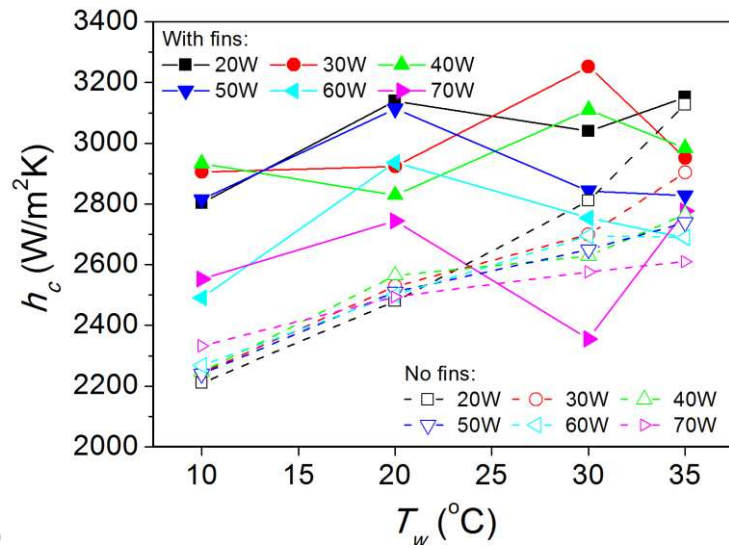
Fig. 5.22 shows the heat transfer coefficients at cooling end in relation to the power input and the cooling temperature respectively. In Fig. 5.22 (a), the heat transfer coefficient obtained from adding fins fluctuated dramatically and if a high power input was given, it dropped greatly irrespective of cooling temperatures. For heat pipe without fins, the tendency of fluctuation was mild, and the heat transfer coefficient can be maintained at either low or high power input under 10 – 30°C. It can be seen from Fig. 5.22 (b) that increasing cooling temperature at the cooling end enhanced the heat transfer coefficient achieving approximately 600 W/m²K increase from 10°C (2,200 W/m²K average) to 35°C (2,750 W/m²K average) under no fins condition. For heat pipe with fins, the heat transfer coefficient stayed fluctuated and almost uniform at all times at an average value of 2,800 W/m²K, slightly higher than that from no fins. Notably, high power input led to an increase in heat transfer coefficient if only

heat pipe was in operation, whereas adding fins made the overall heat transfer coefficient vary less. Furthermore, the degree of heat transfer improvement after adding fins was suggested. At cooling temperature of 10°C or 20°C, heat transfer performance was at the highest compared to those under other cooling temperatures. Fin was able to improve the cooling side heat removal at power inputs of 20 – 50 W under 10°C cooling, but seemed to inhibit the performance at higher powers (60 – 70 W) and also at high cooling temperatures (30 – 35°C).

Adding fins may help the heat removal rate at the cooling end but might not necessarily be beneficial under high power inputs and high cooling temperature. The heat transfer coefficient is calculated based on the temperature difference between the fin or the heat pipe base (if without fins) and the average fluid temperature between the inlet and outlet. As mentioned earlier, contact thermal resistance may lead to low fin temperature measurement, and the fact that only one fin was measured adds uncertainties to the overall conclusion. A more rigorous study in characterising the fin performance is required to give insight into contributing factors, such as the increased surface area, the increased heat transfer coefficient due to changed fluid motion, or lowered ambient fluid temperature for increasing the surface heat transfer rate. More measuring points for the fins as well as the heat pipe base are needed in order to minimise possible errors and uncertainties in parameter calculations including thermal resistance, thermal conductivity and heat transfer coefficient.



(a)



(b)

Figure 5.22: Heat transfer coefficient at the cooling end: (a) versus power input; (b) versus cooling temperature.

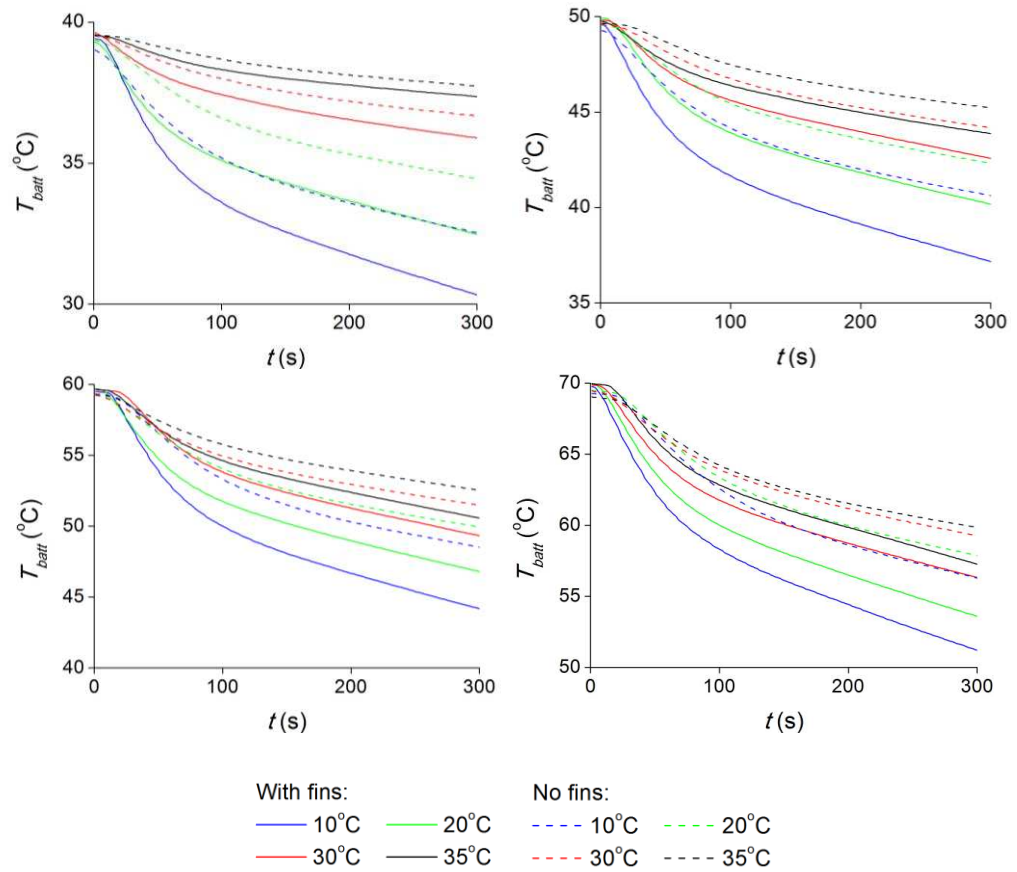


Figure 5.23: A comparison of battery cooling response in 300 s between heat pipe with fins and no fins condition at initial battery surface temperature of 40°C, 50°C, 60°C and 70°C cooled by 10°C, 20°C, 30°C, 35°C discharging coolant.

Fig. 5.23 demonstrates a 300 s transient cooling performance at a given initial battery surface temperature (40 – 70°C) from heat pipe with fins and without fins. This helps to evaluate the fin effect of the transient battery cooling performance. High cooling temperature led to a relatively low cooling effect, but with the help of fins, such effect can be augmented improving system heat transfer limit. At low surface temperature, for instance, cooling the battery under 35°C at 2.38 l/min after 300 s only resulted in an approximate 1.5°C drop and 2.0°C drop under no fins and with fins respectively. As the

battery surface temperature increased, temperature reduction appeared to be remarkably efficient achieving 9.0°C drop (no fins) and 13.0°C drop (with fins) under high cooling temperature (35°C). This suggests that the heat pipe cooling ability becomes evident if high initial battery surface temperature occurs. In addition, supplying low cooling temperature (e.g. 10°C) will enhance the cooling capacity (Fig. 5.24) with 6.5°C drop (no fins) and 9.0°C drop (with fins) at low battery surface temperature of 40°C; and 13.0°C drop (no fins) and 19.0°C drop (with fins) under initial surface temperature of 70°C. Using fins to accelerate the cooling effect was therefore achieved, and a better cooling can be resulted if low cooling temperature coolant was supplied.

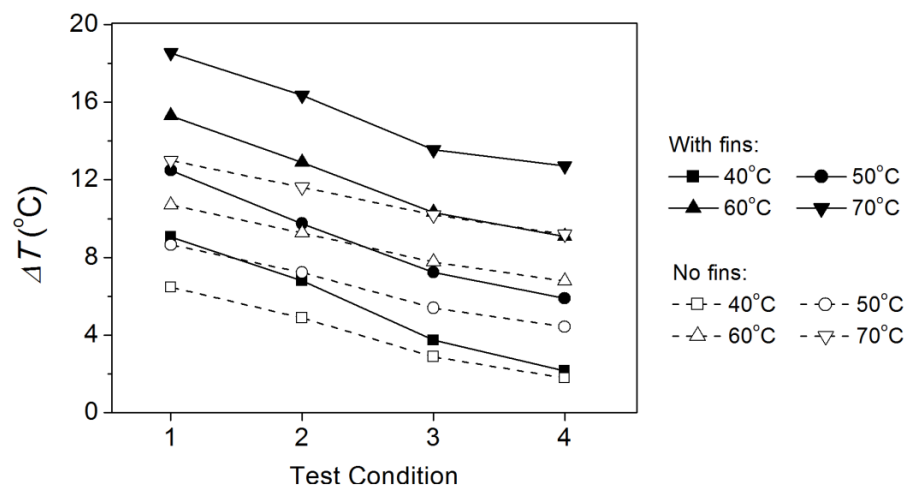


Figure 5.24: Temperature drop in 300 s at a given initial battery surface temperature (40°C, 50°C, 60°C and 70°C) under four test conditions: 1 – 10°C; 2 – 20°C; 3 – 30°C; and 4 – 35°C cooling.

5.5.1.3.2 Fin efficiency

The fin efficiencies ranged from approximately 58% to 70% at a maximum $\pm 15\%$ discrepancy (Fig. 5.25). Predicted and measured values are in a good agreement. For annular fins, low r_f/r_o may help achieve a better fin

efficiency at a constant value of ml_e . This means that fins with big fin height l_f (large extended surfaces) might not necessarily be beneficial to the overall heat transfer. In addition, the heat transfer coefficient can be enhanced by either reducing the hydraulic diameter or selecting a fin shape with a low aspect ratio. Reducing the annular fin height will minimise the hydraulic diameter so as to improve the heat transfer and achieve device compactness. The fin height used in this experiment was equal to the heat pipe outer radius reaching low $r_f/r_o = 2$ requirement. However, the thickness of the fin was 0.5 mm, which was a bit thin causing reduced fin efficiencies. Additionally, thin fins were likely to cause structural failure and corrosion, observed from experiment.

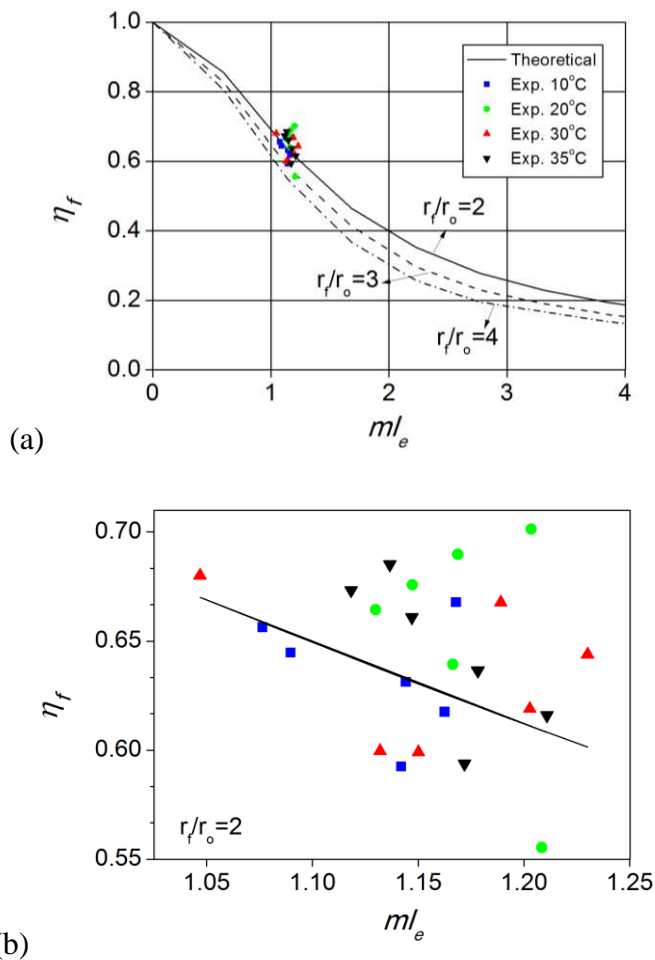


Figure 5.25: Fin efficiency derived from (a) Eq. B.5 – B.6 (Appendix B) under different r_f/r_o and (b) experiment data.

5.5.1.3.3 Steady state cooling and transient cooling cycle

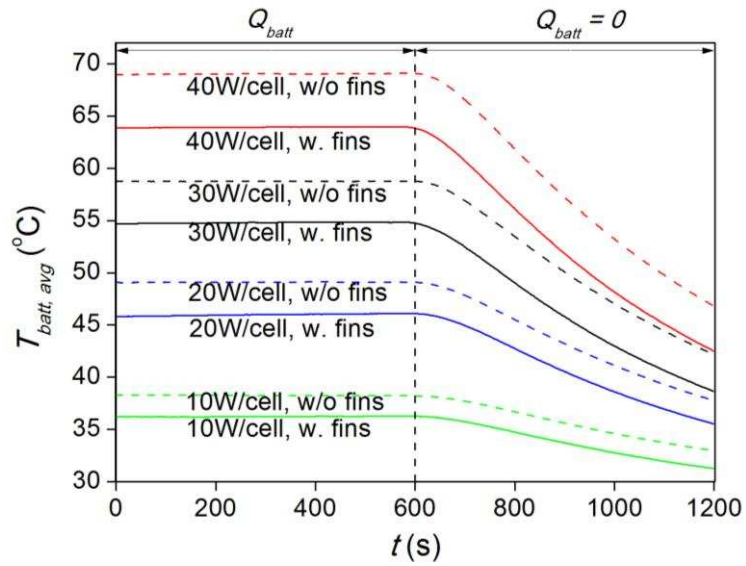


Figure 5.26: A comparison of battery surface temperature change between heat pipe w. fins and w/o fins ($T_{amb} = 35^{\circ}\text{C}$, $T_{g-w} = 20^{\circ}\text{C}$, $q_{g-w} = 2.38 \pm 0.03$ l/min)

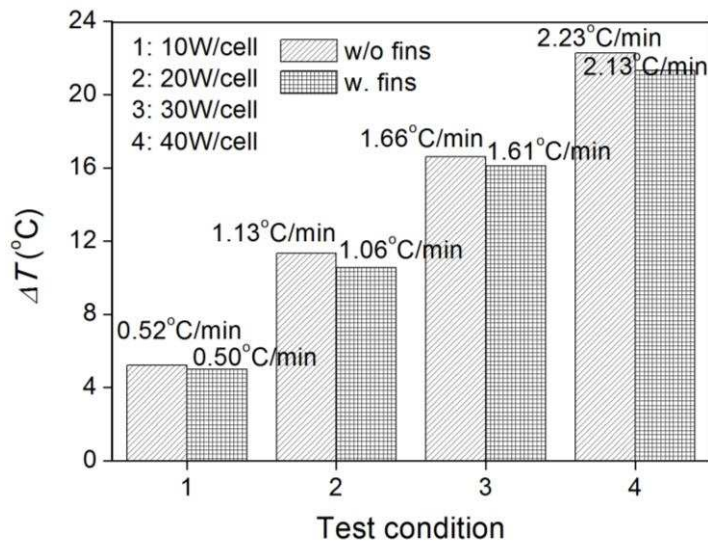


Figure 5.27: A comparison of average battery surface temperature drop rate in 10 minutes between heat pipe w. fins and w/o fins under four test conditions ($T_{amb} = 35^{\circ}\text{C}$, $T_{g-w} = 20^{\circ}\text{C}$, $q_{g-w} = 2.38 \pm 0.03$ l/min)

Fig. 5.26 compares the battery surface temperature change between two conditions: heat pipe with fins and without fins. This helps to evaluate the

forced convection cooling of extended surfaces through heat pipe fin stacks. At high heat fluxes (20 – 40 W/cell), fins at the heat pipe condenser helped decrease the average battery surface temperature by 4 – 5°C under steady state condition; while for low heat flux such as 10 W/cell, 3°C reduction was achieved. The cooling performance by heat pipe fins was improved at higher battery heat fluxes, but not so much at lower power input. Using fins to enhance the cooling performance was realised, but the temperature drop after steady state seemed to be less effective compared to that without fins (Fig. 5.27). A difference of 0.07 – 0.10 °C/min drop rate was obtained. Moreover, transient cycle cooling performance after adding fins was compared (Fig. 5.28 and Fig. 5.29). Fins helped reduce the peak temperature by approximately 5.5°C under Scenario 1 and by 1.5°C under Scenario 2. This suggests that the cooling augmentation from adding fins will only be effective if high heat flux was encountered.

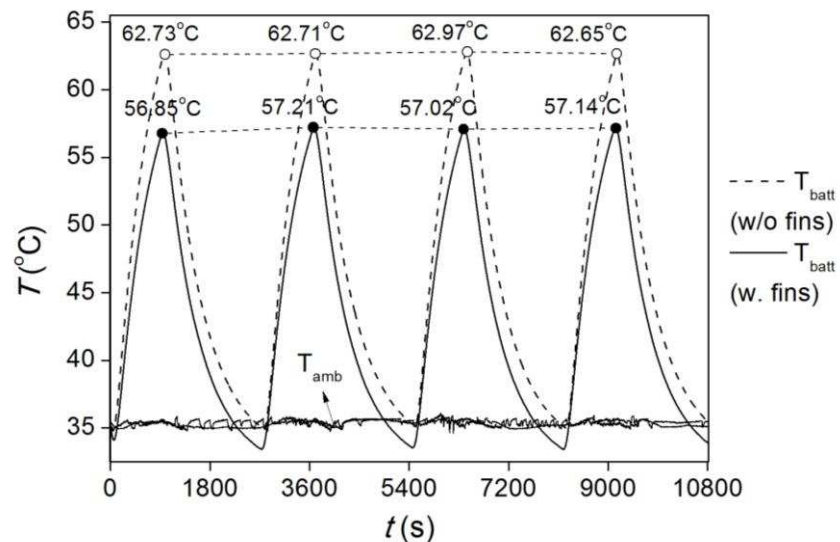


Figure 5.28: A comparison of battery surface temperature transient behaviour between heat pipe w. fins and w/o fins under Scenario 1 – 4 repeated cycles ($T_{amb} = 35^{\circ}\text{C}$, $T_{g-w} = 20^{\circ}\text{C}$, $q_{g-w} = 2.38 \pm 0.03 \text{ l/min}$)

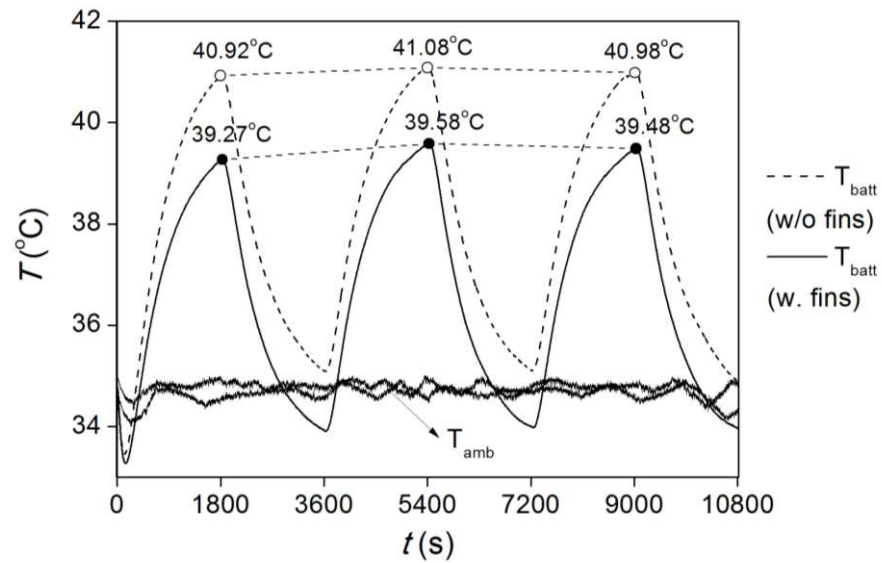


Figure 5.29: A comparison of battery surface temperature transient behaviour between heat pipe w. fins and w/o fins under Scenario 2 – 3 repeated cycles ($T_{amb} = 35^{\circ}\text{C}$, $T_{g-w} = 20^{\circ}\text{C}$, $q_{g-w} = 2.38 \pm 0.03$ l/min).

5.5.1.4 Effect of Perforated Plates

5.5.1.4.1 Infrared imaging

An infrared camera was used to capture the temperature distribution of the target surface in order to analyse the cooling effect after substituting the solid aluminium plate to the perforated plates. 1 – 4C battery discharging conditions were applied with power equivalent to 3.78, 11.92, 24.42 and 41.72 W/cell respectively. The colour range for each obtained thermal image was set from 15°C to 40°C . The target area was selected and analysed by FLIR tool with marked maximum, minimum and average area temperature. With low battery discharge current supply such as 1 – 2C, the temperature of battery itself with only free air convection ($20 \pm 2^{\circ}\text{C}$ ambient) was below 25°C after 30 minutes. But 3 – 4C discharge current led to a significant temperature increase reaching

to an average of 33.7°C and 47.7°C respectively. For the battery with heat pipe cooling at one side, the cooling was effective maintaining the average temperature below 40°C under 4C discharge condition. The average temperature of the right side of battery that attached to the aluminium plate with heat pipe was 8°C, lower than the left side under 3 – 4C discharge conditions (Fig. 5.30).

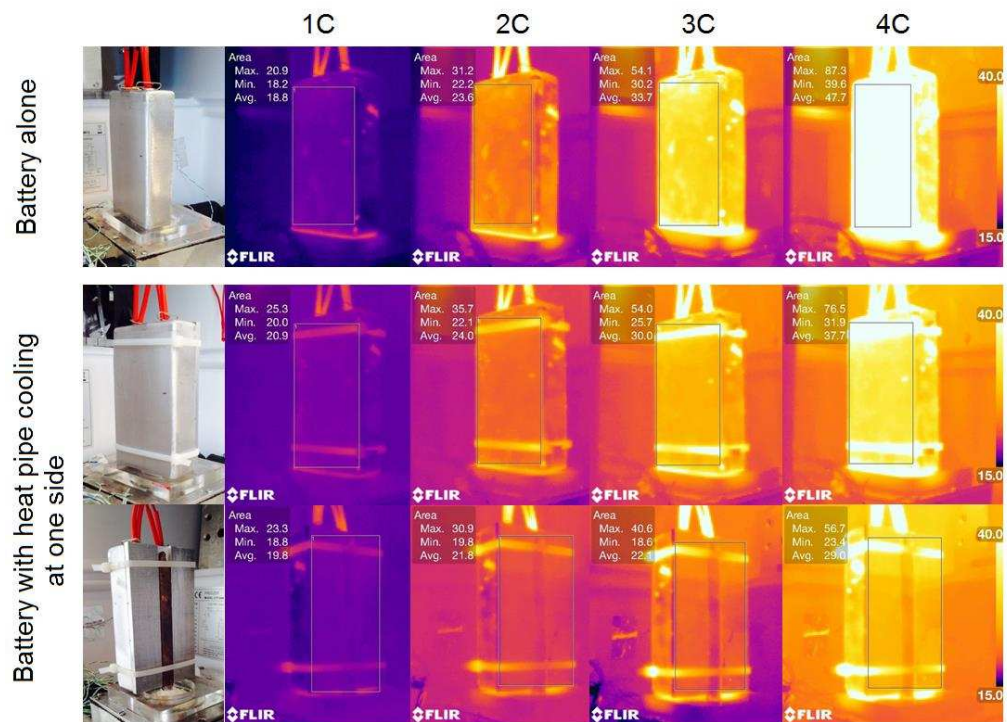


Figure 5.30: A comparison between battery alone and battery with heat pipe cooling at one side through infrared camera ($T_{amb} = 20 \pm 2^\circ\text{C}$, $T_{g-w} = 20^\circ\text{C}$, $q_{g-w} = 2.38 \pm 0.03$ l/min, 1 – 4C battery discharging conditions, colour band range: 15 – 40°C)

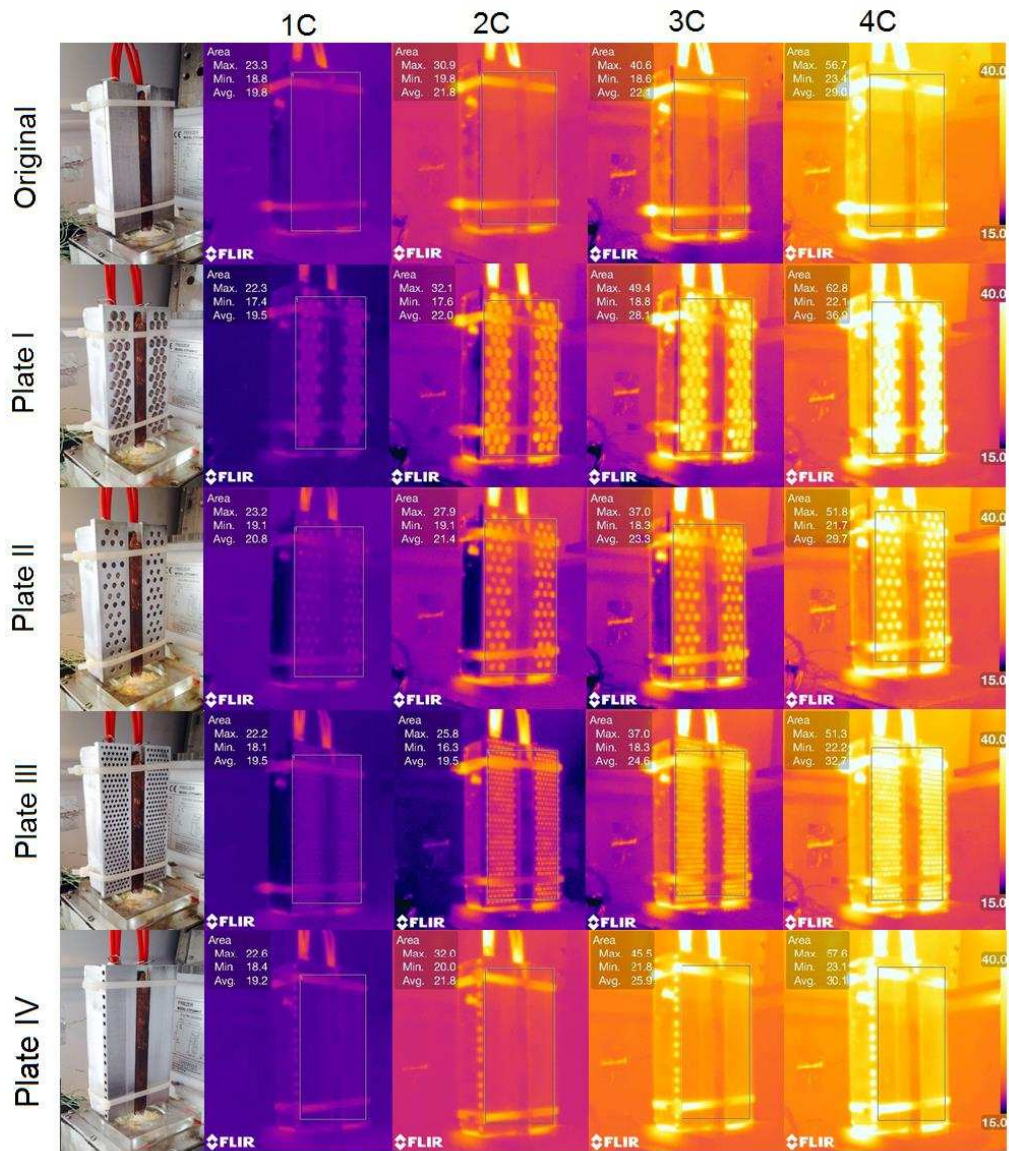


Figure 5.31: A comparison of battery with heat pipe cooling at one side using solid plate and perforated plates (I-IV) through infrared camera ($T_{amb} = 20 \pm 2^\circ\text{C}$, $T_{g-w} = 20^\circ\text{C}$, $q_{g-w} = 2.38 \pm 0.03 \text{ l/min}$, 1 – 4C battery discharging, colour band range: 15 – 40°C).

In addition, a comparison of battery with heat pipe cooling at one side using solid plate and perforated plate I-IV was made. According to Fig. 5.31, with the same amount of holes (Plate I & II), bigger holes impeded the thermal path from the hot end to the cooling end as the effective thermal characteristic

length reduced to half. With the same effective thermal characteristic length (Plate I & III), smaller holes tended to distribute heat much more evenly and uniformly thus achieving a better cooling effect. Free air convection may also attribute to a better performance as the added surface area (Plate III) was 5 times more than that of Plate I. In addition, huge temperature gradient was observed between the heat pipe and the Plate I indicating low degree of temperature uniformity across the battery surface. The results given by Plate IV seemed to be somewhat similar to the original. The surface temperature distribution was slightly higher than that obtained from the original, but high temperature detected at the constructed holes (24 mm deep) may make the overall heat transfer difficult.

5.5.1.4.2 Finite Element Analysis (FEA)

The effect of plate perforation was also investigated through FEA modelling. Steady state surface temperatures of different plates under 2C and 4C discharge rate were obtained in Fig. 5.32 and Fig. 5.33. The thermal behaviour of the plate attached with the surrogate battery differs from that attached with lithium-ion battery.

For surrogate battery, due to low thermal conductivities on all directions, plate perforation seems to be less efficient and less favourable to the overall heat transfer. Only plate with less amount of hole subtraction (Plate II) performs similar to that attached with solid plate. Plate I & IV lead to the worst temperature uniformity on the battery surface under both low and high power inputs, whereas Plate III appears to be good at conducting heat under high power inputs (Fig. 5.32). The average surrogate battery surface temperature

resultant from using Plate III is indeed the lowest, and the area of low temperature distribution across Plate III is bigger than that from solid plate. Plate I also displays low temperature distribution due to the amount of thermal resistance eliminated from holes, but bigger hole size and higher temperature gradients from the top to the bottom prohibits the reduction of average battery surface temperature. This implies that factors such as hole size and distribution, the range of power inputs, and thermal conductivities of the target (battery cell in this case) all need to be taken into account before finalising the conclusion.

If the object has higher thermal conductivities along length and height, for instance lithium-ion batteries, plate perforation seems to have little impact at low heat dissipation rate as heat coming from the battery can be quickly distributed through length and height. Under low battery thermal power, the average battery surface temperature obtained from those plates coupled with heat pipe cooling varies little. The effect of perforation becomes beneficial during high power inputs, since lithium-ion battery cooled by Plate III achieves the lowest temperature distribution, followed by Plate I, IV and II. But Plate I and II make the temperature contour on the battery surface the least smooth, compared to that shown in Plate III and IV (Fig. 5.33). As heat can be quickly distributed across the surface, the amount of thermal resistance eliminated from perforation plays a key role in overall heat transfer enhancement. The hole distribution and direction, in addition, are also important that attribute to contour smoothness and low temperature gradient.

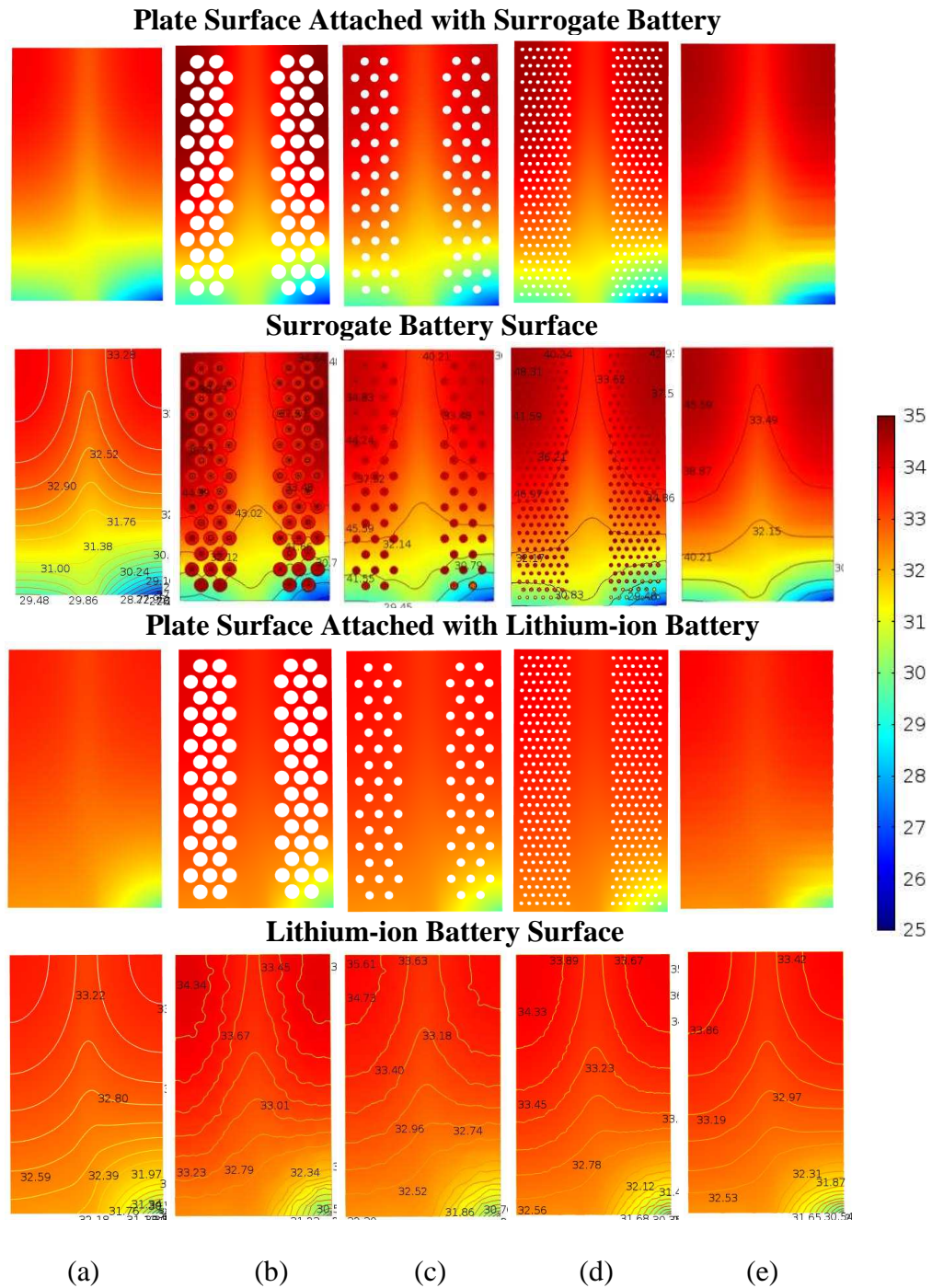


Figure 5.32: Steady state surface temperature of plate and battery from (a) original; (b) I; (c) II; (d) III; (e) IV under 2C discharge (11.92 W/cell), colour range 25 – 35 °C ($T_{\text{amb}} = 35 \text{ }^\circ\text{C}$, $T_{\text{g-w}} = 20 \text{ }^\circ\text{C}$, $q_{\text{g-w}} = 2.38 \text{ l/min}$).

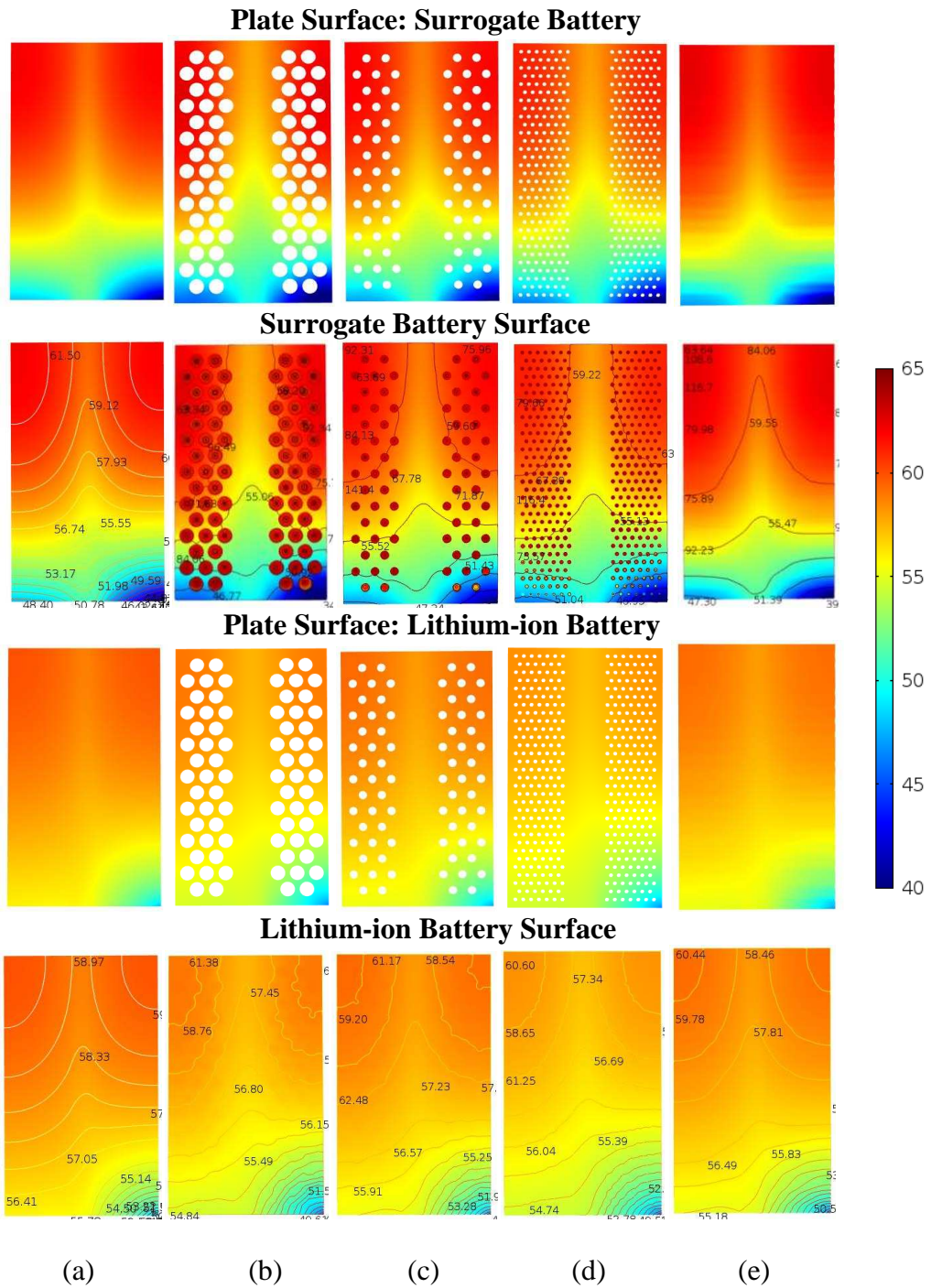


Figure 5.33: Steady state surface temperature of the plate and battery from (a) original; (b) I; (c) II; (d) III; (e) IV under 4C discharge (41.72 W/cell), colour range 40 – 65 °C ($T_{\text{amb}} = 35 \text{ }^\circ\text{C}$, $T_{\text{g-w}} = 20 \text{ }^\circ\text{C}$, $q_{\text{g-w}} = 2.38 \text{ l/min}$).

Transient cooling behaviour using different plates for both surrogate battery and lithium-ion battery has been assessed through a 600 s discharge cycle. The analysis of dynamic thermal response is essential in BTM because the capacity of the battery is limited and will be used up in a certain time period. Results were compared at the end of the cycle time, i.e. at 600 s shown in Fig. 5.34 and Fig. 5.35. Low thermal conductivity along the width of the surrogate battery made the heat difficult to be conducted and transferred to the heat pipe, thus the plate was heated up slowly. For surrogate battery, the surface temperature of the battery from using perforated plates distributed poorly at a sluggish thermal response. Higher thermal conductivities along all axes contribute to a much pleasant heat transfer, as shown by lithium-ion batteries with different plates attached. The surface temperature inclines to be uniformly spread at a higher pace of heat transfer. The average surface temperature change of the surrogate battery and the lithium-ion battery under heat pipe cooling using different plates during the final 60 s in a 600 s cycle time was plotted. As the surface temperature distribution of lithium-ion battery is quite uniform after applying different perforated plates, the criteria for choosing plate focuses on the average temperature. As pointed out by Fig. 5.35, Plate II gives the lowest average battery surface temperature, followed by Plate Original, VI, I, and III.

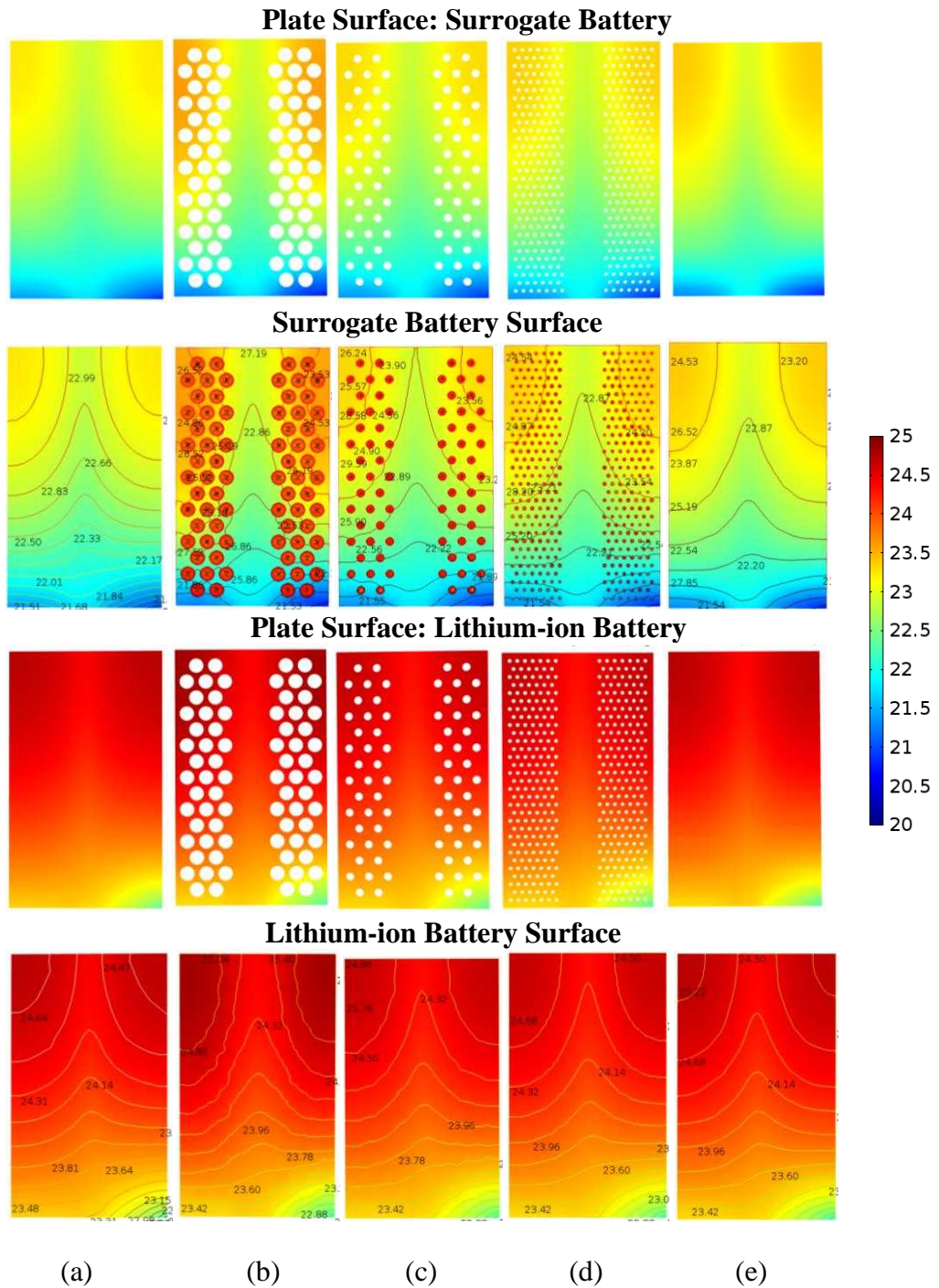


Figure 5.34: Surface temperature of plate and battery from (a) original; (b) I; (c) II; (d) III; (e) IV after 600 s ($T_{\text{amb}} = 20^{\circ}\text{C}$, $T_{\text{g-w}} = 20^{\circ}\text{C}$, $q_{\text{g-w}} = 2.38$ l/min, 2C battery discharge)

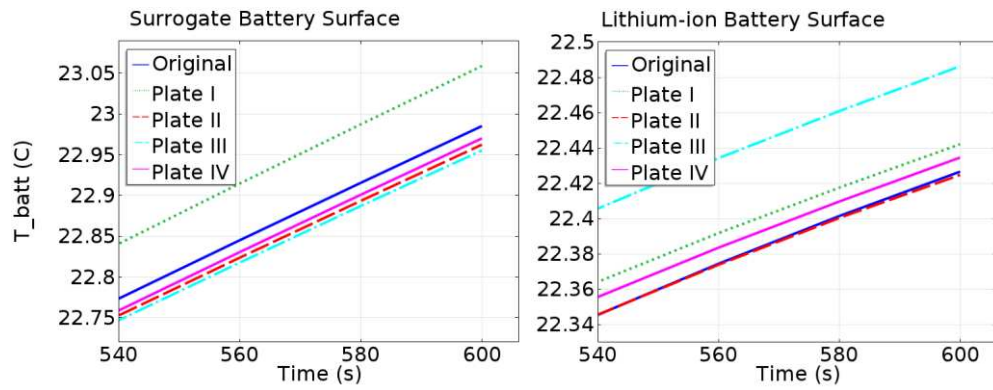


Figure 5.35: 600 s average surface temperature change of surrogate battery and lithium-ion battery with heat pipe cooling using different plates (original, plate I-IV) obtained from FEM ($T_{amb} = 20^{\circ}\text{C}$, $T_{g-w} = 20^{\circ}\text{C}$, $q_{g-w} = 2.38 \text{ l/min}$, 2C battery discharge).

5.5.2 Battery Preheating

5.5.2.1 Heat Pipe Durability Evaluation

The temperature distribution along the heat pipe was monitored so was the ambient temperature. Fig. 5.36 shows raw data collected from overnight freezing under -15°C and -25°C for 14 – 16 hours. By discharging pre-treated coolant to the evaporator, the sintered copper-water heat pipe was able to wake up immediately even after long hours of cold exposure without losing its full function. The reproducibility of such temperature behaviour was performed by repeating the same test under the exact condition for at least 8 times.

An interesting phenomenon was observed and is demonstrated by Fig. 5.37. When cooling the heat pipe down to a sub-zero temperature, the heat pipe behaved interestingly near the 0°C line. There are three phases and two transition points. For battery preheating, the section that immersed into the liquid box is called the evaporator, and the one in contact with the battery cell

surface is the condenser. The adjusting period occurred when all the monitored temperature points along the condenser were below 0°C (Transition 1). A sudden temperature increase was detected at the condenser, and an increase in temperature along the evaporator was resulted. A noticeable pressure drop between the evaporator and the condenser was then created under a small temperature gradient driving the heat transfer from the evaporator to the condenser immediately. The adjusting performance seemed nearly isothermal along the condenser at around 0°C for 50 s. However, with continuous cooling supply from the freezer, the temperatures long the heat pipe began to drop rapidly until the evaporator hit 0°C. A fairly slow temperature decrease was then observed until every monitored temperature point dropped below 0°C (Transition 2). Such phenomenon implied that the sintered copper-water heat pipe has lost its high thermal conductivity property due to the frozen state of the water inside the wicks, and may be treated as a normal hollow copper pipe with low conductivity. The temperature gradient along the heat pipe after the adjusting period was increased leading to deficient isothermality.

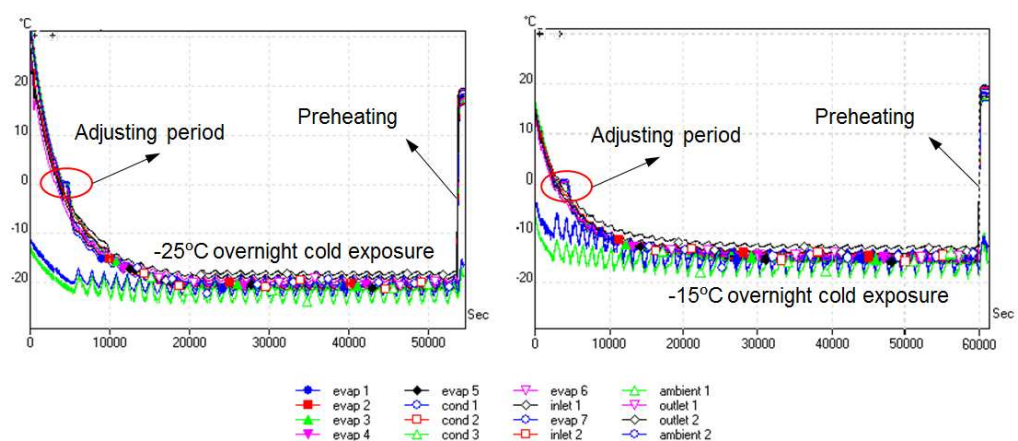


Figure 5.36: Overnight cold exposure under -25°C/-15°C and 20°C preheating afterwards (raw data collected from TC-08 data logger).

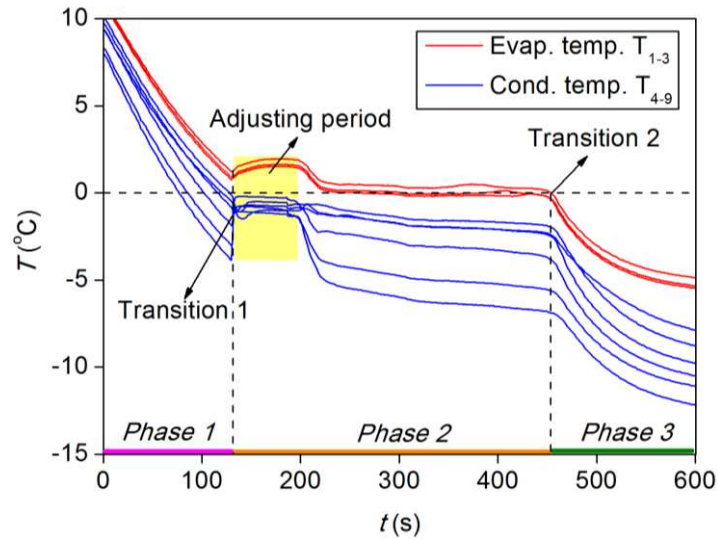
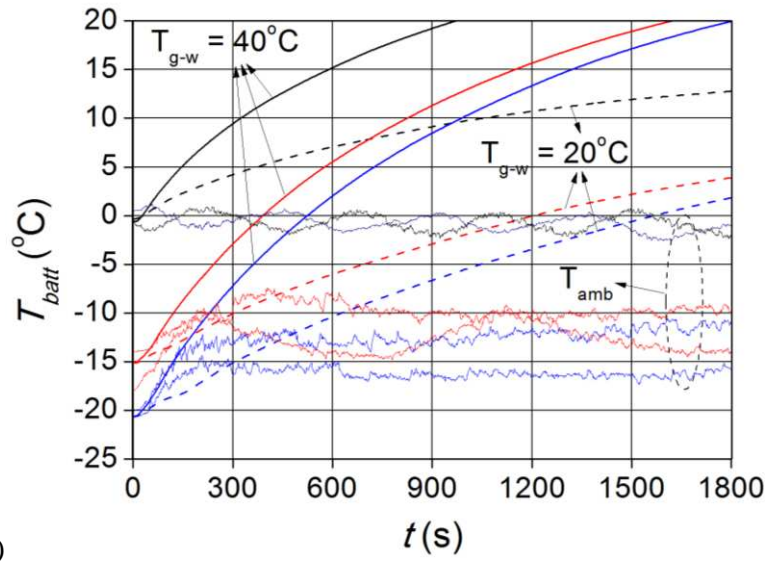


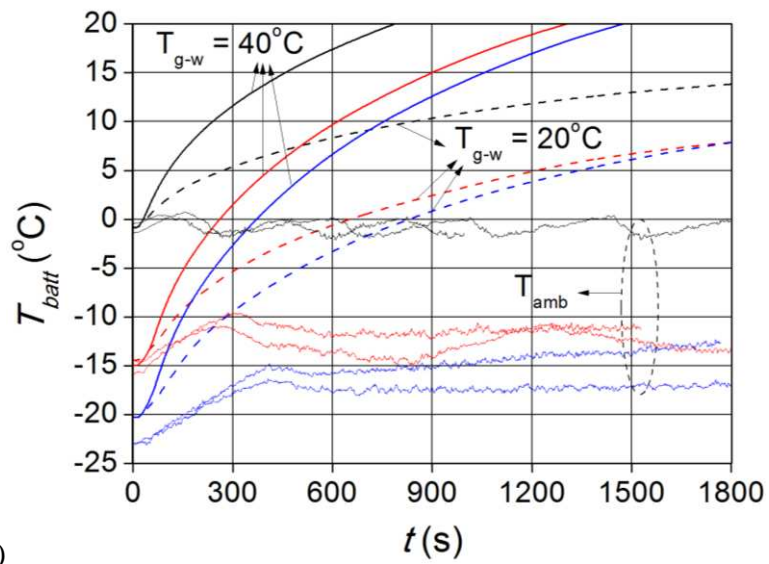
Figure 5.37: Heat pipe temperature change behaviour detected when exposing it under sub-zero temperatures.

5.5.2.2 Preheating Performance

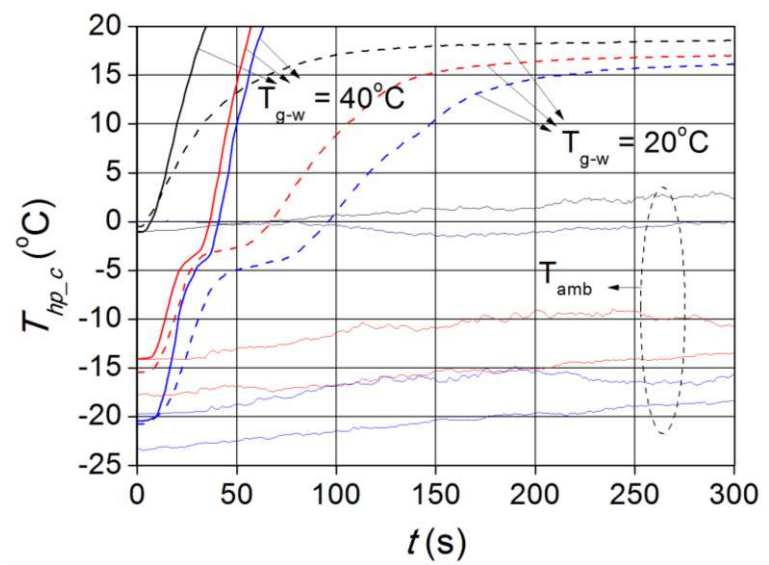
As mentioned earlier, the heat source was assumed to be available on-board, and the heat can be extracted through fluid heating from either an electric heater or a bioethanol heater and be transferred to each battery cell through heat pipes and aluminium plates. The heat pipe was operated under gravity-assisted condition, which means the evaporator was at the bottom. The inlet coolant temperature was set to be 20°C or 40°C at a discharge rate of 1.91 – 2.14 l/min.



(a)



(b)



(c)

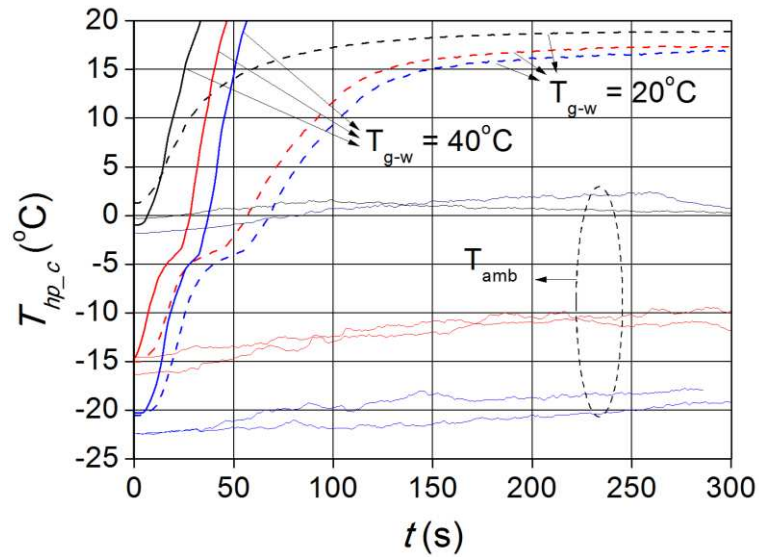


Figure 5.38: Preheating performance obtained from 20°C/40°C glycol-water coolant discharging at constant ambient temperature of 0°C, -15°C and -20°C: (a) average battery surface temperature rise w/o fins; (b) average battery surface temperature rise w. fins; (c) average heat pipe condenser temperature rise w/o fins; (d) average heat pipe condenser temperature rise w. fins.

The preheating performance was evaluated and summarised. The temperature increase of average battery surface temperature under heat pipe preheating and that of heat pipe alone was measured and compared. Adding fins to the heat pipe evaporator was also investigated. Fig. 5.38 demonstrates the average battery surface temperature increase and average heat pipe condenser temperature under 20°C and 40°C heating at a constant ambient environment of 0°C, -15°C and -20°C. Table 5.7 summarises the time consumption within 0.5 hours of heating. Adding fins at the heat pipe evaporator greatly improves the battery heating performance, which reduced the heating time by 216 – 731 s and 82 – 325 s via 20°C and 40°C heating respectively. The degree of heat transfer enhancement by fins was augmented

at low heating temperatures. 211.05 s, 548.29 s and 738.91 s were saved when preheating the battery using fins from 0°C to 10°C, and from -15°C and -20°C to 0 °C under 20°C. Higher temperature such as 40°C shortened the heating time to almost 1/3 or 1/4 (if fins were added) of that resulted from 20°C, but the fin effect seemed to be slightly weak reducing the time consumption to be less than 324.50 s. Still, 20°C preheating even with fins is less preferred due to the fact that it was unable to heat up the battery from -15°C or -20°C to 10°C within 30 minutes. To warm up the battery from 0°C, -15°C or -20°C to 10°C under 40°C preheating condition, a reasonable amount of heating time (320.64 s, 823.02 s, and 985.08 s respectively) were consumed. If the fins were available, the time could be further reduced to 238.45 s, 614.28 s and 748.17 s respectively.

Notably, the heat transfer performance of heat pipe alone was characterised and the obtained results were used to compare with the data collected from heat pipe battery heating. Highly performed heat transfer and quick thermal response were achieved by the heat pipe alone, which took 32.86 – 147.5 s from 0°C, -15°C or -20°C to 10°C under 20°C preheating, and 19.55 – 50 s under 40°C. Adding fins reduced the heating time by 5 – 60 s under 20°C, and by approximately 0 – 10 s under 40°C.

Table 5.7: Heating time consumption within 0.5 hours of heating

Preheating Condition		20°C		40°C	
Battery Cell					
$T_{batt,o}$ (°C)	$T_{batt,i}$ (°C)	t (s) w/o fins	t (s) w. fins	t (s) w/o fins	t (s) w. fins
0	10	1046.81	835.76	320.64	238.45
	15	/	/	586.11	454.53
	20	/	/	966.94	784.44
-15	0	1198.84	650.55	387.78	258.91
	10	/	/	823.02	614.28
	15	/	/	1152.54	897.49
	20	/	/	1620.96	1304.18
-20	0	1561.93	823.02	524.37	372.35
	10	/	/	985.08	748.17
	15	/	/	1317.30	1054.53
	20	/	/	1796.14	1471.64
Heat Pipe					
$T_{hp,c,o}$ (°C)	$T_{hp,c,i}$ (°C)	t (s) w/o fins	t (s) w. fins	t (s) w/o fins	t (s) w. fins
0	10	32.86	27.72	19.55	19.55
	15	65.92	58.59	26.88	25.14
	20	/	/	34.15	33.31
-15	0	67.20	56.91	35.88	28.17
	10	104.95	92.54	45.34	35.88
	15	143.60	126.43	50.87	40.13
	20	/	/	56.91	46.62
-20	0	95.50	68.04	40.58	37.55
	10	147.50	102.83	50.00	44.89
	15	210.55	150.00	55.63	50.48
	20	/	/	62.89	56.46

5.6 Data Repeatability & Reproducibility

The repeatability and reproducibility (R&R) study, also known as the gauge capability study, is to provide the closeness of agreement between replicate measurements on the same tests. Repeatability defines the variability occurred in gauge itself and was obtained under the same operator, laboratory location and time. Reproducibility represents the variability due to different operators/apparatus/locations/times performing on the same task. Due to the nature of the experiment, the estimates of the repeatability and reproducibility can be perceived by comparing plots under several test conditions replicated by Operator A within the same and different periods of time.

Fig. 5.39 – 5.40 show the repeatability of system cooling and preheating conducted by Operator A over a short timescale. Little deviations between the first and second test were seen, which reflects data consistency. Fig. 5.41 – 5.42 indicate the reproducibility performed by Operator A before and after 3 months period. The data collected after 3 months varied within 5°C margin, which is acceptable since system has been tested under extreme worst conditions for quite a long time.

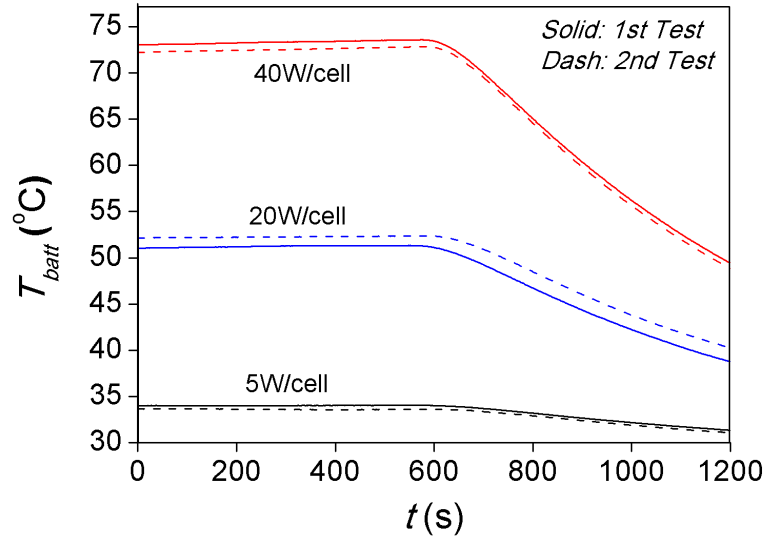


Figure 5.39: Repeatability evaluation of cooling performance conducted by Operator A within a short timescale.

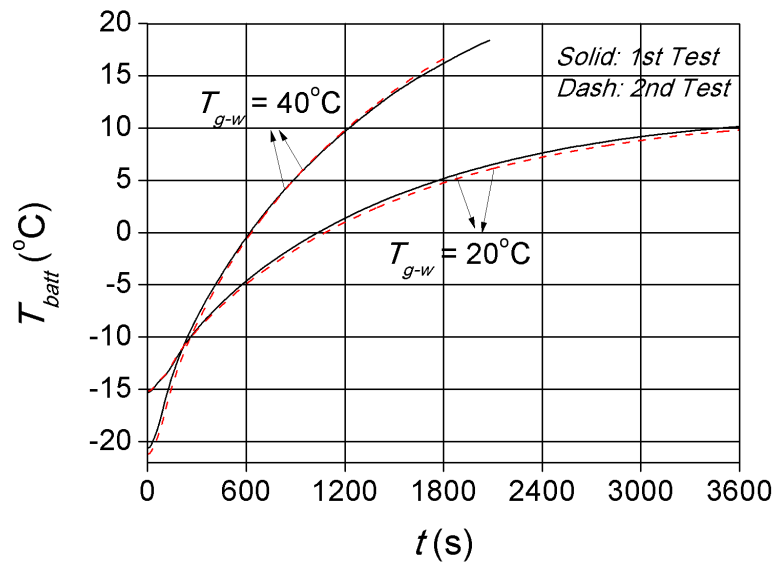


Figure 5.40: Repeatability evaluation of preheating performance conducted by Operator A within a short timescale.

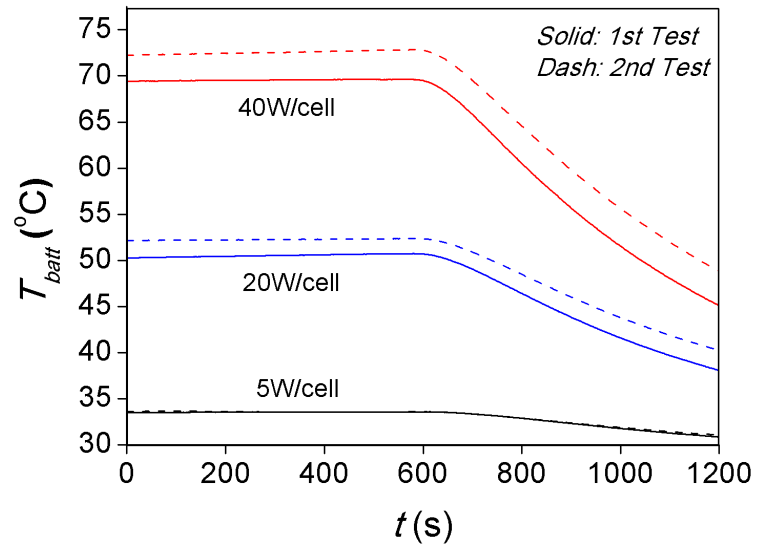


Figure 5.41: Reproducibility evaluation of cooling performance conducted by Operator A over two time periods (3 months interval).

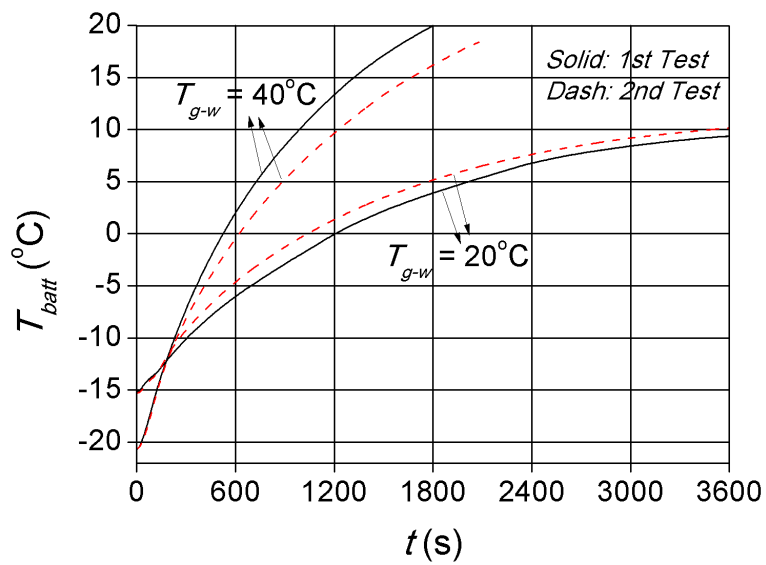


Figure 5.42: Reproducibility evaluation of preheating performance conducted by Operator A over two time periods (3 months interval).

5.7 Data Reductions and Measurement Uncertainties

The thermal conductivity of the heat pipe and that of the heat pipe and the aluminium plate, the thermal conductivity of the heat pipe, and the heat transfer coefficient at the condenser/cooling end can be formulated using Eq. 5.3 – 5.5.

$$R_{hp} = \frac{T_e - T_c}{Q_{out}} \quad R_t = \frac{T_{batt} - T_c}{Q_{out}} \quad (5.3)$$

$$k_{hp} = \frac{4l_{eff}}{R_{hp}\pi d_o^2} \quad (5.4)$$

$$h_c = \frac{Q_{out}}{\pi d_o l_c (T_c - T_f)} \quad (5.5)$$

where

$$T_e - \text{temperature of the evaporator, } T_e = \frac{\sum_{i=1}^7 T_i}{7}$$

$$T_c - \text{temperature of the condenser, } T_c = \frac{\sum_{i=8}^{10} T_i}{3}$$

$$T_{batt} - \text{average temperature of the battery surface, } T_{batt} = \frac{\sum_{i=1}^7 T_{bi}}{7}$$

$$T_f - \text{temperature of the cooling fluid in the liquid box, } T_f = \frac{T_{in} + T_{out}}{2}$$

$$l_{eff} - \text{heat pipe effective length, } l_{eff} = \frac{l_e + l_c}{2} + l_a$$

As mentioned earlier, all thermocouples were calibrated using a portable digital thermometer (RS Portable Digital Thermometer), which is accurate to $\pm 0.2\% \text{ rdg} + 1^\circ\text{C}$ at $-50 - 199.9^\circ\text{C}$. The obtained **average** (maximum) accuracy

of the thermocouples after calibration was $\pm\mathbf{1.80\%}$ ($\pm 6.74\%$) or $\pm\mathbf{0.59^\circ\text{C}}$ ($\pm 1.90^\circ\text{C}$). The TTI precision DC bench power supply (EX354RD) was provided where input voltage (0–35V) can be adjusted accordingly to incrementally adjust the battery power input from 10 W to 35 W. The **average** (maximum) heat flux Q_{out} differed by $\pm\mathbf{4.54\%}$ ($\pm 14.75\%$) from the heat input Q_{in} obtained from the electrical power device. The flow rate was measured from Parker inline flow transmitter and read from DT500 dataTaker. The uncertainty of the flow measurement was $\pm 2.1\%$.

The uncertainty estimates are performed below (Eq. 5.6-5.9) using a standard approach [232]. The **average** (maximum) uncertainties for U_{Rhp} , U_{Rt} , U_{khp} , U_{hc} were $\pm\mathbf{2.76\%}$ ($\pm 12.72\%$), $\pm\mathbf{3.25\%}$ ($\pm 16.67\%$), $\pm\mathbf{2.76\%}$ ($\pm 11.74\%$), $\pm\mathbf{2.33\%}$ ($\pm 11.45\%$) respectively. Individual uncertainties for each test can be found in Table C.1 – C.4, Appendix C.

(Note: the percentage value in **bold** indicates the **average** uncertainty and that in (bracket) refers to the maximum uncertainty.)

$$U_{\text{Rhp}}^2 = U_{\text{Tc}}^2 \left(\frac{1}{Q_{\text{out}}} \right)^2 + U_{\text{Tc}}^2 \left(\frac{1}{Q_{\text{out}}} \right)^2 + U_{\text{Oout}}^2 \left(\frac{T_e - T_c}{Q_{\text{out}}^2} \right)^2 \quad (5.6)$$

$$U_{\text{Rt}}^2 = U_{\text{Tbatt}}^2 \left(\frac{1}{Q_{\text{out}}} \right)^2 + U_{\text{Tc}}^2 \left(\frac{1}{Q_{\text{out}}} \right)^2 + U_{\text{Qout}}^2 \left(\frac{T_{\text{batt}} - T_c}{Q_{\text{out}}^2} \right)^2 \quad (5.7)$$

$$U_{\text{khp}}^2 = U_{\text{Rhp}}^2 \left(\frac{1}{R_{\text{hp}}^2} \right)^2 \quad (5.8)$$

$$U_{\text{hc}}^2 = U_{\text{Qout}}^2 \left(\frac{1}{T_c - T_f} \right)^2 + U_{\text{Tc}}^2 \left(\frac{Q_{\text{out}}}{(T_c - T_f)^2} \right)^2 + U_{\text{Tf}}^2 \left(\frac{Q_{\text{out}}}{(T_c - T_f)^2} \right)^2 \quad (5.9)$$

For heat pipe with fins, Eq. 5.10 – 5.12 can be used to determine the heat pipe thermal resistance, thermal conductivity and heat transfer coefficient at cooling end.

$$R_{hp,wf} = \frac{T_e - T_{fin}}{Q_{out,wf}} \quad (5.10)$$

$$k_{hp,wf} = \frac{4l_{eff}}{R_{hp,wf} \pi d_o^2} \quad (5.11)$$

$$h_{c,wf} = \frac{Q_{out,wf}}{\left[\pi d_o l_c + 20\pi (r_f^2 - r_o^2) \right] (T_{c,fin} - T_f)} \quad (5.12)$$

where

$T_{c,fin}$ – temperature of the condenser (heat pipe with fins),

$$T_{c,fin} = \frac{T_{f8} + T_{f10}}{2}$$

T_{fin} - temperature of the fin stack, $T_{fin} = T_{f9}$

The **average** (maximum) heat flux Q_{out} differed from the heat input Q_{in} obtained from the electrical power device by **$\pm 4.02\%$** ($\pm 10.01\%$) under heat pipe with fins condition. The average (and maximum) uncertainties for $U_{R_{hp,wf}}$, $U_{k_{hp,wf}}$, $U_{h_{c,wf}}$ (Eq. 5.13 – 5.15) were **$\pm 3.03\%$** ($\pm 11.28\%$), **$\pm 2.98\%$** ($\pm 10.42\%$) and **$\pm 5.62\%$** ($\pm 18.56\%$) respectively. Results were summarised in Table C.5 – C.8, Appendix C.

(Note: the percentage value in **bold** indicates the **average** uncertainty and that in (bracket) refers to the maximum uncertainty.)

$$U_{R_{hp,wf}}^2 = U_{T_e}^2 \left(\frac{1}{Q_{out,wf}} \right)^2 + U_{T_{fin}}^2 \left(\frac{1}{Q_{out,wf}} \right)^2 + U_{Q_{out,wf}}^2 \left(\frac{T_e - T_{fin}}{Q_{out,wf}^2} \right)^2 \quad (5.13)$$

$$U_{k_{hp},wf}^2 = U_{R_{hp},wf}^2 \left(\frac{1}{R_{hp},wf} \right)^2 \quad (5.14)$$

$$U_{h_c, wf}^2 = U_{Q_{out}, wf}^2 \left(\frac{1}{T_{c, fin} - T_f} \right)^2 + U_{T_{c, fin}}^2 \left(\frac{Q_{out}, wf}{(T_{c, fin} - T_f)^2} \right)^2 + U_{T_f}^2 \left(\frac{Q_{out}, wf}{(T_{c, fin} - T_f)^2} \right)^2 \quad (5.15)$$

5.8 Summary

This chapter provides a full experimental characterisation based on a 2-cell test rig. With the provision of two surrogate battery cells, a wide range of battery ‘off-normal’ thermal conditions can be simulated facilitating the evaluation of the heat pipe cooling and preheating system.

A conceptual prototype for experiment that contains two surrogate battery cells was introduced. The eligibility of substituting atonal 324 for lithium-ion battery electrolytes has been assessed. The surrogate battery achieved similar temperature results under low power inputs and was more prone to temperature change. This facilitates the extension of applying the proposed thermal management method to a wider range of battery operating conditions implying that the cooling/heating solution is not limited to a certain type of batteries, but suitable for various batteries with a broader range of cooling/heating needs.

The cooling evaluation was performed mainly through: 1) creating steady state battery operating environment to assess the performance of the proposed cooling system; 2) simulating aggressive battery charging/discharge scenarios to evaluate the transient behaviour of the cooling system; 3) analysing the effect of adding fins to the heat pipe condenser to improve heat transfer; and 4)

comparing cooling effectiveness resulted from perforated plates with aim of reducing system weight.

Results show that the proposed method is able to keep the battery surface temperature below 40°C if the battery generates less than 10 W/cell, and helps reduce the battery temperature down to 70°C under uncommon thermal abuse conditions (e.g. 20 – 40 W/cell). Adding annular fins (optimised fin height of $r_f/r_0 = 2$ at fixed fin thickness and fin pitch) to the heat pipe condenser during cooling improves heat transfer but doubles the overall thermal resistance from 0.44 K/W (w/o. fins) to 0.69 – 0.75 K/W (w. fins). Fin also helps maintain the heat transfer coefficient at the cooling end at 2,800 W/m²K and the overall heat transfer was significantly enhanced under power input of 20 – 50 W, 10°C cooling. The fin efficiencies derived from experiment ranged from approximately 58% to 70% with ±15% discrepancy at maximum. Improved cooling effect achieved by fins has also been observed under heat pipe transient cooling, as well as higher velocity fields visualised from FEA modelling.

In addition, it is difficult to conclude the effect of plate perforation. Factors such as hole size, direction and distribution, the range of power inputs, and thermal conductivities of the battery cells are mutually dependent. For surrogate battery, due to low thermal conductivities of all directions, plate perforation seems to be less efficient and less favourable to the overall heat transfer. For lithium-ion battery, plate perforation has little impact under low heat dissipation rate as heat comes from the battery can be quickly distributed through length and height. The effect of perforation becomes beneficial during high power inputs.

Furthermore, the feasibility of using sintered copper-water heat pipes under sub-zero temperatures has been assessed experimentally by exposing the test rig to $-15^{\circ}\text{C}/-20^{\circ}\text{C}$ for more than 14 hours. Data indicates that the heat pipe was able to function immediately after long hours of cold exposure and that sub-zero temperature conditions had little impact on heat pipe performance. A table of heating time consumption under 20°C and 40°C preheating was provided. Results show that high heating temperature and fins both can benefit the heat transfer performance.

Chapter 6

Application to Battery Thermal

Management for Electric Vehicles

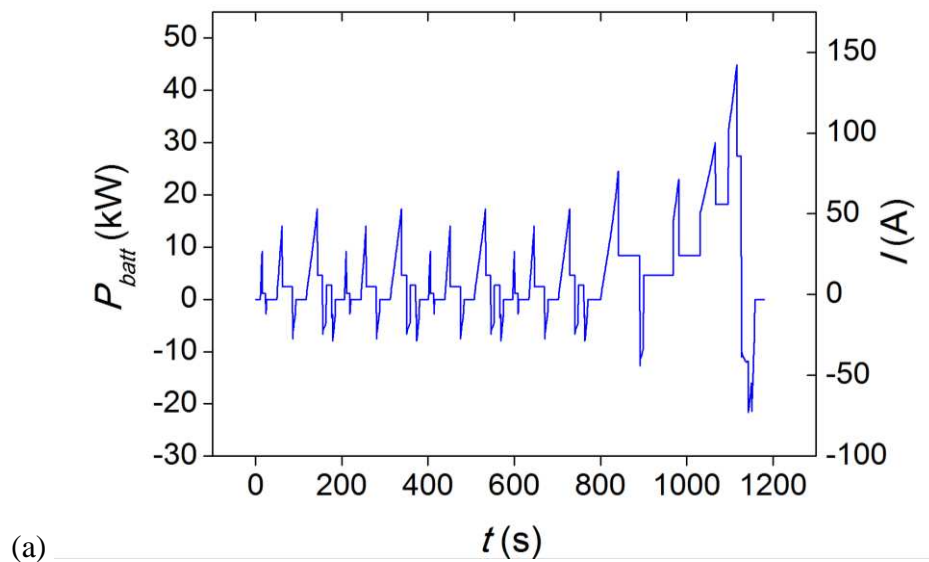
6.1 A 30-Lithium-ion-Cell Battery Pack using Heat Pipe Thermal Management

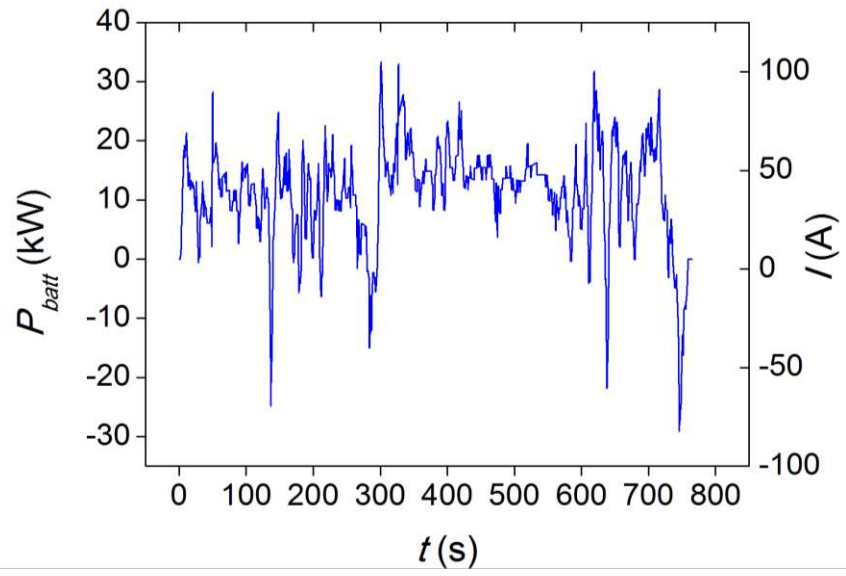
The application to battery thermal management at pack level can be evaluated based on a scale-up model, which contains 30 lithium-ion battery cells as illustrated in Chapter 4, Fig. 4.2. This model simulates the temperature profile in 30 cells and heat pipes in connection with a glycol-water coolant channel. The study aims to accelerate the development of actual solution and reduce the necessity of large-scale experimental prototype building. The average heat source in the lithium-ion battery cell will be calculated using either a combination of experiment data and Eq. 3.18 – 3.19 derived from Sato [97] or a full 1D electrochemical model.

6.1.1 Battery Cell Model

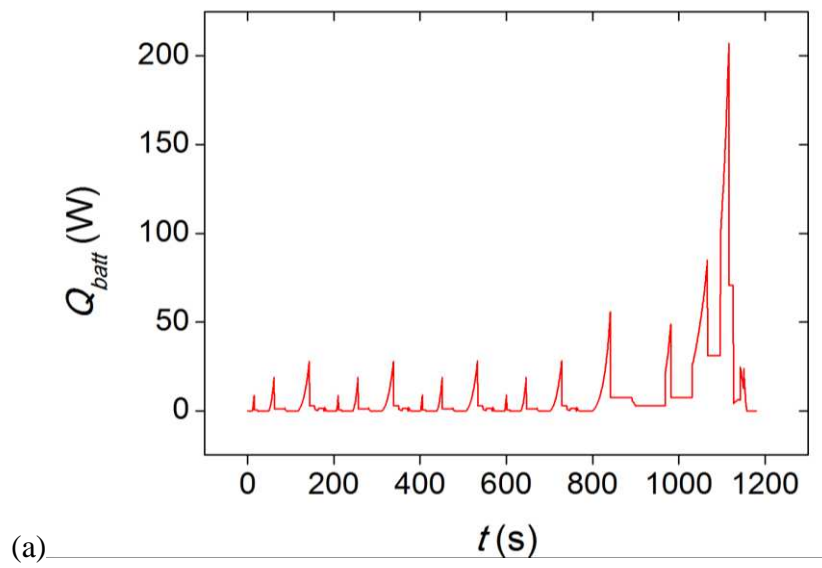
6.1.1.1 Decoupled

Two EV driving cycles are provided by FAW (Fig. 6.1). These experimental data will be used to calculate corresponding dynamic battery heat generation via Eq. 3.18 – 3.19 and to report system transient thermal response. Cycle 1 or 2 will be repeated for 4 – 6 times continuously. The heat pipe method is compared with air cooling. A convective heat transfer coefficient of $h_{\text{air}} = 10.1 \text{ W/m}^2\text{K}$ suggested by Smith and Wang [194] and forced air convection $h_{\text{air}} = 40 \text{ W/m}^2\text{K}$ [233] (low to moderate air speed, 0.7 m/s) are used on the exterior surfaces. The ambient environment and initial module temperature are assumed to be 35°C. The cooling medium temperature is 20°C. Fig. 6.2 calculates the battery cell heat generation obtained from these two cycles.





(b) Figure 6.1: EV driving cycles provided by FAW: (a) Cycle 1; (b) Cycle 2.



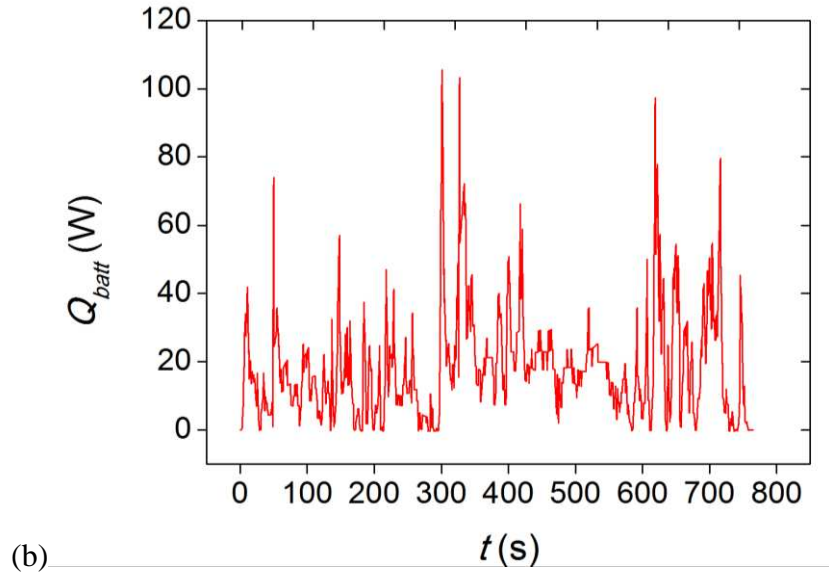


Figure 6.2: Single battery cell heat generation obtained from: (a) Cycle 1; (b) Cycle 2.

6.1.1.2 Coupled

The cell model is created using the lithium-ion battery interface illustrated in Chapter 4, Fig. 4.6. The temperature is set to the mean temperature in the active battery material of the thermal model through an integration component coupling. A square wave function is used to determine the alternating charge-discharge current at a maximum continuous rate of 4C with a cycle time of 600 s followed by a relaxing period after 1500 s (Fig. 6.3). To note, 1C corresponds to the charge/discharge current required for a fully charge or discharge in an hour, and 4C represents a 4 times higher current, which results in a full charge/discharge in 1/4 of an hour, i.e. 15 minutes. Fig. 6.4 gives the total heat dissipation Q_h (W/m^3) obtained from negative electrode, positive electrode, separator, and all domains at selected times ($t = 0$ s, 299.95 s, 300 s, 599.95 s, 600 s, 899.95 s, 900 s, 1199.95 s, 1200 s, 1499.95 s, 1500 s, 2100 s).

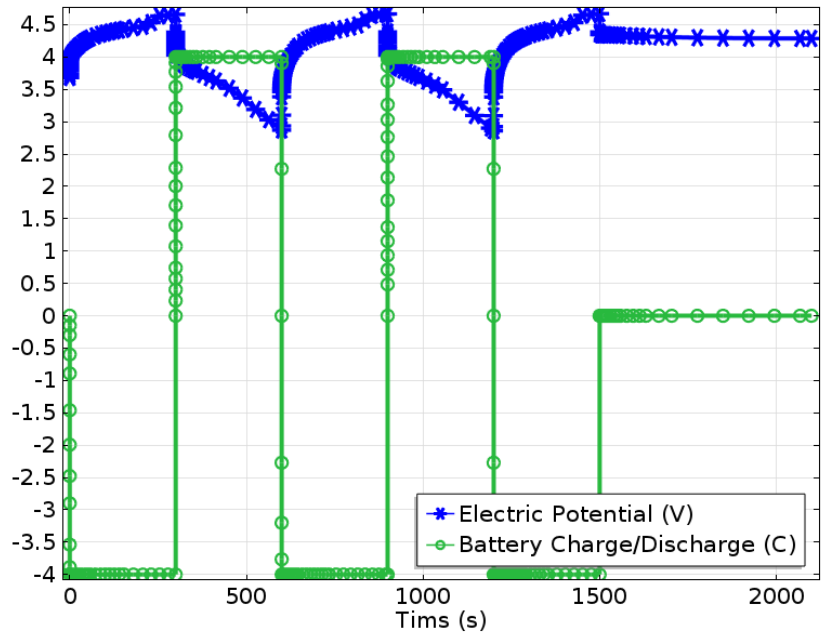


Figure 6.3: Cell potential and current load from an alternating 4C charge-discharge cycle obtained from 1D electrochemical model.

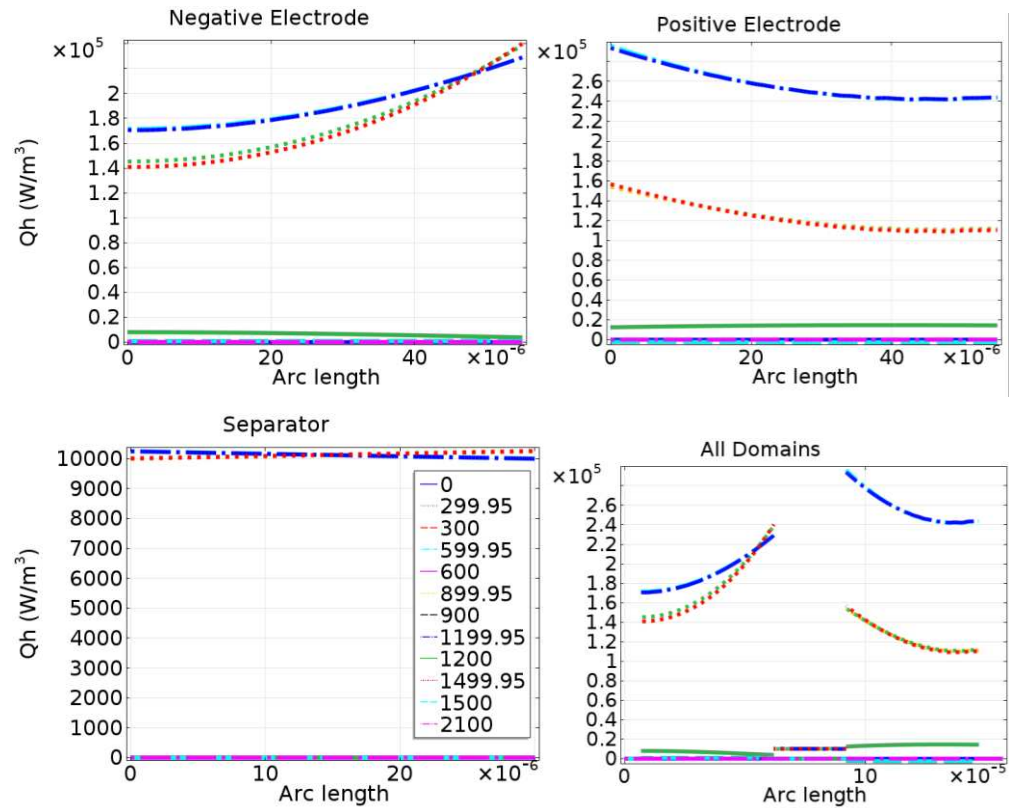


Figure 6.4: Total heat dissipation Q_h (W/m^3) of negative electrode, positive electrode, separator, and all domains at selected times ($t = 0$ s, 299.95 s, 300 s, 599.95 s, 600 s, 899.95 s, 900 s, 1199.95 s, 1200 s, 1499.95 s, 1500 s, 2100 s).

6.1.2 Flow and Heat Transfer Model

The type of fluid flow considered here is incompressible laminar flow. The energy equation can be solved to model conjugate heat transfer problems including conduction, convection and surface-to-surface radiation. The emissivity values of the materials used in the model were taken from [234].

6.1.2.1 Geometry and Mesh

A simplified assembly version of Fig. 4.2 without detailed casing structures was created by SolidWorks and imported to COMSOL 4.3b (Fig. 6.5). Virtual operations such as form composite faces and mesh control faces were used for a better quality mesh. The maximum and minimum element size for general physics is 0.051 m and 0.00918 m respectively. The element size for fluid dynamics boundaries is 0.00885 m maximum and 0.00167 m minimum. The mesh statistics in Fig. 6.7 shows that a total number of elements 1,081,070 were created with 984,430 tetrahedral elements and an average element quality of 0.64.

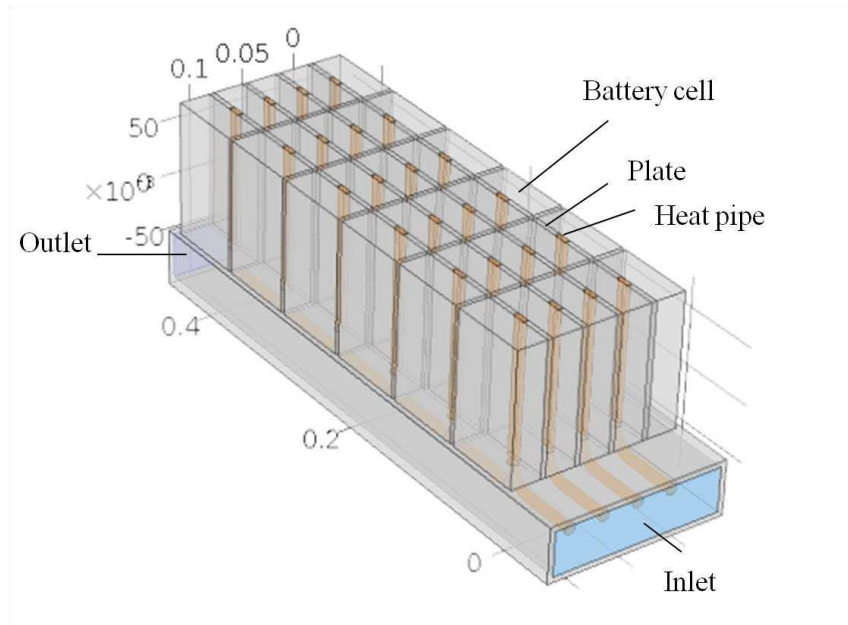


Figure 6.5: A 30-cell battery pack using heat pipe thermal management built in COMSOL 4.3b.

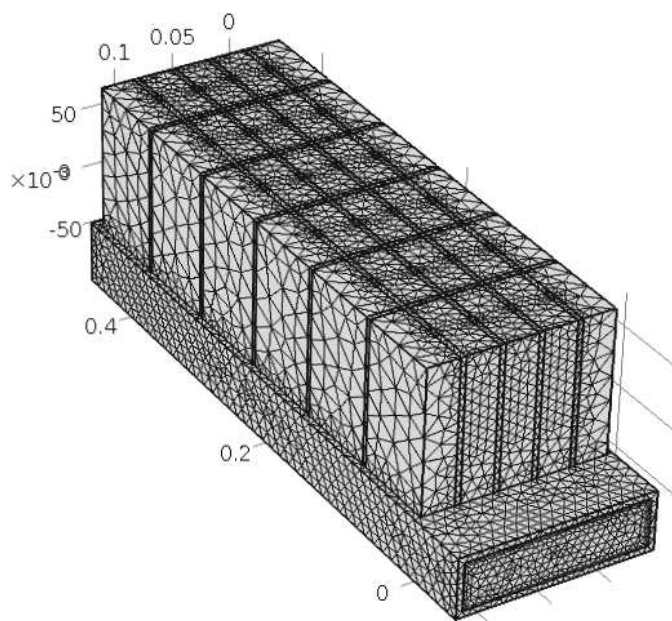


Figure 6.6: Meshing (normal mesh size).

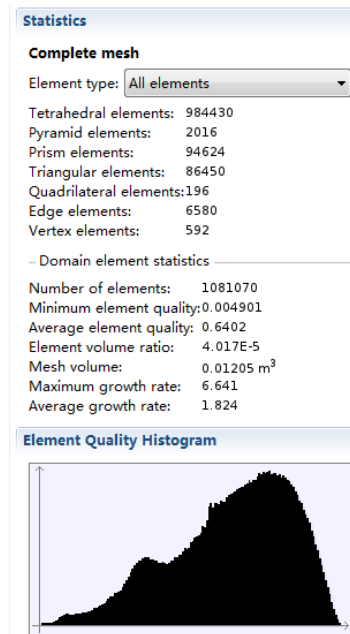


Figure 6.7: Mesh statistics using normal mesh settings.

6.1.2.2 Domain Settings and Boundary Conditions

The flow compartment is a coolant box filled with glycol-water mixture. The fluid properties are calculated using the inlet temperature as input. The flow enters from one side to another passing through heat pipe condensers in a counter direction for a much more effective heat transfer. An average flow rate of $5.95 \times 10^{-4} \text{ m}^3/\text{s}$ (i.e. 0.595 l/s or 0.059 kg/s) is assumed accounting for a steady state temperature difference of 0.5°C between inlet and outlet at a maximum heat generation of 41.27 W/cell for 30 cells ($Re = 1,790$, fully developed laminar flow). This value is also in proportion with the experimental value used for 2 cells. A tenth of this flow rate value (0.0595 l/s) is applied in comparison with the results achieved from high flow rate. The normal inflow velocity will then be given to the inlet, which equals to the flow rate divided by the cross-sectional area of the inlet. For the outlet, 0 Pa is applied. All other boundaries are set to no-slip conditions.

The temperature field is solved for the coolant flow compartment, the heat pipes, the plates, and the batteries. The materials, densities, and heat capacities in those domains are set up in the same way as depicted in Chapter 4. The inlet temperature is 20°C. An outflow condition is specified at the outlet and symmetry conditions are applied when necessary. A convective heat flux is applied to all other boundaries with a heat transfer coefficient of 4 W/m²K at an ambient temperature of 35°C. This accounts for some heat being lost to the surroundings.

6.1.3 Solver Sequence

The model will be solved sequentially in three studies, one study for each physics interface. Two assumptions are made with regard to study analysis: (1) the material properties of the cooling fluid and battery materials are calculated based on an average temperature of the battery pack; (2) the variations in heat generation during the charge-discharge load cycle is slower than the heat transport within the battery pack. This implies that the thermal balance can be considered as quasi-stationary for the given battery heat source and at a given time during the load cycle.

The laminar flow interface will be solved first, assuming a uniform temperature (the inlet temperature) and the properties of the glycol-water mixture in the coolant channel being constant. The average heat source generated from the batteries can be sorted using the second study, which defines a time-dependent study solving the 1D battery model. The simulation starts from the initial condition to a set time within the predefined charge-

discharge cycle (Fig. 6.3). Then, the quasi-stationary temperature of the battery pack at that specified time can be solved in a stationary study step, which will be the third study, coupling the flow velocity from the first study and the average heat source from the last step of the time-dependent simulation in the second study.

The third study can also be made into a time-dependent step that combines battery model and flow and heat transfer model to report temperature change throughout the entire charge-discharge cycle in Fig. 6.2 and Fig. 6.3. To note, in order to improve the convergence of the time-dependent solver and accelerate computing time, only two cut sections (see Chapter 6.2.2) from the battery pack will be performed.

6.2 Battery Cooling (Single Cell, Time Dependent)

6.2.1 Decoupled

Results shown in Fig. 6.8 (a) report that heat pipes kept battery surface temperature almost constant after the second cycle, and after the fourth cycle in Fig. 6.8 (b). The peak temperature was below 36°C and 46°C at all times under four continuous Cycle 1 and six continuous Cycle 2 respectively. Unlike air cooling, which was unable to maintain the battery surface temperature under a safety limit of 70°C after the third cycle, the combination of heat pipes with liquid cooling performs well in dissipating unwanted heat from the battery cells. Higher convective heat transfer coefficient in air cooling may be useful after repeating the second cycle, but air cooling retains ineffective under

aggressive driving scenarios and a higher risk of thermal runaway is very likely to be expected.

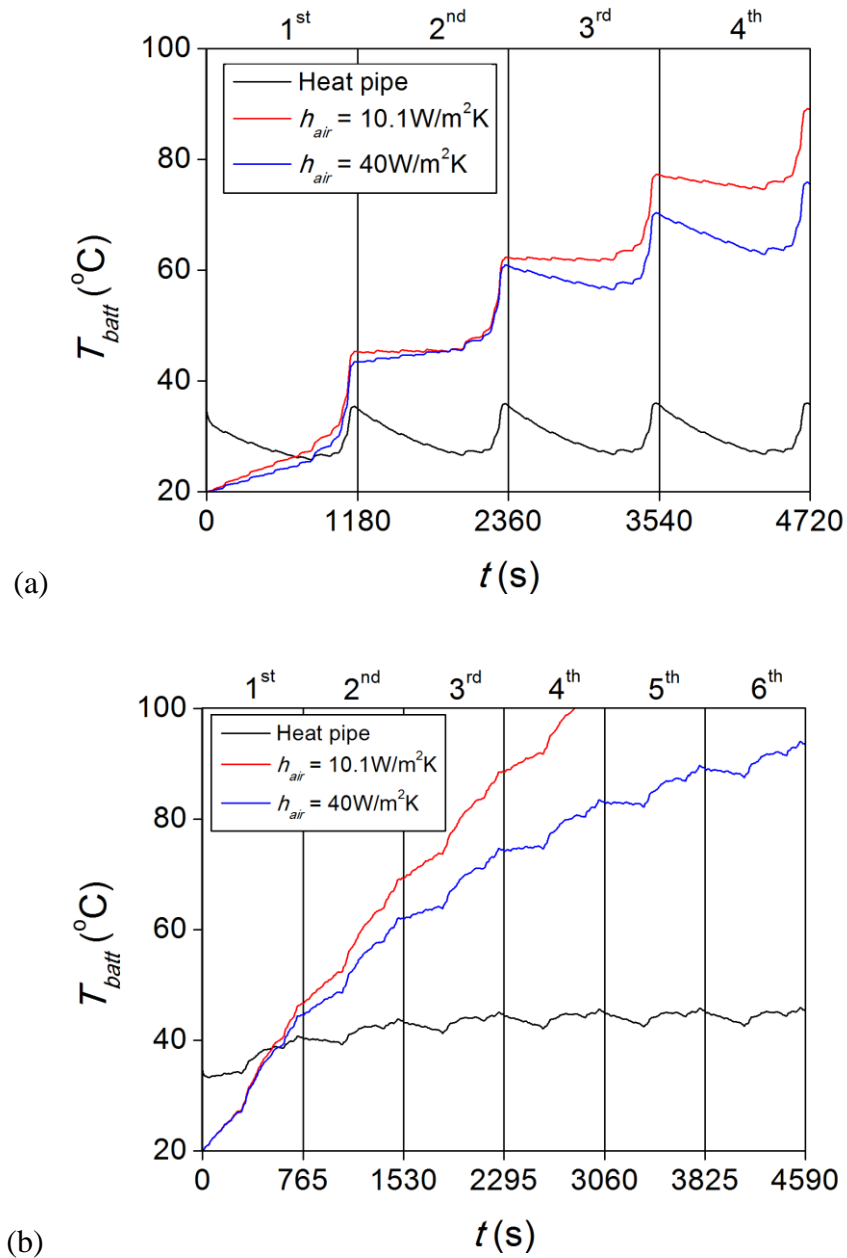


Figure 6.8: BTM comparative analysis between using heat pipe and using air convection under: (a) Cycle 1 – repeated 4 times; (b) Cycle 2 – repeated 6 times ($T_{amb} = 35^\circ\text{C}$, $T_{air} = T_{inlet} = 20^\circ\text{C}$, $v_{air} = v_{g-w} = 0.75 \text{ m/s}$).

6.2.2 Coupled

A fully coupled model for 30 cells using a time-dependent solver can be computationally costly. In order to reduce the computing time and improve convergence, sections from the battery pack are selected. Fig. 6.9 shows two sections cut from the pack. Section A contains one battery cell cooled from both sides while Section B sits at the edge of the pack with only one side cooled by the heat pipe. Symmetrical planes indicated in Fig. 6.9 are applied to both sections.

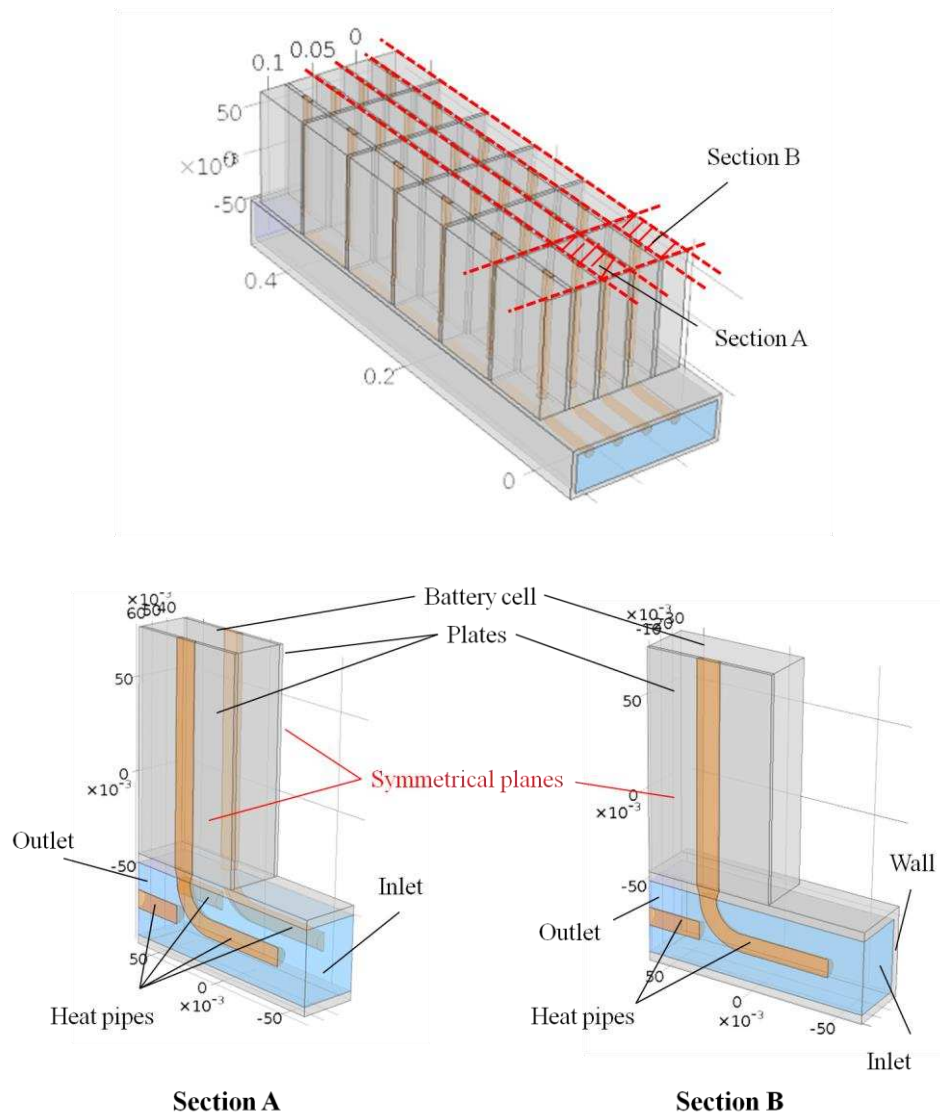


Figure 6.9: Sections cut from the battery pack for model demonstration.

Fig. 6.10 and Fig. 6.11 demonstrate the temperature and velocity profile for Section A and B at $t = 300$ s, 600 s, 900 s, 1200 s, 1500 s, and 2100 s at an initial temperature of 35°C under two flow rates, 0.0595 l/s and 0.595 l/s. The velocities range from $0 - 0.06$ m/s and $0 - 0.6$ m/s respectively. Fig. 6.12 shows the maximum and average temperature change of the battery during a transient simulation. The difference in heating rate between charge and discharge is because the entropy change for the charge and discharge reaction is different.

High liquid rate cools down the battery cell drastically, maintaining the average temperature change below 8°C with respect to inlet temperature of 20°C throughout the entire cycle. The maximum temperature, which occurs mostly on the top of the battery cell, undergoes huge temperature swings showing a maximum of 26°C difference at 1200 s (i.e. the end of the second discharge) for Section B ($T_{\text{batt, max}} = 46^{\circ}\text{C}$), and 15°C for Section A ($T_{\text{batt, max}} = 35^{\circ}\text{C}$). After 1500 s (the end of the third charge), the maximum battery temperature can be effectively reduced by $12 - 14^{\circ}\text{C}$ during the 600 s relaxing time; and the average battery temperature, by $4 - 6^{\circ}\text{C}$. For results obtained from low liquid flow rate, i.e. 0.0595 l/s, the average (maximum) temperature difference is 4°C (6°C) higher for Section A, and 2°C (3°C) higher for Section B. In addition, pressure and velocity distribution across the liquid box are displayed under two flow rates for two sections cut from the battery pack in Fig. 6.13 – 6.16. The velocities change by $\times 10$, while pressure difference results in $\times 10^2$ from inlet and outlet. The resultant pressure change is 270 Pa for 0.595 l/s case.

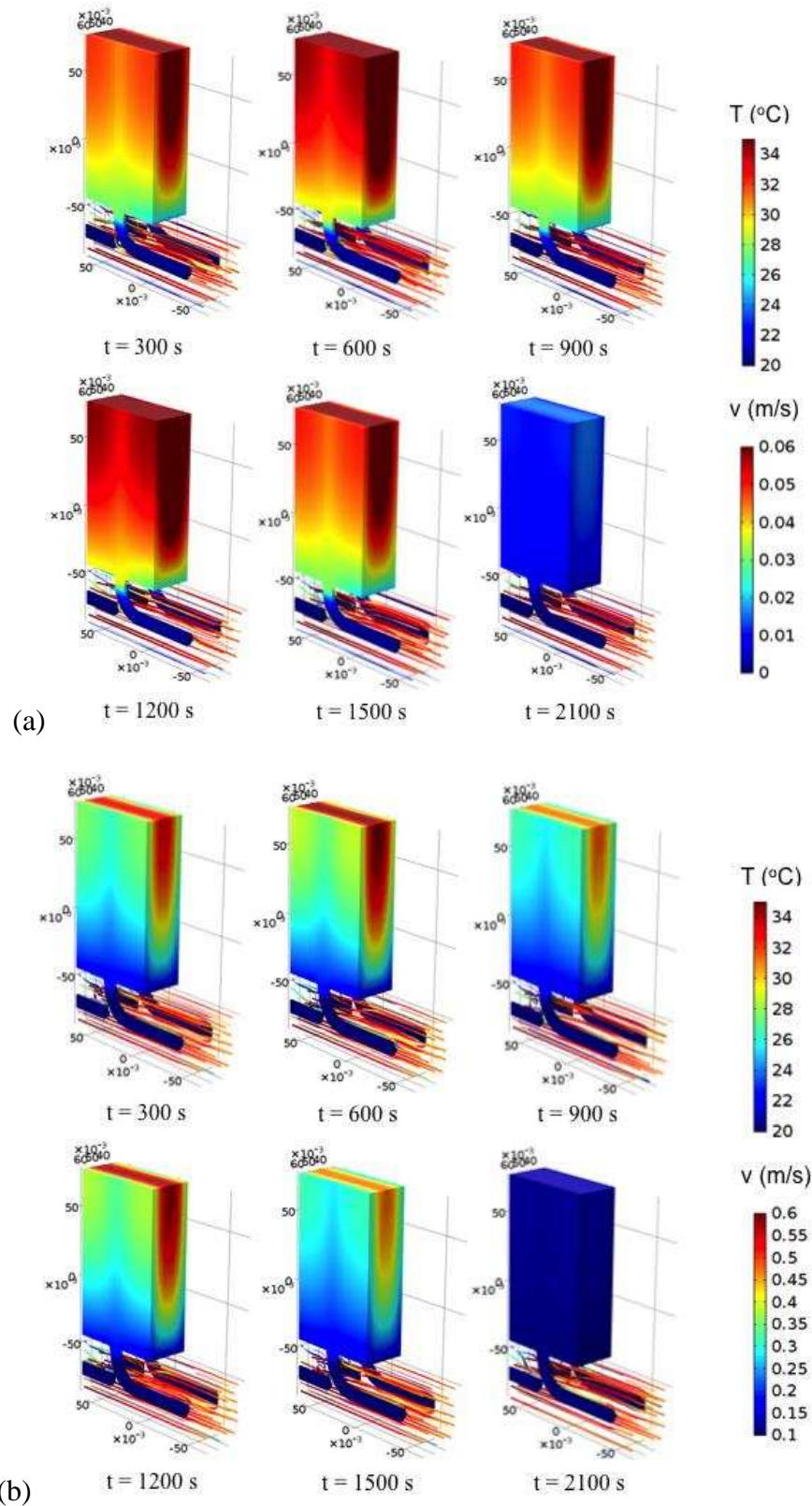


Figure 6.10: Temperature and velocity profile of Section A at $t = 300$ s, 600 s, 900 s, 1200 s, 1500 s, and 2100 s under (a) $q = 0.0595$ l/s and (b) $q = 0.595$ l/s ($T_{\text{amb}} = 35^{\circ}\text{C}$, $T_{\text{inlet}} = 20^{\circ}\text{C}$).

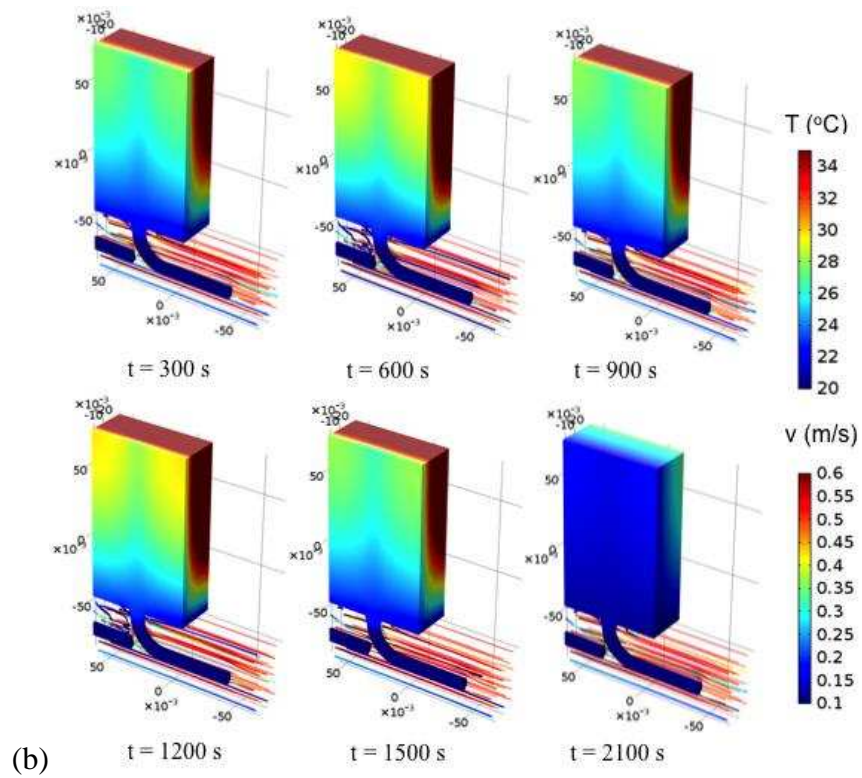
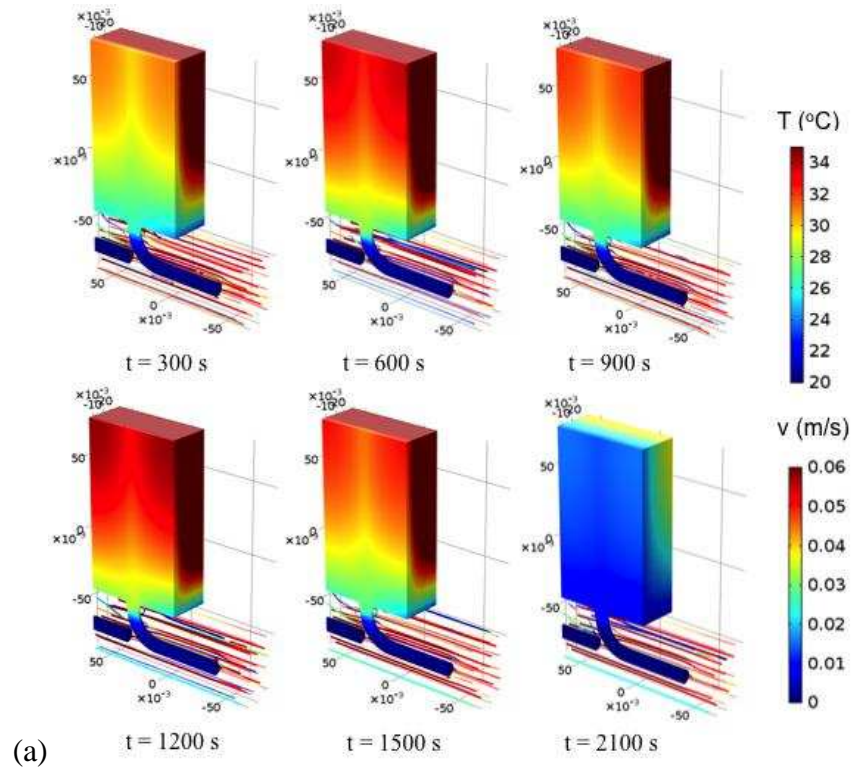


Figure 6.11: Temperature and velocity profile of Section B at $t = 300$ s, 600 s, 900 s, 1200 s, 1500 s, and 2100 s under (a) $q = 0.0595$ l/s and (b) $q = 0.595$ l/s ($T_{\text{amb}} = 35^{\circ}\text{C}$, $T_{\text{inlet}} = 20^{\circ}\text{C}$).

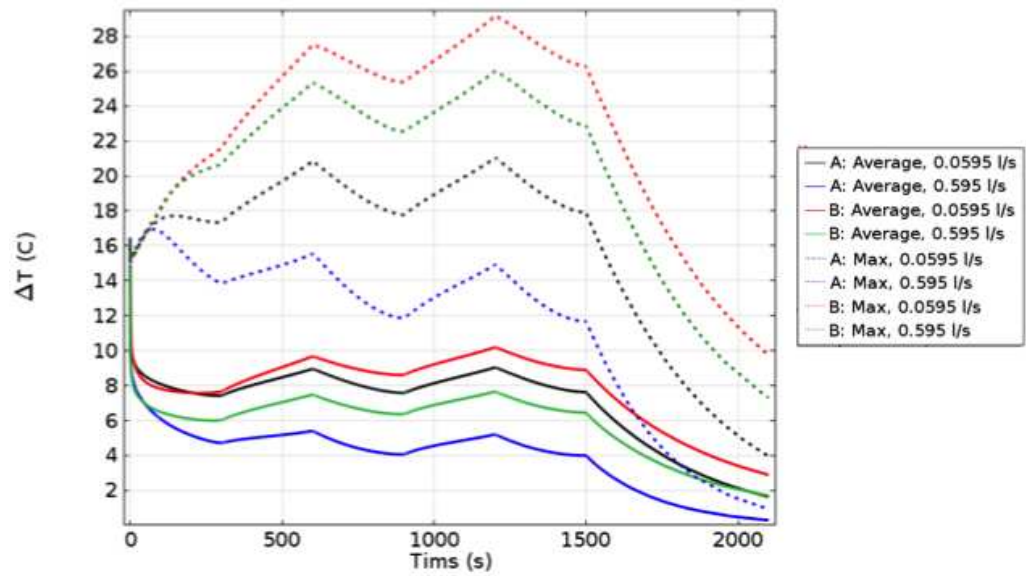


Figure 6.12: Battery temperature change (maximum and average) of the selected battery cells cooled at both sides and one side in a 30-cell battery pack (Section A and Section B) under a 2100 s 4C charge-discharge cycle mentioned in Fig. 6.3 ($T_{\text{amb}} = 35^{\circ}\text{C}$, $T_{\text{inlet}} = 20^{\circ}\text{C}$, $q = 0.0595 \text{ l/s}$ and 0.595 l/s).

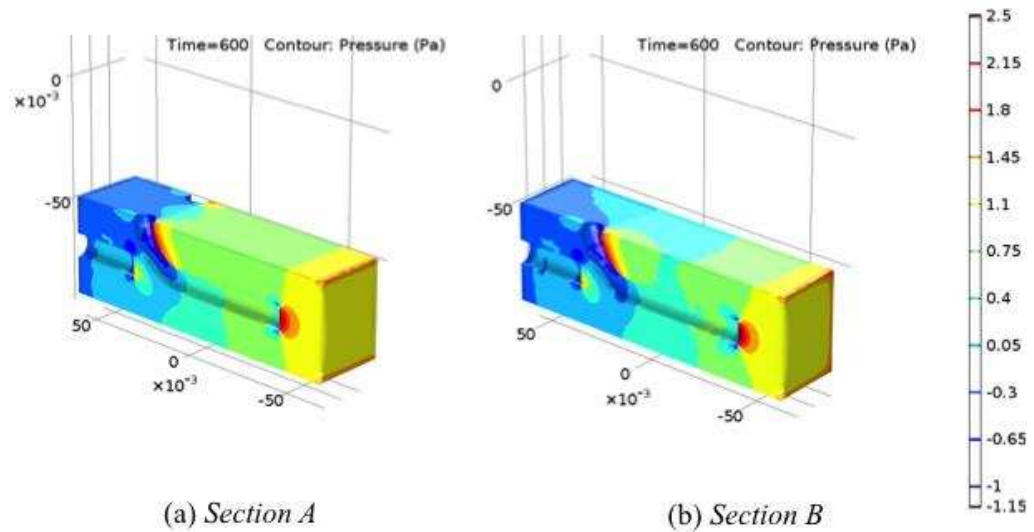


Figure 6.13: Pressure distribution across the liquid zone of (a) Section A and (b) Section B under $v = 0.0595 \text{ l/s}$ at $t = 600 \text{ s}$.

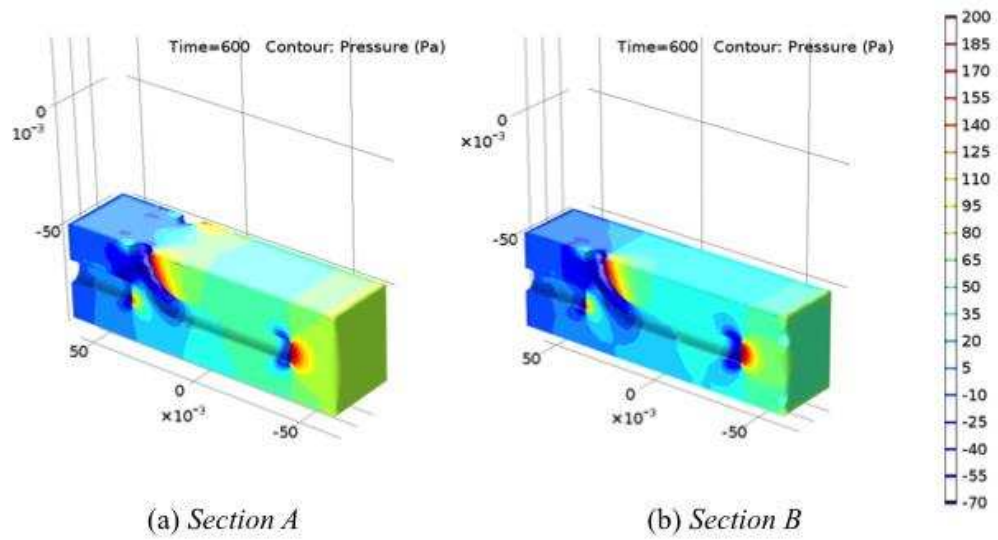


Figure 6.14: Pressure distribution across the liquid zone of (a) Section A and (b) Section B under $v = 0.595$ l/s at $t = 600$ s.

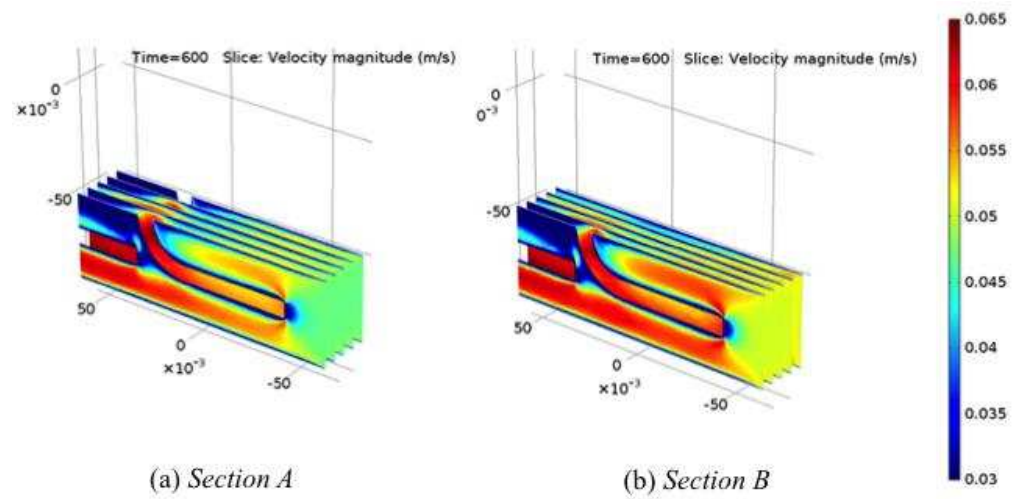


Figure 6.15: Slices of velocity distribution across the liquid zone of (a) Section A and (b) Section B under $q = 0.0595$ l/s at $t = 600$ s.

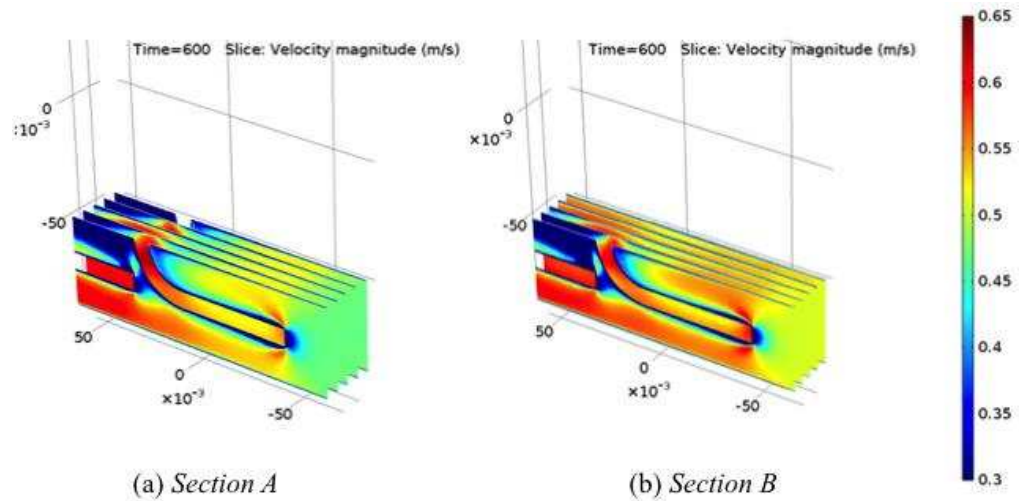


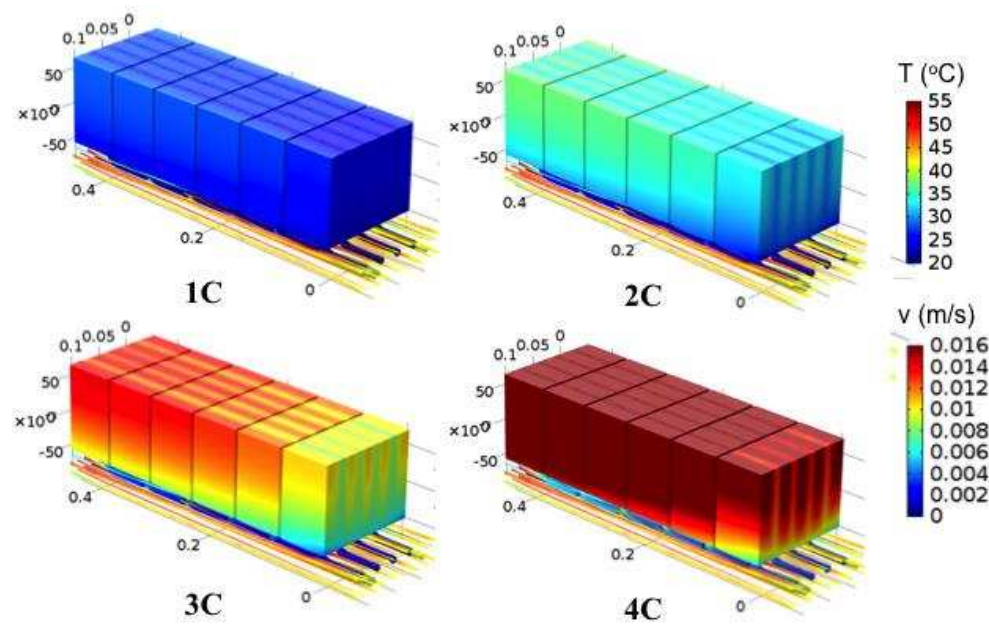
Figure 6.16: Slices of velocity distribution across the liquid zone of (a) Section A and (b) Section B under $q = 0.595$ l/s at $t = 600$ s.

6.3 Battery Cooling (30 Cells, Stationary)

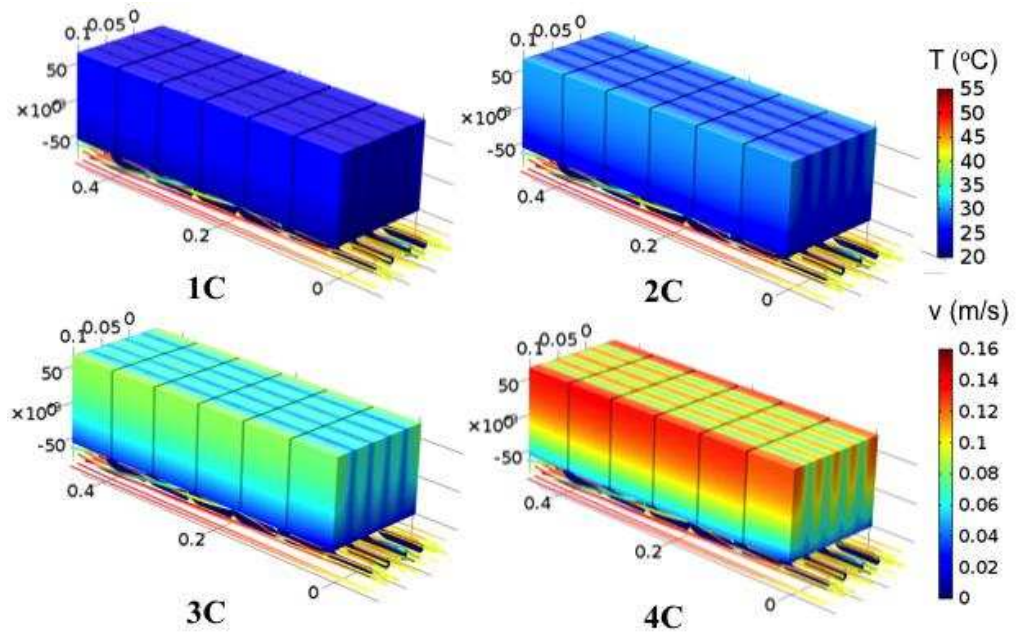
6.3.1 Decoupled

The decoupled model is to apply a constant value for the heat generation of the battery cell treating the whole pack as a standalone thermal model. Steady state temperature distribution across the battery pack under 1 – 4C discharge rate is demonstrated in Fig. 6.17 under both low and high flow rate. Unevenly distributed heat can be found at sides, where only one side of the battery cell is in contact with the heat pipe. Low flow rate is unable to maintain the maximum battery temperature below 50°C especially at high discharging rates. The maximum temperature can be reached to as high as 73.58°C if 4C is constantly discharged and low flow rate (0.0595 l/s) is supplied. High flow rate can help battery dissipate heat well achieving nearly uniform temperature distribution under low and high discharge rates. The maximum temperature

can be therefore reduced to 49.61°C at 4C steady state discharge rate. The pressure contour across the liquid box between the inlet and outlet suggested from Fig. 6.18 is insignificant due to large surface area for inlet assumed in the liquid zone, which is 17 Pa difference maximum under high flow rate. Velocities obtained vary from 0 – 0.016 m/s and 0 – 0.16 m/s across the liquid zone from two applied flow rates (Fig. 6.19). Fig. 6.20 demonstrates the temperature distribution among 18 cells where cooling is available for both sides of the battery cell. Highly uniform temperature distribution is achieved at 0.595 l/s maintaining the maximum temperature below 46.96°C at 4C continuous discharge. Higher flow rate also reduces the average battery surface temperature difference across 18 cells to approximately 6°C under 4C discharge rate compared to 10°C over 30 cells. Nonetheless, low flow rate can be suitable for 1 – 2C continuous discharging where a lower heat dissipation rate is expected.



(a)



(b)

Figure 6.17: Steady state temperature and velocity profile of the 30-cell battery pack under 1 – 4C discharge at (a) $q = 0.0595$ l/s and (b) $q = 0.595$ l/s ($T_{amb} = 35^\circ\text{C}$, $T_{inlet} = 20^\circ\text{C}$).

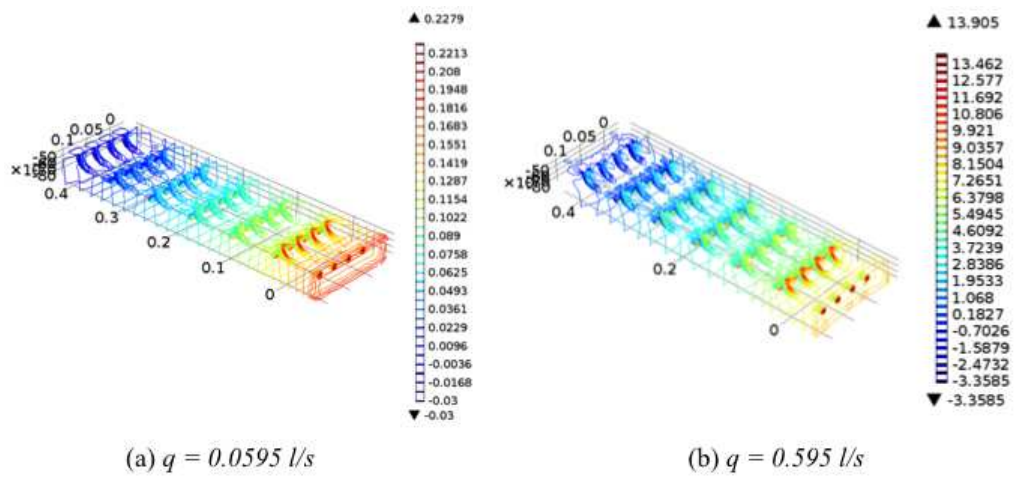


Figure 6.18: Pressure contour profile of the 30-cell battery pack under (a) $q = 0.0595$ l/s and (b) $q = 0.595$ l/s ($T_{amb} = 35^\circ\text{C}$, $T_{inlet} = 20^\circ\text{C}$).

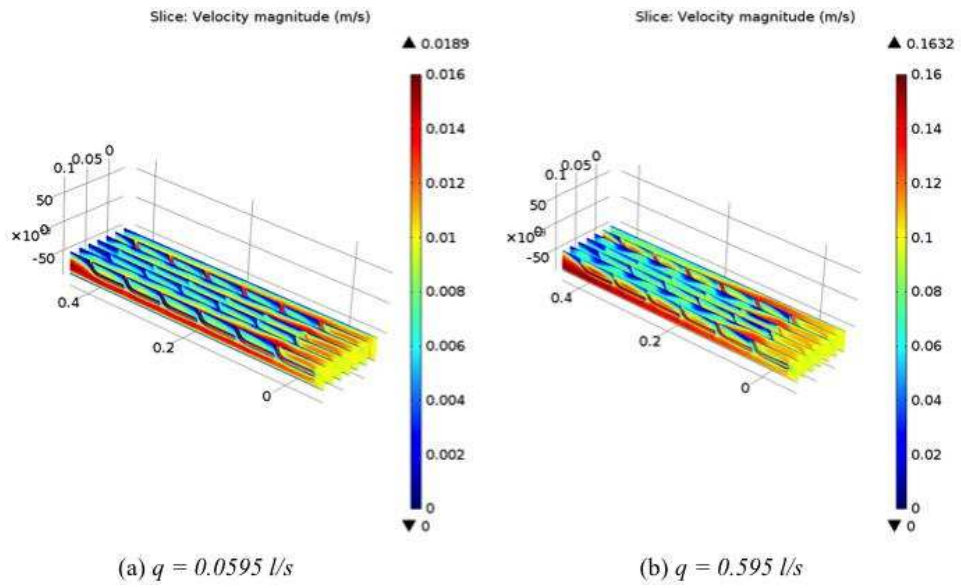
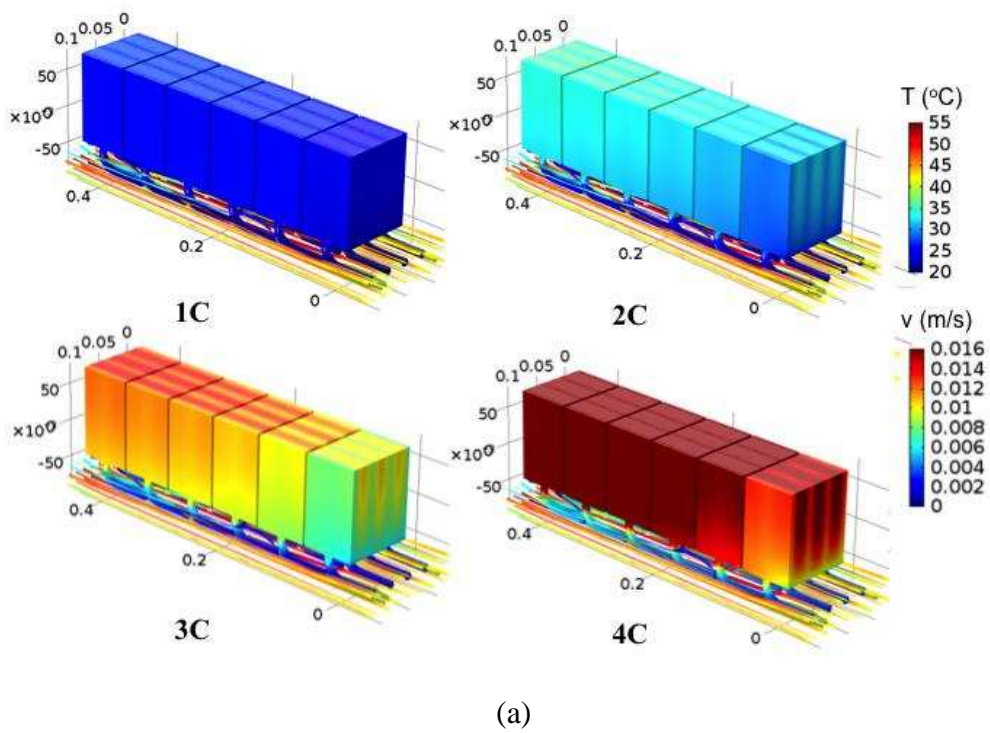


Figure 6.19: Velocity profile (8 slices of y - z plane) of the 30-cell battery pack under (a) $q = 0.0595 \text{ l/s}$ and (b) $q = 0.595 \text{ l/s}$ ($T_{\text{amb}} = 35^\circ\text{C}$, $T_{\text{inlet}} = 20^\circ\text{C}$).



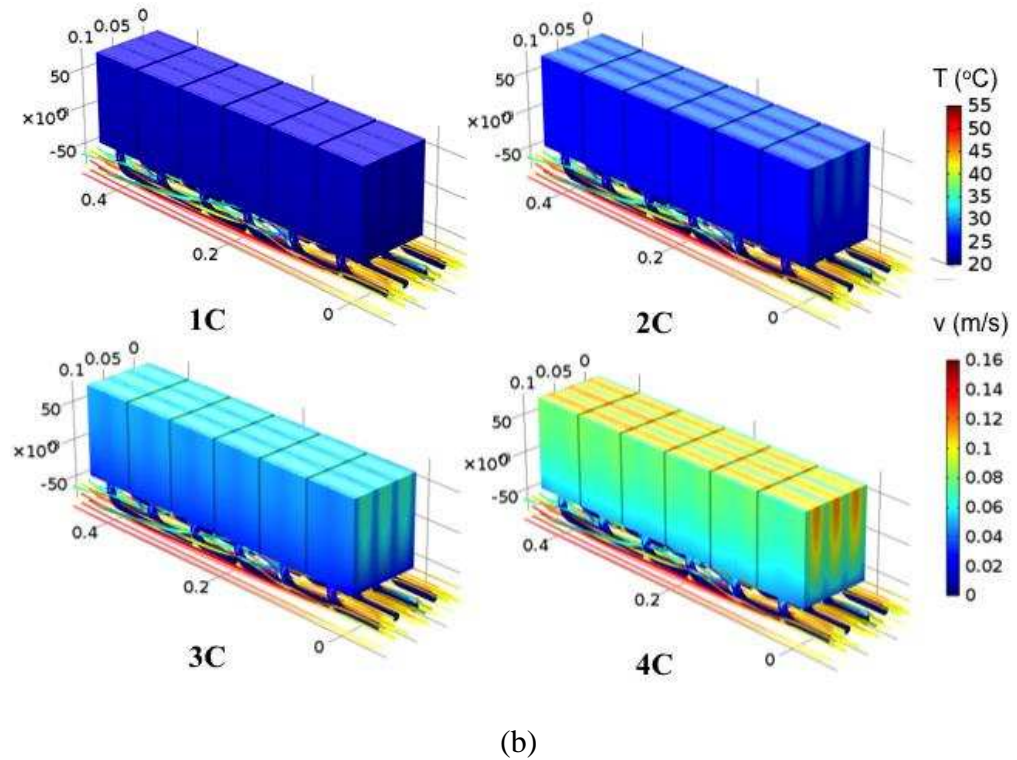


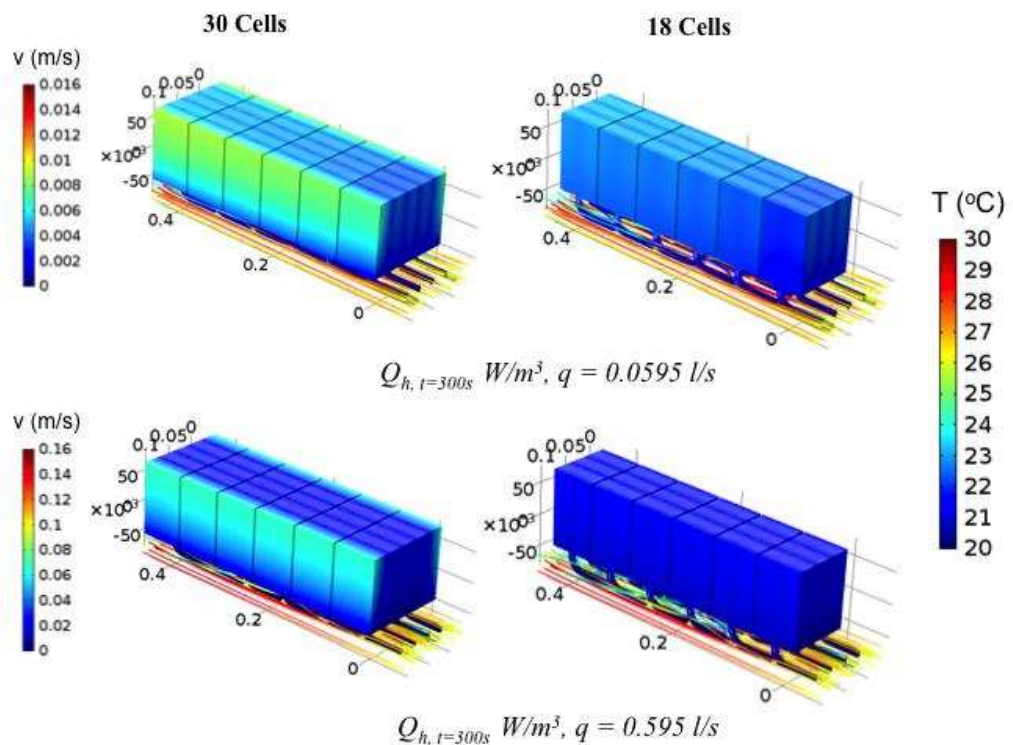
Figure 6.20: Steady state temperature and velocity profile of the 18-cell battery pack (cooled at both sides) under 1 – 4C discharge at (a) $q = 0.0595$ l/s and (b) $q = 0.595$ l/s ($T_{\text{amb}} = 35^{\circ}\text{C}$, $T_{\text{inlet}} = 20^{\circ}\text{C}$).

6.3.2 Coupled (Quasi-Stationary)

As mentioned earlier in solver sequence, a quasi-stationary study will be applied for 30 cells, which couples the laminar flow in the first study and the average heat source from the last step of the time-dependent study in the second study. This implies that the battery heat source used for the quasi-thermal balance is at a given time during the 4C load cycle, written as $Q_{h,t}$ (W/m^3). The heat generation rate varies significantly from 299.95 s (599.95 s) to 300 s (600 s) according to Fig. 4.12 and Fig. 6.4, so it is suggested to use

$Q_{h,t=300s}$, $Q_{h,t=600s}$, $Q_{h,t=299.95s}$ and $Q_{h,t=599.95s}$ as heat source references for 30 cells in the quasi-stationary study.

Results for 30 cells and 18 cells (battery cells cooled by both sides) under those conditions under two cooling rates are displayed in Fig. 6.21 and Fig. 6.22. At higher cooling rate, the temperature difference across the whole pack after reaching to steady state status can be maintained below 5°C under low heat source generation rates (Fig. 6.21), i.e. $Q_{h,t=300s}$ and $Q_{h,t=600s}$, and below 3°C for batteries cooled from both sides. High heat generation rates obtained from 4C charge at 299.95 s (i.e. $Q_{h,t=299.95s}$) and 4C discharge at 599.95 s (i.e. $Q_{h,t=599.95s}$) reduce the temperature uniformity of the battery pack leading to approximately 35°C between the maximum and minimum temperature from 30 cells and 25°C difference from 18 cells under 0.595 l/s. Heat spots are mainly found among top surfaces of the battery cells where no cooling is supplied.



(a)

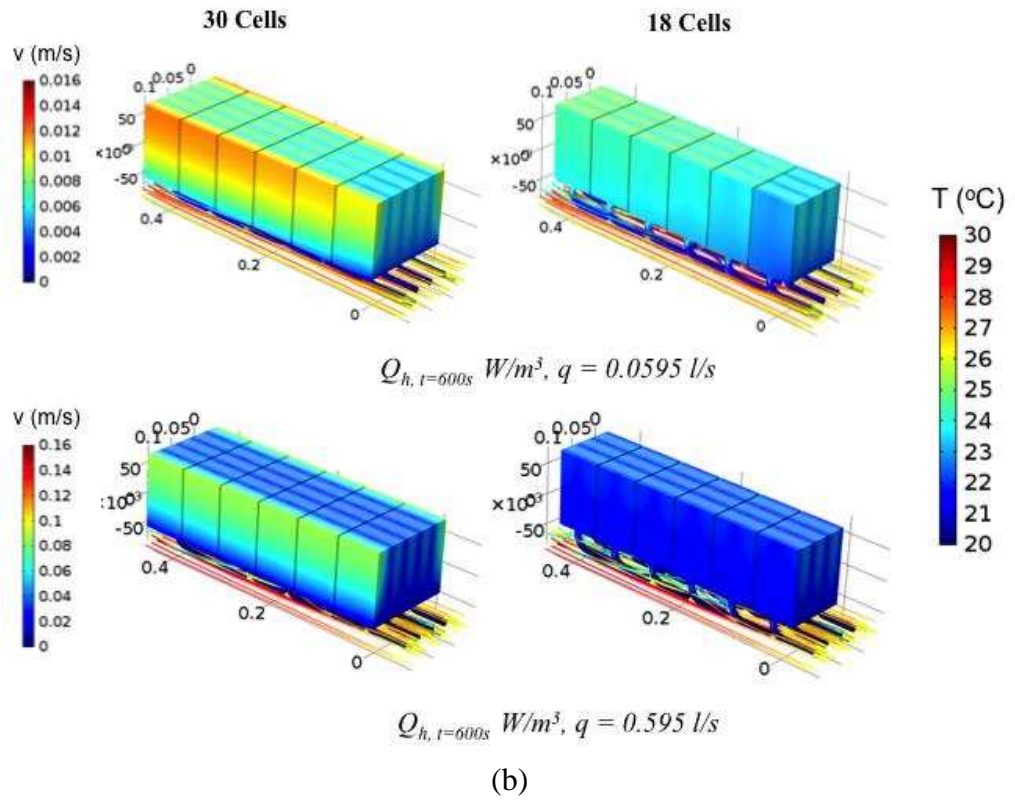


Figure 6.21: Quasi-stationary temperature and velocity profile of the battery pack that contains 30 cells and 18 cells at the heat generation rate $Q_{h,t}$ obtained from coupling 1D electrochemical battery model and heat transfer model at (a) $t = 300 \text{ s}$ and (b) $t = 600 \text{ s}$.

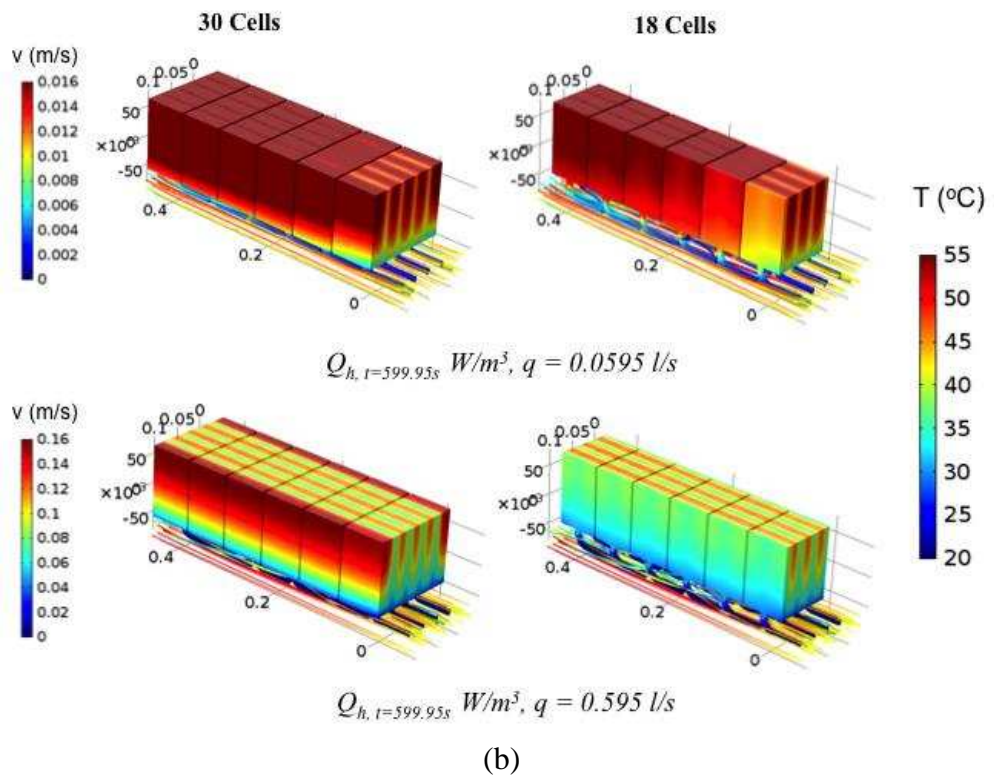
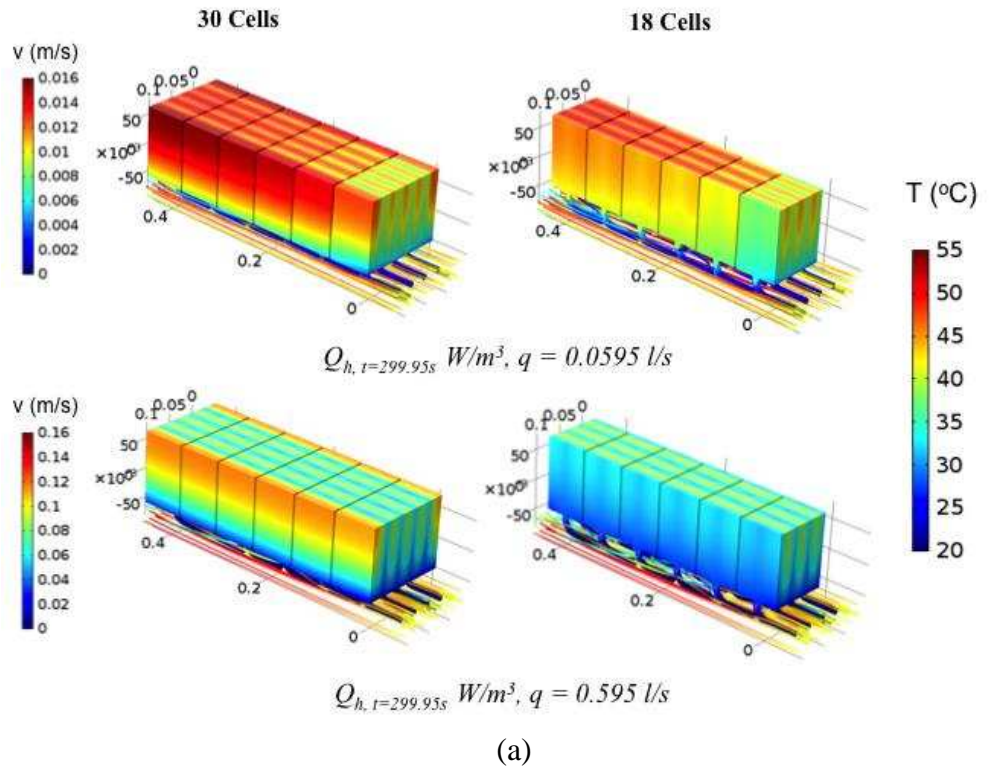


Figure 6.22: Quasi-stationary temperature and velocity profile of the battery pack that contains 30 cells and 18 cells at the heat generation rate $Q_{h,t}$ obtained from coupling 1D electrochemical battery model and heat transfer model at (a) $t = 299.95$ s and (b) $t = 599.95$ s.

6.4 Battery Preheating (30 Cells, Time Dependent)

The thermal management of heat pipe preheating can be effective, where the heat energy is extracted through fluid heating from an electric heater or a bioethanol heater, and is transferred to each single battery cell simultaneously via heat pipes. The heat pipe in this case is operated under gravity-assisted condition. It is assumed that energy or heat is available to warm up the battery, so the focus will be transferring this thermal energy to the battery by using heat pipes.

The heat power estimation was based on a simple lumped capacitance model. This was to calculate the amount of power needed to warm up the battery during winter in a specific amount of time. The efficiency of heat transfer from source to the model was assumed to vary from 50% to 100% dependent on cell formation (e.g. width to length aspect ratio), cell and pack hardware and assembly, and heating methods. The heat transfer equation can be formulated below where the heat loss from the battery $hA(T-T_0)$ was negligible compared to q if assuming 100% heat transfer efficiency.

$$q = mC_p \frac{\partial T}{\partial t} + hA(T - T_0) \quad (6.1)$$

Fig. 6.23 indicates the amount of heat power required per battery mass at the rate of temperature rise. The results were based on a lithium-ion battery cell with mass of 0.453 kg and specific heat capacity C_p of 1,060 J/kg°C (Table 4.1). In order to heat up a 13.59 kg lithium-ion battery pack (30 cells) from -20°C to 0°C in 5 or 10 minutes, a minimum power of 0.96 kW or 0.48 kW can be estimated under 100% efficient process.

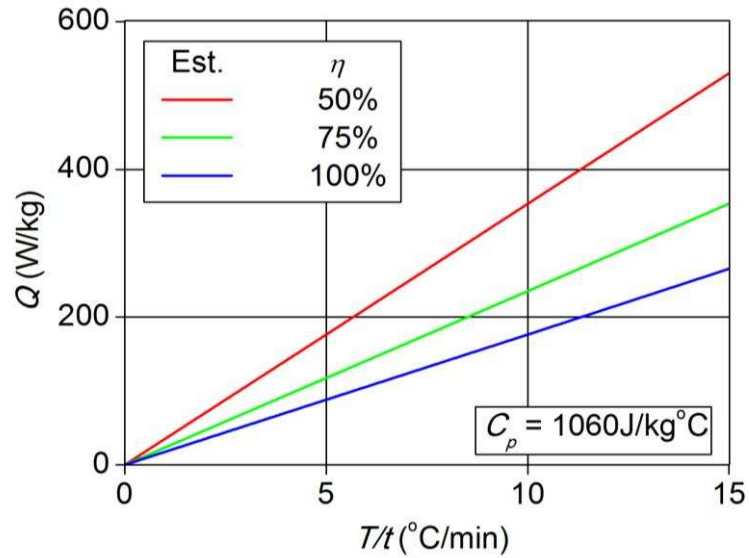


Figure 6.23: Estimated heat power requirement under 50%, 75% and 100% efficiency.

Numerical simulation for the target 30-cell lithium-ion battery pack within 900 s has been performed. Laminar model was used and a number of monitoring points were set to report system transient thermal response in 900 s (time step: 2 s, solution save interval: 10). Natural convection was considered on the exterior surfaces with film coefficient of 2 W/m²K at two sides and 3 W/m²K on the top surfaces. The bulk temperature for all convection surfaces and initial module temperature were assumed to be -20°C. The heat source available on-board is the hot glycol-water mixture discharged through the liquid box underneath, at an inlet temperature of 40°C. The mass flow rate of fluid inlet is 0.059 kg/s (i.e. 0.595 l/s) in proportion with the experiment. The battery pack has 6 rows and each row contains 5 cells. The cell number demonstration can be found in Fig. 4.2 and the results obtained under 40°C preheating is demonstrated in Fig. 6.24.

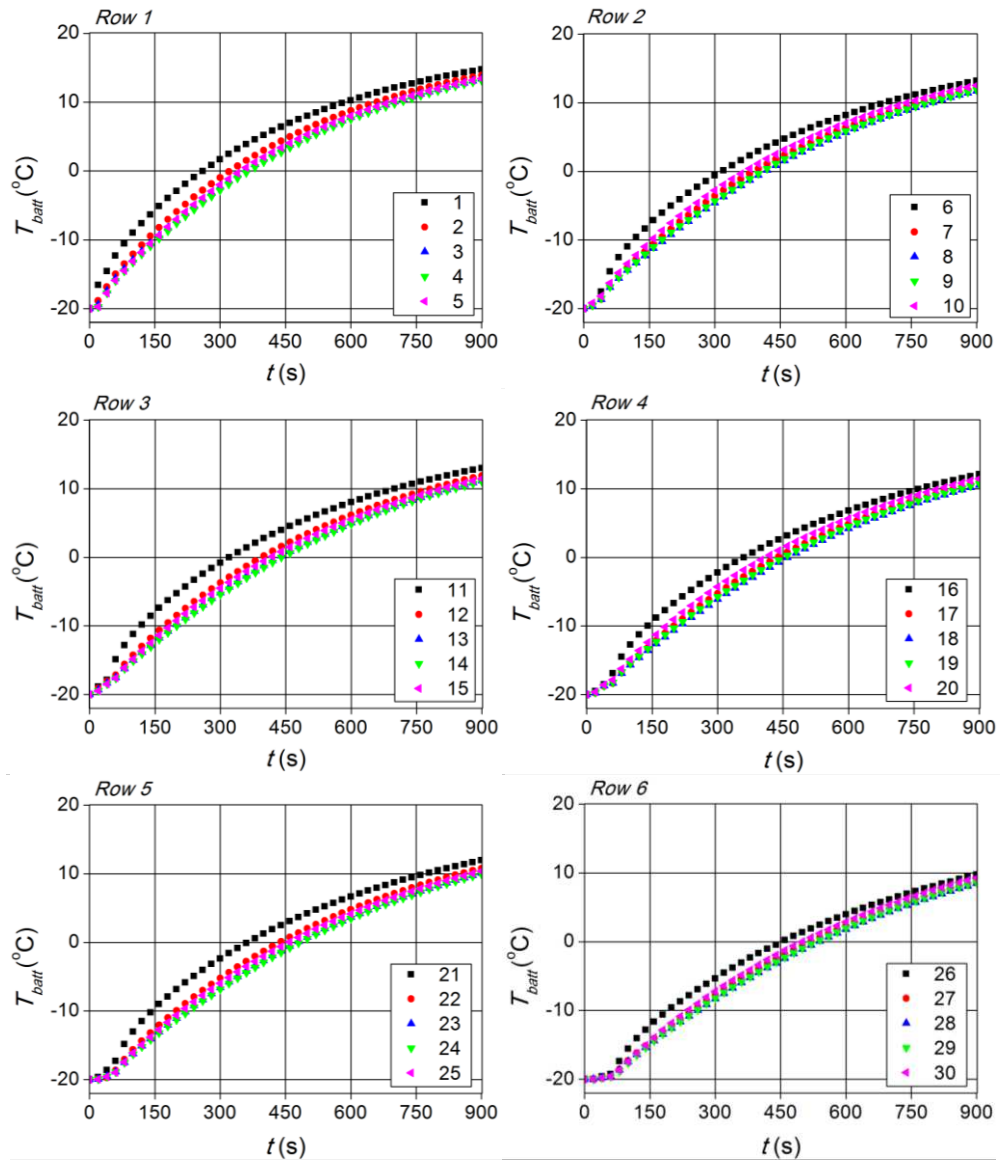


Figure 6.24: Thermal response of 30-cell battery under 40°C preheating in 900s.

In order for all 30 cells (cell 1-30) to reach to at least 0°C, it takes approximately 540 s (9 minutes) under 40°C preheating. From previous calculation, the minimum heat power required to heat up such battery pack from -20°C to 0°C in 9 minutes is 0.43 kW. The temperature increases of the first cell in each row (cell 1, 6, 11, 16, 21, 26) appear to be more significant than the rest cells in the same row, and the temperatures of cell 3, 4, 8, 9, 13,

14, 18, 19, 23, 24, 28, 29 experience the slowest increase among others in the same row. Delays in temperature increase from the last two rows (row 5 & 6) can be seen from the first 80 s. The degree of temperature uniformity across row 1, 3, 5 remains poorer than row 2, 4, 6, reflected by a considerable temperature difference between cell 1, 11, 21 and the rest cells in the same row. The average rate of temperature rise within 540 s is 0.045 °C/s (2.7 °C/min), and within 900 s is 0.035 °C/s (2.1 °C/min). Improving fluid flow inside the liquid zone by constructing buffer plates or creating a dynamic flow velocity profile to compensate for localised temperature increase are therefore suggested for future work in order to increase pack temperature uniformity.

6.5 Summary

The application to battery thermal management at pack level has been evaluated based on a scale-up model, which contains 30 lithium-ion battery cells. This model simulates the temperature profile in 30 cells and heat pipes in connection with a glycol-water coolant channel. Both decoupled/coupled battery cell model and flow and heat transfer model are used to evaluate battery cooling and preheating under stationary and time dependent manner. It aims to reveal the limitation of the proposed method by covering an extensive range of battery operating conditions.

With the provision of two EV driving cycles given by FAW, heat pipe cooling is compared with air cooling under repeated cycles. Higher convective heat transfer coefficient in air cooling may be useful after repeating the second cycle, but air cooling retains ineffective under aggressive driving scenarios.

The heat pipe liquid cooling, however, keeps the peak temperature under 4 continuous cycles (Cycle 1) below 36°C and 46°C at all times within 6 continuous cycles (Cycle 2). In addition, two locations within the battery pack are selected for a fully coupled time dependent analysis. Heat pipe liquid cooling cools down the battery cell drastically, maintaining the average temperature change below 11°C and 8°C throughout the entire cycle under 0.0595 l/s and 0.595 l/s cooling rate respectively.

Results from decoupled model for 30 cells show that high flow rate (0.595 l/s) can effectively reduce the temperature difference across the battery pack to 10°C (30 cells) and 6°C (18 cells) under the worst scenario (continuous maximum 4C discharge rate), maintaining the maximum temperature below 49.61°C (30 cells) and 46.96°C (18 cells). Quasi-stationary evaluation takes battery heat source as the quasi-thermal balance at a given time during the 4C load cycle, and temperature variation seems substantial at higher heat generation rates such as $Q_{h,t=299.95s}$ and $Q_{h,t=599.95s}$. Temperature monitoring for battery preheating under 40°C, 0.595 l/s is performed on a time dependent basis. In order for all 30 cells to reach to at least 0°C, it takes approximately 540 s (9 minutes). The temperature uniformity was reported as 'poor', which generates thoughts of improving fluid flow inside the liquid zone by constructing buffer plates or creating a dynamic flow velocity profile to compensate for localised temperature increase to achieve thermal homogeneity of battery pack temperature distribution.

Chapter 7

Exploring Biomimetic Wicks in Ultra-thin

Flat Plate Heat Pipes for Improved Surface

Wettability and Capillary Limit

7.1 Concept Design

7.1.1 Background

Microelectronics has become the very key element for today's high tech industry due to the fact that it is smaller, thinner, lighter, and more portable. Heat pipe, as one of the many kind to help managing the thermal environment of the devices, also needs to be downsized. Particularly, in areas where spatial limitation is encountered and for device (e.g. battery cell with small gaps) that requires a large surface area to volume ratio to capture as much power density as it possibly can, flat plate heat pipe (FPHP) comes to consideration due to its well defined geometry and the ability in reducing thermal spreading resistance by 40 times compared to normal heat pipes.

The basic mechanism of a heat pipe is performed through three sections: the evaporator, the adiabatic section, and the condenser. Working liquid is heated and vaporised in the evaporator, and the generated vapour flow to the

condenser releasing latent heat. The resultant liquid condensate will then be drawn back to the evaporator due to capillary forces thus repeatedly forming the above cycle. The axial vapour and liquid flow created by induced pressure differences takes credits for heat pipe operation, such that the elimination of external pumping system is possible.

The widely used cylindrical heat pipes have clear advantages because they can be treated as natural pressure vessels, which can endure large pressure differences generated by liquid and vapour inside, and the compressive or tensile forces resultant on the walls. For FPHP with high surface area to volume structural integrity, the large surface area is vulnerable to withstand the pressure difference exerted between pipe internal and external causing material failure. Adding support posts or sintered column posts into the heat pipe becomes the highest priority especially in ultra-thin FPHPs, which help to strengthen the overall structure counteracting the pressure. These structural supports, however, create obstacles prohibiting vapour and liquid two-dimensional flow, and add a significant amount of weight to the entire heat pipe. One aim of this design is to form lighter structural supports that do not clog the flow passage while maintaining excellent capillary force.

Another issue, found in battery cells in particular, requires heat pipe to cope with anti-gravity (evaporator is above the condenser) where capillary limit is challenged. Wick pore size, wick thickness, and wick structure are all required to be optimised such that high capillary pressure and high permeability can be obtained at the same time. Some trade-offs exist. For pore size-wise, smaller pores generate larger capillary head but low wick permeability impeding liquid flow. Thick wick enhances heat transfer ability

by enlarging surface area but considerably results in high radial thermal resistance lowering the allowable maximum evaporator heat flux. Homogenous wick structure is only able to satisfy one beneficial criterion, either high capillary limit or high permeability. In addition, due to contradictory purposes served by heat pipe evaporator and condenser, the wick should be designed separately. The wick criteria associated with capillary limit for the evaporator, adiabatic and condenser are necessary to be individually examined and designed.

In a prior art, common deficiency is often found in ultra-thin FPHPs, especially in anti-gravity condition because optimum heat transfer potential is not fully exploited. The internal structure, either be lacking of vapour voids after flattening, or be failed to satisfy both evaporator and condenser, hindering such heat pipe to be well functioned.

Examples of ultra-thin FPHP devices, which take into account of vapour voids, can be seen by reference to US Pat. 2010/0266864 A1 [235], 2010/0319882 A1 [236], and 2012/0118537 A1 [237]; while heat pipe with different wick structures for evaporator, adiabatic and condenser can be seen from US Pat. No. 4489777 [238].

To date, no one has devised an ultra-thin FPHP with enough vapour space while producing excellent capillary limit by applying different wicks for each heat pipe segment, especially under anti-gravity condition.

7.1.2 Biomimetic Possibility

The possibility of mimicking desirable properties from nature accelerates material improvement and generates commercial interests. For heat pipe

development, many attempts have been made in heat pipe wicks to enhance its capillary performance by using mimic biology. Constructing biporous, composite, or nanopillar wicks with aim of achieving hierarchical structure has been found in many studies, and mimicking beetle shell surface to obtain hybrid wettability shows biomimetic potential in heat pipe wicks.

The diversity and adaptability of the natural world fascinates mankind and enables human revolution. Our attempt in developing new manufacture methods to synthesise an isolated function in nature is encouraged, and the necessity to fully understand such natural occurring process avoiding blindly copying nature is demanded. For heat pipe improvement, a change in wick structure can help generate effective results. With the provision of the wick, a heat pipe can work in any orientation. The wick serves the function of further complicating the boiling process offering additional nucleation sites beneficial for bubble formation and modifying the movement of liquid and vapour towards or from the heated surface Grover [239]. The associated capillary force created by the wick, notably, forms the main criteria in evaluating heat pipe performance, which helps to achieve passive operation, i.e. pulling back the condensed liquid from condenser to evaporator enabling the cycle. Therefore, it is desired to investigate some nature generated capillary effect from plants, insects, to aquatic animals in terms of cell or surface structures.

Many biomimetic studies towards superhydrophobic or superhydrophilic effect [240-243] have been conducted in recent years offering a convenient path for engineers to extract relevant details (e.g. surface structure, contact angles/wettability, materials in contact) for current technology development. In mimic biology, capillary effect is always accompanied by adopting

hierarchical surface structure for micro- or nano-scale applications, which is the response to various mechanisms including dissipation, friction and wetting [244]. It is the hierarchical structure that helps the species to achieve the adaptability in diverse forms of functions based on various characteristic length scales. If such hierarchical structure helps plants and creatures establish their adaptable mechanisms of energy dissipation and transition, it is possible that the engineers can follow the principles in order to develop improved environment-friendly technologies.

In heat pipe development when heat flux exceeds hundreds or thousands of W/cm^2 , constructing biporous or bidisperse [245-248], composite (e.g. sintered-grooved) [249-255], micro- or nano-pillar wicks [256-258] seems to offer a better solution. These can be attributed to hierarchical structure, which helps to achieve high capillary pressure while maintaining relatively high vapour permeability. Mono-porous or single structure will always lead to high capillarity but low permeability or low capillarity with high permeability. In addition, Zhao et al. [259] proposed a beetle inspired superhydrophobic condenser with hydrophilic bumps to accumulate condensate so as to achieve hybrid wettability.

7.1.2.1 Hierarchical Structure from Nature

7.1.2.1.1 Wetting Phenomenon

Many biological structures at the micro- and nano- scale in both plant and animals have demonstrated their interaction with water and hence the wettability. For instance, surface structure or roughness of the xylem in trees varies among species and differs with climates [260]. In hot and dry climate,

xylem with small warts indicates superhydrophilicity, where the contact angle of water within xylem is extremely low, i.e. increased wettability. The water collecting ability of the capture silk of the Cribellate Spider [261] gives light to the surface wettability. With periodic spindle-knots and joints, continuous condensation and directional water drops collection can be achieved. The unique system of cactus [262] composed of well-distributed clusters of conical spines and trichomes on the cactus stem and multi-level grooves from microgrooves to submicorgrooves on the spine intrigues the investigation of structure function relationship and wetting mechanism. Furthermore, desert beetles [263, 264] that use multi-functional elytra surface structure (hydrophilic bumps on hydrophobic base) to capture water from humid air, and a systematic structure of spikes, scales and channels involved in moisture harvesting lizard's skin [265-267] indicate the level of hierarchical order influencing surface properties.

7.1.2.1.2 Capillary Effect

A cohesion-tension theory has often been applied into trees, despite the fact that the exact mechanism of water transport has not been fully understood [268]. It is said that water can be transported by tension forces caused by capillary force and leaf transpiration. The capillarity increases when xylem diameter is smaller, and branching of the xylem increases capillarity [269]. In addition to the surface properties of certain lizards mentioned earlier, they employ capillary transport over their skin to assist drinking. In the case of *Moloch Horridus*, its spikes [266] help to encourage water to run over the skin, and micro-structured scales [265], often covered in a honeycomb structure of walls, increase surface wettability. The channels, which are inter-scalar and

differ from $10\ \mu\text{m}$ [265] to $100 - 150\ \mu\text{m}$ [266] will form inter-scalar capillary system and capillary connections for moisture harvest. A gradient of capillary sizes to passively lift water can vary according to the distance from the mouth, with smaller capillaries near the mouth and larger capillaries far away from it.

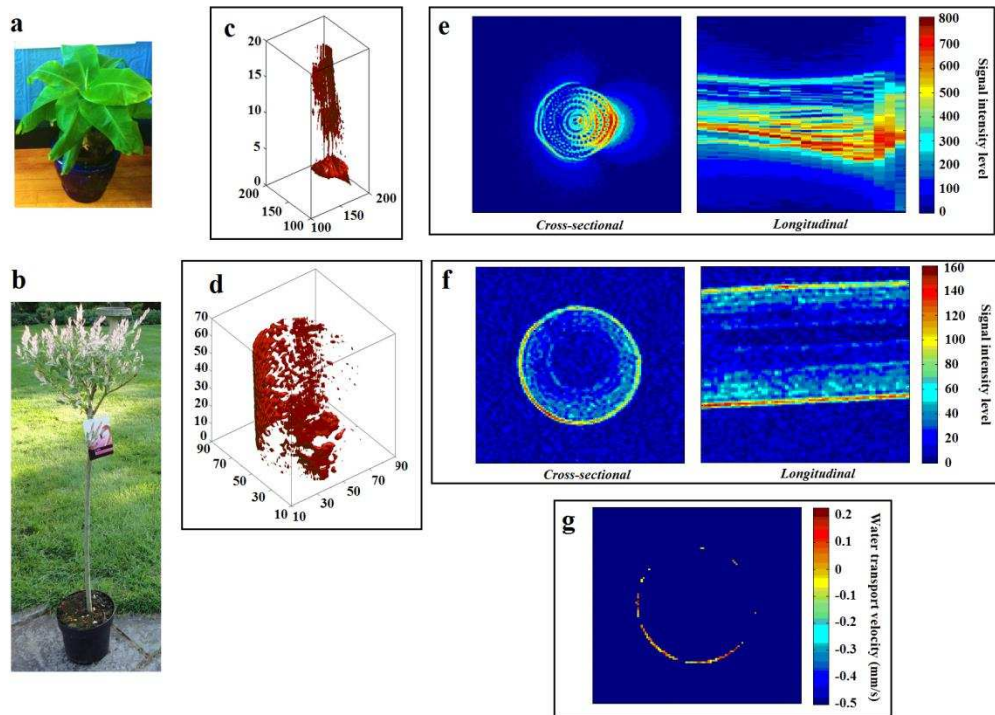


Figure 7.1: **MRI scanning of live plants.** (a) Musa X Paradisiaca. (b) Salix Flamingo. (c-d) 3D water flow distribution in xylem vessels obtained from (c) Musa X Paradisiaca and (d) Salix Flamingo. (e-f) Cross-sectional and longitudinal view of water distribution of (e) Musa X Paradisiaca and (f) Salix Flamingo (Note: signal intensity level helps reflect water distribution, blue indicates low intensity, i.e. less water; red indicates high intensity, i.e. more water). (g) MRI scanned rate of water transport J_v (mm/s) in the xylem vessel of Salix Flamingo (an average peak velocity of $0.2\ \text{mm/s}$ was obtained).

For a more comprehensive study of capillary effect in plant, we introduced MRI scanning (Philip 3T Achieva machine, with resolution of 0.3×0.3 mm with 3 mm layer gap) of two chosen plants: *Musa X Paradisiaca* and *Salix Flamingo* (Fig. 7.1 (a-b)). MRI provides the possibility of visualising internal structures and metabolites of the plants occurring in vivo. The major aims are to study how plants move water upwards, find potential biomimetic solutions to improve fluid flow in porous structures, and form a better understanding of capillary effect in porous media.

Fig. 7.1 (c-d) demonstrate the water flow distribution in 3D and Fig. 7.1 (e-f) display the magnetic signal intensity reported by MRI that reflects the degree of water concentration from both cross-sectional and longitudinal view. Results indicate that water flow through the xylem is very efficient because a considerable amount of water distribution in xylem vessels was seen throughout the entire plant (from the bottom to the top). However, due to machine resolution limit, the precise structure of xylem vessel and water molecule movement was hard to observe. Further work on exploring xylem cell contact angle and capillarity is desired and may be fulfilled by adding tracer to the stem.

Fig. 7.1 (g) shows the rate of transport J_v (mm/s) in the xylem obtained from *Salix Flamingo*, which suggests an average of peak velocity of 0.2 mm/s. Usually for wide xylem vessel that has radius ranging from 100 – 200 μm , the highest peak water transport velocities are 4 – 13 mm/s; for smaller one which varies from 25 – 75 μm , a lower average peak velocity of 0.3 – 1.7 mm/s can be resulted [270]. This implies that for *Salix Flamingo*, it has smaller vessels that tend to result in lower peak velocities. According to Poiseuille's equation

(Eq. 7.1), the pressure gradient $\Delta\psi_p / \Delta x$ can be estimated to overcome the viscous drag that arises as water moves through an ideal xylem vessel at this velocity J_v (0.2 mm/s) through ideal uniform xylem vessel with a radius of 25 μm . If assuming μ ($\mu = 8.9 \times 10^{-4} \text{ Pa}\cdot\text{s}$ at 25°C) is the water viscosity of xylem sap, the pressure gradient $\Delta\psi_p / \Delta x$ required is 2,278 Pa/m. To note, for real vessels, where irregular inner wall surface and constrictions exist, they often have large resistance to water flow.

$$J_v = \frac{r^2}{8\mu} \left(\frac{\Delta\psi_p}{\Delta x} \right) \quad (7.1)$$

7.1.2.1.3 Theory Behind

The concept of hierarchy can be defined as two or more levels created by combinations of structures of different dimensions, and the number of levels or so-called hierarchical order is related to a particular function of each level of material structure [271]. This translates to surface roughness, and if small roughness superimposes onto a smooth surface, such as the mentioned surfaces of cactus, beetles and lizards, changes in system behaviour can be resulted. One of the many system behaviours is the phenomenon of wetting, and it indicates how well the liquid moves to expose its fresh surface and to wet the surface of the solid in turn. Notably, the fundamental parameter that characterises surface wettability is the contact angle (CA) [272]. The CA is defined as the angle formed by the intersection of the liquid-solid interface and the liquid-vapour interface and is determined by a combination of surface tension and external forces such as gravity [273]. Favourable surface wetting has a CA less than 90° while unfavourable wetting has the angle greater than

90°. In various ranges of CA degrees, hydrophilic/hydrophobic (solid in contact with water, $0^\circ < CA \leq 90^\circ$ for hydrophilic and $0^\circ < CA \leq 180^\circ$ for hydrophobic) and superhydrophobicity ($150^\circ < CA \leq 180^\circ$)/superhydrophilicity (almost 0°) can be introduced.

Another classic element of wetting of liquid droplets in systems from centimetre to micro- or nano-meter scales is contact angle hysteresis (CAH) [274]. CAH was firstly explained by Cassie and Baxter [275], and it is the difference between the advancing and receding CAs. A low CAH is a measure of dissipation, and a high CAH is a measure of wetting [276]. CAH intrigues the relationship of the surface texture and solid surface energy and it occurs when the CA is not a fixed value, i.e. can have any value between the advancing and receding CA values [277, 278]. Moreover, CAH is believed to complicate the wetting cycle changing the behaviour from reversible to irreversible qualitatively.

As mentioned by Nosonovsky and Bhushan [276], a small adjustment in surface structure/roughness may lead to a significant change in capillary force. This is because small-scale roughness produces new energy equilibriums and it changes the shape of water meniscus and hence, the meniscus force. The capillary effect is created due to the tendency of a liquid to minimise its free surface energy, which can be defined as the work energy input to the change of surface area. Molecules at a curvature surface have fewer bonds thus higher energy leading to surface tension. Hierarchical structure provides a platform for such energy to be spent on breaking generating cohesive force among the liquid molecules and adhesive force among molecules of other adjacent substances. It has been pointed out that capillarity depends on scale, and a

range of length-scales in hierarchical structure help to respond to different mechanisms such as wetting. Surface with only one scale of roughness cannot perform well [279], so it is desired to have large-scale details that offer structural strength while small-scale details for desired wetting properties and capillary effects.

7.1.2.2 Hierarchical Structure from Heat Pipe Wicks

7.1.2.2.1 Biporous Wicks

Biporous wicks are aimed to overcome heat transfer efficiency in the evaporator and they can be recognised by constructing a low level of hierarchy structure where clusters of smaller particles are present. Many works have been conducted in exploring the benefits [245-248] and a good agreement on producing both high capillary pressure and high vapour permeability is established. It has an advantage in relatively high heat flux transfer performance, more than hundreds of or thousands of W/cm^2 . It has two levels of pore sizes: small solid particles (small pore) within a bigger porous particle. This results in biporous wicks having a special performance in vaporisation because it increases the number of small evaporating menisci with high heat transfer ability in second level pores. The bubbles can easily escape from large pores thus eliminating the chances of blocking the condensate return. The capillary forces developed in smaller pores are larger than those in bigger pores, so if increasing the evaporative heat flux, bigger particles will be filled by vapour but smaller pores still allow more evaporation. Very little variation in temperature drop can be seen when increasing heat flux, because the additional heat is taken away by evaporation in smaller pores. In addition, due

to the fact that capillary forces created in smaller pores are bigger, sucking effect is created enabling liquid to be sucked completely into minor pores [245]. A recent study [246] found that the effectiveness of biporous wicks subjects to an optimal ratio of particle to cluster size. The ratio should allow full wetting of both inter-cluster and inter-particle pores thus achieving maximum volume flow and capillary force. This again indicates the importance of multi-scale in hierarchy structure, at which desirable properties can be obtained.

7.1.2.2.2 Composite Wicks

Composite wick is known as combining two types of single structure such as metal fibres and axial grooves, screen mesh and axial groove, and sintered-groove [249]. It is often designed to decouple capillary pumping from flow resistance in heat pipes. It provides better capillary force while maintaining high permeability. A plurality of documented benefits of integrating groove and sintered wicks suggest a great role the hierarchy structure plays. The combination of groove and sintered wicks can be found in many works, with either longitudinal grooves lining inside the casing covered by sintered powders [249-252] or sintered powders forming groove structures [253-255]. Both configurations tend to utilise the advantages of grooves, which provide high longitudinal capillary pumping; and of sintered wick that provide high capillary pressure and the ability in dealing with anti-gravity. Grooved structure gives lands or channels to help the formation of continuous layer of longitudinal liquid [253], and sintered wicks eliminate the chances of non-uniform circumferential liquid distribution [254]. Non-uniform circumferential

liquid distribution has always been found in groove wicks, both in evaporator and condenser, driving the imbalance of some grooves carrying excess liquid or none, i.e. dryout [253]. Therefore, exploiting advantages of both structures may help to overcome the common deficiency brought by single structure enhancing heat pipe performance efficiently and effectively.

7.1.2.2.3 Micro- or Nano-pillar Wicks

The advantages of micro- or nanopillar wicks are that they sustain higher thermal conductivity compared to sintered wicks, and exhibit high permeability with low liquid pressure drop [257]. For a given wick morphology, the capillary effect can be improved by an order of magnitude if thin nanostructured layer formation is found on the post surface [280]. Pillar structure may always be found in microchannels to enhance the surface to volume ratio while increasing capillary flow. Ding et al. [258] studied the wetting behaviour of the titanium micropillars numerically and experimentally, and Zhang and Hidrovo [256] investigated the wicking principles given by nanopillar. Ranjan et al. [257] analysed wicking and thermal performance for the use in passive heat spreaders. They pointed out that different pillar geometries such as cylindrical, conical and pyramidal structures, being compared at a fixed porosity and permeability, have the potential of producing high capillary pressure and maximising thin-film evaporation. These again indicate the function of nanostructures creating desired wetting properties and capillary effects.

7.1.2.2.4 *'Beetle Shell' Wicks*

A new type of vapour chamber with beetle mimicking condenser wicks was proposed by Zhao et al. [259]. They fabricated a hybrid surface consisting of hydrophilic pillars (185 μm in height) and a superhydrophobic base. Unlike normal heat pipes that eliminate the external forces for liquid return, electrostatic force is applied to drive the accumulated water drops attached on the hydrophilic bumps back to the evaporator. The overall concept of such design is to reduce the use of wicks lowering heat pipe thermal resistance.

7.1.3 Sintered Powder Wick Review

Sintered powder wick is often used in heat pipes for that it can drive the internal condensate flow under any orientation due to the provision of the capillary force. Operating in this fashion, the heat can be continuously absorbed and released achieving an isothermal two-phase transfer. Desired characteristics of a sintered wick to achieve high thermal performance including the capillary pressure and wick permeability have always been the focus of previous investigation. However, these two properties are inversely related to the wick pore size so that the trade-offs between them should be carefully examined. A successful operation requires the capillary pressure that drives the working fluid inside the wicks to balance out the total viscous pressure drop that depends on the wick permeability. Small pores increase the capillary pressure but reduce permeability that induces a higher pressure drop of the liquid. Therefore, the heat pipe thermal performance is strongly

dependent on the wick structure and the ratio K/R_{eff} is considered as a key design parameter for characterising the capillary limit.

Numerous studies on sintered powdered wicks have been carried out to find the optimum geometric properties including wick pattern, size, thickness and shape, as well as fabrication parameters such as the effect of sintering time and temperature. The use of patterned or multi-scale wicks has been proposed by Semenic and Catton [248], who suggested using biporous wicks to improve capillary and boiling performance. The rationale behind is that smaller-scale pores tend to generate large capillary pressure to draw the liquid flow and provide sites for film evaporation or bubble nucleation, while larger-scale pores have low flow resistance for the bulk liquid transport and create vapour ventilation paths due to high permeability. According to Weibel et al. [232], sintered powder wicks exhibit an optimum particle size if a wick thickness is given. For a constant powder size, thicker wick extended the maximum dryout heat flux [248]. The layer thickness-to-particle diameter ratio $t/3 = 3.85$ (0.95 mm/247 μm) was found by Chien and Chang [281], suggested to be the optimum value. Wang and Peterson [282] investigated the thickness effect in relation to the maximum capillary limit by using a two-dimensional analytical model of a square sintered powered evaporator. Increasing the wick thickness resulted in larger capillary limit but led to high surface superheat limiting the evaporative heat flux. Tsai and Lee [283, 284] studied the structural differences and powder shape effect in limiting the evaporative heat transfer. They compared the sintered dendritic-powder wicks with spherical structure and found that dendritic-powder wicks achieved higher heat fluxes at the same superheat level, although low in permeability and effective thermal

conductivity. The reason for this is due to thin-film evaporation. As pointed out by Hanlon and Ma [285] and Wang et al. [286], thin-film evaporation attribute to more than 50% of the overall evaporative heat flux with only small temperature differences. Inter-pores in dendritic sintered powder structure help divide working liquid into smaller volumes thus promoting more menisci and thin films.

In addition to understanding those parametric effects, visual observation of the wicks is given to provide a deep insight into the capillary performance. For instance, Byon and Kim [287] used sintered glass powder wicks and a high speed camera to visualise the capillary flow. This was done by measuring the height of the rising liquid as a function of time and a comparison between biporous and monoporous wicks was made. Their semi-analytic model suggested that to achieve an optimal capillary performance, the cluster size should be 4 – 6 times larger than the particle size. For biporous wicks notably, the effect of gravity on the capillary performance is more cluster size-dependent than particle size-dependent. Weibel et al. [288] visually observed vapour formation characteristics during evaporation/boiling from homogeneous and modified wick structures, and proposed an approach to improve thermal performance by integrating carbon nanotube (CNT) arrays on to the sintered powder. The boiling curve obtained from such method shows that lower superheat for boiling incipience was resulted and lower overall thermal resistance can be achieved at low heat fluxes. Other visualisation methods of the wick capillarity including infrared thermal imaging [251, 289] and fluorescent dye and ultraviolet light characterisation [290] have also been investigated.

Espinosa et al. [291] studied the thermophysical properties of the sintered wicks from fabrication effect. Sintering temperature and time were investigated, and results show that a good agreement with 15% uncertainty was achieved for sintering temperatures below 550°C, and 26% for temperature up to 950°C. In addition, they pointed out that Kozeny-Carman correlation overpredicts the permeability, and the modified Young-Laplace equation has less than 5% accuracy in measuring capillary pressure. Small differences in powder pouring, particle packing, and powder handling prior to sintering all contribute to random sintered wick structure with different thermal conductivities. A ‘two-sphere model’ for estimating thermal conductivity was developed and a thermal conductivity chart in relation to the sintering temperature and time was provided. These two factors have also been investigated by Jiang et al. [292], and they argued that sintering neck growth, porosity and shrinkage can be greatly affected by sintering temperature and time. The proper sintering temperature suggested for 159 μm sintered wick is 950°C, and 900°C for 81 μm and 38 μm . The proper time for 0.45 mm and 0.6 mm thick wicks is 3 hours while for 0.75 mm thick, 1 hour. In addition, Choi et al. [293] prepared sintered porous wicks that meet the design criteria via low temperature sintering method with an isothermal sintering and active cooling process. Capillary pressure was increased while the impact on permeability was minimised.

Based on above findings of sintered powder wicks, the design for current novel heat pipe wicks is encouraged to follow geometric properties and fabrication parameters in relation with capillary pressure and wick permeability.

7.2 Novel Heat Pipe Wick

7.2.1 Potential Mechanism

The wick structure incorporates with a low level of hierarchy structure and the intension of creating such wick structure has been explained. By varying surface roughness and wick pore sizes at each section of the heat pipe and along the heat pipe, wettability at the evaporator as well as the capillary pumping force generated from the condenser to the evaporator will be presumably improved. A two-scale sintered powder (small pores on the top and larger pores at the bottom) in a grooved form at the evaporator is shown, and a slope is created along the heat pipe (three sections with different stack heights) enhancing capillary pumping force (Fig. 7.2). Grooved structure gives lands or channels to help the formation of continuous layer of longitudinal liquid [253], while the sintered wicks eliminates the chances of non-uniform circumferential liquid distribution [254]. Non-uniform circumferential liquid distribution has always been found in grooved wicks, both in evaporator and condenser, driving the imbalance of some grooves carrying excess liquid or none. It is the subject of the present invention to characterise corresponding wick structures for each section namely evaporator, adiabatic and condenser to achieve expected individual functionality, to maximise the overall heat pipe performance in dealing with limited space or anti-gravity, to optimise the balance of gravity, liquid and vapour pressure drops, and to compromise the resultant counter effects in terms of wicks pore size, structure and thickness.

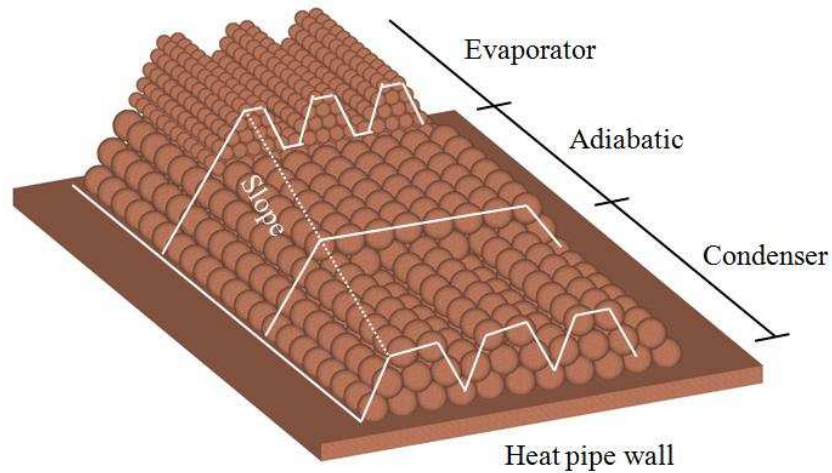


Figure 7.2: Novel integral wick design for evaporator, adiabatic and condenser in flat heat pipes.

For evaporator wicks, distributed liquid supply, effective vapour removal and a short conduction path are considered for optimal design. Limited high flux heat removal is often found in liquid-filled evaporator (large thermal resistance) unless it is very thin [255, 294]. In this evaporator (Fig. 7.3), larger pores will be constructed along the pipe wall with smaller pores on top forming groove structure. Those grooves provide short heat conduction paths, and the arrayed wick structure establishes several acute-angle portions where capillary forces are at large. This helps induce larger capillary pressure drop along the heat pipe. Fig. 7.4 illustrates how liquid forming meniscus bridges at those acute-angles, which develop a negative pressure inducing an intrinsic attractive force. These menisci help the evaporator achieving maximum wetting ability. The layer that consists of larger pores benefits liquid return and distribution, and decreases the chances of nucleate boiling; whereas the layer on the top, which has smaller pores, enhances the ability of lifting the liquid, i.e. maximised wetting.

For adiabatic section, uniform sintered powder size is distributed with medium stack height. Only larger sintered powders are formed with no grooves. This is to provide a transitional path for liquid return from the condenser to the evaporator. As to the condenser, relatively larger pores are needed using groove structure to increase surface area while obtaining great ability in absorbing latent heat of vaporisation. Compared to the evaporator, the pore size should be larger, and the channels created should be smooth to reduce wetting and pressure drop, both from the returning liquid and from the vapour liquid shear forces. Additionally, space for vapour flow passage is maximised in each section eliminating the concern of clogged vapour space after flattening. A slope is created along the heat pipe from the evaporator to the condenser enhancing capillary pumping force especially under anti-gravity condition.

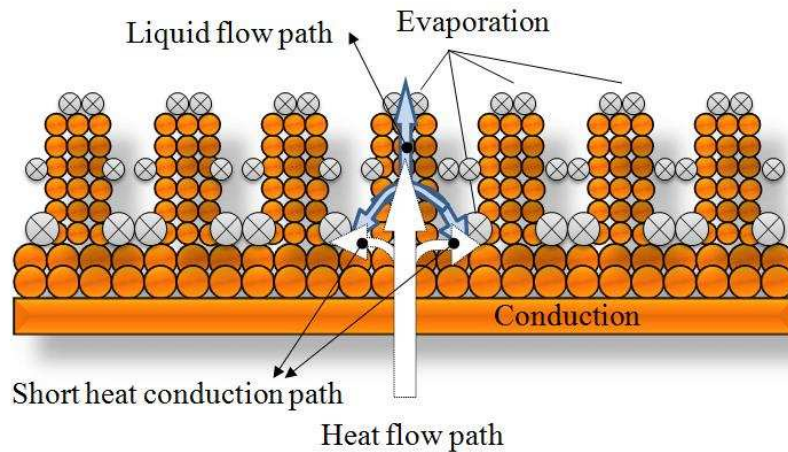


Figure 7.3: Heat and liquid flow path in the evaporator.

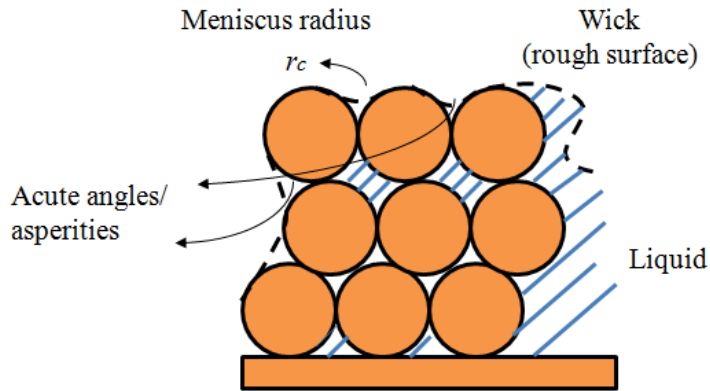


Figure 7.4: Liquid forming meniscus bridges at acute-angles among wick pores.

7.2.2 Mathematical Model

7.2.2.1 Porosity

For such integral wick structure with two-scale sintered powders forming grooves, the effective radius is determined by the sintered wicks and the meniscus is assumed to be a circle, with radius nr and r . The model shown in Fig. 7.5 can be used to calculate the effective capillary radius r_c in both tight and loose alignment.

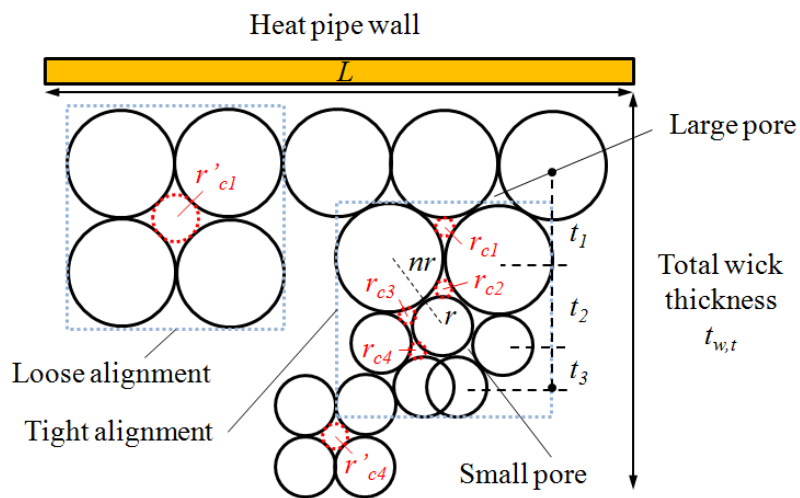


Figure 7.5: Illustrating wick pore distribution scenarios.

For tight alignment, the effective capillary radius r_{c1} among three equally large powders with radius nr is as follows,

$$r_{c1} = \frac{(2 - \sqrt{3})nr}{\sqrt{3}} \quad (7.2)$$

Similarly, for r_{c4} among three equally large powders with radius r ,

$$r_{c4} = \frac{(2 - \sqrt{3})r}{\sqrt{3}} \quad (7.3)$$

For effective capillary radius r_{c2} among two large powders with radius nr and one smaller copper powder with radius r ,

$$r_{c2} = \frac{(n+1) - \sqrt{2n+1}}{(n-1) + \sqrt{2n+1}} \cdot r \quad (7.4)$$

For effective capillary radius r_{c3} among two small powders with radius r and one large copper powder with radius nr ,

$$r_{c3} = \frac{(2n^2 + 2n) - 2n\sqrt{n^2 + 2n}}{2 - 2n + 2\sqrt{n^2 + 2n}} \cdot r \quad (7.5)$$

For loose alignment, the effective capillary radius r'_{c1} and r'_{c4} among three equally large and small copper powders respectively is as follows,

$$r'_{c1} = (\sqrt{2} - 1) \cdot nr \quad (7.6)$$

$$r'_{c4} = (\sqrt{2} - 1) \cdot r \quad (7.7)$$

It can be deduced from Fig. 7.5 that the number of copper powders on each layer with large and small powders is $L/2nr$ and $L/2r$ respectively. The centre distance t between adjacent layers of large or small powders and large and small powders in axial direction is:

For tight alignment,

$$t_1 = 2nr \cos(\pi/6) \quad (7.8)$$

$$t_2 = 2(n+1)r \cos \theta \quad (7.9)$$

$$t_3 = 2r \cos(\pi/6) \quad (7.10)$$

For loose alignment,

$$t'_1 = 2nr \quad (7.11)$$

$$t'_3 = 2r \quad (7.12)$$

Hence, the wick porosity known as the void fraction for such sintered wick in a flat heat pipe can be determined.

If only tight alignment is present, assuming the thickness of the wicks with large pores is $(1/\alpha)t_{w,t}$ and small pores with equivalent thickness $(1/\beta)t_{w,t}$ in which $(1/\alpha)t_{w,t} + (1/\beta)t_{w,t} + t_2 = t_{w,t}$

$$\begin{aligned} \varepsilon = 1 - \frac{(L/2nr) \cdot (t_{w,t} / \alpha) \cdot \frac{4}{3} \pi (nr)^3 + (L/2r) \cdot (t_{w,t} / \beta) \cdot \frac{4}{3} \pi (r)^3 + (L/2r_{ave}) \cdot (t_2 / t_2) \cdot \frac{4}{3} \pi (r_{ave})^3}{L \cdot 2nr \cdot (t_{w,t} / \alpha) + L \cdot 2r \cdot (t_{w,t} / \beta) + L \cdot 2r_{ave} \cdot t_2} \quad (7.13) \end{aligned}$$

Put Eq. 7.8 – 7.10 into Eq. 7.13 and assuming t_2 is negligible enough compared to $t_{w,t}$, the theoretical minimum porosity would be:

$$\varepsilon \approx 1 - \frac{\frac{1}{3}\pi(n/a + 1/\beta)}{\sqrt{3}(n/a + 1/\beta)} = 1 - \frac{\frac{1}{3}\pi}{\sqrt{3}} = 39.5\% \quad (7.14)$$

Similarly, for loose alignment only, the theoretical minimum porosity is:

$$\varepsilon \approx 1 - \frac{\frac{1}{3}\pi(n/a + 1/\beta)}{2(n/a + 1/\beta)} = 1 - \frac{\pi}{6} = 47.6\% \quad (7.15)$$

7.2.2.2 Permeability

The liquid capillary flow within the wick is much more complicated than that through a porous medium, but the underlying physics they offer is similar. Capillary effects are always accounted by two mechanisms: the permeability and the capillary pressure due to surface tension. In order to simplify the discussion, the porous medium can be taken as stable, inert and nondeformable, and the liquid within is incompressible. Photomechanical and thermal effects are neglected. A control volume method is adopted where the amount and identity of matter in that control unit may change with time, but the shape and position of the volume remain fixed. A capillary tube model suggested by Bear [295] will be established where the capillary tubes are non-uniform. Fig. 7.6 shows such configurations under two different flow paths in a heat pipe with diversities in diameters over one direction. The models only give the permeability K in one direction, which is acceptable because the main flow path in that direction is fairly predominant.

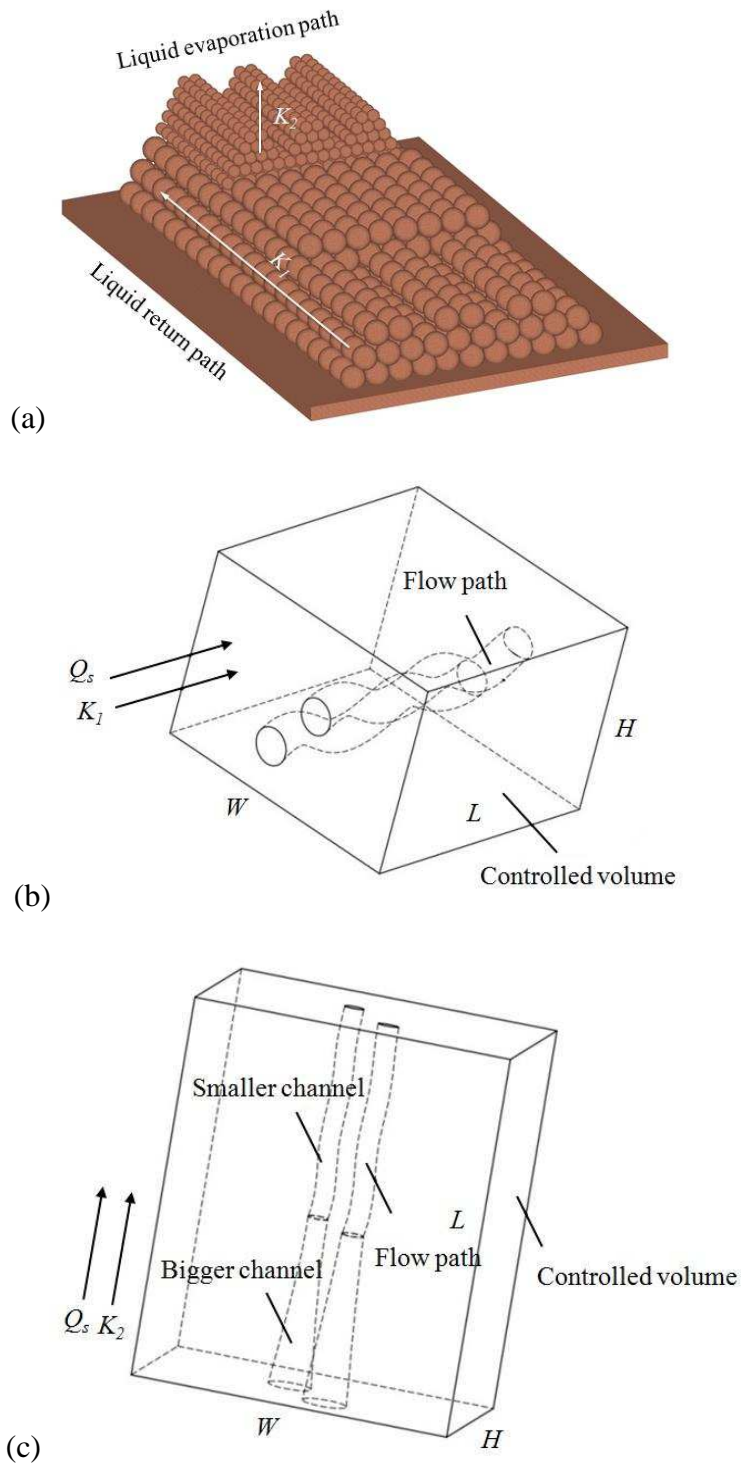


Figure 7.6: Illustrating (a) liquid flow paths in the heat pipe; and schematic of a unit for (b) a one-scale sintered copper powder porous medium from the condenser to the evaporator (liquid return path: one flow direction); (c) a two-scale sintered copper powder porous medium in heat pipe evaporator (liquid evaporator path: one flow direction).

From Hagen-Poiseuille's Law, which governs the steady flow via a straight capillary tube of diameter δ in one direction,

$$Q_s = -\frac{\pi\delta^4 \rho g}{128\mu} \cdot \frac{\partial\phi}{\partial s} \quad (7.16)$$

Where

Q_s – total fluid flow discharge rate

s – tube length

μ – Newtonian fluid viscosity

According to Darcy's law,

$$Q_s = -\frac{KA}{\mu} \cdot \frac{\Delta p}{l} \quad (7.17)$$

The specific discharge through cross section area WH in the controlled volume block for N tubes,

$$\dot{q}_s = Q_s / WH = -N \frac{\pi\delta^4 \rho g}{128\mu} \cdot \frac{\partial\phi}{\partial s} \quad (7.18)$$

Assuming the diameters over one direction in the tube is not uniform,

$$\dot{q}_s = -\sum_{i=1}^m N_i \frac{\pi\delta_i^4 \rho g}{128\mu} \cdot \frac{\partial\phi}{\partial s} \quad (7.19)$$

Hence,

$$K = \sum_{i=1}^m N_i \frac{\pi\delta_i^4}{128\mu} \quad (7.20)$$

$$\phi_i = N_i \frac{(\pi\delta_i^2 / 4)L_1}{L_1} = N_i (\pi\delta_i^2 / 4) \Rightarrow N_i = \frac{4\phi_i}{\pi\delta_i^2} \quad (7.21)$$

Therefore,

$$K = \sum_{i=1}^m \frac{\phi_i \delta_i^2}{32\mu} \quad (7.22)$$

7.2.2.3 Capillary Pressure and Capillary Speed

Fig. 7.7 shows the schematic diagram of a micro-scale capillary with vapour-liquid interfaces (or fluid-fluid interface), the unit vector F exerted on these two fluids phases, and interfaces between the liquid or vapour phase and the solid copper powders. The shape of the fluid meniscus is determined by the imbalance between the surface tension and the solid fluid adhesion force. The movement of the interface makes the equilibrium position to be adjusted at all times. The phenomenon ('drainage' or 'imbibition equilibria') helps to identify the maximum and minimum capillary pressure [296].

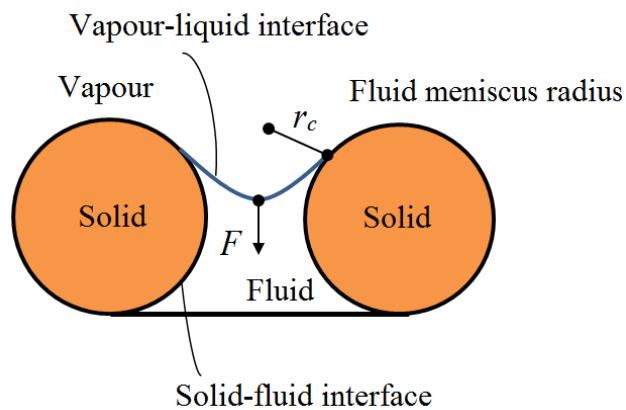


Figure 7.7: Microscale capillary with solid-fluid and fluid-fluid interfaces.

In our integral wicks, the radius of curvature of the menisci in evaporator is small and decreases when the liquid evaporates. It becomes bigger due to the presence of larger pore size at the condenser and also when the vapour condenses. The resultant capillary pressure across the heat pipe is described below:

$$\Delta p_c = 2\sigma \left(\frac{\cos \theta_e}{r_e} - \frac{\cos \theta_c}{r_c} \right) \quad (7.23)$$

$$\Delta p_c = \frac{2\sigma}{r_{\text{eff}}} \quad (7.24)$$

where R represents the effective radius of the wick, θ the contact angle, the maximum value can be achieved when assuming perfect wetting, i.e. $\cos \theta = 1$, $\cos \theta = 0$. The effective radius R is a critical factor in determining capillary head and can be estimated from hydraulic radius r_h ,

$$r_h = \frac{V_p}{S\rho V_s} = \frac{\varepsilon}{S\rho(1-\varepsilon)} \quad (7.25)$$

The capillary speed $\frac{dh}{dt}$ has been used to evaluate the performance of heat pipe wicks. h is the capillary rise distance, μ the water viscosity, ε the porosity, and ρ water density. It can be obtained by a momentum balance, where the capillary pressure equals to the total pressure loss composed of the viscous friction loss and hydrostatic pressure generated by gravity,

$$\Delta p_c = \frac{\mu\varepsilon}{K} h \frac{dh}{dt} + \rho gh \quad (7.26)$$

Therefore,

$$\frac{dh}{dt} = \frac{K}{\mu\varepsilon} \left(\frac{2\sigma}{r_{\text{eff}}} \cdot \frac{1}{h} - \rho g \right) \quad (7.27)$$

The capillary pressure can be also obtained when taking porosity ε into consideration:

$$P_c = \sigma \cos(\theta) S \rho_s \left(\frac{1-\varepsilon}{\varepsilon} \right) \quad (7.28)$$

where σ is the surface tension at the liquid-vapour interface, θ the contact angle, S the specific surface area, which can be approximated by $S = \frac{6\lambda}{\rho D}$ (λ is a particle shape factor, $\lambda = 1$ for spherical powder, $1 < \lambda < 2$ for irregular

powders [297]; D the wick powder diameter), and ρ_s the density of the solid.

Hence for spherical powder, the effective radius is:

$$r_{\text{eff}} = r_h = \frac{\varepsilon D}{6(1 - \varepsilon)} \quad (7.29)$$

Therefore,

$$\frac{dh}{dt} = \frac{K}{\mu\varepsilon} \left(\frac{12\sigma(1 - \varepsilon)}{\varepsilon D} \cdot \frac{1}{h} - \rho g \right) \quad (7.30)$$

7.2.3 Results and Discussions

Adopting hierarchical structure in evaporator, which is a two-scale wick pore distribution, causes low volume porosity, although grooved structure tends to increase the overall porosity and permeability. In this analysis, a range of effective wick pore radius from 25 μm to 200 μm will be considered. Fig. 7.8 presents capillary pressure P_c versus effective radius at two assumed porosities, $\varepsilon_1 = 0.4$ (based on previous calculation, Eq. 7.14) for the evaporator and $\varepsilon_2 = 0.75$ for the condenser (largest porosity expected to get for sintered power wicks [298]). To note, the actual porosity is much more complicated and it depends on several factors including wick size and properties, sintering temperature and time, and fabricating methods.

Large wick pore size makes capillary pressure insignificant, and bigger porosity results in low capillary pressure. At a lower range of wick pore size, capillary pressure varies significantly especially under low porosities; whereas at a higher range, the value of capillary pressure does not change dramatically no matter how big the porosity is. The capillary pressure drop across the heat pipe can be obtained if the effective pore radii in both evaporator and

condenser are known. To quantify the effect, the effective pore radius in the evaporator due to two-scale pore size distribution can be taken as 40 μm , and for the condenser, 100 μm . The resultant capillary pressure drop is 7,175 Pa. If reducing the pore size in the evaporator to 25 μm while maintaining at the same porosity, the total pressure drop increases 4,725 Pa. If increasing the pore radius in the condenser to 200 μm , only 350 Pa is increased. This indicates the dominant role the evaporator plays, such that the two-scale pore size distribution shall be carefully optimised to achieve good porosity and permeability.

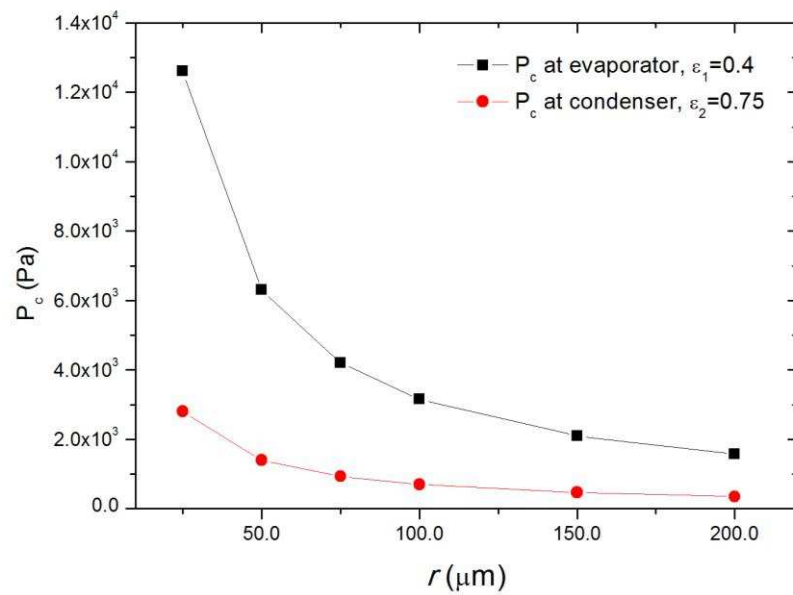


Figure 7.8: Capillary pressure P_c versus wick pore radius r (25~200 μm) at two volume porosities $\epsilon_1 = 0.4$ and $\epsilon_2 = 0.75$, $\eta = 8.94 \times 10^{-4}$ Pa·s, $\sigma = 0.07$ N/m, $\lambda = 1$, $\rho = 5.61 \times 10^3$ kg/m³ (for sintered copper powder density [297]).

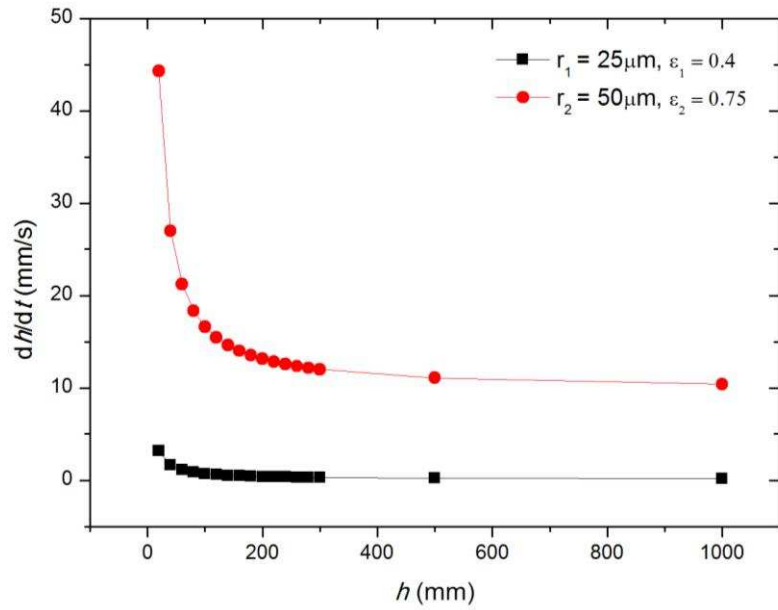


Figure 7.9: Calculated capillary speed dh/dt versus height h (gravity-assisted) at $r_1 = 25 \mu\text{m}$, $\varepsilon_1 = 0.4$, $r_2 = 50 \mu\text{m}$, $\varepsilon_2 = 0.75$, $\eta = 8.94 \times 10^{-4} \text{ Pa}\cdot\text{s}$, $\sigma = 0.07 \text{ N/m}$, $\lambda = 1$, $\tau = \sqrt{2}$.

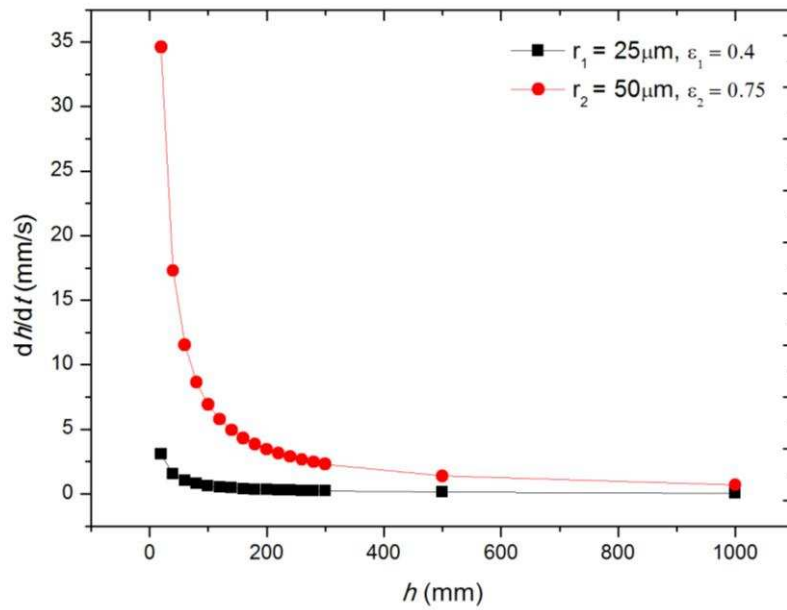


Figure 7.10: Calculated capillary speed dh/dt versus height h (horizontal) at $r_1 = 25 \mu\text{m}$, $\varepsilon_1 = 0.4$, $r_2 = 50 \mu\text{m}$, $\varepsilon_2 = 0.75$, $\eta = 8.94 \times 10^{-4} \text{ Pa}\cdot\text{s}$, $\sigma = 0.07 \text{ N/m}$, $\lambda = 1$, $\tau = \sqrt{2}$.

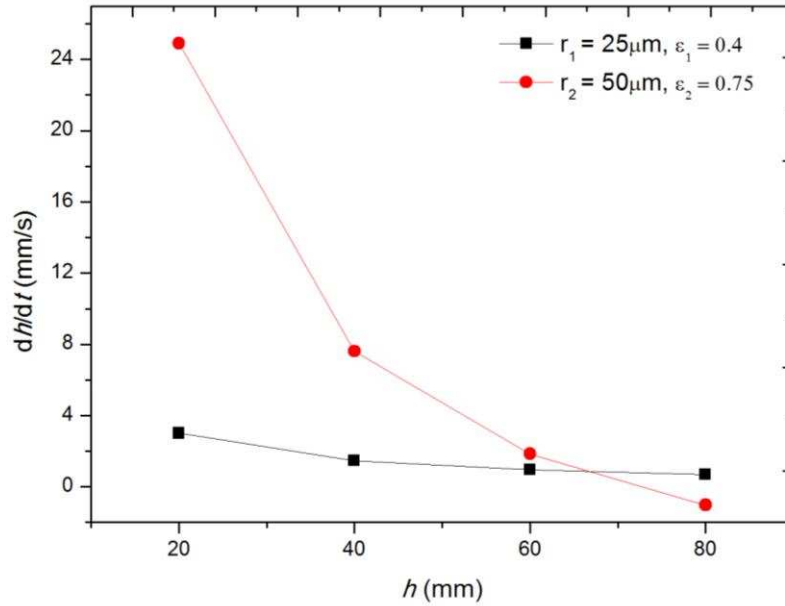


Figure 7.11: Calculated capillary speed dh/dt versus height h (anti-gravity) at $r_1 = 25 \mu\text{m}$, $\varepsilon_1 = 0.4$, $r_2 = 50 \mu\text{m}$, $\varepsilon_2 = 0.75$, $\eta = 8.94 \times 10^{-4} \text{ Pa}\cdot\text{s}$, $\sigma = 0.07 \text{ N/m}$, $\lambda = 1$, $\tau = \sqrt{2}$.

In order to evaluate the capillary speed, Fig. 7.9 – 7.11 demonstrate the calculated capillary speed dh/dt versus height h with suggested parameters under three conditions (gravity-assisted, horizontal, and anti-gravity condition). Particle size and porosity under similar pore morphology (same tortuosity factor τ , same shape factor λ , and same density of sintered powders ρ) have been investigated. The effective radius in evaporator r_1 with two-scale pore size is taken as $25 \mu\text{m}$, and the uniform pore size in condenser r_2 is $50 \mu\text{m}$. Results imply that coarse or big powders are favourable for capillary speed. A particle size of $50 \mu\text{m}$ has a much faster capillary rise rate than that with a mean dimension of $25 \mu\text{m}$. Increasing porosity enhances the capillary rising rate at lower height and maintains at a high rate of capillary rise under gravity-assisted condition even at high range of height. A dramatic drop can be seen under anti-gravity condition from 40 mm to 80 mm indicating the

significant role played by gravity. Additionally, for anti-gravity condition, large pores result in high speed of capillary rise changing from 24 mm/s to 4 mm/s over the height range of 20 mm to 60 mm. For smaller pores with low porosity, capillary speed maintains steady, at 2 mm/s to 3mm/s over the range of 20 mm to 80 mm.

7.3 Fabrication

Fig. 7.12 – 7.15 show the schematic of the novel FPHP and fabricated samples. It consists of an evaporator, a condenser and an adiabatic section in between. The mechanism is similar to conventional cylindrical heat pipes, which transfers heat from one end to the other via two-phase heat transfer loop. The size of the FPHP is 105 mm long, 65 mm wide and 4 mm thick. The wick structure is sintered-grooved composite structure with 150 – 200 μm copper wicks forming narrow and tall grooves ($0.6 \times 1.0 \text{ mm}^2$) in the evaporator, and wide and flat grooves ($0.8 \times 0.8 \text{ mm}^2$) in the condenser. A tapered structure along the FPHP was created aiming at improved heat transfer ability. Small pores and high pitch wicks increase the ability in lifting the liquid achieving maximum wetting at the evaporator and provide large evaporative surface area to increase latent heat of vaporisation. Low pitch wicks create enough smooth lands reducing wetting and pressure drop, and subsequently enhance the absorption rate of late heat of vaporisation. The base thickness for the wicks is 0.2 mm. 4 copper pillars (size $2 \times 4 \text{ mm}^2$) were constructed at the centre of the FPHP for structural support. The amount of de-ionized water was optimised to be 3.5 ml for this particular heat pipe.

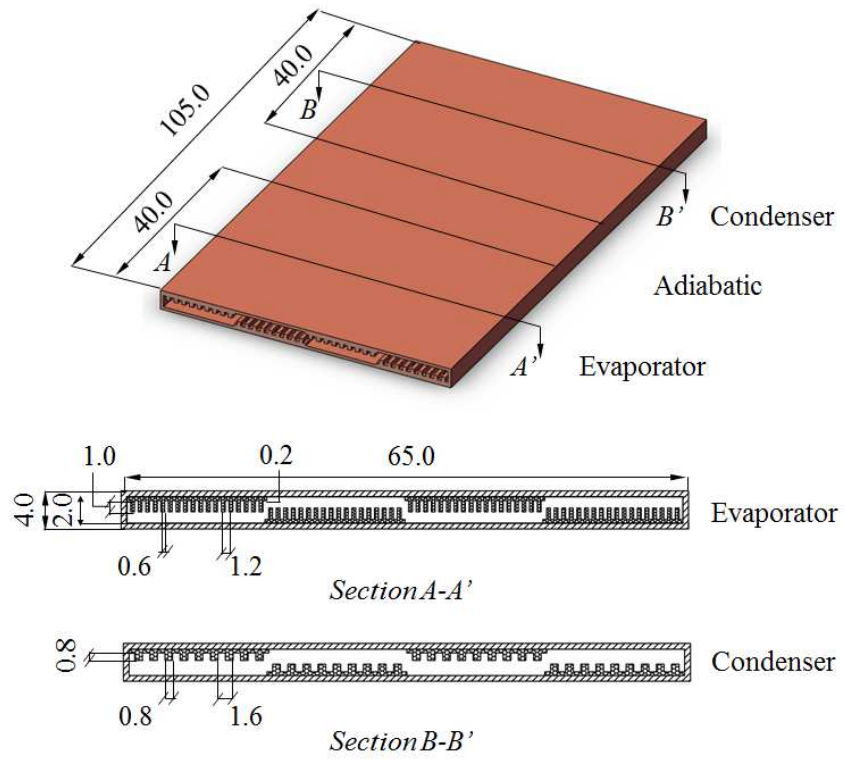


Figure 7.12: Schematic of the present flat plate heat pipe (FPHP) with dimensions in mm.

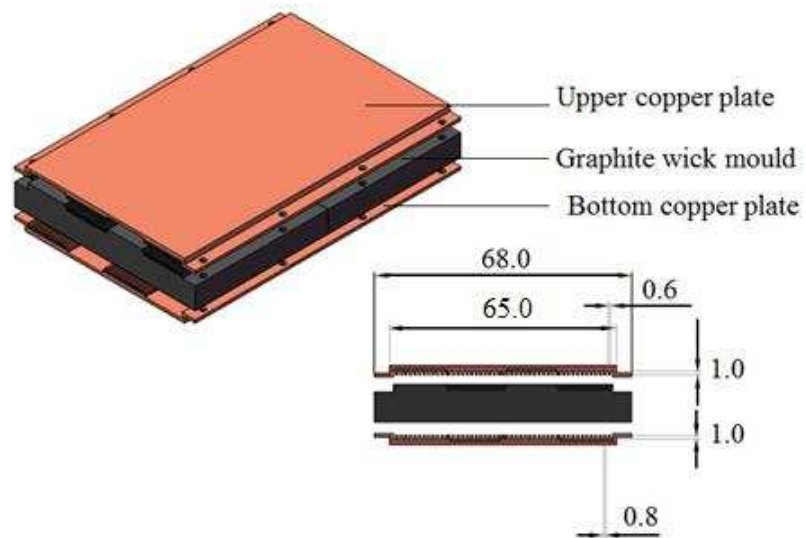


Figure 7.13: FPHP fabricating assemblies with dimensions in mm.

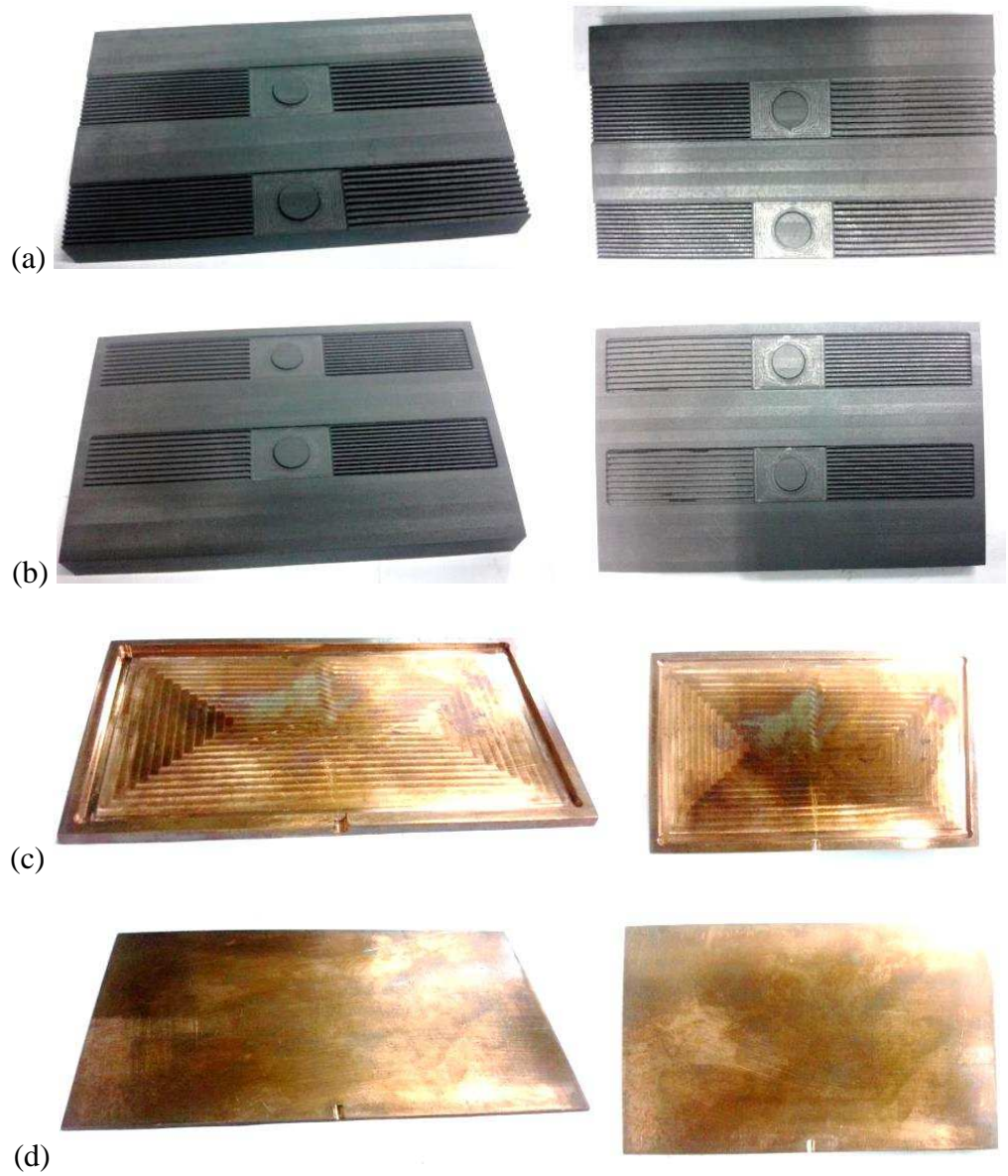


Figure 7.14: FPHP parts: (a) upper wick mould; (b) bottom wick mould; (c) upper copper plate; (d) bottom copper plate.

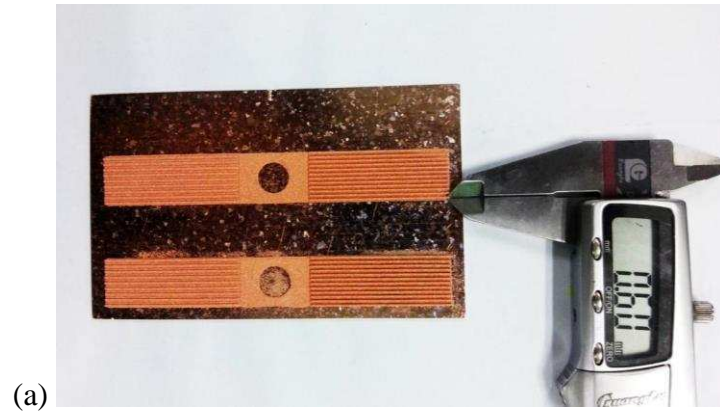


Figure 7.15: Fabricated samples: (a) upper plate; (b) bottom plate; (c) final product.

The main fabrication steps will be briefly described below.

- Cleaning and oven drying

The impurities on upper/lower half copper plate of the FPHP were removed by an ultrasonic vibrator ($75 \pm 5^\circ\text{C}$, 30 minutes) and organic solvent detergent. It will then be put into an oven ($90 \pm 5^\circ\text{C}$, 30 minutes) to dry the surface completely.

- Powder filling

Filling the graphite mould with $150 - 200 \mu\text{m}$ copper powder and give it a good shake to ensure powders with large radius (heavy) will precipitate at the evaporator bottom. The condenser mould was inserted with $200 \mu\text{m}$ copper powders only.



Figure 7.16: Fabrication in process – powder filling.

- Holding and sintering

Hold the moulds and the upper/lower plate, and put them into a sintering furnace at 960°C , N_2 , H_2 environment for 6 hours.



Figure 7.17: Fabrication in process – holding.



Figure 7.18: Fabrication in process – furnace sintering.

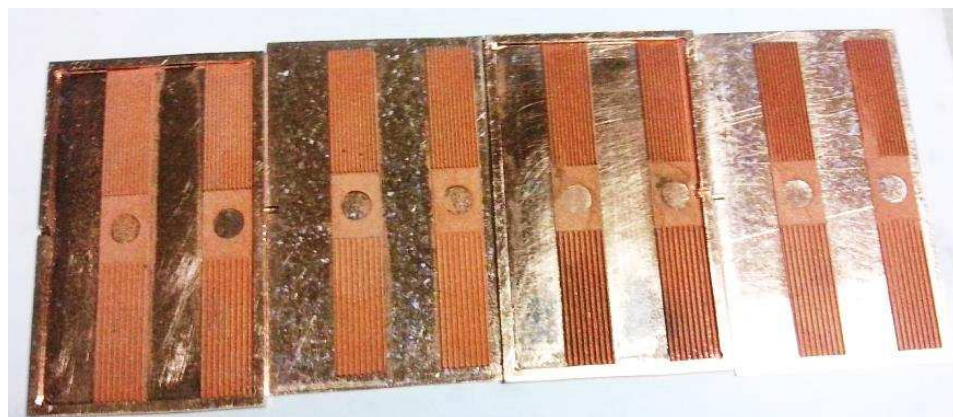


Figure 7.19: Fabrication in process – upper and bottom plates after sintering.

- Inserting copper pillars

4 copper pillars were positioned in the centre of the FPHP. The pillars were used to strengthen the inner structure of the FPHP.

- Welding

Hold the upper/lower plate and the pillars, welding the product at the furnace at 850°C, N₂, H₂ environment (3 Mps, 15 l/min) for 2 hours.



Figure 7.20: Fabrication in process – holding sintered upper and bottom plates.



Figure 7.21: Fabrication in process – product after welding.

- Inserting tail pipe and welding

Insert the tail pipe into the FPHP for future liquid filling purpose. The pipe welding will take place in a high frequency (30 KHz, vacuum) welding machine for 1 minute.



Figure 7.22: Fabrication in process – product after inserting tail pipe and welding.

- Annealing

The annealing will be made in annealing furnace at 500°C, N₂, H₂ environment (15 l/min).

- Evacuating and liquid filling



Figure 7.23: Fabrication in process – water filling trials.

A vacuum pump was used to evacuate the FPHP down to 0.075 torr. The working fluid requires high purification to avoid non-condensable gases

during operation, and this was done via distillation. Once the liquid was in purified condition, it was weighed by a precision digital scale (readability: 0.002 g) and was injected to the wicks through an injector (readability: 0.01 g). After several trials, the optimum water filling was 3.50 g.

- Degassing

The heat pipe will be degassed under 100°C to further eliminates the unwanted gas inside the FPHP. To note, the degassing process may extract a certain amount of water filled in the wicks. The measured final amount of water inside the wick after degassing was approximately 2.00 g.



Figure 7.24: Fabrication in process – (a) 1st degassing equipment; (b) 2nd degassing equipment.

- TIG welding

TIG welding was adopted to seal the FPHP completely by crimping and cold welding the tail pipe (0.62 s).



Figure 7.25: Fabrication in process – TIG welding machine.

Scanning electron microscopy was used to study the surface and structures of the wick samples. The specimens were examined using a Philips scanning electron microscope (FW6800/70) at an accelerating voltage of 20 kV. Fig. 7.26 and Fig. 7.27 show the morphology of the fabricated wick sample at the evaporator and the condenser. Fig. 7.28 demonstrates the surface morphology of the wick particles (150 – 200 μm dendritic powders) sintered at 960°C at four locations: evaporator substrate, evaporator pillar, condenser substrate, and condenser pillar.

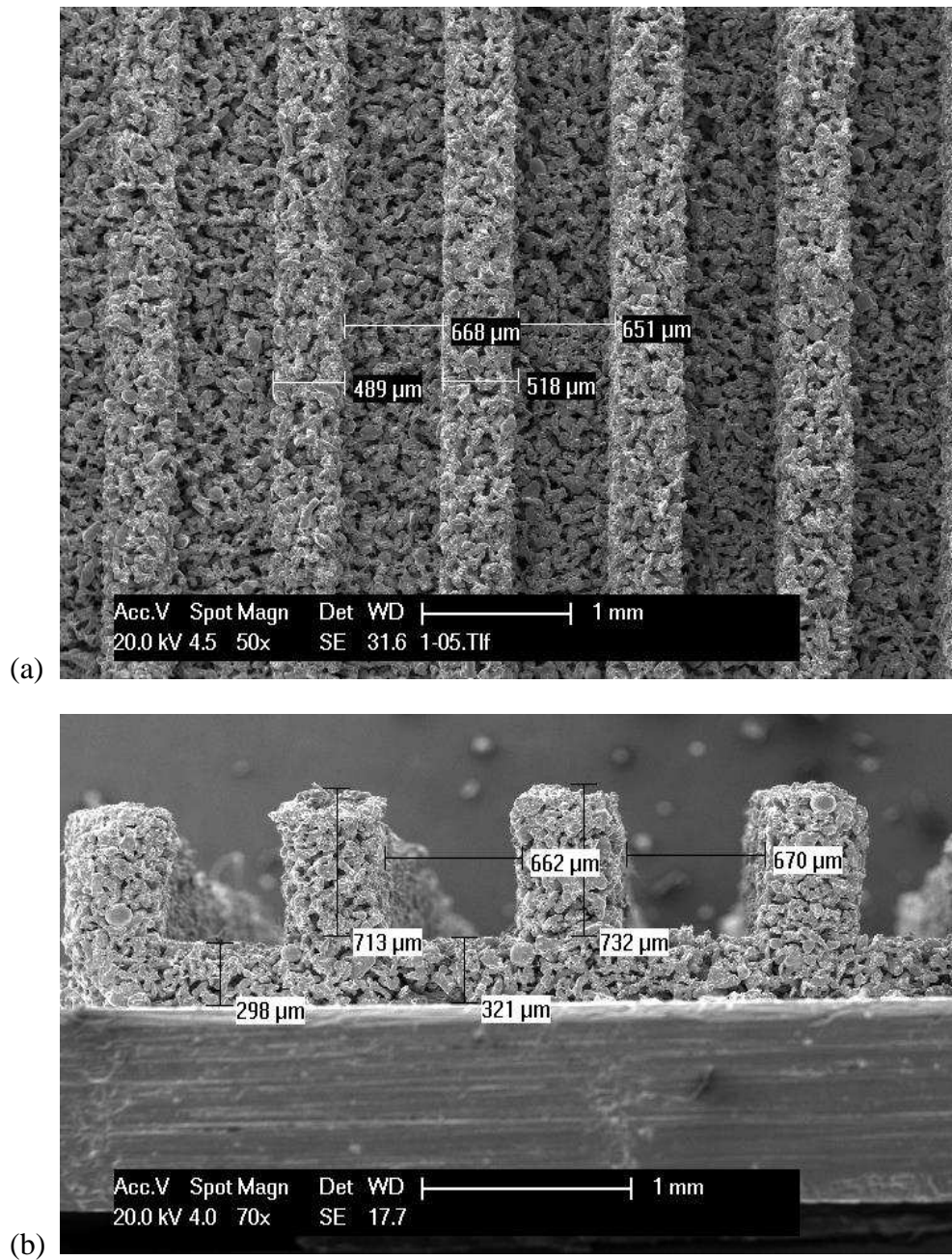


Figure 7.26: SEM micrographs showing the integral wick sample (150 – 200 μm dendritic powders sintered at 960°C at the evaporator: (a) planar view; (b) profile view.

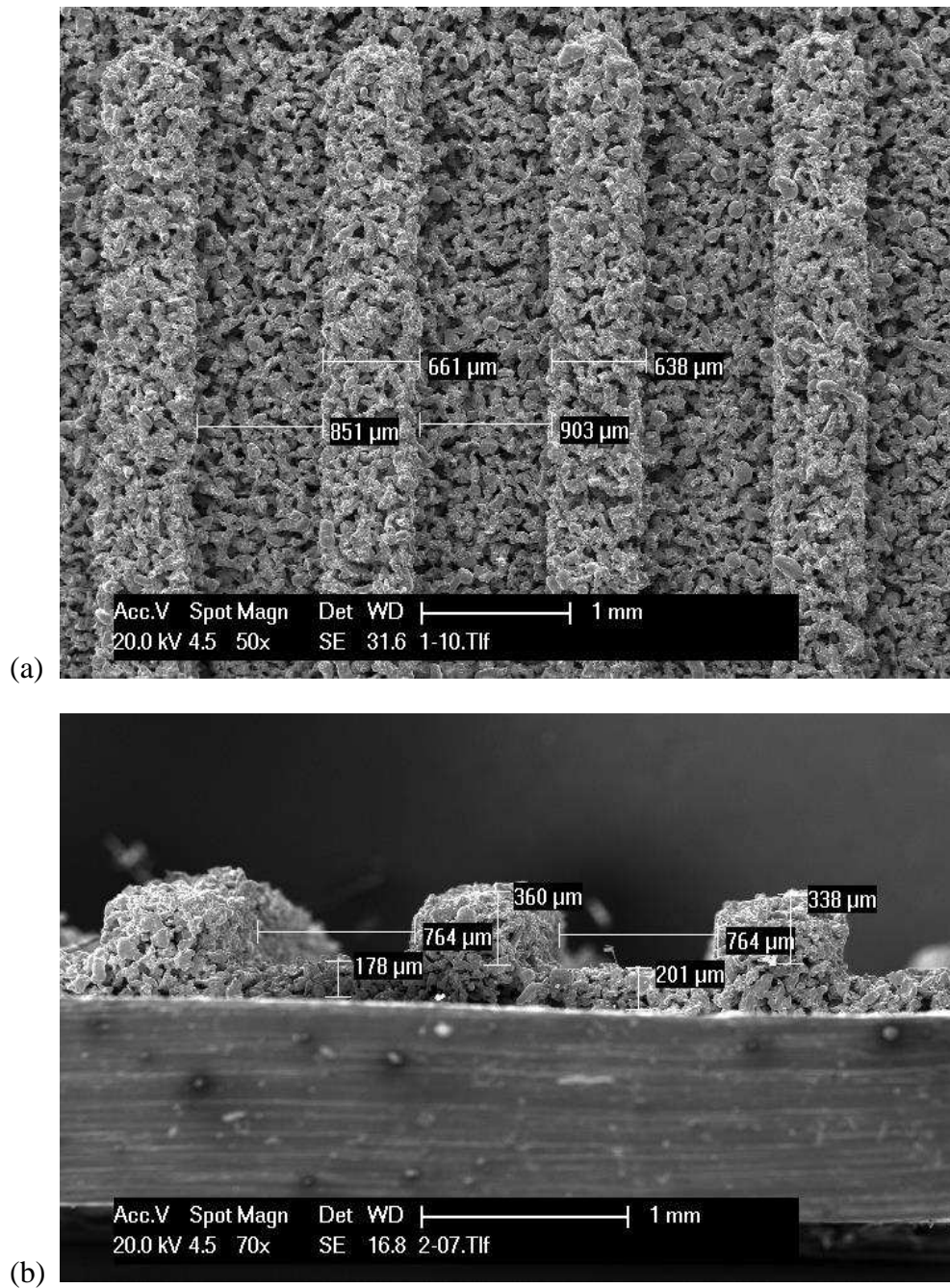
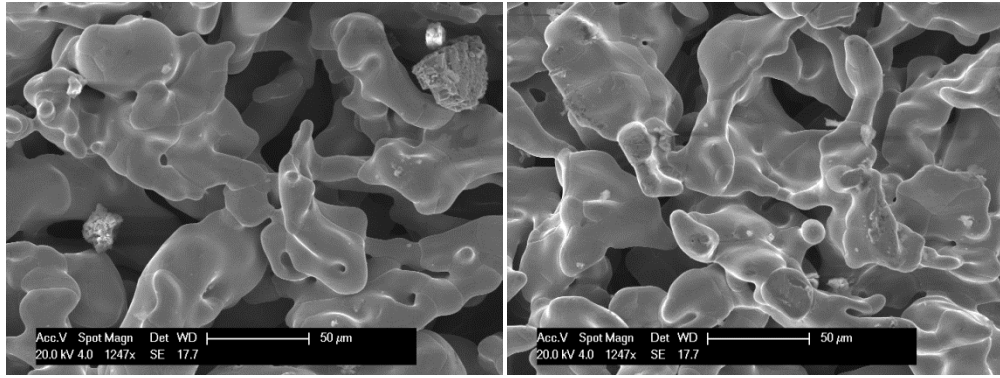
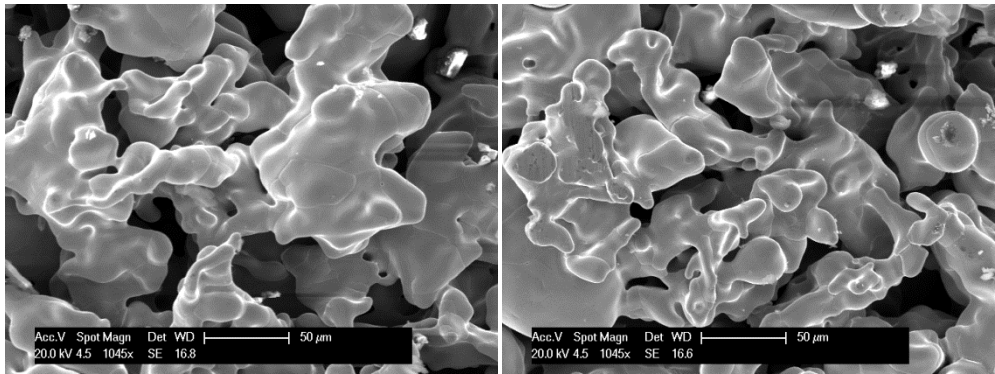


Figure 7.27: SEM micrographs showing the integral wick sample (150 – 200 μm dendritic powders sintered at 960°C at the condenser: (a) planar view; (b) profile view.



(a)

(b)



(c)

(d)

Figure 7.28: SEM micrographs showing the surface morphology of the wick particles (150 – 200 μm dendritic powders sintered at 960°C : (a) evaporator substrate; (b) evaporator pillar; (c) condenser substrate; (d) condenser pillar.

7.4 Summary

This chapter introduces a novel heat pipe wick structure inspired by biomimetic capillary in hierarchical structure. Some fundamental studies of surface wetting and capillary effect from nature have been reviewed. It is the hierarchical structure that helps the species to capture water from humid air based on various characteristic length scales. Contact angle and capillary effect associated with hierarchical structure have been discussed, and a recent study

of MRI scanning of live plants was introduced. This method provides the possibility of visualising how plants move water upwards through the inner structure of vascular system occurring in vivo, and obtains the rate of water transport in the xylem vessel. Significantly, the idea of applying hierarchical structure to heat pipe wicks has been realised and a novel integral wick structure inspired by such structure was demonstrated in detail. With provision of the numerical results in terms of capillary pressure and capillary rise rate, the fundamental behaviour of the biomimetic inspired wick can be identified reflecting the role that biomimetics plays in modern heat pipe technology. Fabrication process was then introduced for this particular heat pipe, assisted by scanning electron microscopy to study the surface and structures of the fabricated wick samples.

Chapter 8

Conclusions and Future Work

8.1 Conclusions

Lithium-ion batteries enable energy storage technology to be applied in many areas. The thermal issues found in lithium batteries, which corresponds to safety, thermal runaway, sub-zero temperature performance were studied in this thesis. An extensive literature review was provided in terms of battery mechanism, configuration, market penetration and BTM strategies such as air cooling, liquid cooling, phase-change materials and heat pipes. With aim of understanding the thermal behaviour of the current lithium-ion batteries, modelling through advanced software such as COMSOL multiphysics was introduced. The approaches used to predict the battery heat generation rate was discussed, which range from simple decoupled models to complex fully coupled models and can be find in area of battery cooling systems.

The development of battery thermal model and validation were fulfilled by an experimental and simulation study. A conceptual 2-cell prototype for experiment that mimics the WEIZHI battery cooling and heating system is introduced. The purpose of this prototype is to evaluate the heat pipe BTM method under pre-defined battery thermal conditions. It also serves the function of validating material properties and parameters for simulation inputs.

The eligibility of substituting atonal 324 for lithium-ion battery electrolytes has been assessed. The surrogate battery achieved similar temperature results under low power inputs, and was more prone to temperature change. This facilitates the extension of applying the proposed thermal management method to a wider range of battery operating conditions, implying that the cooling/heating solution is not limited to a certain type of batteries but suitable for various batteries with a broader range of cooling/heating needs.

As a result, a 2-cell prototype was constructed and implemented to evaluate the heat pipe BTM solution. Battery cooling was assessed through steady state operating conditions and duty cycle scenarios. The effects of adding fins or replacing with perforated plates have been evaluated. Results show an improved heat transfer after adding circular fins at an optimised fin height of $r_f/r_0 = 2$ based on fixed fin thickness and fin pitch. But it is difficult to conclude whether changing perforated plates is beneficial for the overall heat transfer. The feasibility of using sintered copper-water heat pipes under sub-zero temperatures was also assessed by exposing the test rig to $-15^{\circ}\text{C}/-20^{\circ}\text{C}$ for more than 14 hours. Data indicates that the heat pipe was able to function immediately after long hours of cold exposure and that sub-zero temperature conditions had little impact on heat pipe performance.

The application to BTM at pack level was then conducted based on a scale-up validated FEM model, which contains 30 cells. The thesis has presented a computationally efficient modelling by using symmetrical features to predict the dynamic thermal performance of two selected sections within the battery pack. The model developed can serve EV application in the area of

simulating battery packs thermal behaviour, design of cooling/preheating systems, and optimisation of BTM systems.

It is desired to have a higher liquid cooling rate in combination with heat pipes to effectively decrease the peak temperatures and improve the temperature uniformity of the pack. FEM analysis covers a wide range of battery working conditions based on either decoupling or coupling, revealing the limitations of the proposed solution. It is possible to find the best cooling rate for a particular thermal condition eliminating additional energy input. For instance, low coolant flow rates (0.0595 l/s) can be sufficient in reducing the peak temperature below 40°C while achieving good uniformity if the battery dissipates less than 12 W/cell. Moreover, the minimum heat power required to heat up such battery pack from -20°C to 0°C in 9 minutes is 0.43 kW. Thoughts on improving fluid flow by constructing buffer plates or creating a dynamic flow velocity profile to compensate for localised temperature increase are made for future work.

It can be concluded that the proposed heat pipe method for BTM is suitable for EV applications. The heat pipe is able to maintain the surrogate battery below 40°C if it generates less than 10 W/cell and helps reduce the battery temperature down to 70°C under uncommon thermal abuse conditions (e.g. 20 – 40 W/cell). The temperature uniformity has also been evaluated under variable input power and cooling conditions, and it is advised that both sides of the battery should be heat pipe-cooled in order to improve temperature uniformity to a much higher level. Moreover, the durability and feasibility of using sintered copper-water heat pipes under sub-zero temperatures has been assessed and data show that the heat pipe was able to function immediately

after long hours of sub-zero temperature conditions. The degree of thermal performance degradation was seen as little from 8 repeatable tests and data repeatability and reproducibility tests, and reasonably short heating time period under 40°C pre-treated coolant discharge makes it ideal to preheat EV batteries. Other benefits such as material availability, mature manufacturing technique, and the flexibility in maintenance also add to the likelihood of mass production.

In addition, a novel flat plate heat pipe was designed and fabricated. The innovation introduces a low level of hierarchical structure and integrated wicks for different heat pipe sections including evaporator, adiabatic and condenser. Mathematical modelling of capillary pressure and capillary rise rate was performed, followed by fabrication process.

8.2 Future Work

The work presented in this thesis can be extended to a more rigorous study. An experimental setup of an electric vehicle BTM system is being planned to measure the surface temperature distribution across the WEIZHI battery pack. The experimental setup has already been developed and tests are currently planned. This allows the comparison between experimental data and model predictions developed in Chapter 6 thus validating the accuracy and consistency of the FEM modelling. It has been noted that the practicality of the proposed solution can be destroyed by copper-aluminium corrosion, so a substitute for the aluminium plate is required. Phase-change materials (PCMs) would be a better candidate if proper design and melting point are carefully made. PCMs also allow the same methodology to be applied to cylindrical

cells, such that the geometry effect on thermal issues can be compared. Additional analysis will be performed to investigate battery lifespan for both thermal managed and unmanaged packs under aggressive usage patterns. It is planned to calibrate the heat generation rate through experiment enhancing the accuracy of the FEM models.

On the other hand, performance test of the fabricated wick samples is constructed. Thermal characteristics such as thermal resistance and the highest heat flux under anti-gravity condition will be examined. The test unit is demonstrated below. Fig. 8.1 shows the thermocouple arrangement and Fig. 8.2 demonstrates the setup for the flat plate heat pipe at horizontal condition. Angles can be adjusted as indicated by Fig. 8.3 to explore the heat pipe thermal performance under anti-gravity and gravity-assisted conditions.

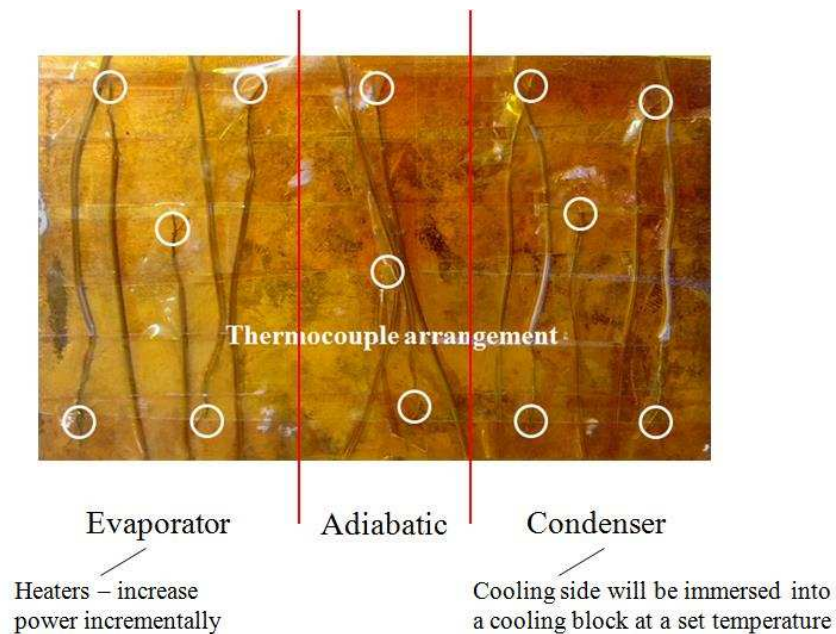


Figure 8.1: Thermocouple arrangement on the flat plate heat pipe.

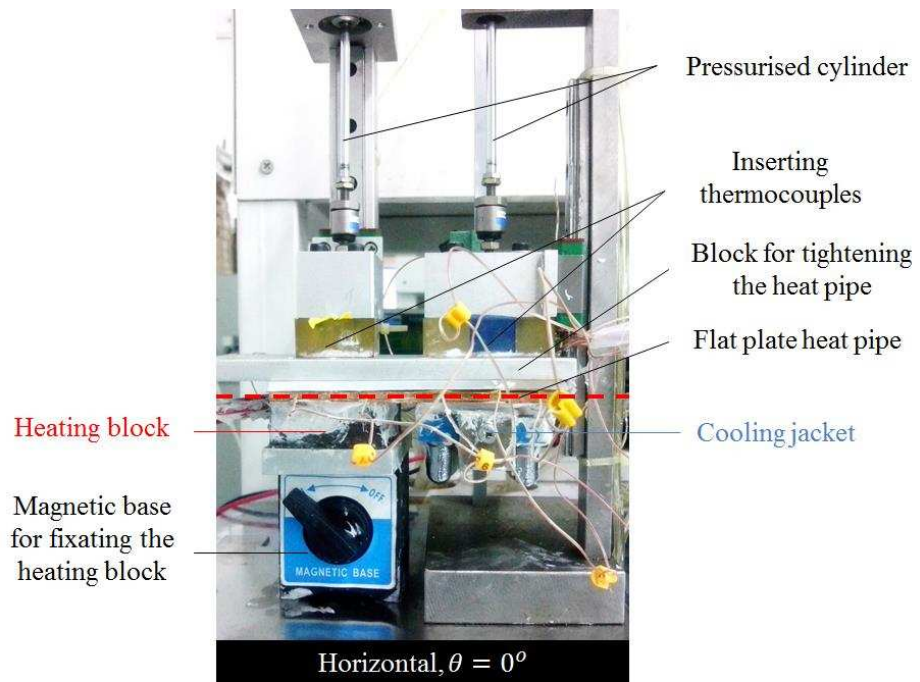


Figure 8.2: Performance test setup for the flat plate heat pipe sample at horizontal orientation.

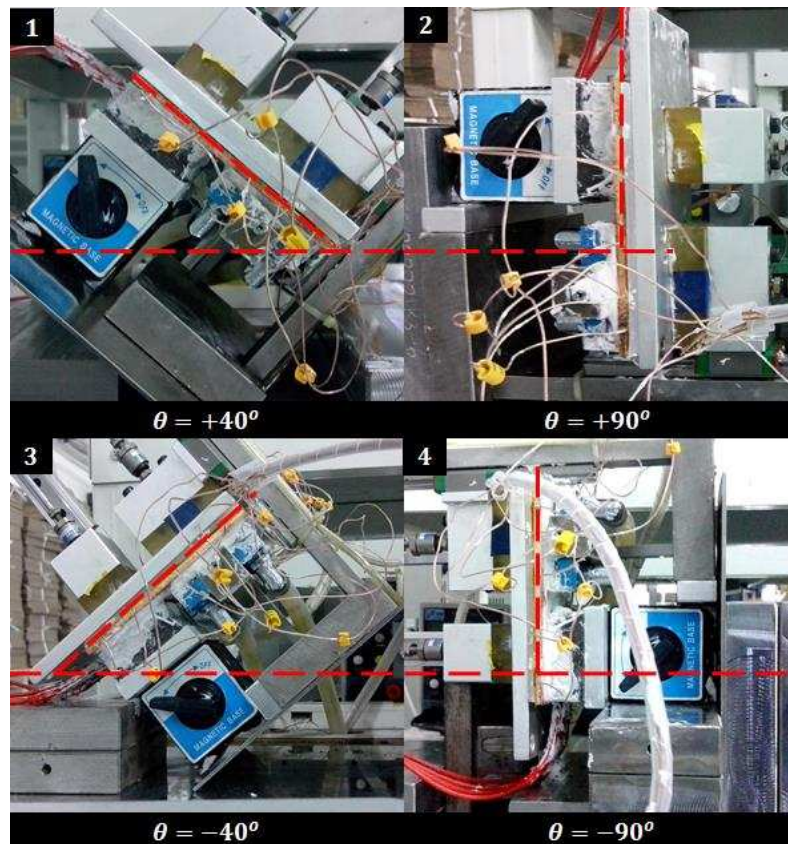


Figure 8.3: Testing the flat plate heat pipe at various angles including anti-gravity conditions (40°, 90°) and gravity-assisted conditions (-40°, -90°).

References

1. Wang, Q., et al., Experimental Investigation on EV Battery Cooling and Heating by Heat Pipes. *Applied Thermal Engineering*, 2014.
2. Chau, K.T., Y.S. Wong, and C.C. Chan, An overview of energy sources for electric vehicles. *Energy Conversion and Management*, 1999. **40**(10): p. 1021-1039.
3. Hirota, Y. and S. Ogasawara, *Electric Vehicle Engineering*. 2010, Morikita, Tokyo.
4. Gkikas, N., *Automotive Ergonomics: Driver-Vehicle Interaction. Human-Machine Interaction (HMI) in the Time of Electric Vehicles*, ed. N. Gkikas. 2013, Boca Raton, Finland: CRC Press.
5. Shimada, M., Magnetic Materials in Vehicles Driven by Electricity, in *The 2010 Hirosaki University International Symposium, The 2nd International Symposium: Energy and Environment in Aomori*. 2011, Hirosaki University Press: Hirosaki. p. 53-56.
6. DieselNet. Emission Test Cycles: Japanese 10-15 Mode. 2012; Available from: http://www.dieselnet.com/standards/cycles/jp_10-15mode.php.
7. Srinivasan, V., *Batteries for Vehicular Applications*. 2008, Lawrence Berkeley National Lab: Berkeley, CA.
8. Wachsman, E.D. and K.T. Lee, Lowering the Temperature of Solid Oxide Fuel Cells. *Science*, 2011. **334**(6058): p. 935-939.
9. Andrews, J. and N. Jelley, *Energy Science: Principles, Technologies, and Impacts*. 2nd ed. 2013, Great Glarendon Street, Oxford, UK: Oxford University Press.
10. Linden, D., *Handbook of Batteries*. 3rd ed. 2002, New York: McGraw-Hill.
11. Axsen, J., A. Burke, and K. Kurani, *Batteries for Plug-in Hybrid Electric Vehicles (PHEVs): Goals and the State of Technology circa 2008*. 2008, Institute of Transportation Studies: Davis, CA.
12. Cluzel, C. and C. Douglas, *Cost and Performance of EV Batteries*, in *Final report for The Committe on Climate Change*. 2012, Element Energy Limited.
13. Gaines, L. and R. Cuenca, *Costs of Lithium-Ion Batteries for Vehicles*. 2000, Argonne National Laboratory.
14. Hsiao, E. and C. Richter, *Electric Vehicles: Special Report*. 2008, CLSA.
15. Irwin, C.E., *Energy Storage: CleanTech Industry Report*. 2008, Merriman Curhan Ford.
16. Lache, R., et al., *Electric Cars: Plugged In - Batteries must be included*. 2008, Deutsche Bank Securities Inc.
17. Westbrook, M.H., *The Electric Car: Development and Future of Battery, Hybrid and Fuel-cell Cars*. 2001, London: The Institution of Electrical Engineers.

18. Daimler, Daimler analysis. 2010.
19. RECHARGE, Safety of lithium-ion batteries. 2013, The European Association for Advanced Rechargeable Batteries.
20. Liu, R., J. Duay, and S.B. Lee, Heterogeneous nanostructured electrode materials for electrochemical energy storage. *Chemical Communications*, 2011. **47**(5): p. 1384-1404.
21. A123Systems. Plug-in: PHEV Safety. 2008; Available from: <http://www.a123systems.com/applications/plug-in-hybrid>.
22. Daniel, C., *Materials and Processing for Lithium-ion Batteries*. The Journal of The Minerals, Metals & Materials Society, 2008. **60**(9): p. 43-48.
23. Exponent. *Batteries & Energy Storage Technology*. 2010; Available from: <http://www.exponent.com/batteries/>.
24. Dillard, T. *Dissecting the Nissan LEAF Battery*. 2014; Available from: <http://insideevs.com/dissecting-leaf-battery-wvideo/>.
25. Cadex. *Basics About Batteries*. 2014; Available from: <http://www.cadex.com/en/batteries/basics-about-batteries>.
26. Doug. *Roadster battery (ESS)*. 2010; Available from: [http://www.teslamotorsclub.com/showthread.php/3810-Roadster-battery-\(ESS\)](http://www.teslamotorsclub.com/showthread.php/3810-Roadster-battery-(ESS)).
27. TeslaMotor. *Increasing energy density means increasing range*. Available from: http://www.teslamotors.com/sv_SE/roadster/technology/battery.
28. Web. *Leaf's Battery Pack*. Available from: <http://www.teslamotorsclub.com/attachment.php?attachmentid=2534>.
29. Wikipedia. *BMW i3*. 2014; Available from: http://en.wikipedia.org/wiki/BMW_i3.
30. Wikipedia. *BYD e6*. 2014; Available from: http://en.wikipedia.org/wiki/BYD_e6.
31. Wikipedia. *Chevrolet Spark*. 2014; Available from: http://en.wikipedia.org/wiki/Chevrolet_Spark_EV.
32. van Agt, J., *Electric Car Citroën C-Zero*. 2010.
33. Wikipedia. *Mitsubishi i-MiEV*. 2014; Available from: http://en.wikipedia.org/wiki/Mitsubishi_i-MiEV.
34. Wikipedia. *Ford Focus Electric*. 2014; Available from: http://en.wikipedia.org/wiki/Ford_Focus_Electric.
35. Wikipedia. *Nissan Leaf*. 2014; Available from: http://en.wikipedia.org/wiki/Nissan_Leaf.
36. Wikipedia. *Tesla Model S*. 2014; Available from: http://en.wikipedia.org/wiki/Tesla_Model_S.
37. Wikipedia. *Venturi Fétish*. 2014; Available from: http://en.wikipedia.org/wiki/Venturi_F%C3%A9tish.
38. Wikipedia. *Volkswagen Up*. 2014; Available from: http://en.wikipedia.org/wiki/Volkswagen_Up.
39. Scott, P. and M. Burton, *The New BMW i3*. 2013.
40. Cole, J., *First BMW i3 Electric Car Test Ride, 2.3 Gallon Range Extender Option To Cost About \$4,000*, in *InsideEVs*. 2013.
41. *BYD: Only 1,000 E6s for 2010*. *ChinaAutoWeb* 2010; Available from: <http://chinaautoweb.com/2010/06/byd-only-1000-e6s-for-2010/>.

42. Woody, T., From China to Los Angeles, Taking the Electric Bus, in *The New York Times*. 2013.
43. Wayland, M., GM insourcing Chevy Spark EV battery production, in *mlive*. 2014.
44. Chevrolet. 2014.
45. Glynn Jones, D., Mitsubishi i-MiEV drive. 2009.
46. Bähnisch, S., Im Prinzip gut, in *Autobild*. 2010.
47. Greencarcongress. Mitsubishi Motors to Premiere the European-spec i-MiEV at the 2010 Paris Motor Show. 2010; Available from: <http://www.greencarcongress.com/2010/08/mitsubishi-motors-to-premiere-the-european-spec-i-miev-at-the-2010-paris-motor-show.html> - more.
48. Charlton, A., Ford Focus Electric: First Drive, in *International Business Times*. 2013.
49. Ford. Ford Focus Electric. 2014; Available from: <http://www.ford.com/cars/focus/trim/electric/>.
50. Laboratory, I.N., 2011 Nissan Leaf – VIN 0356 Advanced Vehicle Testing – Beginning-of-Test Battery Testing Results. 2011.
51. TeslaMotorForum. The Model S Battery. 2011; Available from: http://www.teslamotors.com/fr_CA/forum/forums/model-s-battery-0.
52. TeslaMotor. 2014; Available from: <http://www.teslamotors.com/>.
53. VenturiFetish. Venturi Fetish, top of the art of technology. 2014; Available from: <http://www.ventec-bms.com/venturi-fetish/>.
54. Lard, J. Volkswagen's new e-up! electric car is shockingly good. 2014; Available from: <http://www.techradar.com/news/car-tech/volkswagen-s-e-up-electric-car-is-shockingly-good-1223000>.
55. Wikipedia. List of production battery electric vehicles (table). 2010; Available from: [http://en.wikipedia.org/wiki/List_of_production_battery_electric_vehicles_\(table\)](http://en.wikipedia.org/wiki/List_of_production_battery_electric_vehicles_(table)).
56. Cunningham, T. Think City. 2010; Available from: http://www.oeva.org/presentations/THINKPresentationMar11_2010.pdf.
57. Wikipedia. General Motors. 2014; Available from: http://en.wikipedia.org/wiki/General_Motors_EV1_-_Battery.
58. USDOE. 1999 General Motors EV1 w/NiMH - vehicle specifications. 1999; Available from: http://avt.inel.gov/pdf/fsev/eva/ev1_eva.pdf.
59. Madrid, C., J. Argueta, and J. Smith. Performance Characterization. 1999; Available from: http://avt.inel.gov/pdf/fsev/sce_rpt/altra_report.pdf.
60. Berdichevsky, G., et al., The Tesla Roadster Battery System. 2006.
61. Doughty, D. and E.P. Roth, A general discussion of Li-ion battery safety. *The Electrochemical Society Interface*, 2012. **21**(2): p. 37-44.
62. ISO, ISO 6469-1:2009: Electrically propelled road vehicles - Safety specifications. 2009.
63. Levy, S.C. and P. Bro, Battery hazards and accident prevention 1994, New York: Plenum Press.
64. Bandhauer, T.M., S. Garimella, and T.F. Fuller, A Critical Review of Thermal Issues in Lithium-ion Batteries. *Journal of Electrochemical Society*, 2011. **158**(3): p. R1-R25.

65. Roth, E.P., et al., Advanced Technology Development Program for Lithium-Ion Batteries: Thermal Abuse Performance of 18650 Li-Ion Cells. 2004, Sandia National Laboratories.
66. Doughty, D.H., Li-ion battery abuse tolerance testing - an overview. 2006, Sandia National Laboratories.
67. Balakrishnan, P.G., R. Ramesh, and T.P. Kumar, Safety mechanisms in lithium-ion batteries. *Journal of Power Sources*, 2006. **155**(2): p. 401-414.
68. Investigation concludes fire in BYD e6 collision caused by electric arcs from short circuit igniting interior materials and part of power battery. Green Car Congress 2012; Available from: <http://www.greencarcongress.com/2012/08/byde6-20120810.html>.
69. Christopher, J., Chevy Volt Fire Prompts Federal Investigation Into Lithium-Ion Batteries, in *The New York Times*. 2011.
70. Voelcker, J., Chrysler Yanks Plug-In Hybrid Test Fleet Off Roads, Will Replace Batteries, in *Green Car Report*. 2012.
71. Automotive, F., Fisker: Karma fire caused by fault in low-temperature cooling fan; initiates recall, in *Green Car Congress*. 2012.
72. Loveday, E., Mitsubishi Extends Production Halt on Outlander PHEV as Perplexing Battery Investigation Continues, in *InsideEVs*. 2013.
73. Musk, E. Model S Fire. 2013 Available from: <http://www.teslamotors.com/blog/model-s-fire>.
74. Battery Pack Defects Blamed for Zotye EV Fire. *ChinaAutoWeb* 2011; Available from: <http://chinaautoweb.com/2011/06/battery-pack-defects-blamed-for-zotye-ev-fire/>.
75. Lin, H.P., et al., Low-temperature behavior of Li-ion cells. *Electrochemical and Solid-State Letters* 2001. **4**(6): p. A71-A73.
76. NissanUSA. How conditions affect range. 2012; Available from: http://www.nissanusa.com/leaf-electric-car/range?next=ev_micro.section_nav.
77. (USABC), U.S.A.B.C., Electric vehicle battery test procedures manual. 1996.
78. QC/T 743-2006: Lithium-ion Batteries for Electric Vehicles, in *QC/T 743-2006*. 2006.
79. Huang, C.K., et al., The limits of low-temperature performance of Li-ion cells. *Journal of Electrochemical Society*, 2000. **147**(8): p. 2893-2896.
80. Nagasubramanian, G., Electrical characteristics of 18650 Li-ion cells at low temperatures. *Journal of Applied Electrochemistry*, 2001. **31**(1): p. 99-104.
81. Shidore, N. and T. Bohn, Evaluation of cold temperature performance of the JCS-VL41M PHEV battery using Battery HIL. 2008, SAE Technical Paper.
82. Fan, J. and S. Tan, Studies on charging lithium-ion cells at low temperatures. *Journal of Electrochemical Society*, 2006. **153**(6): p. A1081-A1092.
83. Zhang, S.S., K. Xu, and T.R. Jow, The low temperature performance of Li-ion batteries. *Journal of Power Sources*, 2003. **115**(1): p. 137-140.

84. Shi, R.X., et al., Low Temperature Performance Analysis of Li-ion Batteries for Electric Vehicles. *Bus & Coach Technology and Research*, 2012(2): p. 3.
85. Zhang, S.S., K. Xu, and T.R. Jow, Electrochemical impedance study on the low temperature of Li-ion batteries. *Electrochimica Acta*, 2004. **49**: p. 1057-1061.
86. Ji, Y. and C.Y. Wang, Heating strategies for Li-ion batteries operated from subzero temperatures. *Electrochimica Acta*, 2013. **107**: p. 664-674.
87. Smart, M.C., B.V. Ratnakumar, and S. Surampudi, Electrolytes for low-temperature lithium batteries based on ternary mixtures of aliphatic carbonates. *Journal of Electrochemical Society*, 1999. **146**(2): p. 486-492.
88. Plichta, E.J. and W.K. Behl, A low-temperature electrolyte for lithium and lithium-ion batteries. *Journal of Power Sources*, 2000. **88**: p. 192-196.
89. Wang, C.S., J.A. Appleby, and F.E. Little, Low-temperature characterization of lithium-ion carbon anodes via micro-perturbation measurement. *Journal of Electrochemical Society*, 2002. **2002**(6): p. A754-A760.
90. Zhang, S.S., K. Xu, and T.R. Jow, Charge and discharge characteristics of a commercial LiCoO₂-based 18650 Li-ion battery. *Journal of Power Sources*, 2006. **160**(2): p. 1403-1409.
91. Stuart, T.A. and A. Hande, HEV battery heating using AC currents. *Journal of Power Sources*, 2004. **129**: p. 368-378.
92. Zhang, S.S., K. Xu, and T.R. Jow, Study of LiBF₄ as an electrolyte salt for a Li-ion battery. *Journal of Electrochemical Society*, 2002. **149**(5): p. A586-A590.
93. Allen, J.L., T.R. Jow, and J. Wolfenstine, LiCoPO₄ as Li-ion cathode. *ECS Transactions*, 2012. **41**(29): p. 15-20.
94. Pesaran, A.A., Battery thermal models for hybrid vehicle simulations. *Journal of Power Sources*, 2002. **110**: p. 337-382.
95. Pesaran, A.A., et al., Tools for Designing Thermal Management of Batteries in Electric Drive Vehicles, in the Large Lithium Ion Battery Technology & Application Symposia Advanced Automotive Battery Conference 2013: Pasadena, CA.
96. Ladrech, F., Battery Thermal Management for HEV & EV – Technology overview, in *Automotive Summit*. 2010.
97. Sato, N., Thermal Behaviour analysis of lithium-ion batteries for electric and hybrid vehicles. *Journal of Power Sources*, 2001. **99**(1-2): p. 70-77.
98. Khateeb, S.A., et al., Thermal management of Li-ion battery with phase change material for electric scooter: experiment validation. *Journal of Power Sources*, 2005. **142**: p. 345-353.
99. Lu, L.G., et al., A review on the key issues for lithium-ion battery management in electric vehicles. *Journal of power Sources*, 2013. **226**: p. 272-288.
100. Rao, Z.H. and S.F. Wang, A review of power battery thermal energy management. *Renewable and Sustainable Energy Reviews*, 2011. **15**(9): p. 4554-4571.

101. Kizilel, R., et al., An alternative cooling system to enhance the safety of Li-ion battery packs. *Journal of Power Sources*, 2009. **194**(2): p. 1105-1112.
102. Mahamud, R. and C.W. Park, Reciprocating air flow for Li-ion battery thermal management to improve temperature uniformity. *Journal of Power Sources*, 2011. **196**: p. 5685-5696.
103. Panasonic. Overview: Lithium Ion Batteries. 2007; Available from: <http://industrial.panasonic.com/www-data/pdf/ACA4000/ACA4000PE3.pdf>.
104. Lawson, B. Battery and Energy Technologies. Available from: <http://www.mpoweruk.com/thermal.htm>.
105. Waag, W., S. Kabitz, and D.U. Sauer, Experimental investigation of the lithium-ion battery impedance characteristic at various conditions and aging states and its influence on the application. *Applied Energy*, 2013. **102**: p. 885-897.
106. Ramadasm, P., et al., Capacity fade of Sony 18650 cells cycled at elevated temperatures Part II. Capacity fade analysis. *Journal of Power Sources*, 2002. **112**(2): p. 614-620.
107. Uchida, I., et al., AC-impedance measurements during thermal runaway process in several lithium/polymer batteries. *Journal of Power Sources*, 2003. **119**: p. 821-825.
108. Catherino, H.A., Complexity in battery systems: thermal runaway in VRLA batteries. *Journal of Power Sources*, 2006. **158**(2): p. 977-986.
109. Jhu, C.Y., et al., Thermal runaway potential of LiCoO₂ and Li(Ni_{1/3}Co_{1/3}Mn_{1/3})O₂ batteries determined with adiabatic calorimetry methodology. *Applied Energy*, 2012. **100**: p. 127-131.
110. Choi, K.W. and N.P. Yao, Heat Transfer in Lead-Acid Batteries Designed for Electric-Vehicle Propulsion Application. *Journal of Electrochemical Society*, 1979. **126**(8): p. 1321-1328.
111. Parise, R.J., Quick Charge Battery With Internal Thermal Management, in *Energy Conversion Engineering Conference and Exhibit, 2000. (IECEC) 35th Intersociety 2000: Las Vegas, NV*.
112. Bandhauer, T.M. and S. Garimella, Passive, internal thermal management system for batteries using microscale liquid-vapor phase change. *Applied Thermal Engineering*, 2013. **61**: p. 756-769.
113. Cosley, M.R. and M.P. Garcia, Battery thermal management system, in *Proceedings of the INTELEC 26th annual international telecommunications energy conference. 2004*.
114. Choi, K.W. and N.P. Yao, Heat Transfer in Lead-Acid Batteries Designed for Electric-Vehicle Propulsion Application. *Journal of Electrochemical Society*, 1979. **126**.
115. Chen, Y. and J.W. Evans, Heat transfer phenomena in lithium/polymer-electrolyte batteries for electric vehicle application. *Journal of the Electrochemical Society*, 1993. **140**(7): p. 1833-1838.
116. Pesaran, A.A., S. Burch, and M. Keyser, An approach for designing thermal management systems for electric and hybrid vehicle battery packs, in *Fourth vehicle thermal management systems conference and exhibition. 1999*.

117. Kim, G.H. and A.A. Pesaran, Battery thermal management system design modeling, in 22nd International Battery, Hybrid and Fuel Cell Electric Vehicle Conference and Exhibition. 2006: Yokohama, Japan.
118. Pesaran, A.A., Battery thermal management in EVs and HEVs: issues and solutions, in Advanced Automotive Battery Conference. 2001: Las Vegas, Nevada.
119. Kenneth, J.K. and A. Rajagopalan, Benchmarking of OEM hybrid electric vehicles at NREL, N.R.E. Laboratory, Editor. 2001: Golden, Colorado.
120. Zolot, M., A.A. Pesaran, and M. Mihalic, Thermal evaluation of Toyota Prius Battery pack, in Hyatt Crystal City: Future Car Congress. 2002.
121. Brandbattery. Photo Tour of Hybrid Batteries - Toyota Honda. 2012; Available from: <http://www.brandbattery.com/photo-tour-of-hybrid-batteries/>.
122. BEHR, Thermal Management for Hybrid Vehicles, in Technical Press Day. 2009.
123. Kelly, K.J., M. Mihalic, and M. Zolot, Battery Usage and Thermal Performance of the Toyota Prius and Honda Insight during Chassis Dynamometer Testing, in The Seventeenth Annual Battery Conference on Applications and Advances. 2002: Long Beach, California. p. 247-252.
124. Nelson, P., et al., Modelling thermal management of lithium-ion PNGV batteries. Journal of Power Sources, 2002. **110**(2): p. 349-356.
125. Lou, Y., Nickel-metal hydride battery cooling system research for hybrid electric vehicle. 2007, Shanghai: Shanghai Jiao Tong University.
126. Vlahinos, A. and A.A. Pesaran, Energy efficient battery heating in cold climates, in The future car congress. 2002: Arlington, Virginia.
127. Pesaran, A.A., A. Vlahinos, and T.A. Stuart, Cooling and preheating of batteries in hybrid electric vehicles, in The 6th ASME-JSME Thermal Engineering Joint Conference. 2003: Hawaii Island, Hawaii.
128. Volvo C30 Electric equipped with three climate systems; bioethanol heater. Green Car Congress 2011; Available from: <http://www.greencarcongress.com/2011/03/c30-20110328.html>.
129. Shimada, M., A vehicle driven by electricity, designed for chill and snowy areas. Sensors and Actuators A: Physical, 2013. **200**: p. 168-171.
130. Kohn, S., G. Berdichevsky, and B.C. Hewett, Tunable Frangible Battery Pack System. 2011, Tesla Motors, Inc.
131. TESLA Roadster 纯电动车电池系统拆解分析. 2013.
132. Rugh, J.P., A.A. Pesaran, and K. Smith, Electric Vehicle Battery Thermal Issues and Thermal Management Techniques, in SAE Alternative Refrigerant and System Efficiency Symposium. 2011: Scottsdale, Arizona USA. p. September 27-29.
133. Jarrett, A. and Y. Kim, Design optimization of electric vehicle battery cooling plates for thermal performance. Journal of Power Sources, 2011. **196**: p. 10359-10368.
134. Faass, A. and E. Clough, Battery Module With Integrated Thermal Management System. 2013, Tesla Motors, Inc.

135. Jin, L.W., et al., Ultra-thin minichannel LCP for EV battery thermal management. *Applied Energy*, 2014. **113**: p. 1786-1794.
136. Al-Hallaj, S., Safety and Thermal Management for Li-ion Batteries in Transportation Applications, in *EV Li-ion Battery Forum Europe 2012*. 2012: Barcelona, Spain.
137. Al-Hallaj, S. and J.R. Selman, A novel thermal management system for EV batteries using phase change material (PCM). *Journal of the Electrochemical Society*, 2000. **147**: p. 3231-3236.
138. Al-Hallaj, S. and J.R. Selman, Novel thermal management of battery systems, U.S. Patent, Editor. 2002.
139. Khateeb, S.A., et al., Design and simulation of a lithium-ion battery with a phase change material thermal management system for an electric scooter. *Journal of Power Sources*, 2004. **128**: p. 292-307.
140. Sabbah, R., et al., Active (air-cooled) VS passive (phase change material) thermal management of high power lithium-ion packs: limitation of temperature rise and uniformity of temperature distribution. *Journal of Power Sources*, 2008. **182**: p. 630-638.
141. Rao, Z.H., S.F. Wang, and G.Q. Zhang, Simulation and experiment of thermal energy management with phase change material for ageing LiFePO₄ power battery. *Energy Conversion and Management*, 2011. **52**: p. 3408-3414.
142. Zhang, Z.G. and X.M. Fang, Study on paraffin/expanded graphite composite phase change thermal energy storage material. *Energy Conversion and Management*, 2006. **47**(3): p. 303-310.
143. Zhang, D., S.L. Tian, and D.Y. Xiao, Experimental study on the phase change behaviour of phase change material confined in pores. *Solar Energy*, 2007. **81**(5): p. 653-660.
144. Py, X., R. Olives, and S. Mauran, Paraffin/porous-graphite-matrix composite as a high and constant power thermal storage material. *International Journal of Heat and Mass Transfer*, 2001. **44**(14): p. 2727-2737.
145. Zhou, X.F., et al., Preparation and thermal properties of paraffin/porous silica ceramic composite. *Composites Science and Technology*, 2009. **69**(7-8): p. 1246-1249.
146. Li, W.Q., et al., Experimental and numerical studies on melting phase change heat transfer in open-cell metallic foams filled with paraffin. *Applied Thermal Engineering*, 2012. **37**: p. 1-9.
147. Fukai, J., et al., Thermal conductivity enhancement of energy storage media using carbon fibers. *Energy Conversion and Management*, 2000. **41**(14): p. 1543-1556.
148. Mettawee, E.B.S. and G.M.R. Assassa, Thermal conductivity enhancement in a latent heat storage system. *Solar Energy*, 2007. **81**(7): p. 839-845.
149. Shatikian, V., G. Ziskind, and R. Letan, Numerical investigation of a PCM-based heat sink with internal fins. *International Journal of Heat and Mass Transfer*, 2005. **48**(17): p. 3689-3706.
150. Trp, A., An experimental and numerical investigation of heat transfer during technical grade paraffin melting and solidification in a shell and tube latent heat thermal energy storage unit. *Solar Energy*, 2005. **79**(6): p. 648-660.

151. Akgun, M., O. Aydm, and K. Kaygusuz, Thermal energy storage performance of paraffin in a novel tube-in-shell system. *Applied Thermal Engineering*, 2008. **28**: p. 405-413.
152. Alrashdan, A., A.T. Mayyas, and S. Al-Hallaj, Thermo-mechanical behaviors of the expanded graphite-phase change material matrix used for thermal management of Li-ion battery packs. *Journal of Materials Processing Technology*, 2010. **210**(1): p. 6.
153. Kim, G.H., et al., Thermal Management of Batteries in Advanced Vehicles Using Phase-Change Materials *The World Electric Vehicle Journal*, 2008. **2**(2): p. 134-147.
154. Li, W.Q., et al., Experimental study of a passive thermal management system for high-powered lithium ion batteries using porous metal foam saturated with phase change materials. *Journal of Power Sources*, 2014. **255**: p. 9-15.
155. Duan, X. and G.F. Naterer, Heat transfer in phase change materials for thermal management of electric vehicle battery modules. *International Journal of Heat and Mass Transfer*, 2010. **53**: p. 5176-5182.
156. Rao, Z.H., Research on heat transfer enhancement of lithium-ion power battery. 2010, Guangzhou: Guangdong University of Technology.
157. Rao, Z.H. and G.Q. Zhang, Thermal Properties of Paraffin Wax-based Composites Containing Graphite. *Energy Sources Part a-Recovery Utilization and Environmental Effects*, 2011. **33**(7): p. 7.
158. Swanepoel, G., Thermal management of hybrid electrical vehicles using heat pipes. 2001, University of Stellenbosch.
159. Wu, M.S., et al., Heat dissipation design for lithium-ion batteries. *Journal of Power Sources*, 2002. **109**: p. 160-166.
160. Jang, J.C. and S.H. Rhi, Battery thermal management system of future electric vehicles with loop thermosyphon, in *UK-Korea Conference on Science Technology and Entrepreneurship (UKC)*. 2010.
161. Barantsevich, V. and V. Shabalkin, Heat pipes for thermal control of ISS solar battery drive. *Applied Thermal Engineering*, 2003. **23**(9): p. 1119-1123.
162. Park, Y.J., et al., Design optimization of a loop heat pipe to cool a lithium-ion battery onboard a military aircraft. *Journal of Mechanical Science Technology*, 2010. **24**: p. 609-618.
163. Burban, G., et al., Experimental investigation of a pulsating heat pipe for hybrid vehicle applications. *Applied Thermal Engineering*, 2013. **50**: p. 94-103.
164. Tran, T.H., et al., Experimental investigation on the feasibility of heat pipe cooling for HEV/EV lithium-ion battery. *Applied Thermal Engineering*, 2014. **63**(2): p. 551-558.
165. Rao, Z.H., et al., Experimental investigation on thermal management of electric vehicle battery with heat pipe. *Energy Conversion and Management*, 2013. **65**: p. 92-97.
166. Zhao, R., J.J. Gu, and J. Liu, An Experimental Study of Heat Pipe Thermal Management System with Wet Cooling Method for Lithium ion Batteries. *Journal of Power Sources*, 2015. **273**: p. 1089-1097.

167. Botte, G.G., V.R. Subramanian, and R.E. White, Mathematical Modeling of Secondary Lithium Batteries. *Electrochimica Acta*, 2000. **45**(15-16): p. 2595-2609.
168. Gu, W.B. and C.Y. Wang, Thermal-electrochemical modeling of battery systems. *Journal of the Electrochemical Society*, 2000. **147**(8): p. 2910-2922.
169. Pals, C.R. and J. Newman, Thermal Modeling of the Lithium/Polymer Battery: II. Temperature Profiles in a Cell Stack. *Journal of Electrochemical Society*, 1995. **142**(10): p. 3282-3288.
170. Doyle, M., T.F. Fuller, and J. Newman, Modeling of Galvanostatic Charge and Discharge of the Lithium/Polymer/Insertion Cell *Journal of Electrochemical Society*, 1993. **140**(6): p. 1526-1533.
171. Fuller, T.F., M. Doyle, and J. Newman, Simulation and Optimization of the Dual Lithium Ion Insertion Cell. *Journal of Electrochemical Society*, 1994. **141**(1): p. 1-10.
172. Newman, J., *Electrochemical Systems*. 1991: Prentice Hall.
173. Doyle, M. and J. Newman, Comparison of Modeling Predictions with Experimental Data from Plastic Lithium Ion Cells. *Journal of Electrochemical Society*, 1996. **143**(6): p. 1890-1903.
174. He, H.W., R. Xiong, and J.X. Fan, Evaluation of Lithium-ion Battery Equivalent Circuit Models for State of Charge Estimation by an Experimental Approach *Energies*, 2011. **4**: p. 582-598.
175. Johnson, V.H., A.A. Pesaran, and T. Sack, Temperature-Dependent Battery Model for High-Power Lithium-Ion Batteries, in 17th Electric Vehicle Symposium. 2000: Montreal, Canada.
176. Johnson, V.H., Battery performance models in ADVISOR. *Journal of Power Sources*, 2002. **110**: p. 321-329.
177. Markel, T., et al., ADVISOR: a system analysis tool for advanced vehicle modeling. *Journal of Power Sources*, 2002. **110**: p. 255-266.
178. Lee, S., et al., State-of-charge and capacity estimation of lithium-ion battery using a new open-circuit voltage versus state-of-charge. *Journal of Power Sources*, 2008. **185**: p. 1367-1373.
179. Huria, T., et al., High Fidelity Electrical Model with Thermal Dependence for Characterization and Simulation of High Power Lithium Battery Cells, in IEEE International Electric Vehicle Conference 2012.
180. Feng, J., H.F. He, and G.F. Wang, Comparison Study of Equivalent Circuit Model of Li-Ion Battery for Electrical Vehicles. *Research Journal of Applied Sciences*, 2013. **6**(20): p. 3756-3759.
181. Bandhauer, T.M., S. Garimella, and T.F. Fuller, Electrochemical-thermal modeling and microscale phase change for passive internal thermal management of lithium ion batteries. 2012, Sandia National Laboratories
182. Bernardi, D., E. Pawlikowski, and J. Newman, A general energy balance for battery systems. *Journal of Electrochemical Society*, 1985. **132**(1): p. 5-12.
183. Hallaj, S.A., et al., Entropy Changes Due to Structural Transformation in the Graphite Anode and Phase Change of the LiCoO₂ Cathode. *Journal of Electrochemical Society*, 2000. **147**(7): p. 2432-2436.

184. Hallaj, S.A., J. Prakash, and J.R. Selman, Characterization of commercial Li-ion batteries using electrochemical-calorimetric measurements *Journal of Power Sources*, 2000. **87**(1-2): p. 186-194.
185. Thomas, K.E. and J. Newman, Heats of Mixing and of Entropy in Porous Insertion Electrodes. *Journal of Power Sources*, 2003. **119-121**: p. 844-849.
186. Hong, J.S., et al., Electrochemical-Calorimetric Studies of Lithium-ion Cells. *Journal of the Electrochemical Society*, 1998. **145**(5): p. 1489-1501.
187. Rao, L. and J. Newman, Heat-Generation Rate and General Energy Balance for Insertion Battery Systems. *Journal of Electrochemical Society*, 1997. **144**(8): p. 2697-2704.
188. Çengel, Y.A., *Introduction to Thermodynamics and Heat Transfer*. 2nd ed. 2008, New York: McGraw-Hill.
189. Gu, W.B. and C.Y. Wang, Thermal-electrochemical coupled modeling of a lithium-ion cell. *ECS Proceedings*, 2000. **99**(25): p. 748-762.
190. Wang, C.Y. and V. Srinivasan, Computational battery dynamics (CBD) - electrochemical/thermal coupled modeling and multi-scale modeling. *Journal of Power Sources*, 2002. **110**: p. 364-376.
191. Kim, G.H. and K. Smith, Three-Dimensional Lithium-Ion Battery Model, in *4th International Symposium on Large Lithium Ion Battery Technology and Application 2008*: Tampa, Florida.
192. Lee, K.J., K. Smith, and G.H. Kim, A Three-Dimensional Thermal-Electrochemical Coupled Model for Spirally Wound Large-Format Lithium-Ion Batteries, in *Space Power Workshop*. 2011: Los Angeles, CA.
193. Lin, X.F., et al., A lumped-parameter electro-thermal model for cylindrical batteries. *Journal of Power Sources*, 2014. **257**: p. 1-11.
194. Smith, K. and C.Y. Wang, Power and thermal characterization of a lithium-ion battery pack for hybrid-electric vehicles. *Journal of Power Sources*, 2006. **160**(1): p. 662-673.
195. Fang, W.F., O.J. Kwon, and C.Y. Wang, Electrochemical-thermal modeling of automotive Li-ion batteries and experimental validation using a three-electrode cell. *Journal of Energy Research*, 2010. **34**: p. 107-115.
196. Prada, E., et al., Simplified Electrochemical and Thermal Model of LiFePO₄-Graphite Li-Ion Batteries for Fast Charge Applications. *Journal of the Electrochemical Society*, 2012. **159**(9): p. A1508-A1519.
197. Srinivasan, V. and C.Y. Wang, Analysis of Electrochemical and Thermal Behavior of Li-Ion Cells. *Journal of The Electrochemical Society*, 2003. **150**(1): p. A98-A106.
198. Song, L. and J.W. Evans, Electrochemical-thermal model of lithium polymer batteries. *Journal of Electrochemical Society*, 2000. **147**(6): p. 2086-2095.
199. Gomadam, P.M., et al., Mathematical modeling of lithium-ion and nickel battery systems. *Journal of Power Sources*, 2002. **110**: p. 267-284.
200. Kim, G.H. and K. Smith, Multi-dimensional electrochemical-thermal coupled model of large format cylindrical lithium ion cells, in *212th ECS Meeting, N.R.E.L. (NREL), Editor*. 2007: Washington, DC.

201. Cai, L. and R.E. White, Mathematical modeling of a lithium ion battery with thermal effects in COMSOL Inc. Multiphysics (MP) software. *Journal of Power Sources*, 2011. **196**: p. 5985-5989.
202. Baker, D.R. and M.W. Verbrugge, Temperature and Current Distribution in Thin-Film Batteries. *Journal of the Electrochemical Society*, 1999. **146**(7): p. 2413-2424.
203. Taheri, P. and M. Bahrami, Temperature Rise in Prismatic Polymer Lithium-ion Batteries: An Analytic Approach. *SAE International Journal of Passengers Cars - Electronic and Electrical Systems*, 2012. **5**(1): p. 164-176.
204. Chen, Y.F. and J.W. Evans, Three-dimensional thermal modeling of lithium-polymer batteries under galvanostatic discharge and dynamic power profile. *Journal of Electrochemical Society*, 1994. **141**(11): p. 2947-2955.
205. Chen, Y.F. and J.W. Evans, Thermal analysis of lithium-ion batteries. *Journal of Electrochemical Society*, 1996. **143**(9): p. 2708-2712.
206. Al-Hallaj, S., et al., Thermal modelling and design considerations of lithium-ion batteries. *Journal of Power Sources*, 1999. **83**(1-2): p. 1-8.
207. Chen, S.C., C.C. Wan, and Y.Y. Wang, Thermal Analysis of Lithium-ion Batteries. *Journal of Power Sources*, 2005. **140**(1): p. 111-124.
208. Onda, K., et al., Thermal behavior of small lithium-ion battery during rapid charge and discharge cycles. *Journal of Power Sources*, 2006. **158**(1): p. 535-542.
209. Chen, S.C., Y.Y. Wang, and C.C. Wan, Thermal Analysis of Spirally Wound Lithium Batteries. *Journal of Electrochemical Society*, 2006. **153**(4): p. A637-A648.
210. Kim, U.S., C.B. Shin, and C.S. Kim, Effect of electrode configuration on the thermal behavior of a lithium-polymer battery. *Journal of Power Sources*, 2008. **180**: p. 909-916.
211. Kim, U.S., C.B. Shin, and C.S. Kim, Modeling for the scale-up of a lithium-ion polymer battery. *Journal of Power Sources*, 2009. **189**(1): p. 841-846.
212. Szabo, B.A. and I. Babuška, *Finite Element Analysis*. 1991: John Wiley & Sons. 368.
213. Reddy, J.N., *An Introduction to the Finite Element Method*. 2nd ed. 1993, New York: McGraw-Hill.
214. Pesaran, A.A., A. Vlahinos, and S.D. Burch. Thermal Performance of EV and HEV Battery Modules and Packs. in *Fourteenth International Electric Vehicle Symposium*. 1997. Orlando, Florida.
215. Vlahinos, A., et al. Improving Battery Thermal Management Using Design for Six Sigma Process. in *20th Electric Vehicle Symposium*. 2003. Long Beach, CA.
216. Bharathan, D., et al., Electro-Thermal Modeling to Improve Battery Design, in *2005 IEEE Vehicle Power and Propulsion Conference*. 2005: Chicago, Illinois.
217. Comsol. Comsol Multiphysics - Overview. 2015; Available from: <http://www.comsol.com/comsol-multiphysics>.
218. Comsol. 1D Isothermal Lithium-Ion Battery. 2012 [cited 2014 2 November]; Available from:

- http://www.comsol.asia/model/download/154661/models.bfc.li_battery_1d.pdf.
219. Comsol. Conjugate Heat Transfer. 2014 [cited 2014 4 November]; Available from: <http://www.comsol.com/blogs/conjugate-heat-transfer/>.
 220. Hillston, J. Model Validation and Verification. 2003; Available from: <http://www.inf.ed.ac.uk/teaching/courses/ms/notes/note14.pdf>.
 221. Wei, J., K. Hijikata, and T. Inoue, Fin efficiency enhancement using a gravity-assisted planar heat pipe. *International Journal of Heat and Mass Transfer*, 1997. **40**(5): p. 1045-1051.
 222. Zhao, Z. and C.T. Avedisian, Enhancing forced air convection heat transfer from an array of parallel plate fins using a heat pipe. *International Journal of Heat and Mass Transfer*, 1997. **40**(13): p. 3135-3147.
 223. Legierski, J. and B. Wiecek, Steady state analysis of cooling electronic circuits using heat pipes. *IEEE Transactions on Components and Packaging Technologies*, 2001. **24**(4): p. 549-553.
 224. Pastukhov, V.G., et al., Miniature loop heat pipes for electronics cooling. *Applied Thermal Engineering*, 2003. **23**(9): p. 1125-1135.
 225. Wang, J.C., S.H. Hsiang, and S.L. Chen, Experimental investigations of thermal resistance of a heat sink with horizontal embedded heat pipes. *International Communications in Heat and Mass Transfer*, 2007. **34**(8): p. 958-970.
 226. Liang, T.S. and Y.M. Hung, Experimental investigation on the thermal performance and optimization of heat sink with U-shape heat pipes. *Energy Conversion and Management*, 2010. **51**(11): p. 2109-2116.
 227. Abd El-Baky, M.A. and M.M. Mohamed, Heat pipe heat exchanger for heat recovery in air conditioning. *Applied Thermal Engineering*, 2007. **27**: p. 795-801.
 228. Yang, F., X. Yuan, and G. Lin, Waste heat recovery using heat pipe heat exchanger for heating automobile using exhaust gas. *Applied Thermal Engineering*, 2003. **23**: p. 367-372.
 229. Wu, X.P., et al., Analyzing and modeling on optimized L-ratio of evaporator section to condenser section for micro heat pipe heat sinks, in 19th IEEE semi-therm symposium. 2003. p. 185-190.
 230. Sung, H.J., J.S. Yang, and T.S. Park, Local convective mass transfer on circular cylinder with transverse annular fins in crossflow. *International Journal of Heat and Mass Transfer*, 1996. **39**(5): p. 1093-1101.
 231. Hu, X. and A.M. Jacobi, Local heat transfer behavior and its impact on a single-row, annularly finned tube heat exchanger. *Journal of Heat Transfer*, 1993. **115**(1): p. 66-74.
 232. Weibel, J.A., S.V. Garimella, and M.T. North, Characterization of evaporation and boiling from sintered powder wicks fed by capillary action. *International Journal of Heat and Mass Transfer*, 2010. **53**(19-20): p. 4204-4215.
 233. Kim, G.H., et al., Thermal Management of Batteries in Advanced Vehicles Using Phase-Change Materials, in *Sustainability: The Future of Transportation 2007*: Anaheim, CA.

234. Incropera, F.P. and D.P. DeWitt, Fundamentals of Heat and Mass Transfer. 5 ed. 2002, USA: John Wiley & Sons, Inc.
235. Lee, K.C., Ultra-thin heat pipe, in US Patent, U. Patent, Editor. 2010.
236. Lee, K.C. and S.L. Chung, Ultra-thin heat pipe and manufacturing method thereof, in US Patent, U. Patent, Editor. 2010.
237. Kameoka, H., et al., Flattened heat pipe and manufacturing method thereof, in US Patent, U. Patent, Editor. 2012.
238. Del Bagno, A.C., R.R. Giordano, and F. Rose, Heat pipe having multiple integral wick structures, in US Patent, U. Patent, Editor. 1984.
239. Grover, G.M., Evaporation-Condensation Heat Transfer Device, in US Patent, U. Patent, Editor. 1966.
240. Koch, K. and W. Barthlott, Superhydrophobic and superhydrophilic plant surfaces: an inspiration for biomimetic materials. Philosophical Transactions of the Royal Society A: Mathematical Physical & Engineering Sciences, 2009. **367**(1893): p. 1487-1509.
241. Bhushan, B., Biomimetics inspired surfaces for drag reduction and oleophobicity/philicity. Beilstein Journal of Nanotechnology, 2011. **2**: p. 66-84.
242. Nosonovsky, M. and B. Bhushan, Green Tribology, Biomimetics, Energy Conservation and Sustainability. Lotus versus Rose: Biomimetic Surface Effects. 2012, Berlin: Springer.
243. Ensikat, H.J., et al., Superhydrophobicity in perfection: the outstanding properties of the lotus leaf. Beilstein Journal of Nanotechnology, 2011. **2**: p. 152-161.
244. Nosonovsky, M., Model for solid-liquid and solid-solid friction for rough surfaces in nano- and bio-tribology. Journal of Chemical Physics, 2007. **126**: p. 224701-224706.
245. Wang, J.L. and I. Catton, Biporous heat pipes for high power electronic device cooling. 17th IEEE SEMI-THERM Symposium, 2001: p. 211-218.
246. Chan, B. and S.J. Kim, Capillary performance of bi-porous sintered metal wicks. International Journal of Heat and Mass Transfer, 2012. **55**(15-16): p. 4096-4103.
247. Xiao, H. and G. Franchi, Design and fabrication of hybrid bi-model wick structure for heat pipe. Applied Journal of Porous Material, 2008. **15**: p. 635-642.
248. Semenic, T. and I. Catton, Experimental study of biporous wicks for high heat flux applications. International Journal of Heat and Mass Transfer, 2009. **52**(21-22): p. 5113-5121.
249. Li, Y., H.F. He, and Z.X. Zeng, Evaporation and condensation heat transfer in a heat pipe with a sintered-grooved composite wick. Applied Thermal Engineering, 2013. **50**(1): p. 342-351.
250. Wang, J. and I. Catton, Enhanced evaporation heat transfer in triangular grooves covered with a thin fine porous layer. Applied Thermal Engineering, 2001. **21**(17): p. 1721-1737.
251. Tang, Y., et al., Experimental investigation on capillary force of composite wick structure by IR thermal imaging camera. Experimental Thermal and Fluid Science 2010. **34**(2): p. 190-196.

252. Li, X.B., et al., Capillary limit of micro heat pipe with compound structure of a sintered wick on trapezium-grooved substrate. *Electrical Review*, 2012: p. 141-144.
253. Eastman, G.Y., *Sintered grooved wicks*, U. Patent, Editor. 1981.
254. Garner, S.D., et al., *Sintered grooved wick with particle web*, U. Patent, Editor. 2006.
255. Hwang, G.S., et al., Modulated wick heat pipe. *International Journal of Heat and Mass Transfer*, 2007. **50**(7-8): p. 1420-1434.
256. Zhang, C. and C.H. Hidrovo, Investigation of nanopillar wicking capabilities for heat pipes applications, in *Proceedings of the ASME 2009 2nd Micro/Nanoscale Heat & Mass Transfer 2009*: Shanghai, China.
257. Ranjan, R., et al., Wicking and thermal characteristics of micropillared structures for use in passive heat spreaders. *International Journal of Heat and Mass Transfer*, 2012. **55**(4): p. 586-596.
258. Ding, C., C.D. Meinhart, and N.C. MacDonald, Surface modifications of bulk micromachined titanium pillar arrays - a wicking material for thin flat heat pipes, in *Proceedings of the ASME Micro/Nanoscale Heat and Mass Transfer International Conference*. 2010. p. 415-419.
259. Zhao, Y.J., et al., Beetle Inspired Electrospray Vapor Chamber, in *ASME 2009 Second International Conference on Micro/Nanoscale Heat and Mass Transfer*. 2009: Shanghai, China.
260. Kohonen, M.M., Engineered wettability in tree capillaries. *Langmuir*, 2006. **22**(7): p. 3148-3153.
261. Zheng, Y.M., et al., Directional water collection on wetted spider silk. *Nature*, 2010. **463**: p. 640-643.
262. Ju, J., et al., A multi-structural and multi-functional integrated fog collection system in cactus. *Nature Communications*, 2012. **3**: p. 1247-1252.
263. Parker, A.R. and C.R. Lawrence, Water capture by a desert beetle. *Nature* 2001. **414**: p. 33-34.
264. Nørgaard, T. and M. Dacke, Fog-basking behaviour and water collection efficiency in Namib desert darkling beetles. *Frontiers in Zoology*, 2010. **7**: p. 23-30.
265. Carl, G., R. Merlin, and W.F.C. Blumer, The water-collecting mechanism of *molochhorridus* re-examined. *Amphibia-Reptilia*, 1982. **3**: p. 57-64.
266. Sherbrooke, W.C., et al., Functional morphology of scale hinges used to transport water: convergent drinking adaptations in desert lizards (*Moloch horridus* and *Phrynosoma cornutum*). *Zoomorphology*, 2007. **126**(2): p. 89-102.
267. Comanns, P., et al., Moisture harvesting and water transport through specialized micro-structures on the integument of lizards. *Beilstein Journal of Nanotechnology*, 2011. **2**: p. 204-214.
268. Hodson, M.J. and J.A. Bryant, *Functional biology of plants*. 2012, Chichester: John Wiley & Sons.
269. Denny, M., Tree hydraulics: how sap rises. *European Journal of Physics*, 2012. **33**: p. 43-53.
270. Taiz, L. and E. Zeiger, *Plant Physiology*. Fifth ed. 2010, Sunderland, Massachusetts: Sinauer Associates Inc. 782.

271. Lakes, R., Materials with structural hierarchy. *Nature*, 1993. **361**: p. 511-515.
272. Nosonovsky, M. and B. Bhushan, Hierarchical roughness optimization for biomimetic superhydrophobic surfaces. *Ultramicroscopy*, 2007. **107**: p. 969-979.
273. Yuan, Y.H. and T.R. Lee, *Surface Science Techniques*. Chapter 1: Contact Angle and Wetting Properties, ed. G. Bracco and B. Holst. Vol. 51. 2013, New York: Springer.
274. Eral, H.B., D.J.C.M.t. Mannelje, and J.M. Oh, Contact angle hysteresis: a review of fundamentals and applications. *Colloid and Polymer Science*, 2013. **291**(2): p. 247-260.
275. Cassie, A.B.D. and S. Baxter, Wettability of porous surfaces. *Transactions of the Faraday Society*, 1944. **40**: p. 546-551.
276. Nosonovsky, M. and B. Bhushan, Multiscale effects and capillary interations in functional biomimetic surfaces for energy conversion and green engineering. *Philosophical Transactions of the Royal Society A: Mathematical Physical & Engineering Sciences*, 2009. **367**(1893): p. 1511-1539.
277. Nosonovsky, M., On the range of applicability of the Wenzel and Cassie equations. *Langmuir*, 2007c. **23**: p. 9919-9920.
278. Nosonovsky, M. and B. Bhushan, Patterned non-adhesive surfaces: superhydrophobicity and wetting regime transitions. *Langmuir*, 2008c. **24**(4): p. 1525-1533.
279. Furstner, R., et al., Wetting and self-cleaning properties of artificial superhydrophobic surfaces. *Langmuir*, 2005. **21**(3): p. 956-961.
280. Nam, Y.S., et al., Fabrication and characterization of the capillary performance of superhydrophilic Cu micropost arrays. *Journal of Microelectromechanical Systems*, 2010. **19**(3): p. 581-588.
281. Chien, L.H. and C.C. Chang. Experimental study of evaporation resistance on porous surfaces in flat heat pipes. in *Thermomechanical Phenomena in Electrical Systems - Proceedings of the Intersociety Conference*. 2002.
282. Wang, Y.X. and G.P. Peterson, Analytical model for capillary evaporation limitation in thin porous layers. *Journal of Thermophysics Heat Transfer*, 2003. **17**(2): p. 145-149.
283. Tsai, Y.Y. and C.H. Lee, Experimental study of evaporative heat transfer in sintered powder structures at low superheat levels. *Experimental Thermal and Fluid Science*, 2014. **52**: p. 230-238.
284. Tsai, Y.Y. and C.H. Lee, Effects of sintered structural parameters on reducing the superheat level in heat pipe evaporator. *International Journal of Thermal Sciences*, 2014. **76**: p. 225-234.
285. Hanlon, M.A. and H.B. Ma, Evaporation heat transfer in sintered porous media. *ASME Journal of Heat Transfer*, 2003. **125**(4): p. 644-652.
286. Wang, H., S.V. Garimella, and J.Y. Murthy, Characteristics of an evaporating thin film in a microchannel. *International Journal of Heat and Mass Transfer*, 2007. **50**(19-20): p. 3933-3942.
287. Byon, C. and S.J. Kim, Capillary performance of bi-porous sintered metal wicks. *International Journal of Heat and Mass Transfer*, 2012. **55**: p. 4096-4103.

288. Weibel, J.A. and S.V. Garimella, Visualization of vapor formation regimes during capillary-fed boiling in sintered-powder heat pipe wicks. *International Journal of Heat and Mass Transfer*, 2012. **55**: p. 3498-3510.
289. Deng, D., et al., Evaluation of capillary performance of sintered porous wicks for loop heat pipe. *Experimental Thermal and Fluid Science*, 2013. **50**: p. 1-9.
290. Chamarchy, P., et al. Novel fluorescent visualization method to characterize transport properties in micronano heat pipe wick structures. in *Proceedings of the ASME 2009 InterPACK*. 2009. San Francisco, California, USA.
291. Espinosa, F.A.D., T.B. Peters, and J.G. Brisson, Effect of fabrication parameters on the thermophysical properties of sintered wicks for heat pipe applications. *International Journal of Heat and Mass Transfer*, 2012. **55**: p. 7471-7486.
292. Jiang, L., et al., Design and fabrication of sintered wick for miniature cylindrical heat pipe. *Transactions of Nonferrous Metals Society of China*, 2014. **24**: p. 292-301.
293. Choi, J., et al., Experimental investigation on sintered porous wicks for miniature loop heat pipe applications. *Experimental Thermal and Fluid Science*, 2013. **51**: p. 271-278.
294. Hwang, G.S., et al., Multi-artery heat pipe spreader: Experiment. *International Journal of Heat and Mass Transfer*, 2010. **53**(13-14): p. 2662-2669.
295. Bear, J., *Dynamics of Fluids in Porous Media*. 1972, New York: American Elsevier Publishing Company, Inc.
296. Hassanizadeh, S.M. and W.G. Gray, Thermodynamics basis of capillary pressure in porous media. *Water Resources Research*, 1993. **29**(10): p. 3389-3405.
297. Lin, Y.J. and K.S. Hwang, Effects of powder shape and processing parameters on heat dissipation of heat pipes with sintered porous wicks. *Materials Transactions*, 2009. **50**(10): p. 2427-2434.
298. Jinwang, L., et al., Effect of fabricating parameters on properties of sintered porous wicks for loop heat pipe. *Powder Technology*, 2010. **204**: p. 241-248.
299. EAL, *Laboratory Procedure for Preparation, Attachment, Extension and Use of Thermocouples, in Calibration of Thermocouples*. 1997, European Cooperation for Accreditation of Laboratories.
300. Shah, R.K. and A.L. London, *Laminar flow forced convection heat transfer and flow friction in straight and curved ducts*. 1971, Office of Naval Research, Washington, D. C.
301. Shah, R.K., Compact heat exchangers, in *Handbook of Heat transfer Applications*, W.M. Rohsenow, J.P. Hartnett, and E.N. Ganić, Editors. 1985, McGraw-Hill: New York. p. 4-174 to 4-311.

Appendix A – Thermocouple Calibration

Welded tip thermocouples (K-type) are the most widely used temperature sensors in laboratories due to wide operating range (-200 – 1250°C) and fast responding. The standard accuracy given by K-type thermocouple is $\pm 2.2^\circ\text{C}$ or $\pm 0.75\%$ above 0°C , affected by deviations in the alloys (nickel-chromium). However, deviations between thermocouples differ little and a much higher accuracy can be achieved by individual calibration.

A thermocouple consists of two dissimilar metal wires intimately welded together at one end (a junction) that generates a small thermoelectric voltage in relation to temperature when the junction is heated. Thermocouple calibration is an important measure to improve experimental accuracy. A direct calibration can be done by measuring either at a series of fixed point temperatures (e.g. melting/freezing point) or by comparing with standard thermometers in thermally stabilised baths or furnaces [299].

For this Ph.D. experimentation, a 9-point calibration from -20°C to 70°C was run. The monitored temperature points (in water bath) are -20°C , 0°C , 10°C , 20°C , 30°C , 40°C , 50°C , 60°C and 70°C . This was sufficient as the working range of tests were set within this range. 16 K-type thermocouples were connected with two TC-08 thermocouple data loggers. A water bath filled with glycol-water mixture was provided for a stable and constant temperature environment.

The apparent temperature readings recorded from the Pico software were compared with the standard temperature obtained from RS 206-3738 portable

digital thermometer (Fig. 5.9) in Table A.1. Results prior to calibration are demonstrated in Fig. A.1 – A.2. Linear fitting curve was used to calibrate each thermocouple and an example can be found in Fig. A.3. The total values of temperature readings and offsets after calibration are plotted in Fig. A.4 – A.5 and summarised in Table A.2. Before calibration, the average (maximum) accuracy of these thermocouples was $\pm 2.06\%$ ($\pm 8.60\%$) or $\pm 0.61^\circ\text{C}$ ($\pm 2.01^\circ\text{C}$). After calibration, the average (maximum) accuracy was improved to $\pm 1.80\%$ ($\pm 6.74\%$) or $\pm 0.59^\circ\text{C}$ ($\pm 1.90^\circ\text{C}$).

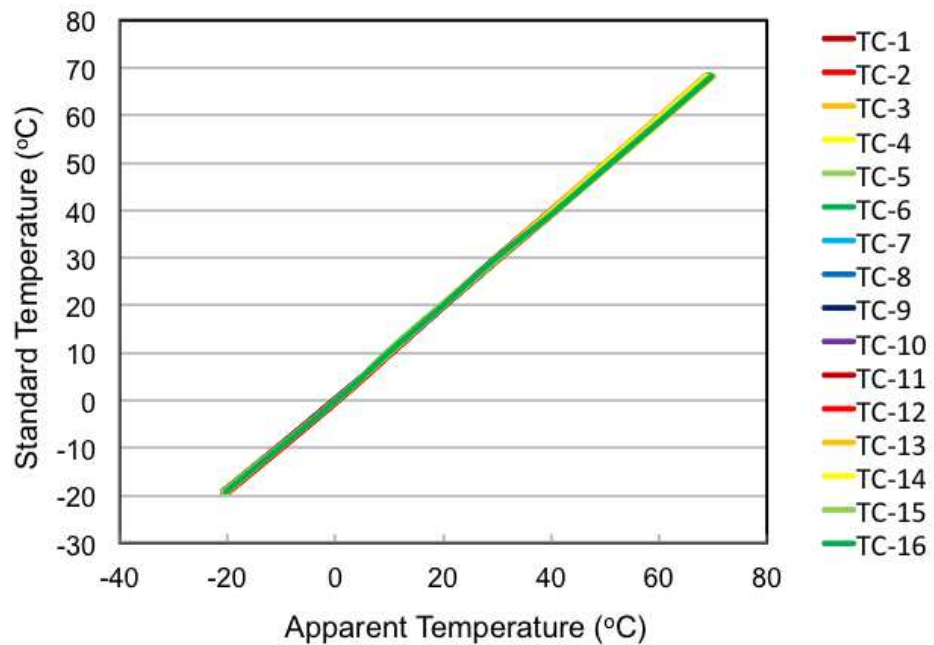


Figure A.1: 16 K-type thermocouples measured readings compared with standard readings before calibration.

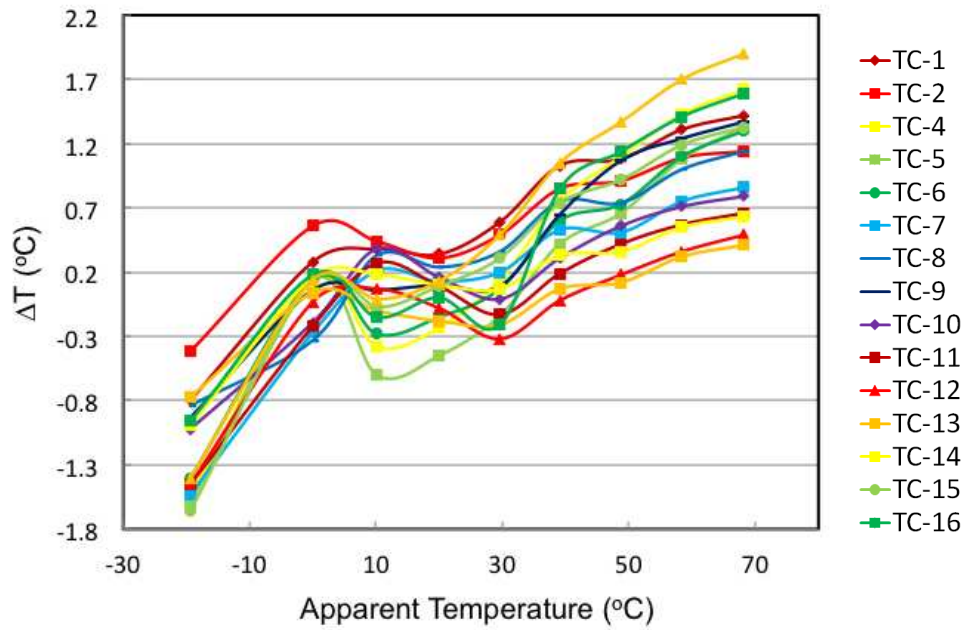


Figure A.2: 16 K-type thermocouples offsets prior to calibration.

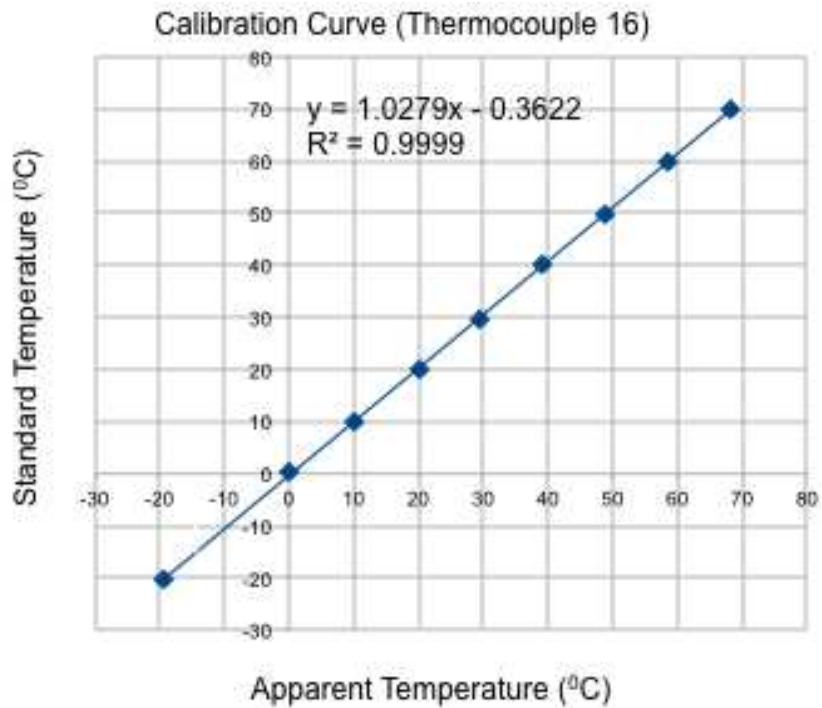


Figure A.3: Example of using fitting curve for thermocouple 16.

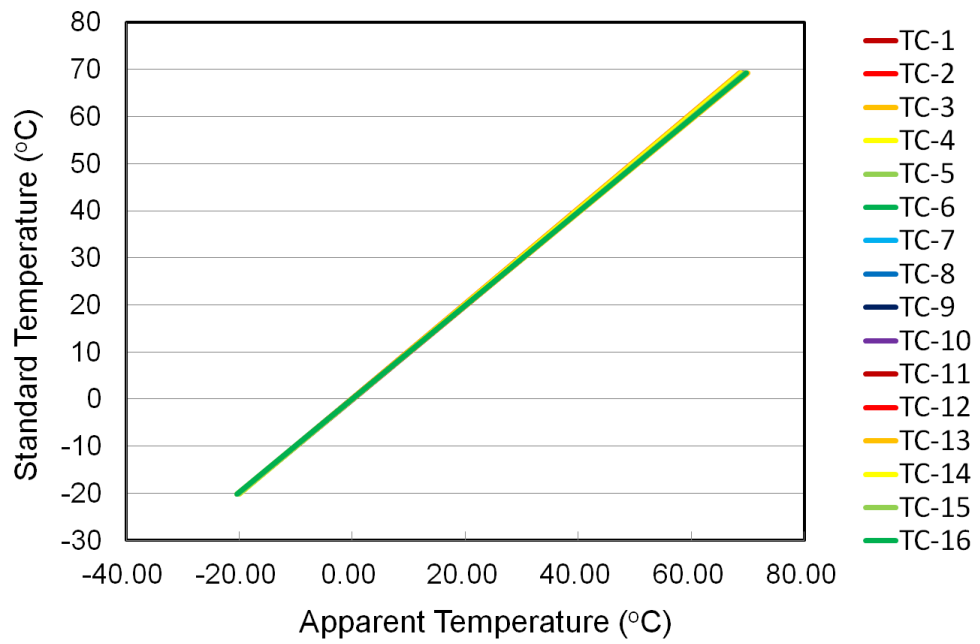


Figure A.4: 16 K-type thermocouples measured readings compared with standard readings after calibration.

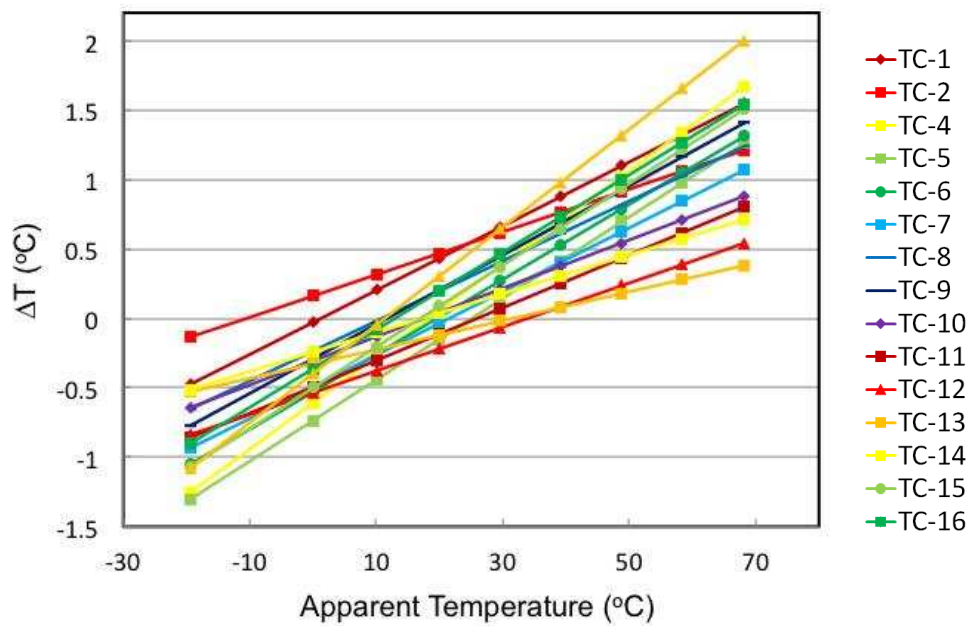


Figure A.5: 16 K-type thermocouples offsets after calibration.

Table A.1: K-type thermocouple measurements before calibration

Standard (°C)	Apparent Reading (°C)							
	TC-1	TC-2	TC-3	TC-4	TC-5	TC-6	TC-7	TC-8
-19.3	-20.10	-19.72	-20.70	-20.84	-20.90	-20.71	-20.83	-20.14
0	0.28	0.56	0.14	0.13	0.14	0.14	-0.27	-0.33
10.1	10.48	10.54	10.09	9.72	9.50	9.82	10.31	10.43
20.0	20.34	20.31	20.13	19.77	19.55	19.85	20.13	20.24
29.6	30.19	30.09	30.09	29.74	29.46	29.67	29.80	29.96
39.1	40.13	39.95	40.15	39.85	39.52	39.70	39.63	39.85
48.8	49.88	49.71	50.17	49.90	49.46	49.53	49.31	49.54
58.4	59.71	59.49	60.10	59.83	59.48	59.50	59.15	59.40
68.2	69.62	69.34	70.10	69.82	69.53	69.50	69.06	69.34
	TC-9	TC-10	TC-11	TC-12	TC-13	TC-14	TC-15	TC-16
-19.3	-20.23	-20.32	-20.75	-20.75	-20.07	-20.29	-20.96	-20.26
0	0.06	-0.19	-0.22	-0.03	0.04	0.16	0.15	0.18
10.1	10.16	10.48	10.37	10.17	10.00	10.28	10.03	9.95
20.0	20.10	20.16	20.09	19.92	19.82	20.10	20.09	20.00
29.6	29.69	29.59	29.47	29.28	29.39	29.67	29.91	29.39
39.1	39.75	39.41	39.29	39.08	39.17	39.43	39.84	39.95
48.8	49.87	49.36	49.22	48.98	48.92	49.16	49.72	49.94
58.4	59.64	59.11	58.97	58.76	58.72	58.95	59.59	59.81
68.2	69.57	68.99	68.86	68.69	68.61	68.83	69.53	69.79
Accuracy								

Maximum	$\% = \pm \left \frac{T_{\text{apparent}} - T_{\text{standard}}}{T_{\text{standard}}} \times 100 \right _{\text{max}} = \pm 8.60\%; \text{ or } \Delta = \pm T_{\text{apparent}} - T_{\text{standard}} _{\text{max}} = \pm 2.01^{\circ}\text{C}$
Average	$\% = \pm \frac{\sum_0^n \left \frac{T_{\text{apparent}} - T_{\text{standard}}}{T_{\text{standard}}} \times 100 \right _i}{n} = \pm 2.06\%; \text{ or } \Delta = \pm \frac{\sum_0^n T_{\text{apparent}} - T_{\text{standard}} _i}{n} = \pm 0.61^{\circ}\text{C}$

Table A.2: K-type thermocouple measurements after calibration

Standard (°C)	Apparent Reading (°C)							
	TC-1	TC-2	TC-3	TC-4	TC-5	TC-6	TC-7	TC-8
-19.3	-19.78	-19.44	-20.38	-20.55	-20.60	-20.35	-20.24	-19.95
0	-0.03	0.16	-0.40	-0.61	-0.74	-0.53	-0.49	-0.24
10.1	10.30	10.42	10.06	9.83	9.66	9.84	9.84	10.08
20.0	20.43	20.47	20.30	20.06	19.85	20.01	19.96	20.20
29.6	30.25	30.22	30.24	29.98	29.73	29.87	29.78	30.00
39.1	39.97	39.86	40.08	39.80	39.51	39.63	39.50	39.71
48.8	49.90	49.71	50.12	49.82	49.49	49.59	49.42	49.62
58.4	59.72	59.46	60.06	59.74	59.38	59.45	59.24	59.43
68.2	69.75	69.41	70.20	69.87	69.46	69.51	69.27	69.44
	TC-9	TC-10	TC-11	TC-12	TC-13	TC-14	TC-15	TC-16
-19.3	-20.07	-19.94	-20.16	-20.14	-19.83	-19.81	-20.37	-20.20

0	-0.29	-0.31	-0.49	-0.54	-0.33	-0.24	-0.50	-0.36
10.1	10.06	9.97	9.80	9.72	9.88	10.00	9.90	10.02
20.0	20.21	20.04	19.89	19.78	19.88	20.04	20.09	20.20
29.6	30.05	29.81	29.67	29.53	29.58	29.77	29.97	30.06
39.1	39.78	39.47	39.35	39.18	39.18	39.40	39.75	39.83
48.8	49.72	49.34	49.23	49.03	48.98	49.24	49.73	49.80
58.4	59.56	59.11	59.02	58.79	58.68	58.97	59.62	59.67
68.2	69.61	69.08	69.00	68.74	68.58	68.91	69.70	69.74

Accuracy

Maximum	$\% = \pm \left \frac{T_{\text{apparent}} - T_{\text{s tandard}}}{T_{\text{s tandard}}} \times 100 \right _{\text{max}} = \pm 6.74\%; \text{ or } \Delta = \pm T_{\text{apparent}} - T_{\text{s tandard}} _{\text{max}} = \pm 0.59^{\circ}\text{C}$
Average	$\% = \pm \frac{\sum_0^n \left \frac{T_{\text{apparent}} - T_{\text{s tandard}}}{T_{\text{s tandard}}} \times 100 \right _i}{n} = \pm 1.80\%; \text{ or } \Delta = \pm \frac{\sum_0^n T_{\text{apparent}} - T_{\text{s tandard}} _i}{n} = \pm 1.90^{\circ}\text{C}$

Appendix B – Fin Analysis

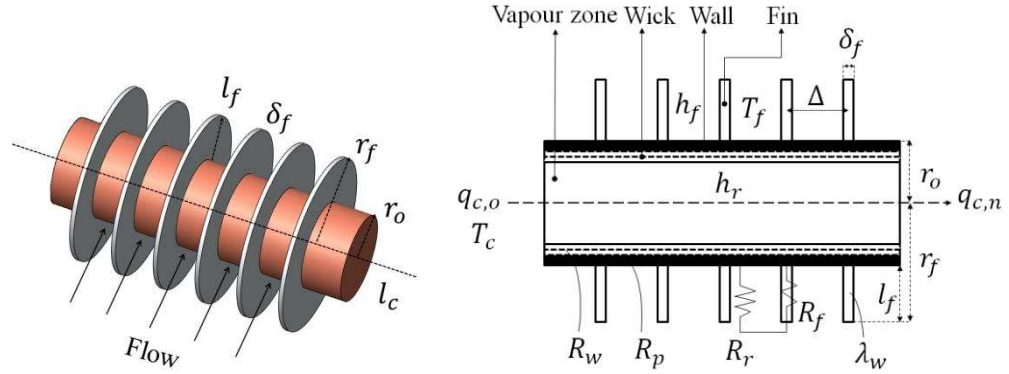


Figure B.1: Thermal resistance network at the condenser.

Fig. B.1 shows the thermal resistance model at the condenser section. The total thermal resistance R_t is the sum of two contributions: R_r (unfinned portion of the heat pipe) and R_f (fin). R_w (heat pipe wick) and R_p (heat pipe wall) can be included into R_r if h_r is known. The thermal resistance of the unfinned portion of the heat pipe R_r :

$$R_r = \frac{1}{h_r A_r} \quad (\text{B.1})$$

where

h_r – heat transfer coefficient of the heat pipe

A_r – surface area of unfinned portion of the heat pipe, $A_r = 2\pi r_o (l_c - N\delta_f)$

N – number of fins, $N = l_c / \Delta - 1$ for a fixed fin pitch

δ_f – fin thickness

The heat transfer coefficients h_r , h_f that determine R_r and R_f depend on the flow patterns of the ambient fluid. For h_r ($h_r = \frac{Nu_r k}{D}$), the Nusselt number Nu_r can be obtained according to cross flow past a cylinder [234] (Eq. B.2). The Reynolds number can be calculated by using a characteristic velocity v , which is based on the average fluid velocity across the fins.

$$Nu_r = 0.683 Re_D^{0.466} Pr^{1/3} \quad (B.2)$$

For

$$40 < Re_D \quad (Re_D = \rho v D_h / \mu) < 4,000, \quad Pr \geq 0.7$$

For h_f , the Nusselt number Nu_f can be expressed assuming developing flow across an array of parallel plates with isothermal fin surfaces [300]. Nu_f is presented as functions of x^* and Prandtl number Pr from 0.01 to 50.

$$Nu_f = 7.55 + \left(\frac{0.024 x^{*-1.14}}{1 + 0.0358 x^{*-0.64} Pr^{0.17}} \right) \quad (B.3)$$

where

x^* - dimensionless flow axial distance, known as Graetz number ($x^* = x/D_h Re Pr$);

Fin performance can be characterised by fin efficiency. It accounts for the temperature reduction between the fin and the ambient fluid due to fin conduction and convection from or to the fin surface. The definition of the fin efficiency is the ratio of the fin heat transfer rate to the heat transfer rate of the fin of same geometry and condition where the entire fin were at the base temperature (i.e. infinite thermal conductivity) (Eq. B.4).

$$\eta_f = \frac{Q}{Q_{\max}} = \frac{Q_{wf}}{h_f A_f (T_b - T_\infty)} \quad (\text{B.4})$$

where

$$A_f - \text{total surface area, } A_f = 2\pi r_o l_c + 2N\pi(r_f^2 - r_o^2)$$

T_b – fin base temperature

T_∞ – medium temperature

Shah [301] presented the fin efficiency formulas for circular fin of uniform fin thickness (thin fins) using Eq. B.5 – B.6. The correlation of η_f is indicated as functions of a dimensionless group ml_e .

$$\eta_f = a(ml_e)^{-b} \quad (\text{B.5})$$

If $\phi > 0.6 + 2.257(r^*)^{-0.445}$

$$\eta_f = \frac{\tanh \phi}{\phi} \quad (\text{B.6})$$

If $\phi \leq 0.6 + 2.257(r^*)^{-0.445}$

where

$$m = \left(\frac{2h_f}{\lambda_w \delta_f} \right)^{1/2}, \quad l_e = l_f + \frac{\delta_f}{2}, \quad r^* = \frac{r_f}{r_o}, \quad a = (r^*)^{-0.246}$$

$$\phi = ml_e (r^*)^{(\exp 0.13ml_e - 1.3863)}$$

$$b = 0.9107 + 0.0893r^* \text{ for } r^* \leq 2, \quad b = 0.9706 + 0.17125 \ln r^* \text{ for } r^* > 2$$

Appendix C – Measurement Uncertainties

System without fins

Table C.1: Measurement uncertainties for system without fins under 10°C

Test	Heat input (W)	Heat output (W)	Uncertainty (U) (%)				
			Heat Flux (P)	Resistance (R)		Thermal conductivity (K_{hp})	Heat transfer coefficient at cooling end (h_c)
				Total (R_t)	Heat pipe (R_{hp})		
1	20.09	21.89	8.9	16.67	12.72	11.74	2.09
2	31.06	33.00	6.24	6.71	4.84	5.10	0.58
3	39.68	39.87	0.47	0.73	0.24	0.75	0.43
4	49.24	53.82	9.3	3.44	2.83	2.40	0.76
5	59.63	62.30	0.61	7.94	5.51	5.30	0.51
6	70.1	69.54	0.8	12.73	9.46	9.88	3.35

Table C.2: Measurement uncertainties for system without fins under 20°C

Test	Heat input (W)	Heat output (W)	Uncertainty (U) (%)				
			Heat Flux (P)	Resistance (R)		Thermal conductivity (K_{hp})	Heat transfer coefficient at cooling end (h_c)
				Total (R_t)	Heat pipe (R_{hp})		
1	19.96	19.14	4.08	7.96	6.51	6.21	1.32

2	30.96	29.37	5.15	1.01	1.32	1.40	0.63
3	39.61	37.44	5.48	1.14	1.26	1.17	2.05
4	49.08	52.78	7.54	1.40	1.26	1.18	0.10
5	59.49	60.22	1.22	4.67	2.29	2.25	0.50
6	69.09	71.53	3.53	1.76	3.01	3.00	0.76

Table C.3: Measurement uncertainties for system without fins under 30°C

Test	Heat input (W)	Heat output (W)	Uncertainty (U) (%)				
			Heat Flux (P)	Resistance (R)		Thermal conductivity (K_{hp})	Heat transfer coefficient at cooling end (h_c)
				Total (R_t)	Heat pipe (R_{hp})		
1	19.96	21.63	8.37	0.74	1.41	1.42	4.99
2	30.83	32.46	5.29	0.64	0.13	0.13	0.86
3	39.36	37.35	5.11	0.41	1.20	1.19	1.78
4	48.82	52.22	6.96	1.83	0.98	0.98	1.01
5	59.44	58.02	2.39	0.17	0.34	0.33	0.69
6	68.75	66.66	3.04	0.23	0.56	0.55	3.74

Table C.4: Measurement uncertainties for system without fins under 35°C

Test	Heat input (W)	Heat output (W)	Uncertainty (U) (%)				
			Heat Flux (P)	Resistance (R)		Thermal conductivity (K_{hp})	Heat transfer coefficient at cooling end (h_c)
				Total (R_t)	Heat pipe (R_{hp})		
1	19.85	19.54	1.58	1.62	3.67	4.33	11.45

2	30.78	35.32	14.75	2.31	1.46	1.32	3.48
3	39.40	39.25	0.4	0.71	0.54	0.68	1.46
4	48.77	48.29	0.98	1.28	1.20	1.34	2.39
5	59.14	56.14	5.07	0.66	1.79	1.91	4.12
6	68.68	69.78	1.6	1.28	1.66	1.72	6.96

System with fins

Table C.5: Measurement uncertainties for system with fins under 10°C

Test	Heat input (W)	Heat output (W)	Uncertainty (U) (%)				
			Heat Flux (P)	Resistance (R)		Thermal conductivity ($K_{hp,wf}$)	Heat transfer coefficient at cooling end ($h_{c,wf}$)
				Total ($R_{t,wf}$)	Heat pipe ($R_{hp,wf}$)		
1	20.01	21.39	6.9	7.57	11.28	10.42	1.95
2	31.00	28.88	6.83	1.97	3.13	3.35	5.66
3	39.55	37.66	4.78	0.72	0.67	0.35	6.63
4	50.17	51.27	2.19	2.51	5.38	5.35	2.35
5	59.38	56.28	5.22	3.44	4.55	4.44	9.43
6	68.83	71.11	3.31	2.87	3.81	3.62	7.17

Table C.6: Measurement uncertainties for system with fins under 20°C

Test	Heat input (W)	Heat output (W)	Uncertainty (U) (%)				
			Heat Flux (P)	Resistance (R)		Thermal conductivity ($K_{hp,wf}$)	Heat transfer coefficient at cooling end ($h_{c,wf}$)
				Total ($R_{t,wf}$)	Heat pipe ($R_{hp,wf}$)		
1	19.95	20.26	1.55	4.30	7.40	7.08	6.48
2	30.86	32.61	5.67	2.26	3.19	3.28	0.81
3	39.38	39.28	0.25	0.79	0.47	0.67	4.02
4	48.84	49.21	0.75	0.31	0.45	0.25	5.61
5	60.19	61.77	2.55	3.36	4.86	4.89	0.38
6	68.71	67.04	2.44	3.69	5.76	5.89	6.89

Table C.7: Measurement uncertainties for system with fins under 30°C

Test	Heat input (W)	Heat output (W)	Uncertainty (U) (%)				
			Heat Flux (P)	Resistance (R)		Thermal conductivity ($K_{hp,wf}$)	Heat transfer coefficient at cooling end ($h_{c,wf}$)
				Total ($R_{t,wf}$)	Heat pipe ($R_{hp,wf}$)		
1	20.17	20.06	0.55	1.42	0.26	0.20	5.08
2	30.77	32.17	4.57	1.40	2.56	2.56	12.45
3	39.26	35.55	9.45	2.21	3.19	3.15	7.51
4	48.64	47.38	2.60	0.47	0.52	0.57	1.70
5	59.07	61.84	4.68	1.54	2.93	2.96	4.77
6	68.54	64.36	6.10	1.21	3.09	3.12	18.56

Table C.8: Measurement uncertainties for system with fins under 35°C

Test	Heat input (W)	Heat output (W)	Uncertainty (U) (%)				
			Heat Flux (P)	Resistance (R)		Thermal conductivity ($K_{hp,wf}$)	Heat transfer coefficient at cooling end ($h_{c,wf}$)
				Total ($R_{t,wf}$)	Heat pipe ($R_{hp,wf}$)		
1	20.09	22.11	10.01	4.46	4.55	4.72	8.80
2	30.74	31.16	1.38	0.07	0.62	0.66	1.90
3	39.21	37.01	5.61	0.92	1.78	1.79	3.01
4	48.64	51.09	5.04	1.60	1.16	1.19	2.38
5	59.29	59.04	0.43	1.44	1.06	1.09	7.19
6	68.49	70.99	3.65	0.57	0.07	0.02	4.14

Appendix D – Selected Raw Data from Tests

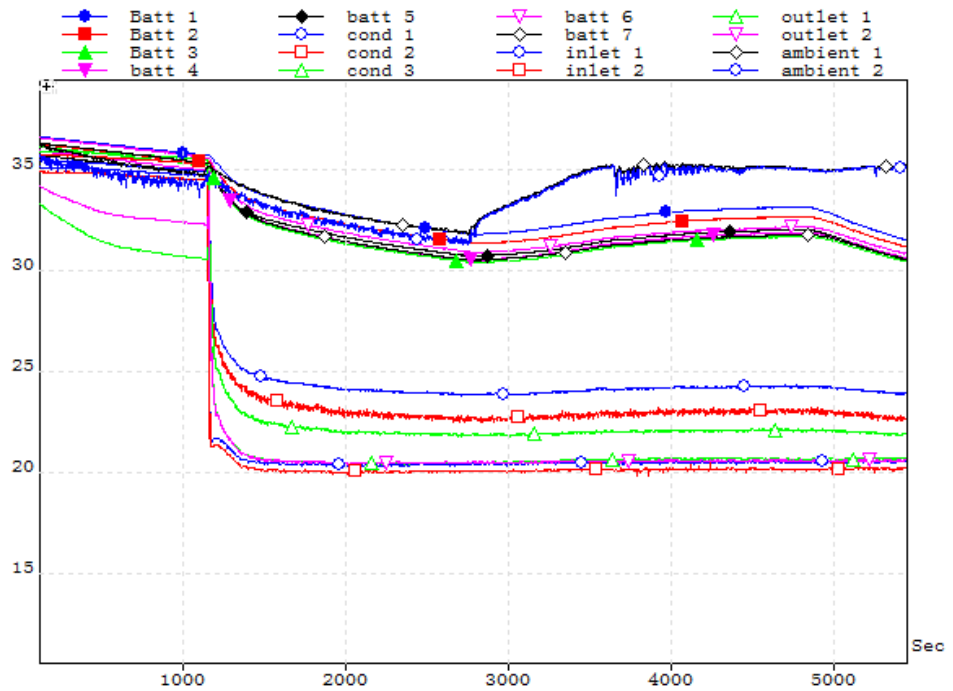


Figure D.1: Steady state cooling, 2.5 W/cell 35°C ambient 20°C cooling.

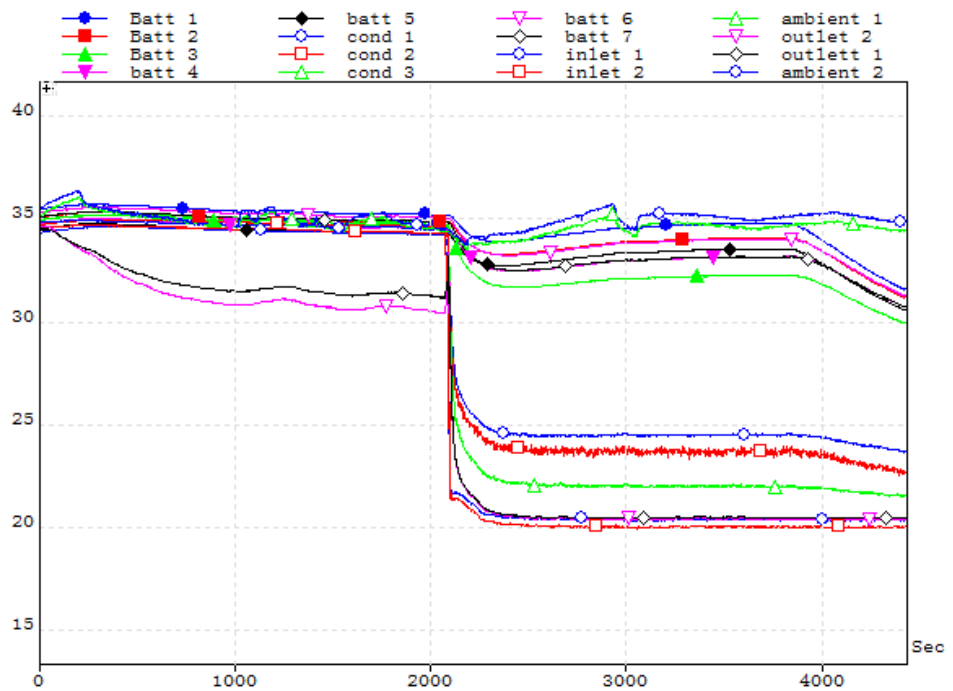


Figure D.2: Steady state cooling, 5 W/cell 35°C ambient 20°C cooling.

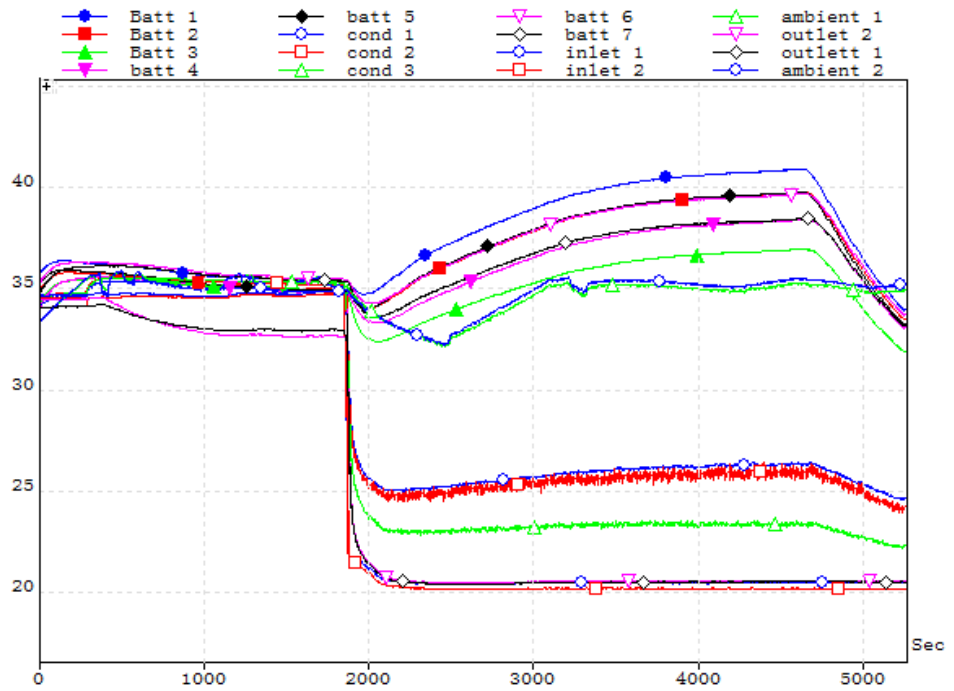


Figure D.3: Steady state cooling, 10 W/cell 35°C ambient 20°C cooling.

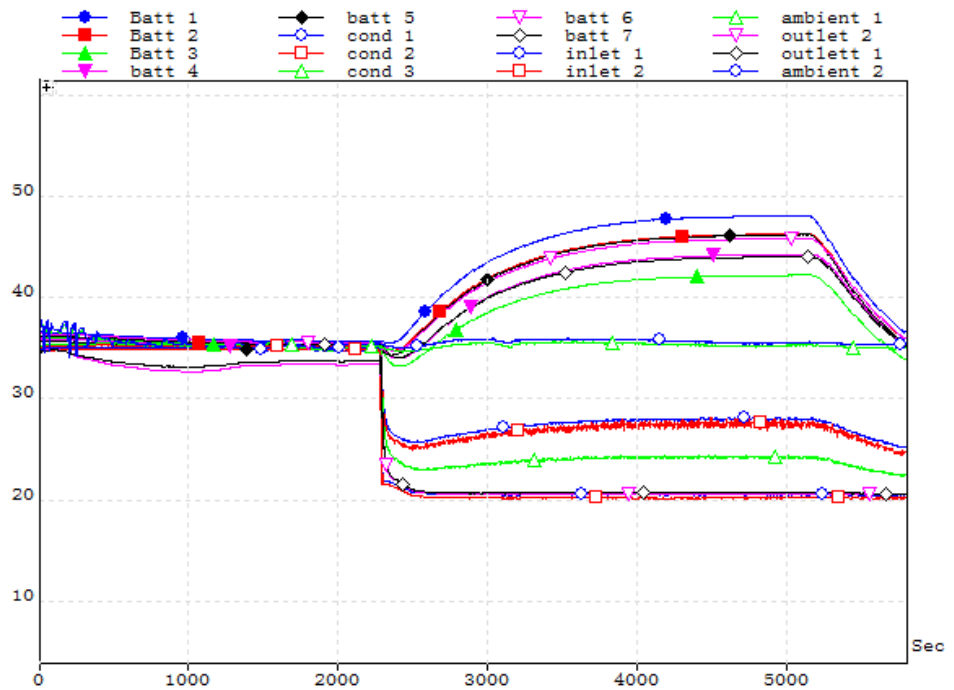


Figure D.4: Steady state cooling, 15 W/cell 35°C ambient 20°C cooling.

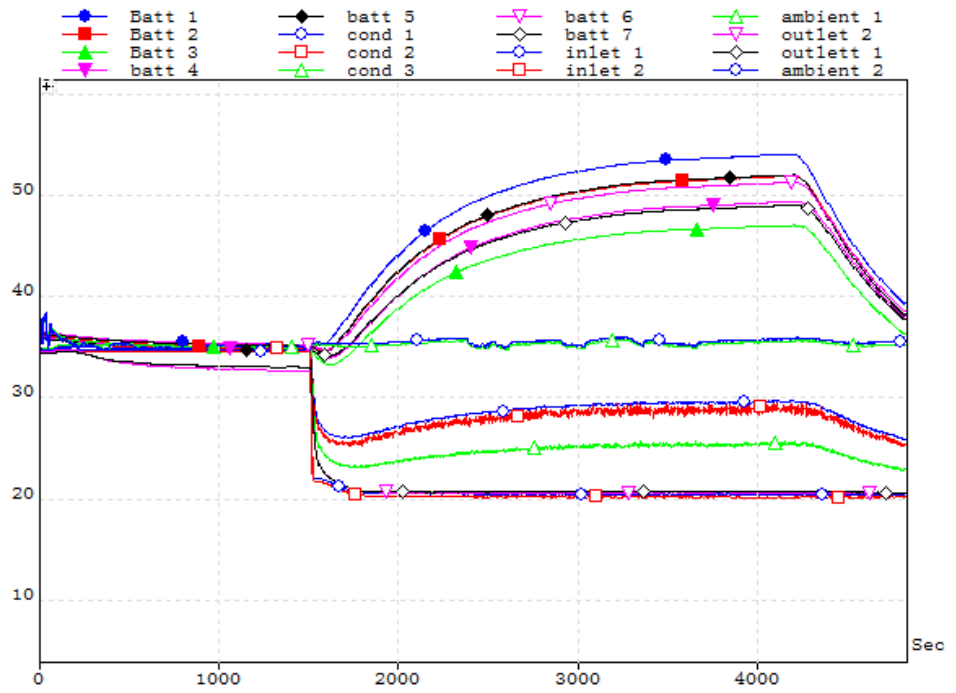


Figure D.5: Steady state cooling, 20 W/cell 35°C ambient 20°C cooling.

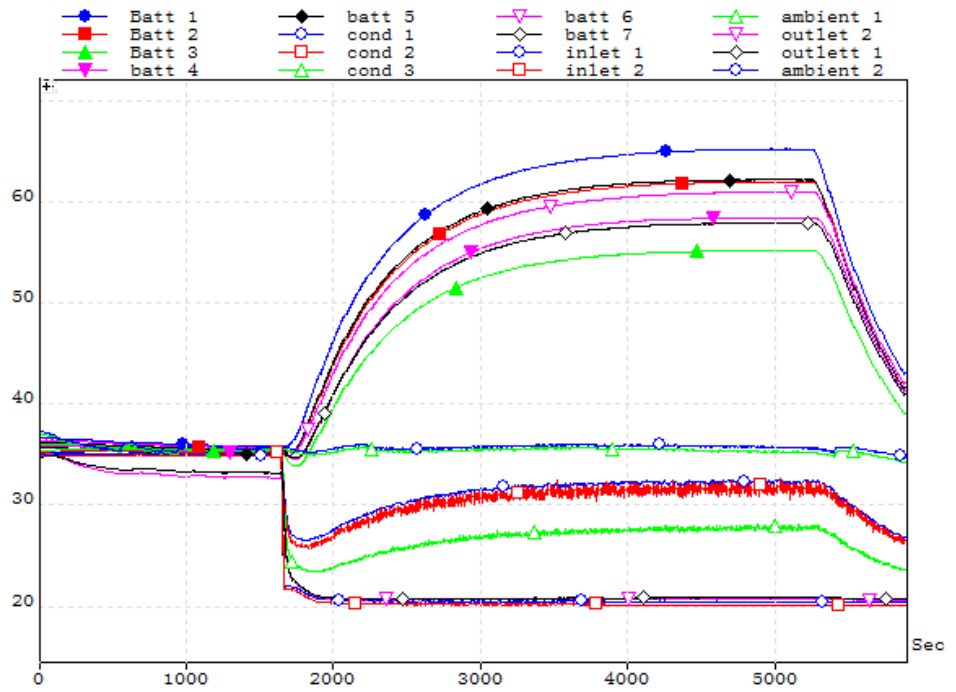


Figure D.6: Steady state cooling, 30 W/cell 35°C ambient 20°C cooling.

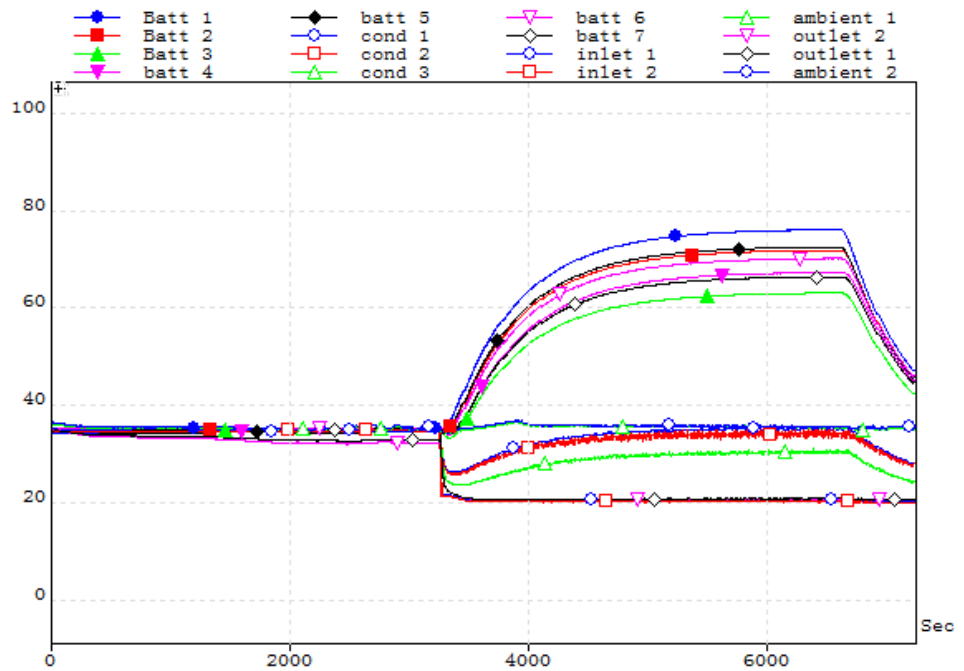


Figure D.7: Steady state cooling, 40 W/cell 35°C ambient 20°C cooling.

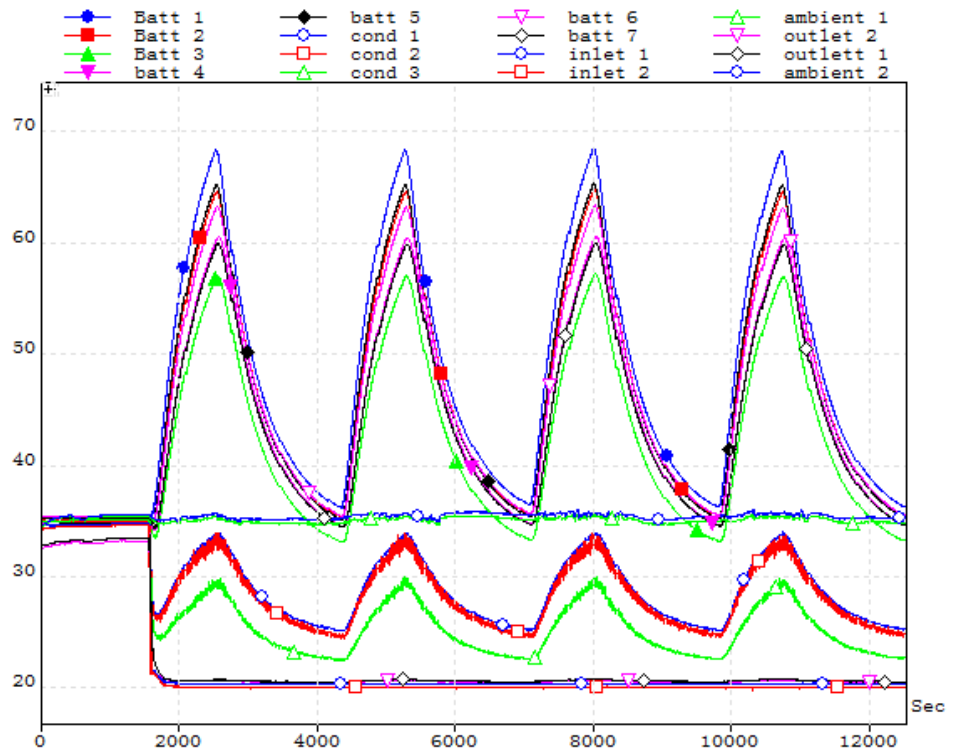


Figure D.8: Transient cooling, 4 repeated cycles at 35°C ambient 20°C cooling.

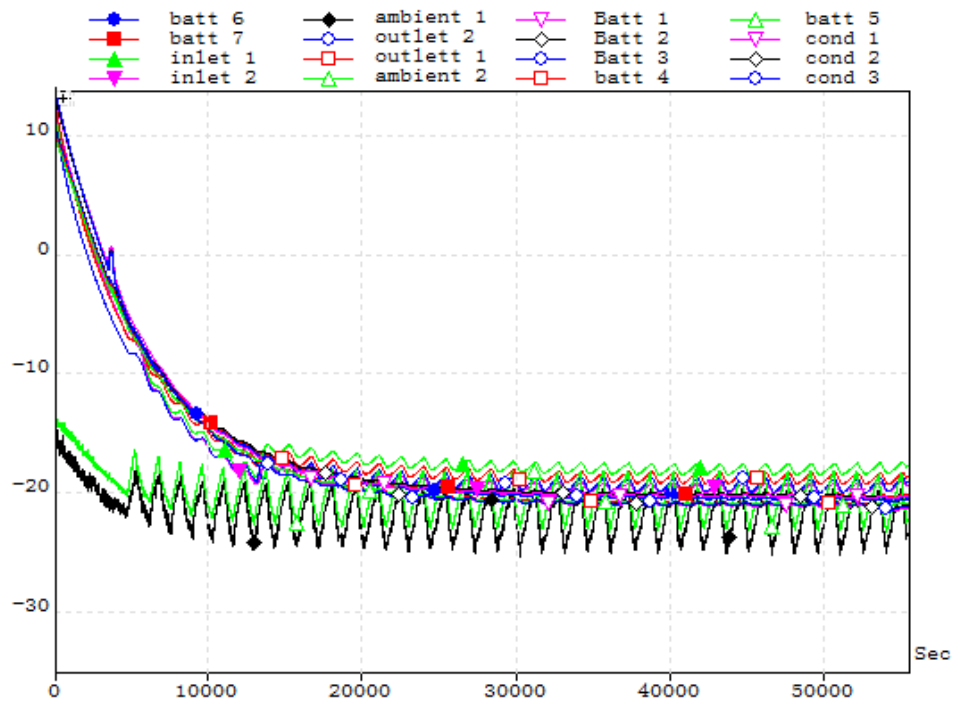


Figure D.9: $-22 \pm 3^\circ\text{C}$ overnight for 15+ hours.

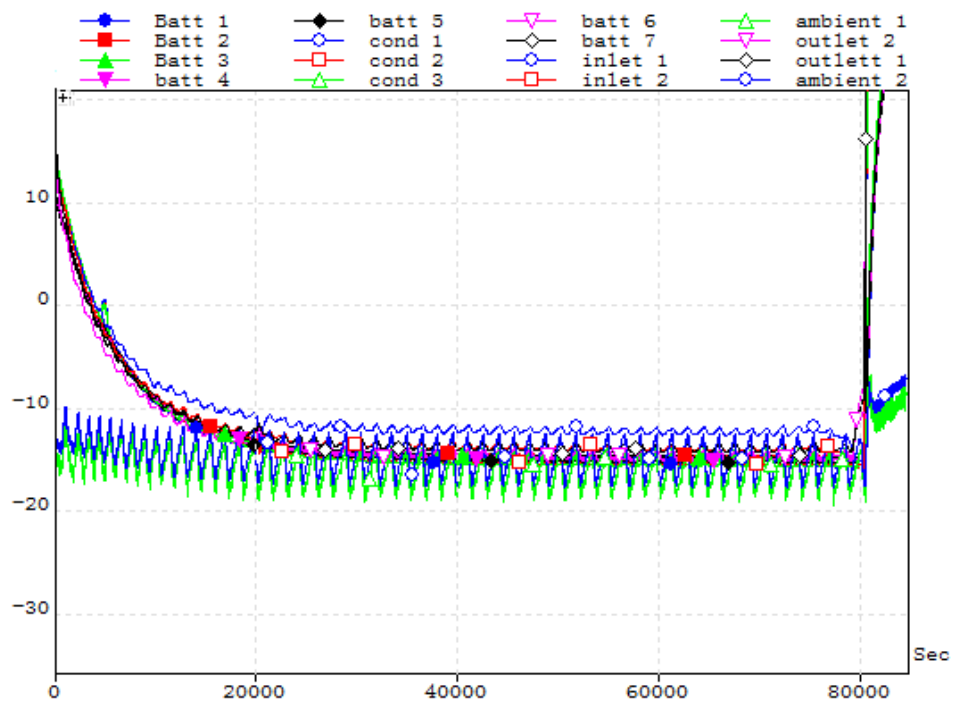


Figure D.10: $-15 \pm 3^\circ\text{C}$ overnight for 20+ hours.

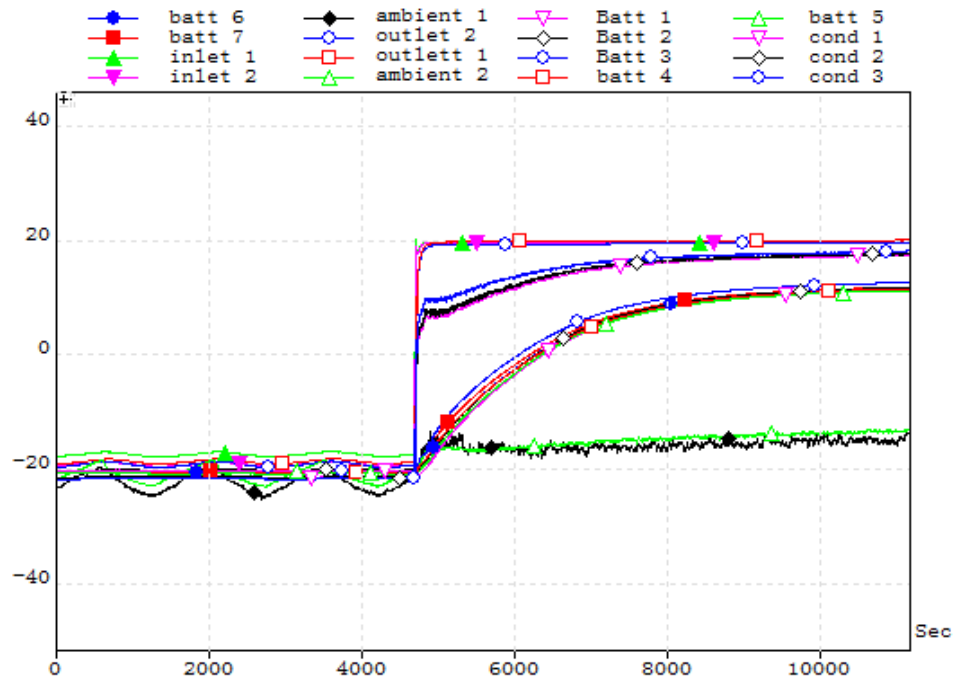


Figure D.11: $-15 \pm 1^\circ\text{C}$ ambient 20°C preheating.

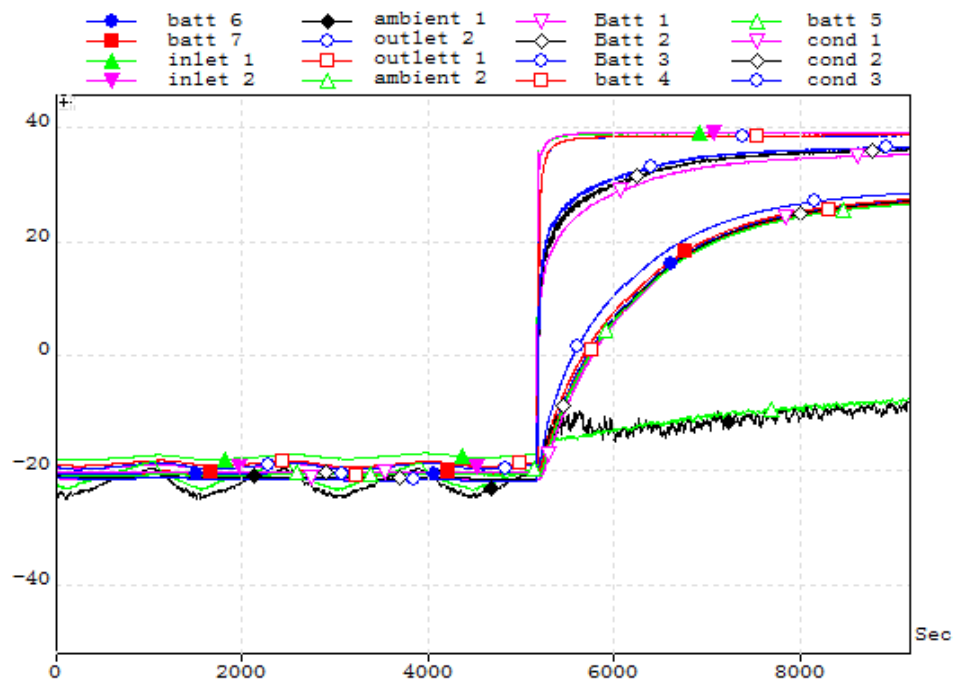


Figure D.12: $-15 \pm 1^\circ\text{C}$ ambient 40°C preheating.

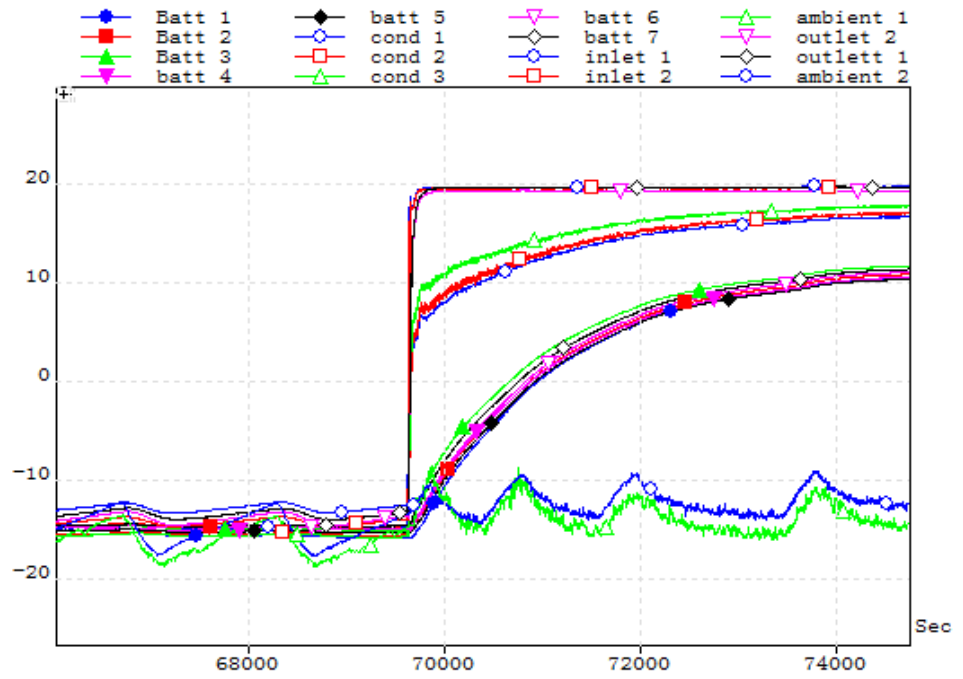


Figure D.13: $-12 \pm 2^\circ\text{C}$ ambient 20°C preheating.

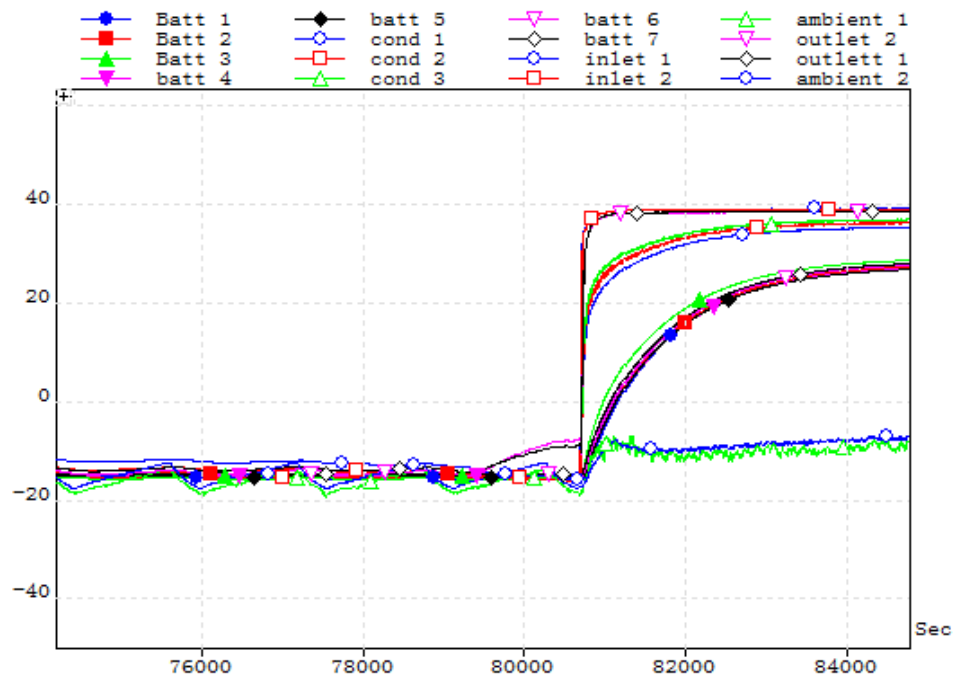


Figure D.14: $-10 \pm 2^\circ\text{C}$ ambient 40°C preheating.